PROPOSAL FOR A COST-EFFECTIVE CENTRIFUGAL ROTARY BLOOD PUMP: DESIGN OF A HYBRID MAGNETIC / HYDRODYNAMIC BEARING

by

Andrew Hilton, MEng

A thesis submitted to the University of Nottingham in partial fulfilment
of the requirements for the degree of Doctor of Philosophy

The University of Nottingham

December, 2010

ABSTRACT

The growing worldwide prevalence of cardiovascular diseases (CVD) such as chronic heart failure (CHF) highlights the need for an effective treatment method. Annually, there are an estimated 17.5 million deaths caused by cardiovascular diseases worldwide, representing 30% of all global deaths; of these deaths approximately 50% are due to CHF [1] and about 80% occur in low- and middle-income countries [2]. If current trends are allowed to continue, by 2015 an estimated 20 million people annually will die from CVD [3]. Each year, only about 3,000 people receive a heart transplant as the only current definitive long-term treatment for end-stage CHF. To compound the severity of the situation, organ donations are decreasing [4]. Implantable blood pumps offer an effective treatment to CHF, either as a bridge to transplantation / recovery, or as destination therapy i.e. use of long term mechanical circulatory support in patients with end-stage heart failure without the intention of eventual heart transplantation. With the number of sufferers of CHF rising in both the developed and developing world it becomes pertinent to design a cost-effective device.

It is the objective of this work to investigate the proposal of a new cost-effective Centrifugal Rotary Blood Pump (CRBP), which employs previously unutilized design methodology. Through the replacement of those complex, custom components seen within existing CRBPs with standard off-the-shelf components, and the implementation of high-throughput manufacturing processes, such as injection moulding, a reduction in component parts allows for a reduced profit margin and hence a reduced total cost of device. It is proposed by the author that the current production cost of LVAD devices may be reduced by up to 95%.

The work presented in this thesis identifies the principal difference between current pump designs; this is their bearing system. It is proposed here to form a new classification of bearing type that combines a passive magnetic bearing and a hydrodynamic bearing such that the relative potential merits of both systems may be exploited. Through the amalgamation of established design techniques with other more modern design practices a rigorous, adaptive design tool has been produced that CRBP designers may use to quickly obtain full impeller and volute geometry from few input parameters. The geometry output

provides a platform from which a new conceptual Left Ventricular Assist Device (LVAD) has been envisaged.

Through experimental and computational analysis of the magnetic coupling, this investigation has shown that it is possible to integrate the magnetic bearing and the drive system into one component of design; it is possible to design a magnetic coupling that not only acts as the drive system for a CRBP, but as a bearing system that offers both axial and radial bearing forces.

A spiral groove bearing (SGB) has been implemented as the hydrodynamic bearing as part of the hybrid system. Experimental investigation has shown the spiral groove bearing to be anti traumatic, which may be attributed to the short residence time of blood in the bearing. However, a reduction in the anticipated load capacity shows that the bearings are operating on a reduced viscosity; this is an indication of cell exclusion within the SGB. Comparisons to aqueous glycerol tests of known viscosities have shown that the blood bearing is operating on a viscosity close to that of plasma. It is suggested that a "shear front differential" is the mechanism behind cell exclusion, in which RBCs migrate away from areas of high shear stress into areas of relatively low shear stress.

This investigation has demonstrated the suitability of the hybrid magnetic / hydrodynamic bearing for use in a new CRBP. It has been shown that the electromagnetic drive system intended for implementation in to this CRBP can be used as an effective passive magnetic bearing. It is intended that the axial and radial bearing forces produced by the drive system are balanced by a conical spiral groove thrust bearing.

The incorporation of the hydrodynamic bearing into the magnetic bearing transforms the previously unstable passive magnetic bearing to a stable hybrid bearing. The stability of the system has been predicted through numerical analysis of the stiffness matrix and through satisfaction of the stability criteria. The natural frequencies of the system have been calculated; these are shown to be sufficiently different from any excitation frequencies identified that may cause the system to behave in an unstable fashion at the operational speed of the pump.

The main point to be realized from the analysis of the hybrid bearing system, however, is that the proposed set-up of the hybrid bearing is not feasible due to the effect of cell exclusion, which causes the SGB to operate on a reduced viscosity. The reduction in viscosity reduces the load capacity of the SGB; the magnetic preload on the impeller cannot be balanced by the chosen SGB geometry. Recommendations have been made as to the design parameters that may be altered such that the design intent of the proposed system may be realised. Future work must concentrate on the realization of that design intent through the manufacture of a prototype, which can provide a proof-of-concept for the proposed system.

The work presented here provides a feasibility study for the novel hybrid bearing / drive system and provides sound foundation upon which a prototype may be based.

Work in this thesis is also presented in the following publications:

- Hilton A, Tansley G, Coleman, M. *Spiral Groove Bearings: Haemolysis and Cell Exclusion.* Currently under review for publication in Artificial Organs.
- Hilton A, Garvey S, Tansley G. *A Novel Magnetic / Hydrodynamic Bearing for a Centrifugal Rotary Blood Pump.* Accepted and under revision for publication in Artificial Organs.
- Hilton A, Tansley G. *Creating a Magnetic Bearing / Drive System for a New Centrifugal Rotary Blood Pump.* Electronics Manufacturing and Test - consumer medical feature. Awaiting press.
- Hilton A, Tansley G. *Redesigned Blood Pump Could Save Lives and Dollars.* MedicalDesign.com, June 2009.
- Hilton A, Tansley G, *Magnetic Drive System for a New Centrifugal Rotary Blood Pump.* Artificial Organs, 2008. 32: p. 772-777.
- Patent Application: *Rotary Blood Pump.* Application No. GB 0816883, 2008.

TABLE OF CONTENTS

LIST OF FIGURES

LIST OF TABLES

ACKNOWLEDGMENTS

There are many people in my life who deserve thanks and recognition for their valued support throughout my life and times. Unfortunately, there is not enough time or space to list them all here, but all should know that I am truly thankful. Special thanks go to my nearest and dearest friends and family.

To my parents: Thank you for the best of all opportunities from the start. It is because of your continued love and support that I am able to write this. I could not have asked for more.

To my Nana and Pops: Always there, even now, to help me with my Lego.

To Geoff Tansley: Thank you for moving back to England, bringing with you the project that has undoubtedly changed the course of my life.

To Jodie: Every letter of this thesis has a part of you in it – nice choice on font. All I Wanna Be...

My Capri also deserves a mention.

"Woke up this morning with a wine glass in my hand,

Whose wine, what wine, where the hell did I dine?

Must have been a dream I don't believe where I've been,

Come on – Let's do it again?" - Peter Frampton

GLOSSARY

ACC American College of Cardiology

AHA American Heart Association

AIHA Australian Institute of Health and Welfare

ASIAO American Society for Internal Artificial Organs

Amyloidosis A group of diseases that result from the abnormal deposition of a particular protein, called amyloid, in the heart (with reference to this work).

Atherosclerosis A process of progressive thickening and hardening of the walls of medium-sized and large arteries as a result of fat deposits on their inner lining

BEP Best Efficiency Point

BEM Boundary Element Method

BiVAD Bi-Ventricular Assist Device

CCS Canadian Cardiovascular Society

CHD Coronary Heart Disease

CHF Congestive Heart Failure

CAE Computer Aided Engineering

CRBP Centrifugal Rotary Blood Pump

CVD Cardiovascular Disease

Divergence An operator that measures the magnitude of a vector field's source at a given point; the divergence of a vector field is a scalar

DOF Degree of Freedom

Dyspnea Difficult or laboured breathing; shortness of breath

ECHOES Echocardiographic Heart of England Screening

FDA Food and Drug Administration

FEM Finite Element Method

The Framingham Study The Framingham study is an ongoing epidemiologic study involving more than 5,000 people among the population of Framingham, MA. It has been conducted since 1949 by the National Institutes of Health and Boston University.

Haemolysis The lysis, or release, of haemoglobin from red blood cells into the surrounding plasma due to the breakdown of the cell membrane

Hemochromatosis Genetic disorder in which there is excessive accumulation of iron in the body

HDD Hard Disc Drive

HUD Humanitarian Use Device

Hypertension High blood pressure

Hyperthyroidism A condition in which an overactive thyroid gland produces an excessive amount of thyroid hormones that circulates in the blood.

INTERMACS Interagency Registry for Mechanical Assisted Circulatory Support

Ischemia A restriction to blood supply with resultant damage or dysfunction to tissue

LOS Length of Stay

LVAD Left Ventricular Assist Device

LVSD Left Ventricle Systolic Dysfunction

MI Myocardial Infarction

Myocarditis Inflammation of heart muscle caused by a variety of infections and conditions

NHANES National Health and Nutrition Examination Survey

NHLBI National Heart, Lung and Blood Institute

OHT Orthotopic Heart Transplant

REMATCH Randomized Evaluation of Mechanical Assistance for the Treatment of Congestive Heart Failure

RVAD Right Ventricular Assist Device

TAH Total Artificial Heart

TIC Texas Institute of Cardiology

$VO_{2\,MAX}$ Is the maximum capacity of an individual's body to transport and utilize oxygen during incremental exercise, which reflects the physical fitness of the individual, measured in liters of oxygen per minute.

WHO World Health Organisation

SYMBOLS

A Cross sectional area $\qquad$ (m^2)

B Magnetic flux density $\qquad$ (T)

B$_r$ Magnetic flux density vector $\qquad$ (T)

c$_2$ Resolved outlet velocity $\qquad$ (m/s)

c$_{u2}$ Tangential outlet velocity $\qquad$ (m/s)

c$_m$ Meridional velocity at impeller discharge $\qquad$ (m/s)

c$_{m1}$ Meridional inlet velocity $\qquad$ (m/s)

c$_{m2}$ Meridional outlet velocity $\qquad$ (m/s)

c$_{u2}$ Tangential outlet velocity $\qquad$ (m/s)

c$_{u2}$' Actual tangential outlet velocity $\qquad$ (m/s)

C$_2$ Correction factor of SGB

D$_1$ Diameter of impeller vanes at inlet $\qquad$ (m)

D$_2$ Diameter of impeller vanes at outlet $\qquad$ (m)

$\underline{f}$ Force vector $\qquad$ (N)

F* Dimensionless load capacity

F Bearing load capacity $\qquad$ (N)

F$^{(s)}$ Magnetic suspension force $\qquad$ (N)

F$_{xyz}$ Force in the x- y- z-direction $\qquad$ (N)

g$_1$ Main factor of SGB

h$_0$ Film thickness of SGB $\qquad$ (m)

h$_2$ Groove height of SGB $\qquad$ (m)

H Magnetic field intensity $\qquad$ (A/m)

H Pump head $\qquad$ (m)

J$_D$ Diametral inertia $\qquad$ (Kgm^2)

K_{m1} Inlet capacity constant

K_{m2} Outlet capacity constant

$K_{x y z}$ Stiffness in the x- y- z-direction (N/m)

K_r Radial stiffness (N/m)

$[K]$ Stiffness matrix (Nm^{-1})

$\underline{q}$ Displacement vector (m)

K_u Speed constant

m Mass (Kg)

P_{s1} Inlet recirculation ratio

Q Pump capacity (m^3/s)

r_i Inner radius of SGB (m)

r_o Outer radius of SGB (m)

R_1 Recirculation ratio

Ra Arithmetic average of the roughness profile (m)

s_{u1} Vane inlet thickness (m)

s_{u2} Vane outlet thickness (m)

u_2 Actual impeller tip speed (m/s)

U_2 Free jet velocity (m/s)

W Work (J)

z Vane number

α Spiral groove angle (deg)

α_2 Outlet angle (deg)

α_2' Actual outlet angle (deg)

β Flux density vector angle (deg)

β_1 Vane inlet angle (deg)

β_1' Actual vane inlet angle (deg)

β_2 Vane discharge angle   (deg)

β_2' Actual vane discharge angle   (deg)

γ Ridge to groove ratio of SGB

η Dynamic viscosity   (Pas)

θ Orientation angle between magnet flux density vectors (cone angle of SGB)   (deg)

λ Relative radial width of groove pattern

μ Magnetic permeability (N/A^2)

μ_r Relative permeability

μ_0 Permeability of free space $(= 4\pi \times 10^{-7})$ (N/A^2)

σ Slip

ω Angular velocity of SGB   (rads/s)

$\varphi_m^{(s)}$ Magnetic scalar potential

Φ Capacity coefficient

Ψ Head coefficient

∇ Divergence

CHAPTER 1

1   CARDIOVASCULAR DISEASE: EPIDEMIOLOGY & TREATMENT

1.1 Introduction

The growing worldwide prevalence of cardiovascular diseases (CVD) such as chronic heart failure (CHF) highlights the need for an effective treatment method. Annually, there are an estimated 17.5 million deaths caused by cardiovascular diseases worldwide, representing 30% of all global deaths; of these deaths approximately 50% are due to CHF [1] and about 80% occur in low- and middle-income countries [2]. If current trends are allowed to continue, by 2015 an estimated 20 million people annually will die from CVD [3]. Each year, only about 3,000 people receive a heart transplant as the only current definitive long-term treatment for end-stage CHF. To compound the severity of the situation, organ donations are decreasing [4]. Implantable blood pumps offer an effective treatment to CHF, either as a bridge to transplantation / recovery, or as destination therapy i.e. use of long term mechanical circulatory support in patients with end-stage heart failure without the intention of eventual heart transplantation. With the number of sufferers of CHF rising in both the developed and developing world it becomes pertinent to design a cost-effective device.

The current overall cost of a Centrifugal Rotary Blood Pump (CRBP) is approximately £42,000 [5], which produces a barrier to markets, especially in developing countries. Considering that the levels of heart disease in these areas are some of the highest in the world, the aim of this project is to design a new cost-effective device that could be produced at around 5% of the cost of current art. This is possible by designing around standard stock parts available from engineering suppliers and by using high-throughput manufacturing processes. Independent analysts have estimated the potential annual market for blood pumps in the US alone (based on the number of prospective recipients of CRBP treatment) could sit at £4,400 million before the end of 2010 [6].

This chapter identifies the severity of the problem of CHF worldwide, looks at current treatment to the problem, and through examination of current devices on the market, recognises the need for a more accessible treatment.

1.2 Cardiovascular Diseases and Chronic Heart Failure

Cardiovascular disease refers to the class of diseases that involve the heart or blood vessels that can impair the pumping action of the ventricles. For example, the failure to supply adequate circulation to cardiac muscle and surrounding tissue (caused through atherosclerosis) results in the weakening of the ventricular muscles. It is this weakening of the muscle that leads to CHF; a condition in which the heart can no longer function as an adequate pump and is unable to deliver enough oxygen rich blood to meet the body's needs. CHF can be classified as:

1. Systolic dysfunction – The diminished pumping ability of the ventricles due to muscle weakening by myocardial infarction or myocarditis. As a consequence, the ventricles become enlarged in an attempt to compensate for this decreased pumping volume (Figure 1b).

2. Diastolic dysfunction – A stiffening of the heart muscles causes a decreased volume of blood to be pumped from the ventricles (Figure 1c). Diseases such as hemochromatosis or amyloidosis can cause this stiffening, thus impairing the capacity of the ventricle to relax and fill. The most common cause of this is longstanding hypertension resulting in a thickening of the muscle.

3. In addition, although the filling capacity and pumping action of the heart may be normal (Figure 1a), an increased oxygen demand by the body's tissues (for example, with hyperthyroidism) makes it difficult for the heart to supply an adequate blood flow. This is referred to as high output heart failure.
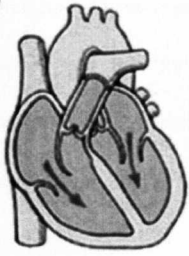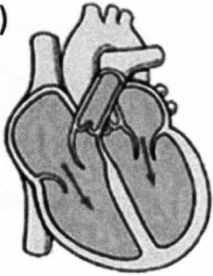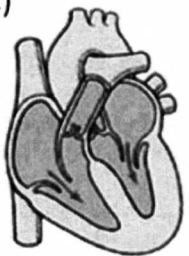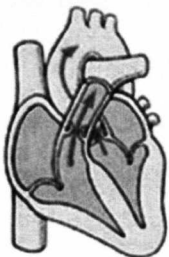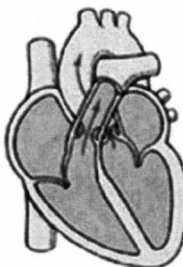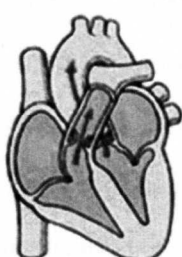
Normal Heart Function	Systolic Dysfunction	Diastolic Dysfunction
Diastole a)	b)	c)
Ventricles fill normally with blood	Enlarged ventricles	Stiff ventricles – reduced volume
Systole		
60% of blood pumped from ventricle	Reduced pumped volume 40-50%	60% of reduced volume pumped

Figure 1: Comparison of ejection fraction a) Normal heart function. b)

Systolic dysfunction. c) Diastolic dysfunction. Adapted from [7].

1.3 Epidemiology

The prevalence of CVD differs between the developed and developing world; death rates have decreased in North America and many western European countries over the past few decades, whilst a converse trend may be seen in the developing world [8].

Declining trends in CVD are due to improved prevention, diagnosis, and treatment, in particular reduced cigarette smoking among adults, and lower average levels of blood pressure and blood cholesterol. As a result of the successes in treating heart attacks and other cardiac conditions, people with damaged hearts

are living longer and are becoming more susceptible to heart failure; the prevalence of CHF is on the increase. It is expected, however, that 82% of the future increase in CHF mortality will occur in developing countries [1].That fact still remains though that there are 14.9 million people suffering from CHF within the developed world. The Framingham Study demonstrated that 30% of CHF patients died within one year of diagnosis and 60% died within the first five years [9]. The following section describes the worldwide prevalence of CHF, each geographical area receiving a different focus covering age, sex and cost, in order to develop an understanding of the global picture of the disease.

1.3.1   Prevalence of CHF in the Developed World

In the developed world, the incidence of CHF ranges from 1 – 5 cases per 1,000 in the general population and is higher in men than in women at all ages. The prevalence of CHF ranges from 3 – 20 % and is dependent upon age [10-12]. Table 1 displays the prevalence of CHF in the developed world as a proportion of the population. NB: Prevalence and incidence are different measures of a disease's occurrence. The prevalence of a condition means the number of people who currently have the condition, whereas incidence refers to the annual number of people who have a case of the condition.

Table 1: Prevalence of CHF in the Developed World [13-16].

Region	Sufferers (Millions)	% Population
USA	5[13]	1.7
Australia	0.3[14]	1.5
Canada	0.4[15]	1.2
Europe	6.5[16]	0.9
Total 14.9		

USA

Every 32 seconds an American dies from CVD; half of these deaths are due to CHF [1, 17]. According to the National Heart, Lung and Blood Institute (NHLBI), CHF is a "major disease burden in the United States". The mortality rate due to CHF has continued to rise contrarily to the downward trend in death rates for CVD over

the past 40 years; there are estimated 58,000 deaths per year due to CHF. Concurrent to this, both hospitalization rates (approaching 1 million per year) and the prevalence of CHF have shown an upward trend since the 1970s. Latest estimates suggest that there are currently a total of 5 million CHF patients in the USA [13]; such a number may be attributed to the recent rise of the major risk factors of the disease, such as hypertension, aging, obesity, diabetes and ischemia.

Figure 2 shows the prevalence of CHF in the USA by sex and age; it shows that the rate of CHF is consistently higher for men than women across all age ranges, and that the risk of CHF is far greater as age increases. In 2009, the AHA [18] reported that, "the incidence of CHF approaches 10 per 1000 population after 65 years of age and 75% of all CHF cases have antecedent hypertension. At 40 years of age, the lifetime risk of developing CHF for both men and women is 20%. At 80 years of age, remaining lifetime risk for development of new CHF remains at [more than] 20% for men and women, even in the face of a much shorter life expectancy". In addition, CHF prevalence is at least 25% greater among the Afro-American population compared to the Euro-American population [19].
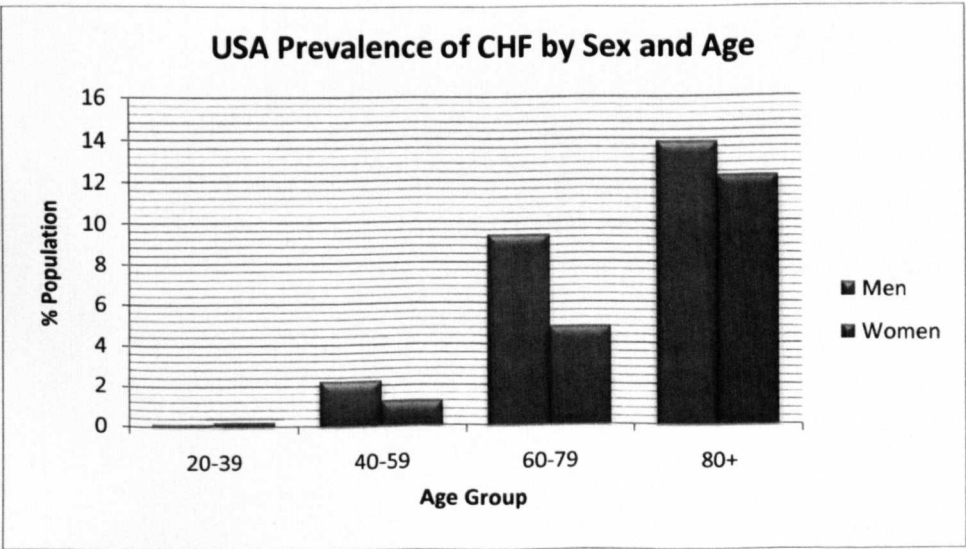
Figure 2: USA prevalence CHF displayed as age and sex. Source
National Health and Nutrition Examination Survey (NHANES)
Adapted from AHA [18].

Australia

According to a study that used the Australian Bureau of Statistics population data, there were 325,000 cases of CHF, with 22,000 new cases in the year 2000 [14]. Considering the population over the age of 45, the prevalence of CHF is 4% (approximately 300,000 current patients), and the incidence of heart failure is approximately 30,000 individuals per year, which is equal to 0.4% of the population [19].

However, as the diagnosis of patients with mild heart failure is commonly missed, Mirzaei [12] states, "the actual numbers of these estimates could be as high as twice these estimates".

The Australian Institute of Health and Welfare (AIHW) [19] points out a lack of data about the prevalence of CHF amongst Indigenous Australians. They do state however that the hospitalization rate in 2001-2002 for HF among Aboriginal and Torres Strait Islander People was approximately two to three times that of other Australians.

Canada

The Canadian Cardiovascular Society (CCS) [15] estimate that there are 400,000 Canadians living with CHF, representing 1.2% of the population. Depending on the severity of symptoms (heart dysfunction, age and other factors) CHF can be associated with an annual mortality of between 5% and 50%. The average annual mortality rate for CHF is 10% per year with a 50% five-year survival rate [20]. The Cardiology Pre-eminence Roundtable estimates the increase in the prevalence of CHF in Canada up to 2030; the figure could reach 5.6 million as shown in Figure 3.
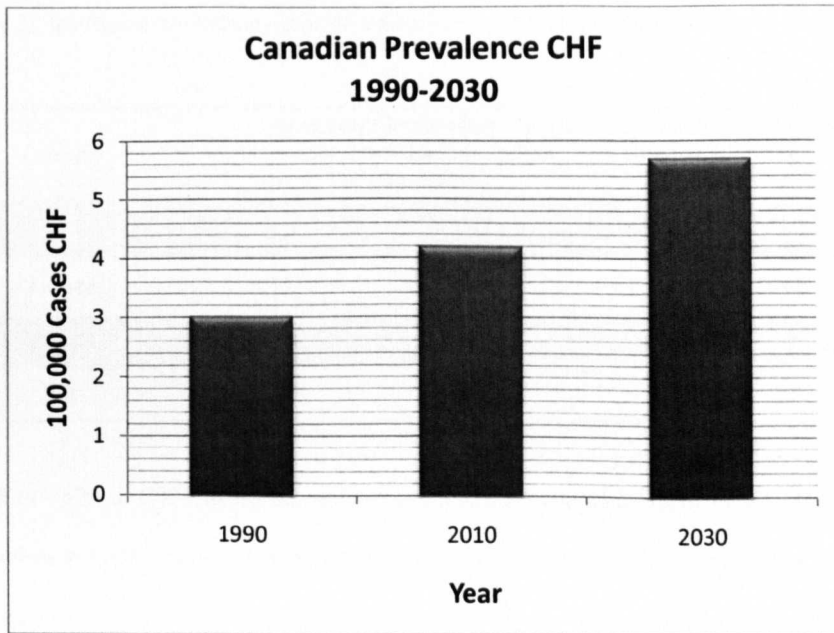
Figure 3: Canadian prevalence of CHF 1990 – 2030 [21].

Europe

In the largest recent prospective evaluation of CHF in the community, the Echocardiographic Heart of England Screening (ECHOES) study, Davies et al. [22] showed that Left Ventricle Systolic Dysfunction (LVSD) was present in 1.8% of the population over 45 years of age. Borderline left ventricle dysfunction was identified in a further 3.5% and definitive CHF in 2.3%.

In one hospital in the UK, Sutton [23] records that 4.9% of admissions were for CHF; this extrapolates to 120,000 admissions nationally per year; Erikkson asserts that this figure is rising [24]. As a consequence, CHF accounts for at least 2% of total healthcare expenditure; this represents the values shown in Table 2 [25]. (NB: The average cost per hospital admission in Europe is £9,000 [26].) It may be inferred from Table 2 that the UK as a nation are healthier than other European nations as the healthcare expenditure is around 65% of that spent in France and Germany. In reality, the fact is that due to the nature of the National Health Service (NHS), the UK simply has less money to spend on healthcare as a whole, and thus expenditure towards CHF treatment is smaller than other nations.

Table 2: Healthcare expenditure that HF accounts for in developed countries. Adapted from [25].

Country	Healthcare Expenditure Due to CHF (£million per million population)	Total Healthcare Expenditure Due to CHF Treatment (£million)
USA	62	1,860
France	34	210
Germany	33	270
UK	23	140

Considering that 90% of CHF patients die within 5 years of diagnosis, as demonstrated by the Framingham study, the values in Table 2 reveal the substantial burden on the healthcare systems that these patients have on their respective countries; this highlights the need for an effectual, cost-effective treatment to help patients with end-stage CHF within the developed world.

1.3.2 Prevalence of CVD in the Developing World

The burden of CVD varies significantly between the developed and developing world. Whereas such disease remains the number one cause of death in Europe and the USA, contributing to 50% of all deaths, CVDs account for only about 25% of deaths in the developing world [2, 27]. Despite this, CVDs are increasingly recognised as an important cause of morbidity and mortality in developing countries. This is due to at least two factors: powerful demographic changes within the population means more people are reaching the age at which CVD manifests; and, the better control of infectious, parasitic and nutritional disease [28, 29]. As information on diagnosed cases of CHF is extremely limited, the incidence and prevalence of the condition are extremely difficult to assess. The best way to estimate the levels of CHF in the developing world is to examine the mortality rate from CVDs. Table 3 displays the mortality rate for CVD in the developing world as a proportion of the population.

The University of
Nottingham

Table 3: Prevalence of CVD in the Developing World [8, 30-32].

Region	Mortality Rate (Millions / year)	% Population
Latin America	2.7[8]	0.7
China	4[30]	0.3
India	2 [31]	0.18
Africa	1.4 [32]	0.15
Total 10.7		

Projections to the year 2020 predict that deaths from CVDs will exceed deaths from infectious and parasitic diseases for the first time in all regions of the world, except sub-Saharan Africa, leading to a global CVD epidemic [27-29, 33]. Table 4 summarizes the trends seen within regions of the developing world.

Table 4: Epidemiology of CVD in the Developing world [8, 24, 29-31, 33-39].

Region			
Latin America	Asia	India	Africa
Over the past 30 years Latin American countries have experienced profound changes in their demographic, epidemiological and socio-cultural profiles, and as a result, have had a significant increase in the prevalence and incidence of heart failure	CVD has become the leading cause of death in Asian countries such as China, India and Indonesia	CVDs, especially CHF, are the major causes of death in India. There has been an exponential increase in CHF prevalence in India as identified by population-based prevalence studies over a 40-year period	As a result of the achievement in the control of communicable diseases and malnutrition, CVDs are increasingly recognised as a significant cause of morbidity and mortality in most African countries
The ratio of deaths from CVD to deaths from infectious and parasitic diseases is expected to rise from 1.1 to 4.75 during the period from 1985 to 2015	In China the mortality rate from CVD has increased from 86 per 100 000 in 1957 (and 12.1% of the total deaths) to 214 per 100 000 in 1990 (and 35.8% of all deaths) in urban areas with CHD as the leading cause of death	Absolute mortality due to CHF has increased from 1.59 million in the year 2000 (0.14 % of the population) to 2.03 million (0.18 %) in the year 2010, and is projected to increase to 2.58 million (0.22 %) by the year 2020	Nowadays, CVDs in sub-Saharan Africa account for 7-10% of all medical admissions
The proportion of annual deaths from CVD has increased from 20 to 27% in the last 20 years, with CVD being the leading cause of death (in 31 of the 35 countries reporting mortality statistics in Latin America)	Such a rise in the incidence of CVD is likely to translate into an increased incidence and prevalence of HF		

1.4 Diagnosis and Classification of CHF

In 2001 the 1995 guidelines for the evaluation and management from the American College of Cardiology (ACC) and the American Heart Association (AHA) were reviewed and amended due to the development of both pharmacological and non-pharmacological approaches to the treatment of CHF [40]. During the process, four stages of CHF were identified and treatment of each stage was recommended. Figure 4 summaries the results from the review.

Stage 1
High risk of CHF - No structural heart disease but potential for HF e.g. hypertension or family history of HF

- Treat hypertension
- Lifestyle modifications (See section 1.5.1)

Structural Heart Disease

Stage 2
Structural heart disease *without* symptoms of CHF e.g. Previous MI, LV systolic dysfunction or valvular disease

- All measures under Stage 1
- Medication in appropriate patients (See section 1.5.3)

Development of CHF Symptoms

Stage 3
Structural heart disease *with* syptoms of CHF e.g. dyspnea

- All measures under Stage 2
- Surgey to reverse symptoms (See section 1.5.2)
- Routine use of medication (See section 1.5.3)

Refractory symptoms of CHF

Stage 4
Refractory CHF requiring specialist treatment e.g. Patients who have marked symptoms at rest despite maximal medical therapy

- All previous measures
- Heart transplant (See section 1.5.4)
- Mechanical assist devices (See section 1.5.5)

Figure 4: Stages in the evolution of CHF and the recommended therapy by stage. Adapted from [41].

1.5   Prevention and Treatment of Chronic Heart Failure

Given the expected worldwide epidemic of CHF, it has become pertinent to develop effective treatment methods for the condition. Considered below are the various treatment options / combinations that are implemented to combat this chronic disease.

1.5.1   Lifestyle Modifications

Perhaps the most important and yet most neglected aspect of treatment involves lifestyle modifications for those people who are at high risk of being diagnosed with CHF, but are yet to develop symptoms of the disease. Once diagnosed, patients are expected to undertake the adjustment to their lifestyle in order to help combat the disease.

Sodium & Fluid Intake

High risk candidates for CHF and patients with CHF are sensitive to intake levels of sodium; they are therefore recommended to restrict sodium (2000 mg / day) intake due to the tendency for fluid to accumulate in the lungs and the surrounding tissue. (A point of interest: An American "no added salt" diet can still contain up to 6000 mg / day of sodium.) Similarly, the total volume of fluid imbibed should be limited to less than 2 litres / day, as the action of diuretic medication may be overwhelmed by excess fluid intake. These guidelines vary with the severity of the condition.

Aerobic & Anaerobic Exercise

Exercise was once discouraged for CHF patients. However, recently there is evidence to establish the efficacy of aerobic and resistance training for patients with CHF, and has been shown to be beneficial in maintaining overall functional capacity, quality of life, and even improving survival. "Aerobic exercise was shown to improve $VO_{2\ MAX}$, dyspnea, work capacity, and left ventricular function. Resistance exercise was shown to improve left ventricular function, peak lactate levels, muscle strength, and muscle endurance" [42]. These results support the inclusion of aerobic exercise programs and resistance training for patients with CHF. Each patient's body has its own unique ability to compensate for the failing heart. Given the same degree of heart muscle weakness, patients may display widely varying degrees of functional limitation. Regular exercise,

when matched to the patient's tolerance level, provides significant benefits, but should only be used when the patient is compensated and stable i.e. an adequate blood flow to cardiac tissue is maintained without distressing symptoms, accomplished by cardiac and circulatory adjustments.

Alcohol Consumption

Alcohol consumption is generally associated with increasing the risk of CVDs. However, moderate alcohol use is associated with a lower risk of incident CHF among older adults, even after accounting for incident MI and other factors [43]. Even among heavy drinkers (Men: $\geq$ 15 drinks per week. Women: $\geq$8 drinks per week), alcohol consumption is not associated with increased risk for CHF. When consumed in moderation, alcohol appears to protect against congestive CHF [44].

1.5.2   Surgical Procedures & Reversible Factors

There are a certain number of conditions that may be reversed to cure the underlying cause of CHF. For example, for those patients where an inadequate blood flow to the heart muscle is leading to CHF, the blood flow to the heart may be restored through coronary artery surgery, such as angioplasties and intracoronary stents. Valve surgery may be carried out to alleviate CHF that is due to severe disease of the valves. When CHF is caused by chronic hypertension, aggressive blood pressure control will often improve the condition.

1.5.3   Drug Therapies

Until recently, there has been a limited selection of medications available for the treatment of CHF, which have focused mainly on controlling the symptoms. Medications have now been developed that both improve symptoms, and, importantly, prolong survival. In the United States, approximately $500 (US) million annually is spent on drugs for the treatment of CHF [41]. Listed below are the most common types of medications that are used to treat CHF.

Angiotensin Converting Enzyme (ACE) Inhibitors

ACE inhibitors are now considered as the primary treatment for, and are the foundation of, CHF drug therapy; they reduce morbidity and mortality in selected CHF and post-MI patients. Patients with

symptomatic CHF benefit most from ACE inhibitor therapy, and treatment should be continued indefinitely [45]. ACE inhibitors work by preventing the body from creating angiotensin, a substance in the blood that causes vessels to tighten and raises blood pressure. If the blood vessels are relaxed, your blood pressure is lowered and more oxygen-rich blood can reach your heart. ACE inhibitors also help to lower the amount of salt, which also helps to lower your blood pressure.

Beta-blockers

The failing heart tries to compensate for its weakened pumping action by beating faster. Beta blockers reduce the heart's tendency to beat faster; the drugs block specific beta receptors on the heart tissue cells, reducing the effects of chemical messengers that increase heart rate. This allows the heart to maintain a slower rate and lowers blood pressure. Beta blockers are used for mild to moderate CHF and often with other drugs such as diuretics and ACE inhibitors.

Recent multicentre trials have proved that beta-blockers reduce mortality and morbidity, are well tolerated and improve quality of life. Even in a subset of severely compensated CHF patients beta-blockers have been shown to be safe and to reduce mortality and hospitalisation by 35–50 % in addition to conventional CHF treatment with diuretics, digitalis and ACE-inhibitors. All patients with stable compensated systolic CHF should therefore be challenged with a beta-blocker [46].

Diuretics

Diuretics remain an important and effective (as rated by the ACC and AHA) part of the medical therapy for patients with CHF [41]. They control fluid retention and rapidly relieve the congestive symptoms of CHF, by causing the kidneys to remove more sodium and water from the bloodstream than usual and convert it into urine. Diuretics are the only drugs used in the treatment of CHF that solely control fluid retention and that rapidly produce symptomatic benefits in patients with pulmonary and/or peripheral oedema. Because diuretics alone are unable to effect clinical stability in patients with CHF, they should always be used in combination with an ACE inhibitor (a diuretic itself) and a beta-blocker [47].

1.5.4   Heart Transplantation

Heart transplantation must be considered for those patients with Stage 4 CHF i.e. those patients who have

marked symptoms at rest despite maximal medical therapy. The procedure of an orthotopic heart transplant

(OHT) is a procedure involving just three operations: the harvesting of the donor organ; the removing of the

recipient's damaged heart; and the implantation of the donor heart – an operation that requires the creation

of only five lines of stitches that connect the large blood vessels of the heart. The first human heart transplant

was completed in South Africa in 1967 by Dr. Cristiaan Barnard; the patient lived for only 18 days. However,

widespread clinical application of OHTs was not realised until 1983 when the Food and Drug Administration

(FDA) approved cyclosporine, a drug that helps prevent the recipient from rejecting the donor organ.

Currently there are approximately 3000 OHTs worldwide [4] each year with 15,000 people currently on the

waiting lists for transplants [6]. Figure 5 shows the increase in OHTs from 1982 to a peak of near 4500

transplants per year 1994. Since then the number of procedures has been slowly decreasing.

Of those 3000 transplants, over two thirds are performed in the USA; the AHA reports that there were 2210

transplants in the USA in 2007; of these 73.7% were preformed on male patients; 67.6% of the patients were

Caucasian; 19.9% were aged 35-49; 54.7% were 50+ years old. As of May 2008, the 1-year, 3-year and 5-year

survival rates were 87.5%, 78.8%, 72.3% and 85.5%, 76.0%, 67.4% for male and female patients respectively.

The average cost (net revenue spent) of an OHT is approximately £120,000 [48].
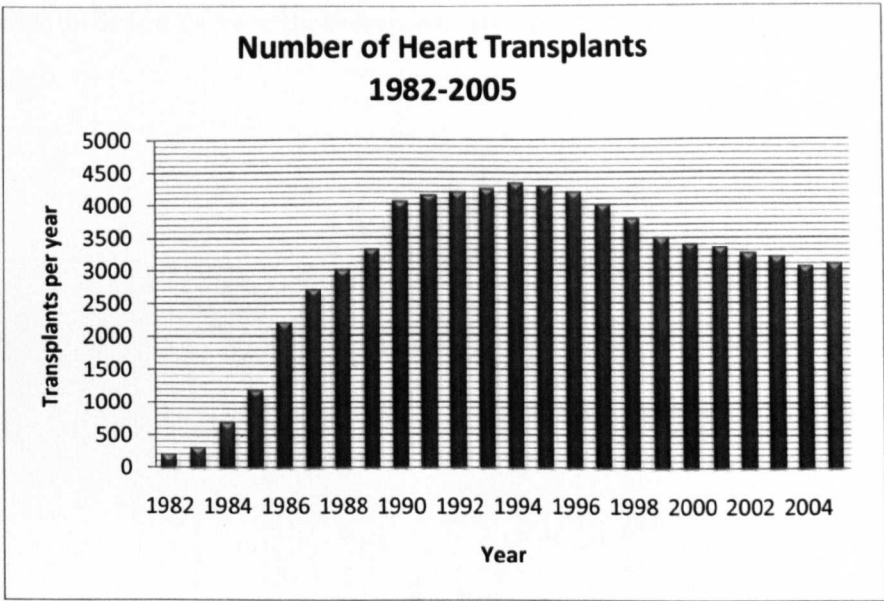
Figure 5: Number of worldwide heart transplants 1982 –
2005. Adapted from [4].

1.5.5 Mechanical Blood Pumps

Mechanical blood pumps offer two alternatives to an OHT: Total Artificial Hearts (TAH) and Ventricular Assist Devices (VAD). The difference being, a TAH acts as a complete replacement to the biological heart; a VAD works in parallel with the biological heart supplementing the diminished pumping capacity of the ailing heart. The team "artificial heart" is commonly used to inaccurately describe the term VAD. TAHs may be used only as a bridge-to-transplantation whilst VADs may act in one of three ways; as a bridge-to-transplantation, a bridge-to-recovery, or as a destination therapy i.e. use of long term mechanical circulatory support in patients with end-stage heart failure without the intention of eventual heart transplantation.

Total Artificial Hearts

The current use of TAHs is extremely limited and the devices are only regarded as an option for patients with irreversible bi-ventricular failure, and only as a bridge-to-transplantation. The CardioWest™ temporary TAH (TAH-t) was the first TAH to receive FDA approval as a bridge-to-transplant in 2004 following a 10 year clinical study, which showed that 79% of patients survived to transplantation [49]. Figure 6 shows the device as

implanted into the body; it is a pneumatic device powered percutaneously by a portable trolley containing air compressors.
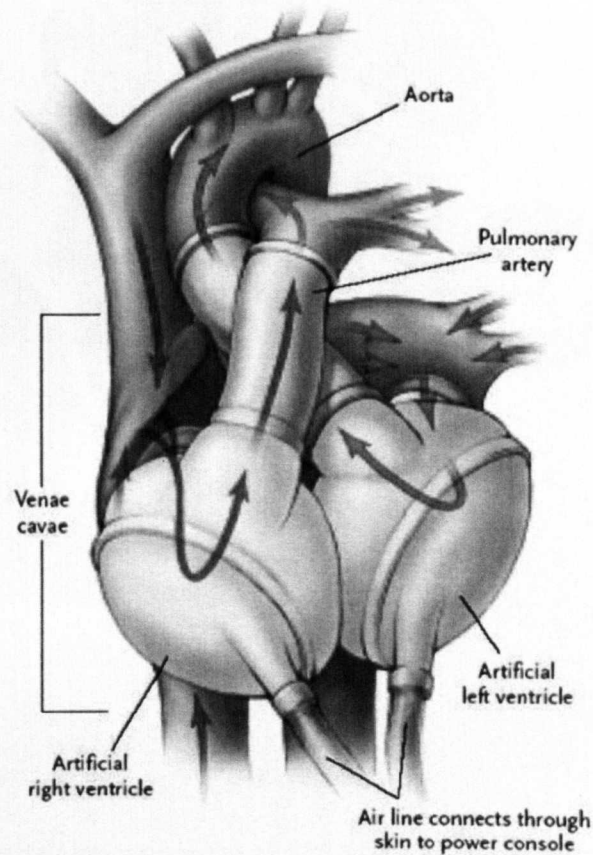
Figure 6: CardioWest™ TAH-t [50].

The AbioCor™ TAH was the second TAH to be approved for use in 2006 as a Humanitarian Use Device[A] (HUD) only due to its incompatibility to patients other than large-framed males. It too is used as a bridge to transplantation with a life of 18 months, but differs from the CardioWest™ TAH-t due to a transcutaneous energy transmission system which charges an internal battery; the device is fully implantable. Figure 7 shows the AbioCor™ TAH.

[A] A HUD is a device that is intended to benefit patients by treating or diagnosing a disease or condition that affects fewer than 4,000 individuals in the United States per year.

Figure 7: AbioCor™ TAH [51].

Ventricular Assist Devices

VADs may be classified by their role in supporting an ailing heart; they may be used to assist either the right (RVAD) or left (LVAD) ventricle, or both at once (BiVAD). The choice of device depends on the underlying cause of CHF and the pulmonary arterial resistance which determines the load on the right ventricle. LVADs are most commonly used but when pulmonary arterial resistance is high, right ventricular assist becomes necessary. VADs are most commonly used as a bridge-to-recovery or transplantation, and in some cases they are used as a destination therapy. (Peter Houghton (1938-2007) is shown in the Guinness World Records as the longest surviving recipient of a LVAD implantation at 7 ½ years [52];. the device implanted was the Jarvik 2000 as shown in Figure 9b; at the time of implantation in the year 2000, the procedure cost £170,000.)

Most LVADs are implanted through similar methods; the inlet of device is cannulated into the apex of the left ventricle; the outlet is then connected to the ascending aorta. Blood therefore flows directly from the left

atrium into the LVAD, which relieves the workload on the left ventricle. The device is connected to an external controller and power-pack by a percutaneous lead. Figure 8 shows the Thoratec HeartMate® II (Thoratec Corporation, Pleasanton CA, USA) and illustrates a typical LVAD implantation.
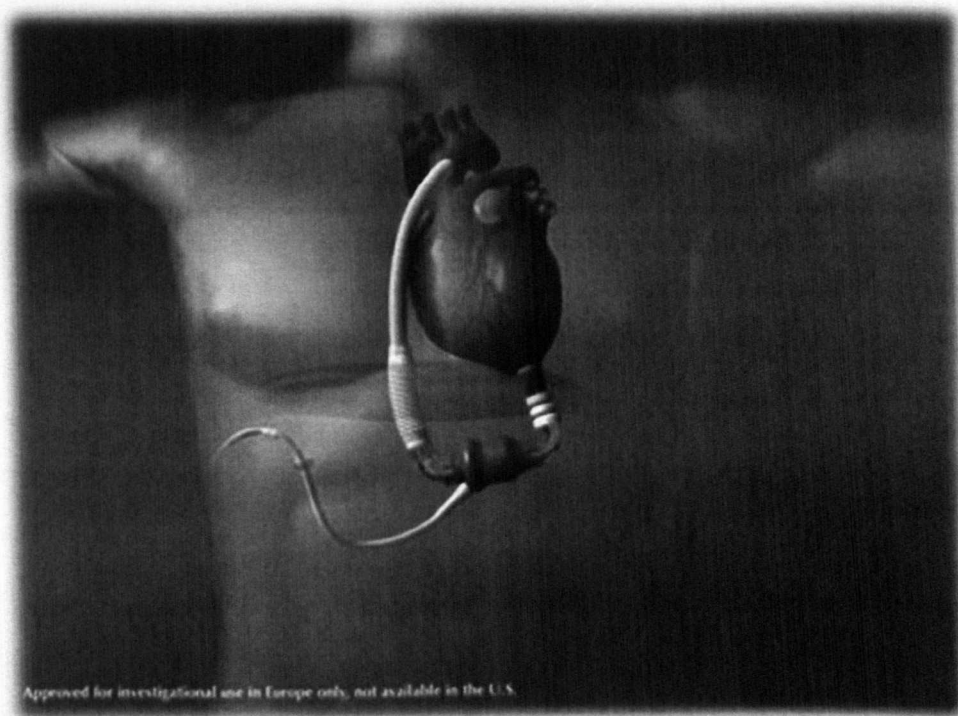
Figure 8: Thoratec HeartMate® II – schematic of implantation [53].

However, not all pumps are implanted in the same manner. The Jarvik 2000 FlowMaker® (Jarvik Heart, Inc., New York, NY, USA) for example, is a tiny pump that sits within the left ventricle itself. It operates on similar principles and the outlet is connected to the ascending aorta. Figure 9 shows x-rays of the two above mentions devices: Figure 9a shows the Thoratec HeartMate® II; the cannula is seen within the left ventricle; the device sits below the diaphragm. Figure 9b shows the Jarvik 2000 FlowMaker® contained entirely within the ventricle.
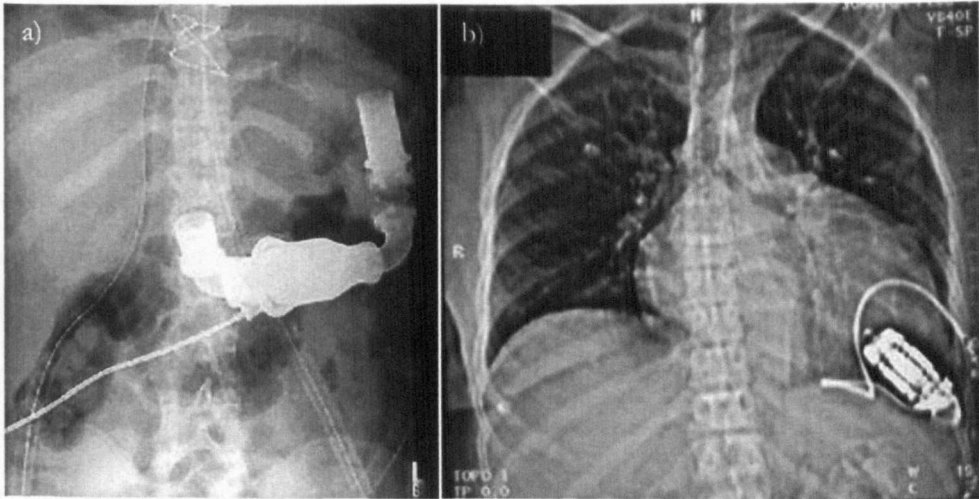
Figure 9: X-rays of implanted LVADs. a) Thoratec
HeartMate® II [54] b) Jarvik 2000 FlowMaker® [55].

VADs may provide an answer to the escalating problem of worldwide CHF. The technology has been proven and further advances, such as increased reliability and efficiency, and capacity to treat men, women and children, will only serve to validate VADs as the preferred treatment option not only for end-stage CHF, but for use in less severely ill patients. Medical device companies are demonstrating the effectiveness of LVAD therapy for use in patients who are ineligible for a heart transplant because of old age or other contraindications (e.g. intolerance of immunosuppressants); for such patients, LVADs are identified as a destination therapy. Douglas et al. [6] believe that there is a far larger patient population (other than those with Stage 4 CHF) that may benefit from LVAD therapy, including those after myocardial infarction (MI), or suffering from post-surgical cardiac failure, acute myocarditis, or dilated cardiomyopathy. Hetzer et al. [56] identify that the implantation of an LVAD reduces the stresses within the heart muscles and as such the devices may be used as a bridge-to-recovery.

The use of LVADs as a destination therapy has faced opposition and has withstood scrutiny, having been compared to presently accepted drug therapies. The publication of the Randomized Evaluation of Mechanical Assistance for the Treatment of Congestive Heart Failure (REMATCH) study in 2001, sponsored by the NHLBI and the Thoratec Corporation, provided important evidence for the support of LVADs as a destination therapy [57]. REMATCH compared the outcomes of 129 patients with Stage 4 HF, of which 61 were treated

with conventional drug therapies and 69 received a LVAD (HeartMate® VE). Rose et al. [57] comment that the results were impressive; the median survival time in the medical therapy group was 150 days compared to 408 days in the LVAD group. Figure 10 displays the results of the REMATCH study and shows the differing survival rates between drug and LVAD therapies. Figure 11 illustrates the improvement in survival rates between the HeartMate® VE and XVE devices. It serves to demonstrate the continual work that is undergoing to improve the reliability of LVADs, and further promotes their application as a destination therapy. Yusuf and Pitt summarise the factors that have lead to the ultimate demand for LVADs to be used as a destination therapy; these are the mismatch between supply and demand of transplant organ availability, the increasing incidence of CHF in the aging population in both developed and developing countries and the increasing prevalence of risk factors for HF [58]. (It is worthy of note that the longevity of the HeartMate® devices was limited by the mechanical failure of the contact bearings; this encouraged the design of 3rd generation devices, like the device exemplified in later chapters, that do not suffer from mechanical failure.)
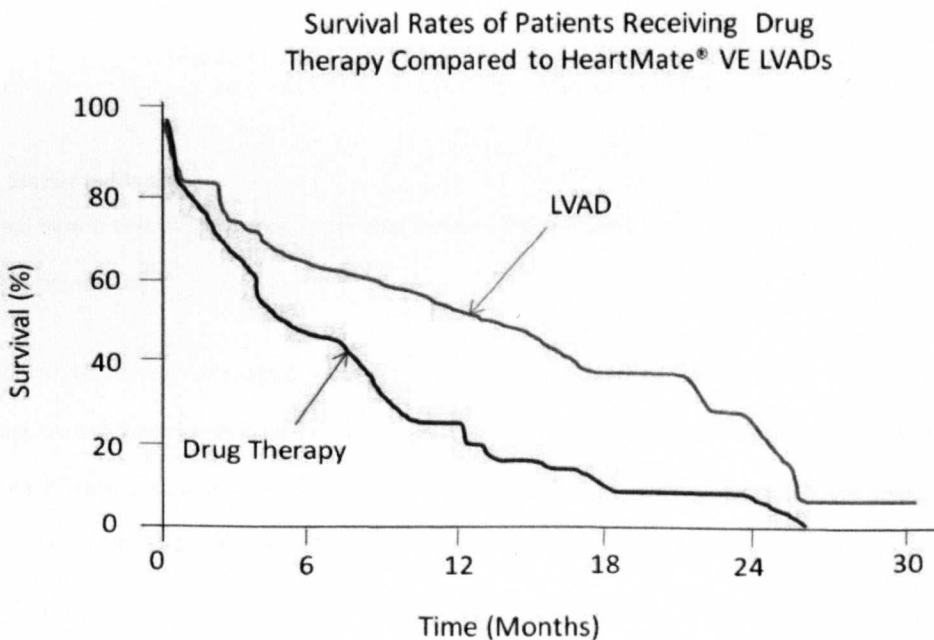
Figure 10: Analysis of survival of patients in the REMATCH study. Adapted from [57].
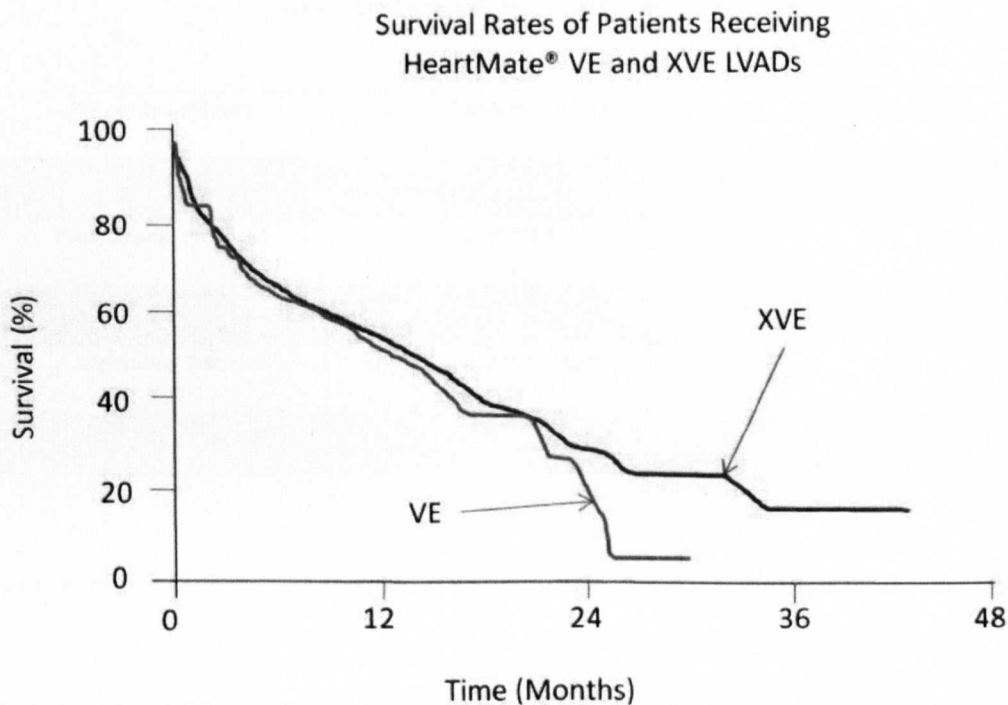
Figure 11: Difference in survival rates for patients receiving
HeartMate® VE and XVE LVADs. Adapted from [59].

1.6 Barrier to Market

Identified here is the major limiting factor that restricts the prevalence of LVADs as a viable treatment for CHF; that factor is cost.

Consider the US market for example, where there are 5 million sufferers of CHF [13]; the cost of a LVAD implantation, and the associated medical care, is especially expensive. Moskowitz et al. [5] asserted that as of 2001, the 1st year cost of LVAD implantation was around £140,000, which includes £88,000 for the initial implant related hospitalization of which £42,000 is the cost of the device. Table 5 summarizes the associated costs of CRBP; the cost of the device to the hospital is approximately 50% of the total costs.

Table 5: CRBP Hospitalization costs (adapted from [5])

Resource Category	Average Cost (£)	% of Total Cost
CRBP	42,000	48
Professional Payment	15,000 ± 6,850	17
Length of Stay	13,700 ± 11,500	15
Operating Room	6,800 ± 1,100	8
Aftercare	10,900 ± 8,400	12

However, despite a variation in devices across the range of LVADs available, their cost is comparable to that of an OHT; Digiorgi et al. [48] affirm that both treatments are far more than drug therapy for HF due to the associated longer length of stay (LOS) and higher cost for initial hospitalization for LVADs compared to OHTs. "LVAD patients have higher re-admission rates compared to OHT, but similar costs and LOS. OHT is linked to a greater number of out-patient services." Digiorgi et al. [48] also point out that, "if LVAD therapy is to become a viable alternative [to OHT] improvements in cost-effectiveness and reimbursement will be necessary."

The usage of LVADs is set to increase, driven by an underlying improvement in the technology, residual reduction in costs and the change in risk/benefit calculation by the physicians for the patient. When the approval of usage was limited to bridge-to-transplantation, the market for the device was limited to the number of patients eligible for heart transplants, which is in turn is limited by the availability of donors. By expanding the viable applications of LVADs i.e. to non-Stage 4 CHF patients, a rapidly growing market for the devices is created. Any future approval for use with less severely ill patients i.e. as a bridge-to-recovery will result in further expansion.

Estimates for the ultimate size of the market in the USA vary significantly between analysts. Moskowitz et al. [5] project that there will be 35,000 – 75,000 candidates for LVADs per year by 2020. An independent investment firm (EInvestmentBank™) in 2002 predicted that the size of the American market for LVADs could be as high as 100,000 units per year if the devices are to be used as a bridge-to-recovery. The optimism about

the future growth of the market is seen by the number of firms developing such devices (See Table 6 for classification of current devices). The aggregate costs of widespread usage of the LVAD could be astounding: At £140,000 per patient, with a market of 100,000 devices per year, the total medical costs are equivalent to £15,000 million for the costs of implantation and 1st year patient care alone [6].

Douglas et al. therefore posed the question to governments, "is it acceptable to deny patients the potential lifesaving treatment of LVADs due to the size of the aggregate costs, which may become high enough to have adverse effects in other areas of social welfare?" It is impossible for governments to provide both high-tech medical services whilst simultaneously ensuring equitable care to the entire population [6]. This therefore demonstrates the call for a reduction in the cost of technologies such as LVADs.

It is the aim of this project is to dismiss the barriers to market that currently exist by establishing a cost-effective device. By designing a LVAD that may be used as bridge-to-recovery, the market in the developed world is widened to include pre-Stage-4 CHF patients, whilst the potential market in the developing world may be entered. It is proposed to reduce the cost of these devices through implementation of standard, off-the-shelf engineering components to replace those expensive, bespoke parts that must be manufactured for current devices. Further to this, it is proposed to install high through-put processes in order to reduce the cost of manufacture. Details of the design are presented in Chapter 2.

CHAPTER 2

2   LVAD DESIGN

2.1   Introduction

This chapter evaluates the different types of LVADs that are currently on the market, and classifies them in

terms of their operation. Further to this, a new conceptual design is shown to occupy previously unexploited

design criteria. The resulting pump geometry has been produced using an amalgamation of standard

industrial centrifugal rotary pump design principles, based around that of Stepanoff [60], and has been

combined with other more modern design practices, such as Lobanoff [61] and Karassik [62], to produce a

rigorous, adaptive design tool that CRBP designers may use to quickly obtain full impeller and volute

geometry from relatively few input parameters. The geometry that is output provides the platform from

which a new conceptual LVAD may be envisaged. The full design procedure is shown in Appendix A.

This chapter also identifies the potential areas within current designs where drastic cost reductions may be

made as to facilitate the production of a new cost-effective device that may be used as a treatment to the

highlighted problem of worldwide CHF.

2.2   Classification of LVAD Designs

The history of LVAD begins in 1966 with the first successful clinical implantation of a VAD performed by M.E.

DeBakey (Houston). The device was a pneumatically-actuated paracorporeal diaphragm pump and paved the

way for the 1st generation of implantable LVADs (identified by the use of a pulsatile volume displacement

pump) as a bridge-to-transplant. These devices greatly contributed to the advancement of the mechanical

circulatory support by providing improved survival and a better quality of life. However, they were not

without their limitations such as high thromboembolic rate, high incidence of mechanical failure due to the

large number of components, large pump size and a high rate of infections [57, 63].

Rotary pumps emerged as the successor to 1st generation pumps, and eliminated the need for external

venting and prosthetic valves, which served to reduce the size of the devices. Goldstein characterizes 2nd

generation pumps by "pump technology with blood immersed mechanical contact bearings" [64], which may be employed in either axial or centrifugal flow devices. The 3rd generation pumps saw the elimination of all mechanical contact within the pump, accomplished through the use of magnetic or hydrodynamic (fluid film) levitation to produce a full non-contact bearing between the impeller and the pump casing during the operation of the device. The elimination of the contact bearing between the components (and associated heat generation) provides a reduced potential for pump thrombosis and the increase in mechanical reliability that is necessary for long-term cardiovascular support.

Previously rotary blood pumps have been classified by their bearing systems; Bearnson [65] states that they are the distinguishing feature between designs. Modern pumps may therefore be labelled under one of three categories: Miniature, blood-immersed, mechanical bearings e.g. MicroMed DeBakey VAD® (MicroMed Cardiovascular, Inc., Houston, TX, USA); full (active) magnetic suspension e.g. TerumoHeart VAD (Terumo Heart Inc., Ann Arbor, MI, USA); full (passive) hydrodynamic suspension e.g. VentrAssist® Left Ventricular Assist System (LVAS) (Ventracor, Chatswood, NSW, Australia). It is the aim of this thesis to examine the feasibility of a proposed additional category of device that uses a magnetically preloaded hydrodynamic bearing. The unity of such technologies allows for the use of passive magnetics without the need for active control; the hydrodynamic features may also be reduced allowing for increased manufacturing tolerances and more elegant blade geometry

The design of a LVAD is a hugely involved process. Table 6 summarizes some current LVADs in terms of their flow (axial / centrifugal), bearing type (hydrodynamic / magnetic), and approval type and status by region. It demonstrates that there is no preferred bearing type for 3rd generation devices; each bearing has its own relative merits. Magnetic bearings can offer large operational clearances which reduces the levels of shear stress that the blood is exposed to. However, magnetic bearings require active control in at least one degree of freedom (DOG), which results in complicated control systems that increase power consumption.

Hydrodynamic bearings offer lower power consumption, typically 35% less than active magnetic control; operational clearances are however smaller than those in magnetic bearings, which increases blood shear stress, and therefore the risk of pump thrombus through platelet activation and levels of haemolysis.

Table 6: Current LVADs classified by operation

Device (Manufacturer)	Flow			Bearing			Approval Status					
	Pulsatile	Continuous		Contact	Magnetic	Hydrodynamic	Region				Bridge / Destination	
		Axial	Centrifugal				EU	USA	Australian	Japan	Bridge	Destination
Novacor (World Heart)	•						•	•		•	•	•
Heartmate II (Thoratec)	•							•		•	•	•
Heartmate II (Thoratec)		•		•			•	•			•	•
Incor (Berlin Heart)		•			•		•				•	
Jarvik 2000 (Jarvik Heart)		•		•			•				•	•
MicroMed DeBakey VAD (MicroMed)		•		•			•	•*			•	•
MiTiHeart (MiTiHeart Corporation)			•		•							
DuraHeart (Terumo)			•		•				•			
VentrAssist (Venracor) **			•			•	•				•	•
HVAD (HeartWare) ***			•			•						

* Infants Only ** Ventracor folded Agust 2009 *** As of February 2009, HeartWare was aquired by Thoratec Corporation for $282 Million

2.3 LVAD Design

In this section, the operation of three different types of LVAD is analysed, each one with a different bearing type. The aim is to identify the benefits of the relative technologies used in different designs, and to identify an unexplored avenue through which a new category of LVAD may be envisaged.

2.3.1 Axial Flow with Contact Bearing – MicroMed DeBakey VAD® HeartAssist 5™

Figure 12 shows a schematic of the MicroMed DeBakey VAD® HeartAssist 5™. The device is a miniaturized (71 x 31 mm), electromagnetically actuated, fully implantable, titanium, axial flow VAD weighing 93 g [66].
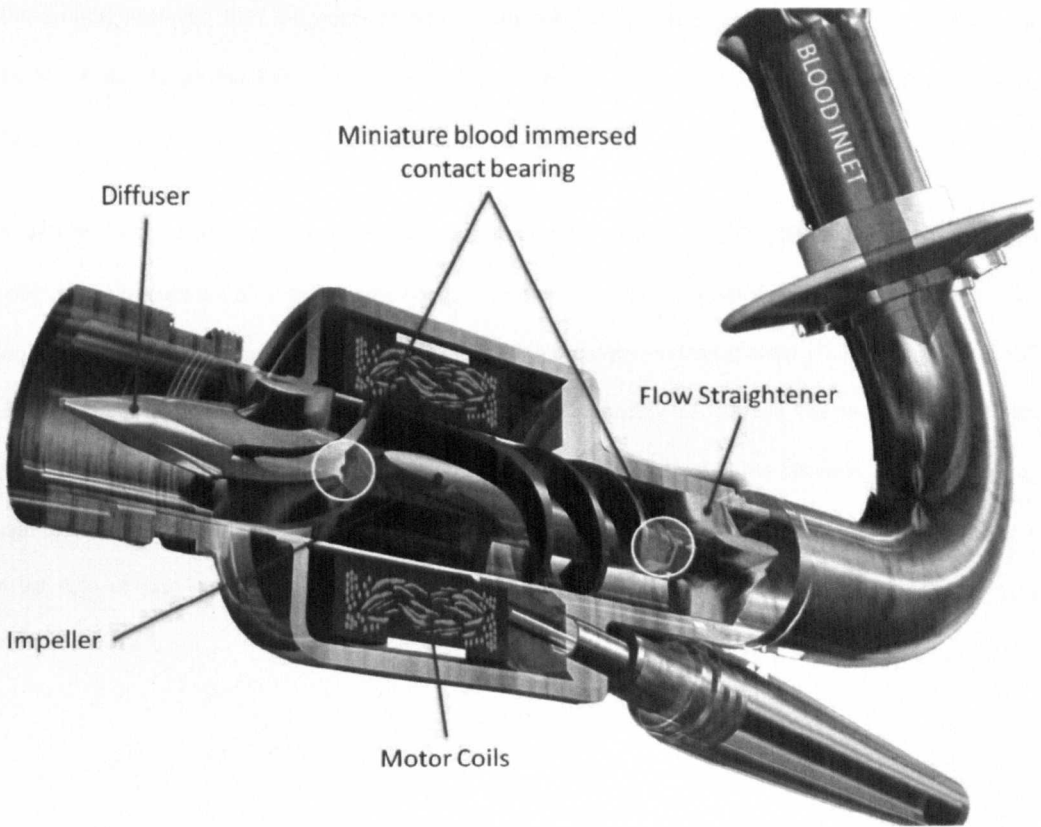
Figure 12: MicroMed DeBakey VAD® schematic [67].

The device is capable of pumping blood at 1-10 L/min but is designed to achieve 5 L/min flow against 100 mm Hg pressure, operating at a speed of 10,000 RPM [64]. The impeller is borne by two miniature, ceramic, blood-immersed contact bearings which are housed within the flow straightener and the diffuser. These

bearings ensure that the impeller remains in the optimum position and that it does not touch the casing.

Rare-earth magnets are sealed into the core of each impeller blade, which act to rotate the impeller within

the electromagnetic field generated by the coils. It is the only FDA and CE[B] approved paediatric VAD. The

HeartAssist 5™ implants above the diaphragm in the pericardial space. Most full support VADs are implanted

in the abdominal area, which increases the risk for complications including bleeding and infection. Designers

of the device state that the "efficiency of the magnet configuration provides an optimum impeller design

leading to longer battery life, which gives patients more freedom", and, "To facilitate mobility and eventual

hospital discharge, the pump can be actuated by two 12-volt DC batteries for 4-6 hours [68]". It is the opinion

of the author, however, that 4-6 hours of battery life does not provide the patient with any substantial

mobility – if the design has been optimised to the best of the designers' ability, a new solution must be

found.

Over 440 implants worldwide of the MicroMed VAD account for more than 130 patient years of life [67]. This

equates to an average life of only 105 days for each pump, although the longest support time has been 492

days. In the initial trial of the MicroMed DeBakey VAD® as a bridge-to-transplantation, the progress of 150

recipients was tracked from 1998 to 2002. Table 7 shows the outcomes from all the patients [64]. Whilst

acknowledging the outstanding work involved in the design of this device and the potential for the device as

bridge-to-transplantation or as a bridge-to-recovery, the results (as shown in Table 7) clearly demonstrate a

survival rate of just fewer than 50%, which pertinently confirms that the device is not suitable as a

destination therapy.

[B] The CE mark is a mandatory conformity mark on many products placed on the single market in the European Economic
Area (EEA). The CE marking certifies that a product has met EU consumer safety, health or environmental requirements.

Table 7: Outcome of 150 patients receiving the MicroMed
DeBakey VAD®. Adapted from [64].

Outcome	Number of Patients
Bridged to Transplant	62
Died	68
Ongoing	19
Bridged to Recovery	1
Total	150

Goldstein [64] carries on to examine the incidence of adverse event to the patient from those 150 devices implanted: 4 accounts of mechanical failure; 18 occurrences of haemolysis (defined as plasma free haemoglobin > 40 mg/dL); 17 occurrences of pump thrombus (based upon the Interagency Registry for Mechanical Assisted Circulatory Support (INTERMACS)). This means that in approximately 25% of patients the pump was cause of the adverse event. Savage et al. [69] and Yamane et al. [70] summarized that it is the stagnation area i.e. areas of low shear stress around the mechanical bearings that leads to thrombus formation. It may be concluded that the high rotational speed and the mechanical contact bearing are the causes of the haemolysis levels and pump thrombus respectably.

2.3.2   Centrifugal Flow with Full Magnetic Bearing - DuraHeart®, Terumo Heart

The DuraHeart™ LVAD is an implantable CRBP made of titanium and stainless steel. It is 72 mm in diameter by 45 mm thick, and weighs 540 g. It uses a full magnetic bearing to suspend the impeller within the blood chamber, and is comprised of four principal components: A magnetic bearing (three position sensors, three electromagnets); an impeller; a pump casing; and a DC brushless motor. Figure 13 shows a schematic of the device.

Magnetic Bearing:
Electromagnets

BLOOD INLET

DC
Brushless
Motor

Magnetic Bearing:
Position Sensors
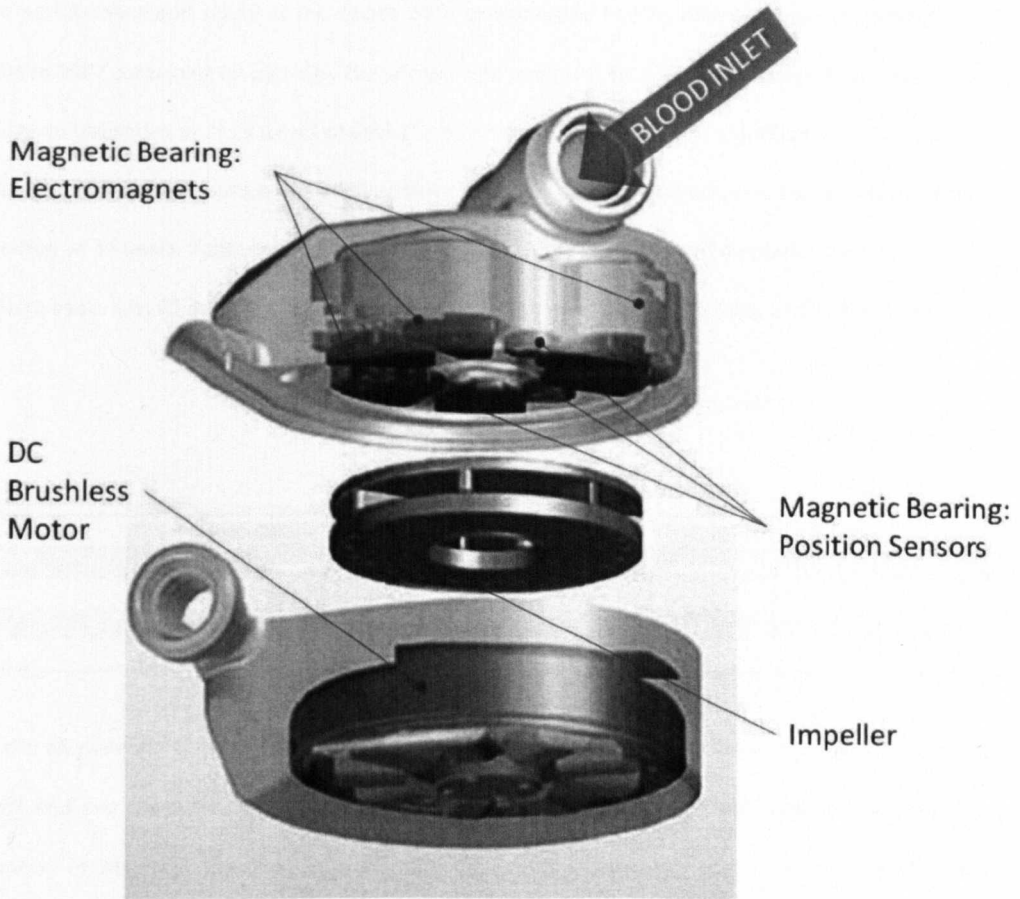
Impeller

Figure 13: DuraHeart™, Terumo Heart schematic [71].

The closed (fully shrouded) impeller is actuated electromagnetically by the brushless DC motor; the impeller is suspended by the three electromagnets, the current to which is controlled by the position sensors. The device is capable of generating pressures of 50 mmHg at 1200 RPM to 180 mmHg at 2400 RPM, producing a flow rate from 2-8 L/min. Optimal pressure of 120 mmHg occurs at a capacity of 8 L/min [63].

The DuraHeart™ LVAD features a hydrodynamic bearing which serves as a backup should the magnetic bearing fail, but does not contribute to the support of the impeller during normal operation. (Hydrodynamic separation stands at 250 µm which provides washout to the bearing whilst not in operation.)

The performance and safety of the device were characterized in a multicentre, non-randomized trial from 2004 to 2007 containing 68 patients. The primary end point was to evaluate the survival of patients either to bridge-to-transplant or at 13 weeks of device support. Secondary endpoints identified the adverse events and device performance. Results of the study showed the mean support duration was 242 days with a cumulative duration of 45 years. Table 8 summarizes the results of the study. Of the 14 patients that died, the median time to death was 62 days. The survival rate during support was 81% at 6 months and 77% at 1 year.

Table 8: Outcome of 68 patients receiving the DuraHeart™
LVAD. Adapted from [63].

Outcome	Number of Patients
Ongoing	35
Bridged to Transplant	18
Died	14
Explanted	1

Of the 68 patients, 13 were supported for more than 1 year. Of these, 4 were supported for more than 2 years and one for over 3 years. As of December 2008, 9 patients were still ongoing with mean support duration of 744 days. Examination of the adverse events showed that there was no incidence of pump mechanical failure, pump thrombus or haemolysis [63]. In comparison to the MicroMed DeBakey VAD®, the decrease in adverse events due pump design demonstrates the benefits of a full non-contact bearing system and slower running speed due to the centrifugal configuration.

2.3.3 Centrifugal Flow with Full Hydrodynamic Bearing – VentrAssist ™, Ventracor

The VentrAssist™ is a 3rd generation, implantable, CRBP with full hydrodynamic suspension designed for patients who potentially require long-term circulatory support. The device was conceived in 1998, with the first human implant in June 2003. Once implanted, the VentrAssist™ sits in a small pocket created on the left side of the body, below the diaphragm and behind the posterior rectus sheath. The pump weighs 298 g (just over half the mass of the DuraHeart™ LVAD) and measures 60 mm in diameter, making it suitable for both adults and children. The pump runs at 1800 - 3000 RPM in the normal setting. Blood pump components are hermetically sealed in the titanium housing [72].

Permanent magnets
(inside rotor vanes)

Motor coils

Impeller

Hydrodynamic
Surfaces
(upper and lower)
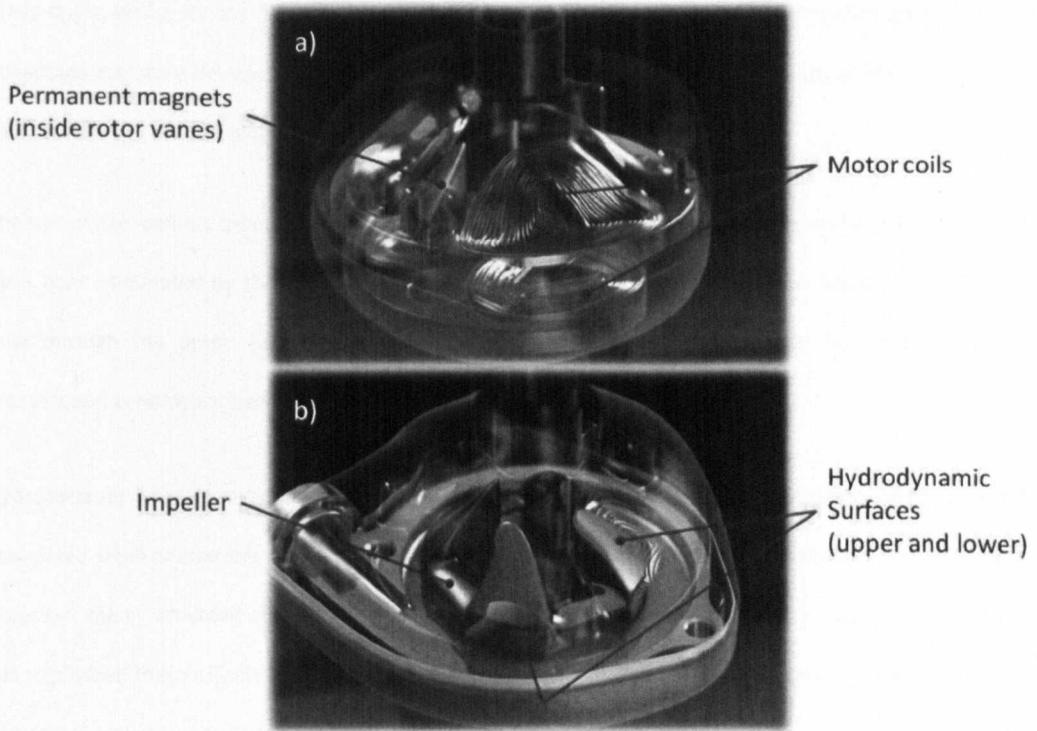
Figure 14: VentrAssist™, Ventracor schematic. a) Motor coils
and permanent magnets. b) Hydrodynamic bearing [73].

Figure 14 shows a schematic of the VentrAssist™ device. The pump comprises of six electromagnetic coils housed within the titanium casing (three above and three below the impeller) (Figure 14a). Permanent magnets are hermetically sealed within the vanes of the impeller. Each vane on the impeller has an upper and lower hydrodynamic surface (Figure 14b). Dynamic interplay between the eight hydrodynamic bearing forces, fluid forces and gravitational forces prevents the spinning impeller from touching any part of the pump's housing.

The VentrAssist™ was primarily designed as an alternative to heart transplantation for those patients with CHF, and has considered critical aspects that are important when designing a device for destination therapy. Centrifugal flow with an open impeller (non-shrouded) contributes to obstruction-free blood flow through the pump, amplified by elimination of extraneous components such as flow straighteners and diffusers. The elimination of these stationary blades reduces the risk of thrombosis formation. Further to this, Ayre et al. [74] state that the VentrAssist™ pump offers the advantage of flat pressure-flow characteristics due to outlet

blade angle, which means flow can be readily estimated from pump power and impeller speed. This is an advantage over axial devices, Stepanoff [60] adds, which cannot be designed with such an ideal pressure-flow relationship over a wide range of flows.

The use of non-contact bearings is crucial to the design of a long-term implantable device. Friction and wear have been eliminated by the full hydrodynamic bearing system; this feature helps towards an unimpeded flow through the pump that reduces the risk of stasis thrombosis caused by flow disturbances and recirculation zones associated with other types of bearings [72].

Hydrodynamic bearings may however increase levels of shear stress that the blood is exposed to due to the associated small operational clearances. Koster et al. [75] report that platelet activation may occur in areas of excessive shear; activated platelets can then form adherent thrombus or platelet emboli. The VentrAssist™ has minimized these effects by coating all blood contacting surfaces with a proprietary diamond-like carbon material, which may have a lower affinity for platelet deposition in a variety of shear environments, according to Esmore et al. [72].

The performance of the VentrAssist™ was first described in a prospective, single-arm, multicentre international clinical trial (CE Mark trial) in bridge to transplant patients (n=30) in Australia, Norway and the UK between 2004 and 2006. The outcome of the trial, at postoperative day 154, was 25 of the 30 patients (83%) were transplanted or transplant-eligible. There were no unexpected safety issues and no reported uncontrolled stops of the device. The survival rate for the pump was higher than reported for any other LVADs at the time of the trial. The overall number of implants with the VentrAssist™ had surpassed that of any other 3rd generation CRBP [72]. Although the trial demonstrated a favourable efficacy and safety profile for use of the VentrAssist™ LVAD in bridge to transplant patients [76], use of the device as a destination therapy has yet to be demonstrated. As of January 2007, the maximum implant duration stood at 2 years 8 months [72]. (As a side note, Ventracor Ltd., the manufacturers of the VentrAssist™, folded as a company in August 2009. Consequently, more up-to-date data is not available.)

2.4   Cost Reduction of a LVAD

It is proposed by the author that the current production cost of LVAD devices may be reduced by up to 95%. This becomes possible by replacement of those complex, custom components seen within existing LVADs with standard parts from engineering suppliers, and the implementation of high-throughput manufacturing processes, such as injection moulding. Figure 15 shows the proposed reduction in the cost of manufacture of the CRBP. The cost of manufacture and assembly of the pump may, typically, be estimated to be 20% of the total cost of the device (approximately £8,400); the remaining 80% is the profit margin required in order to cover the costs of development. A lower development cost through a reduction in component parts allows for a reduced profit margin and hence a reduced total cost of device.

Cost Breakdown of a CRBP

Legend: Manufacture & Assembly; Margin to Cover Other Costs

x-axis: Cost (£), 0, 10, 20, 30, 40, 50
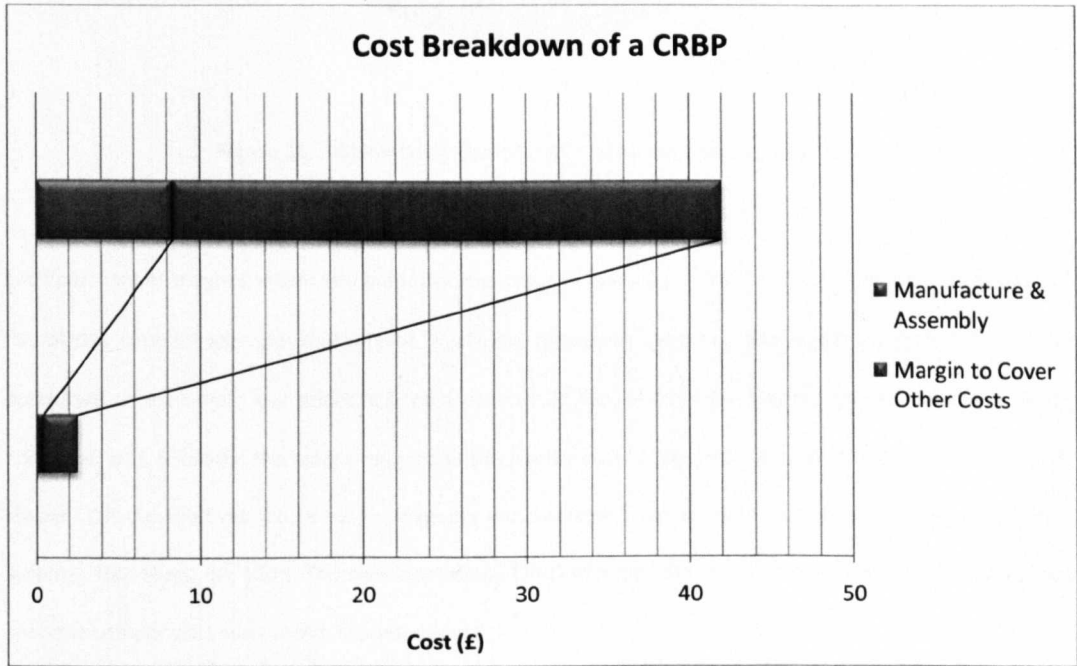
Figure 15: Proposed cost reduction

The VentrAssist™ LVAD is now considered as an example of exactly where such cost savings may be made; Figure 16 shows some detail of the VentrAssist™ LVAD. It highlights three key components where drastic cost reductions may be made: The permanent magnets in the impeller, the electromagnets in the volute case and the CNC-milled titanium volute case.
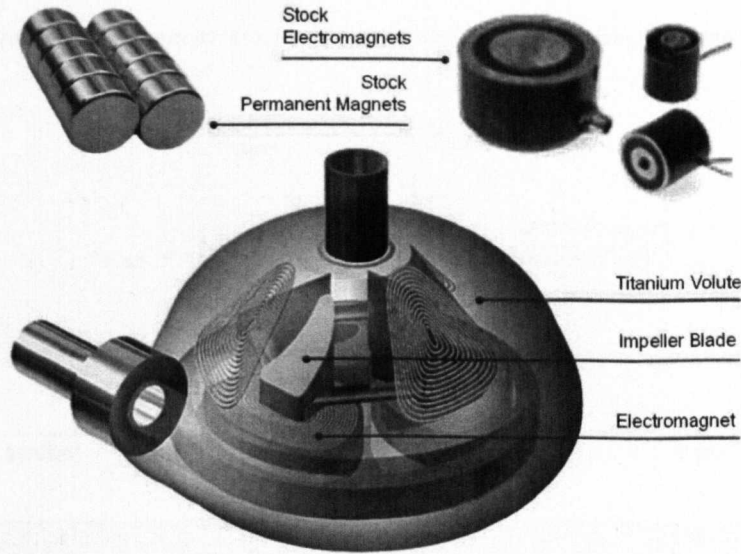
Figure 16: Schematic of VentrAssist™ LVAD detailing areas of cost reduction [73].

Each permanent magnet within the blades of the impeller costs £425. This is due to the intricate shapes of the blades coupled with the difficulty of machining rare-earth magnets. Rare-earth magnets can now be purchased at extremely low prices, £2 for a pack of 20 for example (e-magnets UK Ltd, Sheffield, South Yorkshire, UK). Similarly, the electromagnet sub-assembly costs £260 each to produce due to their complex shapes. Off-the-shelf miniature electromagnets are available from as little as £10 each (Magnetic Sensor Systems, Van Nuys, CA, USA). The new conceptual LVAD incorporates these standard parts, replacing those bespoke components seen within modern pumps.

Secondly, it is proposed to manufacture the new design using high-through-put processes such as injection moulding. Mass production of the devices in biocompatible rigid materials such as Polyetheretherketone (PEEK) means they may be manufactured more cheaply than existing rotary blood pumps, and so may be more widely used in the developing world as well as for shorter term applications within the developed world. Beiter et al. [77] evaluate the cost of an injection-moulded part; Table 9 identifies the parameters

considered in Equation 1. Figure 17 describes the potential benefit from reducing the cost of the intrinsic components of the bearing / motor in combination with a high-throughput manufacturing process.

$$C_{PART} = \frac{(C_{MACH} + C_{LABOUR})}{3600} \times t_c + (m_{PART} \times C_{MAT}) \tag{1}$$

$$C_{PART} = \frac{(100 + 50)}{3600} \times 120 + (0.025 \times 2.75) = £5.07$$

Table 9: Injection moulding cost breakdown

Symbol	Definition	Units
C_{PART}	Cost of the part	£
C_{MACH}	Cost of the machine	£/hour
C_{LABOUR}	Cost of the labour	£/hour
C_{MAT}	Cost of the material	£/kg
t_c	Cycle time per part	s
m_{PART}	Mass of the part	kg

It has been shown, through Equation 1, that it is possible to manufacture a part for as little as £5.07. If a tooling cost of £50,000 is assumed, the total cost of moulding 500 pumps (impeller, top casing and bottom casing) is £57,500. If these parts were to be machined, the estimated cost would be £200,000 (based upon a machine cost of £50 / hour and a cycle time of 8 hours for the three parts). The point at which the two procedures are comparable is for the production of 130 units. Considering the potential number of pumps that would be needed in order to meet the prospective market (a number orders of magnitude above current manufacturing levels) it is clear that the current methods of manufacture need to be readdressed.

a) **Ventrassist Manufacting Cost - Total Cost = £8,400**

Impeller

Electromagnets

Surface Coating

PCB

Canulae

Magnets

Laser Welding

Assembly

Volute Casing

b) **Proposed Cost Reduction - Total Cost = £450**

Saving

Assembly

PCB

Impeller

Electromagnets

Hydrodynamic Bearing

Magnets

Volute Casing
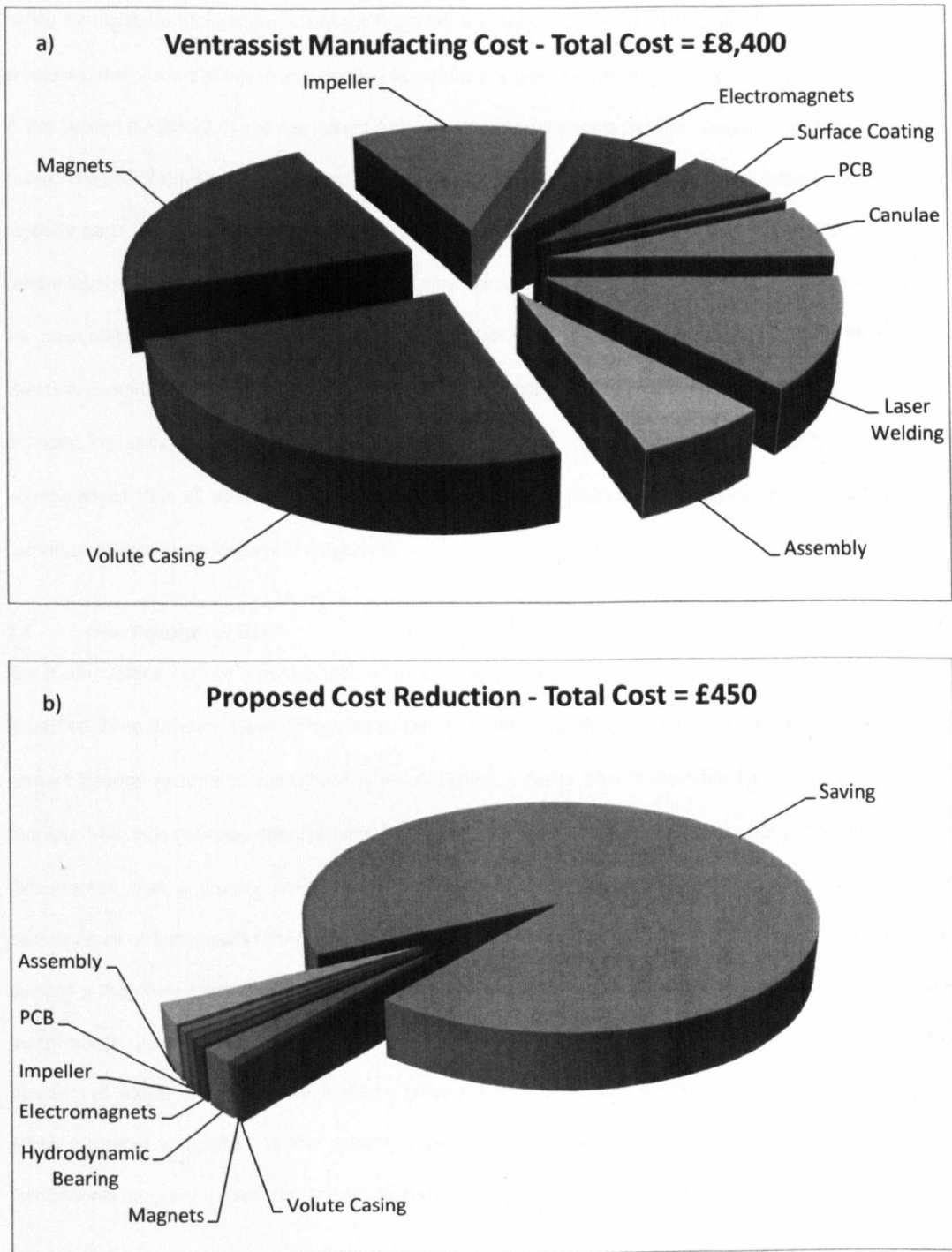
Figure 17: a) Breakdown of VentrAssist manufacturing cost
b) Proposed cost reductions

Figure 17 highlights the potential savings that may be realised by implementation of the aforementioned processes; the process of injection moulding allows for the over-moulding of the stock components identified in this Section (Section 2.4) and the integration of ancillary components (such as cannulae) to the main volute casing. The use of the stock components not only reduces the intrinsic cost through the replacement of those bespoke parts, but negates the need for the hermetic sealing (laser welding) of titanium components when combined with over-moulding methods. In this way, complete processes may be removed from production line. Cost may be further reduced though the use of established biocompatible materials, such as PEEK, in the injection moulding process; the surface treatment of those custom-machined components (such as a diamond-like carbon coating to machined, titanium surfaces) also becomes unnecessary. (The author acknowledges that all data presented on the costing of the Ventrassist is anecdotal through personal communication with ex-Ventracor employees.)

2.5   A New Conceptual LVAD

The distinguishing feature between rotary blood pumps is said to be their bearing system [65]. Section 2.3 identified three different types of bearing system that are currently used in LVADs. The importance of non-contact bearing systems is highlighted when designing a device that is intended for use as a destination therapy. Magnetic bearings offer fantastic haemolytic performance, but do require active control. It is well documented that a passive magnetic field alone cannot provide stable support of a structure as a consequence of Earnshaw's (1842) theorem [78]. As a corollary of this, a LVAD implementing a full magnetic bearing is therefore more complex due to the integration of the active control required to maintain bearing performance; power consumption is much in these bearing systems. The DuraHeart™ exemplifies the demerits of active control: Its mass is almost twice the mass of the VentrAssist™ hydrodynamic counterpart, which increases discomfort to the patient; active control is reliant upon the functionality of associated components, hence the need for, and additional cost of, a "back-up" hydrodynamic bearing,.

Hydrodynamic bearings are intrinsically much simpler, and offer an elegant solution to the problem of non-contact suspension. With the diminished power requirements comes greater mobility for the patient due to reduced battery size; a reduction in the number of components reduces the potential for a component to fail whilst simplifying the assembly of the device. Hydrodynamic bearings do however require precise

manufacturing tolerances in conjunction with close operational requirements which contribute to the high manufacturing cost of the devices. The close operational requirements mean that blood is exposed to high shear stress levels, and as such measures need to be taken to address potential problems of haemolysis. Hydrodynamic bearings typically require large surface areas on their bearing pads and have a large solidity on the rotor which reduces stage efficiency and increases power draw [79].

It is proposed here to form a 4th classification of bearing type (within 3rd generation pumps) that combines passive magnetic and hydrodynamic technologies; the unity of such technologies negates the need for active magnetic control and may simplify the hydrodynamic bearing design.

2.5.1 Design of Pump Geometry

To start the design procedure, the requirements for the pump performance need to be established. First of all, the pump has to replicate the pressures seen in the heart; the systolic pressure of the left ventricle is 120 mm Hg. The flow rate of blood through the heart is approximately 5 litres per minute. This design procedure has been standardized from various sources such as Stepanoff [60], Lobanoff [61] and Karassik [62]. The amalgamation of established design techniques with other more modern design practices produces a rigorous, adaptive design tool that CRBP designers may use to quickly obtain full impeller and volute geometry from a few input parameters. The geometry that is output provides the platform from which a new conceptual LVAD may be envisaged. Figure 18 describes the process taken when designing a rotary pump.
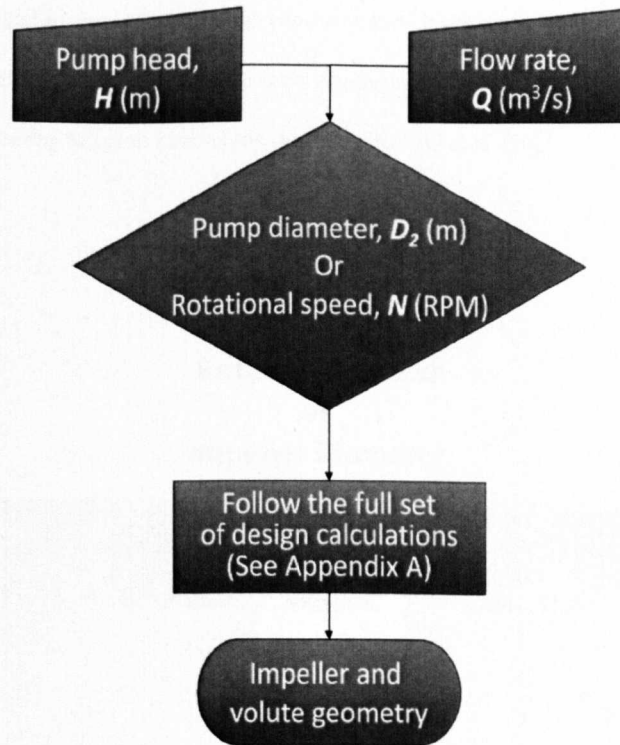
Figure 18: Flowchart showing input parameters that lead to
full impeller and volute geometry.

In an effort to produce a universal design process, input parameters must be in SI units. Therefore, the pump

head H is 1.54 m of blood (equivalent to 120 mm Hg taking densities to be: $\rho_{mercury}$ = 13579.04 kg/m^3 and

average ρ_{blood} = 1055 kg/m^3, where ρ_{plasma} = 1025 kg/m^3, ρ_{blood_cells} = 1125 kg/m^3). Pump capacity Q is taken to

be 8.3 x 10^{-5} m^3/s (equivalent to 5 L/min). At this stage, having understood the two initial requirements of

head and capacity, the designer must make the choice between axial and centrifugal flow – this is a choice

between pump size and rotational speed, both of which are critical to the performance of the end device.

Section 2.3 identified the key differences between three current LVAD designs – the key point to be taken is

that the smaller the device the faster it must spin, exemplified by the MicroMed DeBakey VAD®. Figure 19

shows the relationship between rotational speed and impeller diameter for a CRBP that is required to pump

fluid at a rate of 5 L/min against 120 mmHg; it identifies an area where size is balanced against rotational

speed. Since the rotational speed increases asymptotically with decreasing impeller diameter, it can be seen

by Equation 2 that the shear rate is larger in smaller, faster devices. High speeds are therefore associated

with an increased level of haemolysis. (Although residence time is greater for larger, slower pumps, it is still sufficiently low (less than 250 ms for a pump with displacement volume of 20 mL) such that it may be discounted as a contributing factor to haemolysis, according to Paul et al. [80].)

$$\gamma = \frac{\omega r}{h}$$

(2)

**Rotational Speed
vs
Impeller Diameter**
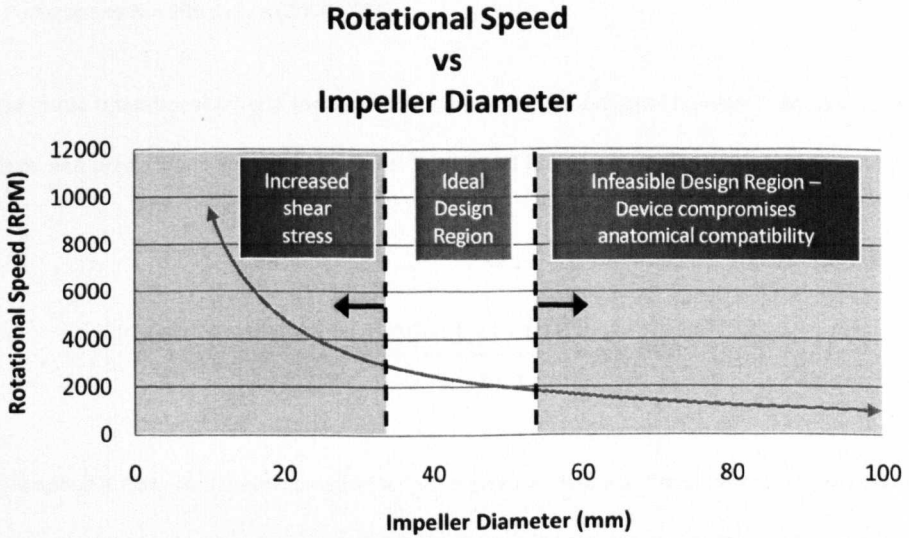
Figure 19: Relationship between impeller diameter and rotational speed
(Using Equations A1-A4 in Appendix A).

Impeller diameter affects the overall implantable LVAD size, with larger devices compromising the anatomical compatibility, thus imposing limits on the size of the patient that can receive the implant. Ideally, the pump would be as small as possible, and operate at the lowest possible rotational speed. The slowest operational speed possible for an anatomically compatible pump is around 2000 RPM in order to maintain the required pump head. The chosen design parameter is therefore a minimum operational speed of 2000 RPM; the impeller diameter can be calculated using this value.

2.5.2   Pump Geometry Design Procedure

Described in this section are some of the key calculations needed in order to produce the full design geometry for a CBRB. The full list of design calculations are detailed in Appendix A. The geometry that is

output provides the platform from which a new conceptual LVAD may be envisaged. As shown from Figure 18, the three required design parameters are therefore specified as:

- Pump head **H** = 1.54 m blood (120 mm Hg)

- Pump capacity **Q** = 8.33 x 10^{-5} m^3/s (5 L/min)

- Pump speed **N** = 209 rad / s (2000 RPM)

From these three operational criteria the specific speed, a non-dimensional number used to classify pumps by their type and proportions, may be calculated. Equation 3 [60] shows the specific speed of the proposed design.

$$n_s = \frac{N Q^{\frac{1}{2}}}{H^{\frac{3}{4}}} = \frac{2000 \times \left(8.33 \times 10^{-5}\right)^{\frac{1}{2}}}{1.544^{\frac{3}{4}}} = 680 \qquad (3)$$

The specific speed is now used, in combination with a choice for the vane discharge angle β_2 to produce a full set of design equations based upon the principle of velocity triangles as presented by Stepanoff [60], which yield the critical geometries used to dimension the pump. The vane discharge angle is the secondary geometrical parameter, after the impeller diameter, in the centrifugal pump design process, as all design constants depend directly or indirectly on β_2 (see Appendix A). Selection is based on consideration of the desired steepness of the head-capacity curve and whether or not a maximum output is desired from an impeller of given diameter as both normal head and capacity increase with angle β_2. If no limitations are applied to the pump characteristic curve, the selection of β_2 can be made for optimum efficiency. Tansley et al. [81] assert that it is desirable for the head-capacity curve of a CRBP be as flat as possible such that the pressure head is insensitive to the flow through the pump; this flat curve characteristic is associated with steeper blade outlet angles and as such β_2 is set as 70°.)

Impeller

The full set of design calculations, shown in Appendix A, describe the impeller by vane number, inlet and outlet diameter, vane heights/ widths at inlet and outlet, and vane inlet and outlet angles summarized by Table 10. Figure 20 shows a conceptual model of the impeller.

Table 10: Impeller geometrical parameters

Parameter	Value
Vane Number z	7
Vane Inlet Angle β_1	41.8°
Vane Outlet Angle β_2	70°
Vane Inlet Thickness S_{u1}	1 mm
Vane Outlet Thickness S_{u2}	2 mm
Inlet Diameter D_1	12.2 mm
Outlet Diameter D_2	44.8 mm
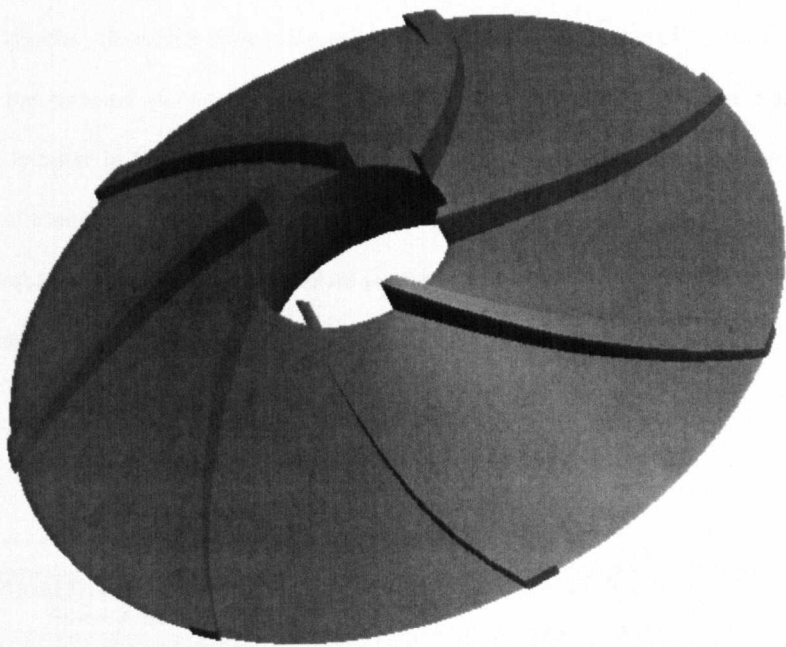
Figure 20: CAD model of the proposed impeller design

Volute

Calculations or the sizing of the volute are based upon the principle of constant velocity within the volute channel. If the impeller is designed correctly, and is manufactured just as it was designed, it is possible for the rotating impeller to continually add just the right amount of liquid to this volute area; this prevents the velocity of the liquid from changing. If the velocity of the liquid decreases, the pressure increases. Pressure acting on an area creates a force that displaces the impeller, which will impact on the performance of the pump. Volute designs are derived from the average velocity of the fluid. Since these average velocities change at different pump capacities, the final volute is designed to operate at the best efficiency point (BEP), and the performance conditions are estimated either side of the BEP [61, 82].

However, centrifugal pumps seldom run at their BEP. If there is not enough head in the system the velocity of the liquid will increase as it approaches the discharge nozzle, causing the pressure to decrease, thus displacing the impeller. Likewise if there is too much head on the system, some of the fluid will re-circulate back through the cutwater causing the velocity of the liquid to increase, making the pressure fall, and displacing the impeller in the opposite direction. The results also yield full geometry for the volute to maximise the efficiency of the pump. Parameters include base circle diameter D_3, throat area A_{th}, volute height b_3 and volute angle α_v. The resultant volute geometry is described in Table 11; Figure 21 shows a CAD model of the conceptual volute.

Table 11: Volute geometrical parameters

Parameter	Value
Base Circle Diameter D_3	47.7 mm
Throat Area A_{th}	39 mm2
Volute Height b_3	1.57 mm
Volute Angle α_v	9.15°

a)

b)
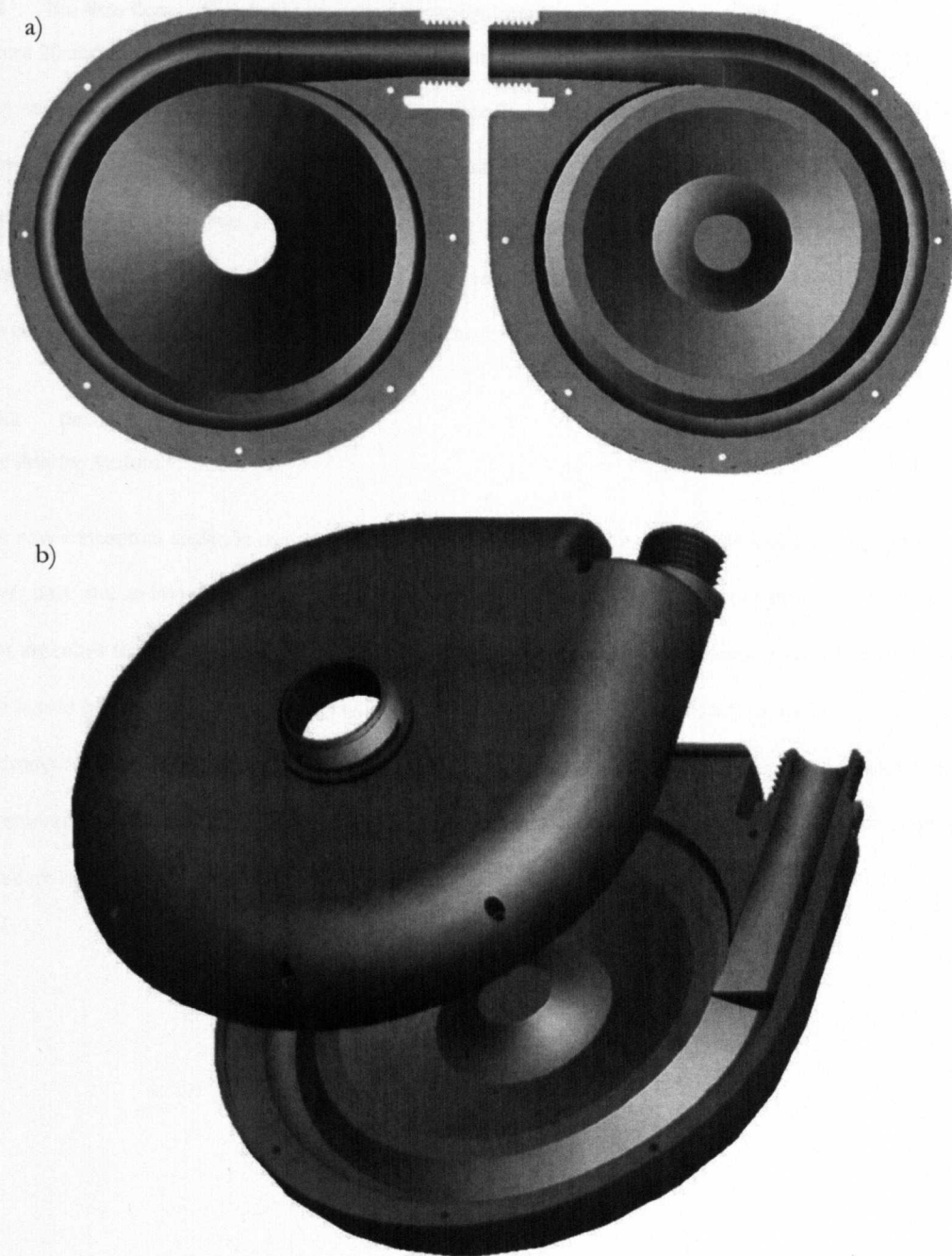
Figure 21: a) Plan view of upper volute (left) and lower volute (right). b) Isometric view.

2.6   The New Concept - Hybrid Magnetic / Hydrodynamic Bearing

Figure 20 and Figure 21 show the proposed pump geometry, which provides the start point for consideration

of a new type of bearing for a LVAD. This section describes the key features that define the invention of a

new hybrid bearing, which uses a hydrodynamic bearing that is preloaded with a magnetic one. Whilst

neither of the two bearings would provide a stable system independently, their unity provides a hybrid

configuration that exploits the potential merits of each system. Appendix B contains comprehensive details of

the design as part of the patent application for such an invention.

2.6.1   Description of the New LVAD

The Bearing System

The new conceptual design is comprised of two components: a volute casing, split into an upper part and a

lower part, and an impeller. It is the interaction between the lower half of the volute casing and the impeller

that describes the first aspect of the design – the hybrid passive-magnetic / hydrodynamic bearing system.

The hybrid bearing system is designed to work such that the two different constituents to the system (the

hydrodynamic and the magnetic bearing) support (in tandem) the five degrees-of-freedom in which support

is required (Δx, Δy, Δz, $\Delta\theta_x$ and $\Delta\theta_y$ as identified by Figure 22); hence a system exists where each degree of

freedom is supported by both constituent bearings.
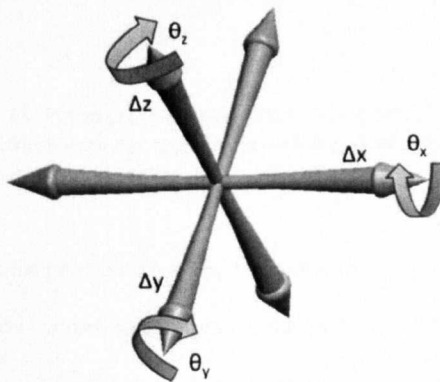
Figure 22: Degrees of Freedom (DOF)

It is proposed that the lower volute case houses six electromagnets with iron cores that interact with permanent magnets housed inside the impeller to form the passive magnetic bearing. The lower volute case has a hydrodynamic bearing surface that reacts with a corresponding hydrodynamic surface on the underside of the impeller. The volute bearing magnets and the impeller bearing magnets are arranged to form an axial magnetic bearing for preloading the hydrodynamic bearing by providing a magnetic force which acts to force the hydrodynamic bearing surfaces axially together. The impeller hydrodynamic bearing surface and the volute hydrodynamic bearing surface are arranged to form an axial hydrodynamic bearing that provides a hydrodynamic force which acts to force the two surfaces axially apart during rotation of the impeller; Figure 23 describes this interaction. The impeller is not reliant on either one of the bearings for support in a specific direction; the two bearings share the support of the impeller in all five of the required DOFs.
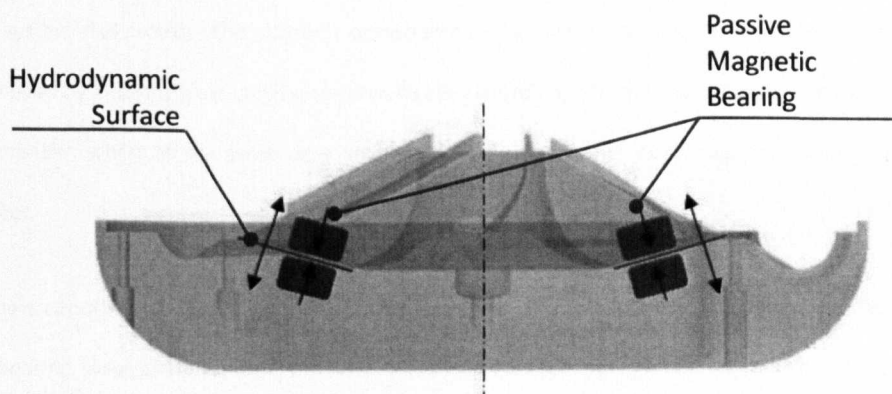
Figure 23: Pump cross-section: Passive magnetic bearing acts to force impeller and casing together. Hydrodynamic bearing acts to force the components apart.

The performance of the hybrid bearing is enhanced by the inclusion of a conical bearing surface. Whereas a planar bearing would only develop hydrodynamic forces in the z-axis translation, and the x- and y-rotations, a conical bearing develops additional forces in the x- and y-translations; a conical bearing thus provides bearing forces in all three translational DOFs, and two rotational DOFs. This has the advantage of increasing the operational stability of the pump [83], as shown in Chapter 3.

A key feature of the LVAD is the axial magnetic preload of the axial hydrodynamic bearing. The advantage of this, compared to preloading by another hydrodynamic bearing on an opposing surface, is the possibility of a semi-open impeller, the advantage of which is that the pump allows for wider manufacturing tolerances, since a hydrodynamic bearing is only present on one surface. Lower manufacturing tolerances may lead to the implementation of high-throughput manufacturing processes e.g. injection moulding, which would serve to reduce the cost of the device.

The Drive System

The second aspect of the design describes the drive system for the LVAD; the new design incorporates ferromagnetic cored electromagnets in the lower volute casing. The salient principle here is the employment of the ferromagnetic cores of the electromagnets as a magnetic preload. In other words, the electromagnetic drive system also provides the magnetic component of the hybrid bearing used to support the impeller.. This is achieved by applying time-varying currents to the electromagnets at their circumferential locations around the impeller, whilst at the same time ensuring that a uniform net axial magnetic force is applied to the impeller.

The new conceptual design may therefore be described as a hybrid electromagnetic / hydrodynamic drive and bearing system; the system provides a full non-contact, passive bearing that is integrated into the electromagnetic drive system of the pump.

Figure 24 shows a schematic of the new LVAD. The impeller houses a ring of 16 individual cylindrical NdFeB (grade N42) magnets (5 mm $\emptyset$ by 3 mm thick) arranged on a 15° (included) cone angle. The 16 magnets are arranged into 8 pairs, each pair with an alternating direction of magnetic flux through the thickness of the ring. The drive system for the pump consists of six electromagnets (iron cores 4 mm $\emptyset$ by 10 mm thick) beneath the impeller arranged on the corresponding cone angle. The drive system is therefore referred to as an 8/6 permanent magnetic drive. The hydrodynamic bearing surfaces are shown (inset and inverted); the volute hydrodynamic surface is a conical surface with low surface roughness ($R_a < 2$ µm); the impeller

hydrodynamic surface is on the underside of the impeller and is a conical spiral groove bearing (SBG), specifications of which are detailed in Chapter 4.
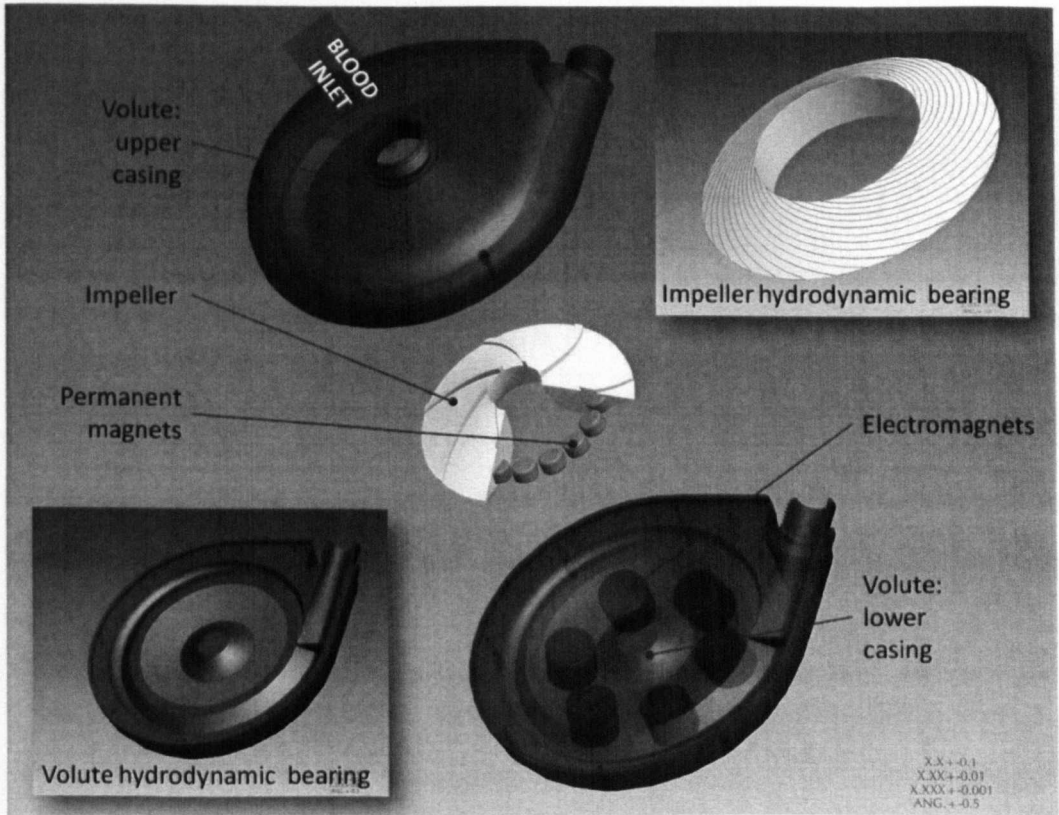
Figure 24: Schematic of new concept LVAD. The hydrodynamic surfaces are shown (inset).

The intended constitution of the drive system is a single-sided, double 3-phase motor, such that coils are fired in diametrically opposed pairs. Only two pairs are ever active at one time; each energised pair produces opposite electromagnetic fields such that there is zero net axial or radial force projected onto the rotor, whilst transferring electromagnetic torque to the impeller. There exists an underlying magnetic preload formed between the permanent magnets and the ferro-magnetic cores of the electromagnets, which is balanced by the hydrodynamic bearing.

Chapter 3 describes the experimental techniques that have been involved in the design of the magnetic arrangement that forms the bearing / drive system. It involves the experimental testing of simple permanent

magnet arrangements, and the computational modelling of more complex arrangements. Results show how magnetic force varies with hydrodynamic separation gap and the torque characteristics of different setups. Chapter 3 also details how a cone angle affects the radial restoring force, thus highlighting the benefits of the inclusion of a cone angle. The computational analysis yielded results for the axial force and the torque between the components at angles of misalignment, and showed how the coupling may be used as a radial bearing by examining how the radial forces vary with an increasing cone angle. Chapter 3 also serves to validate the computational analysis subsequently used in Chapter 5.

Chapter 4 continues by analysing the performance of the hydrodynamic bearing. It details the design process involved in choosing optimum bearing geometry by looking at how the different design parameters affect performance. Further to this, Chapter 4 examines the haemolytic performance of the bearing as a function of hydrodynamic film thickness. Also, groove cross-sectional geometry is investigated to evaluate the haemolytic performance, as well as how the bearing affects haematocrit levels of the blood in the bearing gap.

Chapter 5 then investigates the overall stability of the proposed hybrid bearing / drive system. The performance of the bearings under shock excitation has been estimated through numerical differential methods. The stiffness matrixes for each bearing are produced independently, and then are combined to show that the bearing is inherently unstable due the effects of cell exclusion identified in 4. Modifications are suggested of how the system may be augmented in order to realised the intended design remit.. The natural frequencies of the combined bearing are calculated so show that the bearing will be stable under start-up and full operational conditions.

C H A P T E R   3

3   MAGNETIC COUPLINGS & BEARINGS

3.1 Introduction

The aim of this chapter is to report the interaction between permanent magnet arrangements that exemplify the magnetic component of the hybrid bearing system; this chapter also aims to validate the computational methods subsequently used (in Chapter 5) to analyse the proposed arrangement for incorporation into the design of the novel electromagnetic drive/magnetic bearing system for a new centrifugal rotary blood pump. The aim also was to identify the influence of different magnetic arrangements on the behavior of the magnetic bearing; to investigate intrinsically how the introduction of a cone angle may be beneficial to any proposed magnetic bearing system. The experiments in this chapter are not indicative of the final design choice, but merely serve as a precursor to the design work through validation of the BEM analysis and justification of the inclusion of a cone angle.

A new conceptual LVAD has been proposed in Chapter 2; the design incorporates electromagnets into the pump casing that not only serve as the drive system to the CRBP, but also as part of the hybrid non-contact bearing. The drive system consists of two components: (i) permanent magnets within the impeller of the CRBP; and (ii) the driving electromagnets. The magnetic component of the bearing consists of the preload produced from the attraction between the permanent magnets within the impeller and the ferromagnetic cores of the electromagnets. Passive magnetic preload with permanent magnetic bearings offers a number of advantages, namely zero power consumption and extreme reliability and longevity due to the inherent simplicity of a passive system. It is the aim of the analysis presented in this chapter to characterise some basic principles that may be employed in the final design, such as how magnetic backing conditions and angular orientation of the magnetic arrangement may affect the preload produced by the magnetic bearing.

A convenient starting point for this investigation was a permanent magnetic coupling. Simple experiments were conducted analysing the force / torque characteristics for various conical magnetic configurations.

Further to the bench-top experiments, magnetic arrangements were modelled computationally and analysed using the Boundary Element Method (BEM) software Amperes (Integrated Engineering Software, Winnipeg, Canada). The modelling allowed for simulation of more complex magnetic arrangements that would have been difficult to test experimentally. It was shown that magnets in the drive system may be orientated not only to provide adequate coupling to drive the CRBP, but to provide significant axial and radial bearing forces capable of withstanding over 10 g shock excitation on the impeller.

3.2 Permanent Magnet Theory

Permanent magnets may be used to provide passive levitation and / or positioning of a structure [84]. There are many geometric configurations that show the capability and diversity for permanent magnets applications. Coey [85] states that permanent magnets are unique in their ability to deliver magnetic flux into the air gap of a magnetic circuit without any continuous expenditure of energy.

It is well documented that a passive magnetic field alone cannot provide stable support of a structure. This is a consequence of Earnshaw's theorem [78], which states that there is no stable system of levitating permanent magnets. As a consequence a passive magnetic bearing may not be used exclusively to support a structure.

Delamere et al. [86] show for a passive magnetic bearing, "that never will a radial bearing be axially stable nor will a thrust bearing be radially stable". Consequently, they must be used in conjunction with a mechanical system or active magnetic bearings in order to achieve complete, stable suspension. A passive magnetic bearing will be either a radial bearing if it controls a rotation axis, or an axial one, when it maintains the position of the rotor against displacement along the axis of rotation [87]. However, the proposed design of this magnetic bearing would incorporate both radial and axial bearing forces due to a conical magnet arrangement.

3.2.1 Force and Stiffness of a Magnetic Coupling

In order to evaluate the forces between two magnets some simplifying assumptions are made. The magnetic material is assumed to be ferromagnetic and neither paramagnetic nor diamagnetic (e.g. rare earth magnets

such as NdFeB magnets are modelled). For rotating applications, the separation between the magnets is small in comparison to the radius of the bearing. The length of the magnet perpendicular to the cross section is large compared to the gap size, and thus flux lines are organised in cross sectional planes - this yields a two-dimensional problem. Yonnet [87] considers the forces and stiffness involved in a radial magnetic bearings; Equations 3-5 establish the forces and stiffness of a magnetic coupling in the centred position, adapted from [87]; **Error! Reference source not found.** Table12 identifies the parameters.

Yonnet [87] describes the axial and radial forces of a magnetic bearing as:

$$F_z \approx \frac{-B_{r1}B_{r2}}{2\pi\mu} \frac{2}{r^3} A_1 A_2 \sin(\theta) \tag{4}$$

$$F_{x/y} \approx \frac{-B_{r1}B_{r2}}{2\pi\mu} \frac{2}{r^3} A_1 A_2 \cos(\theta) \tag{5}$$

Table 12: Parameters for magnetic theory

Parameter	Symbol (units)
Force in x / y / z direction	$F_{x/y/z}$ (N)
Stiffness in the x / y / z	$K_{x/y/z}$ (Nm^{-1})
Flux density vector	B_r (T)
Area of bearing cross-section	A (m)
Magnetic permeability ($\mu = \mu_0 \mu_r$ where $\mu_0 = 4\pi \times 10^{-7}$ WbA^{-1}m^{-1} and μ_r is the relative permeability of the material in the separation gap)	μ (WbA^{-1}m^{-1})
Separation gap between the magnets	r (m)
Angle of flux density vector to the x-axis	β (degrees)
Orientation angle between magnet flux density vectors	θ (degrees)

Figure 25 shows three possible bearing configurations and extends the theory presented above to now consider ring magnets. Yonnet [87] describes the stiffness of such a magnetic ring bearing:

$$K_z \approx \frac{B_{r1}B_{r2}}{4\pi\mu} \frac{6}{r^4} A_1 A_2 \cos(2\theta) = C\cos(2\theta) \tag{6}$$

If a magnetic bearing were to be made solely from permanent magnets, for the system shown in Figure 25, the magnitude of the axial stiffness would be exactly twice that of the radial stiffness: $K_z = -2K_r$ [87]. Solving Equation 4 for C:

$$\alpha\text{-type: } C = K_x = -\frac{K_z}{2} \qquad \beta\text{-type: } C = K_x = K_z = 0 \qquad \gamma\text{-type: } -C = K_x = -\frac{K_z}{2}$$

↑ **Magnetic Flux Density Vector**

| α-type bearing | β-type bearing | γ-type bearing |
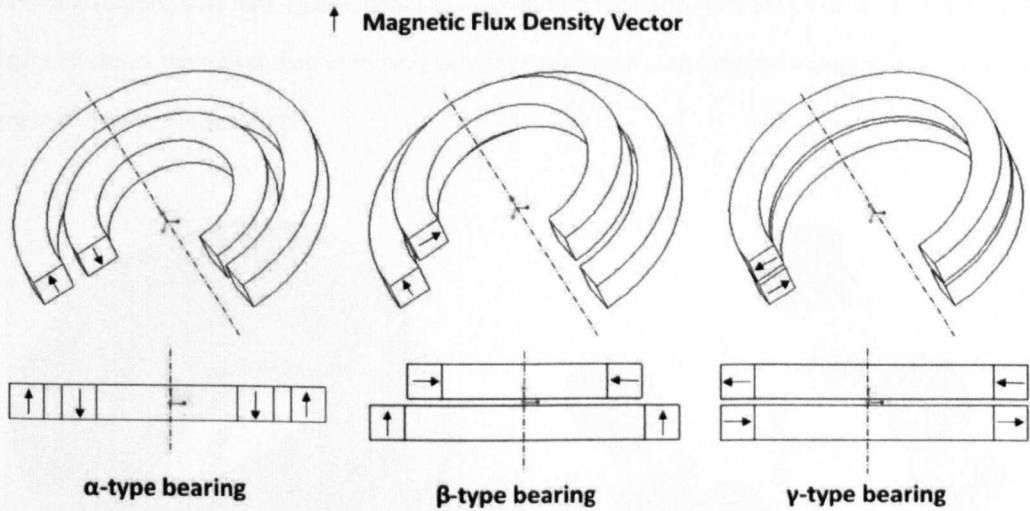
Figure 25: Possible arrangements of magnetic bearing
(direction of magnetic flux density shown)

The **α**-type leads to highly unstable radial stiffness, but the axial force is null for the middle position. The **β**-type does not produce any significant stiffness. The **β**-type is therefore advantageous in applications where the strains on the bearings have to be minimised. The **γ**-type leads to a high axial force and contributes to maintaining the rotation in a centred position. Therefore for an application of a magnetic coupling as suggested by the design of this CRBP, it is desirable to have a **γ**-type coupling.

3.3   Physical Testing of Magnetic Coupling

A magnetic coupling can be used to transmit either rotational or linear motion. In order to create a coupling, the device must consist of two multi-pole ring magnets, with an alternating flux density vector through the thickness of the ring. Like a magnetic bearing, all the possible configurations for a coupling can be obtained

by convenient arrangement of the magnetisation (i.e. flux density vector), through a given cross sectional plane of the magnet.

Discussion so far has centred on the arrangement of ring magnets with alternating magnetic flux densities to produce a coupling with the desired bearing potential. If we now consider replacing the ring magnets with a number of identical small disc magnets, the same bearing configuration may be achieved by inverting every other disc magnet, thus forming an alternating magnetic field similar to that produced by the ring magnets. Figure 26 shows the substitution of the ring magnets mentioned in the magnetic theory for the small disc magnets identified in Section 2.4.

a)
b)
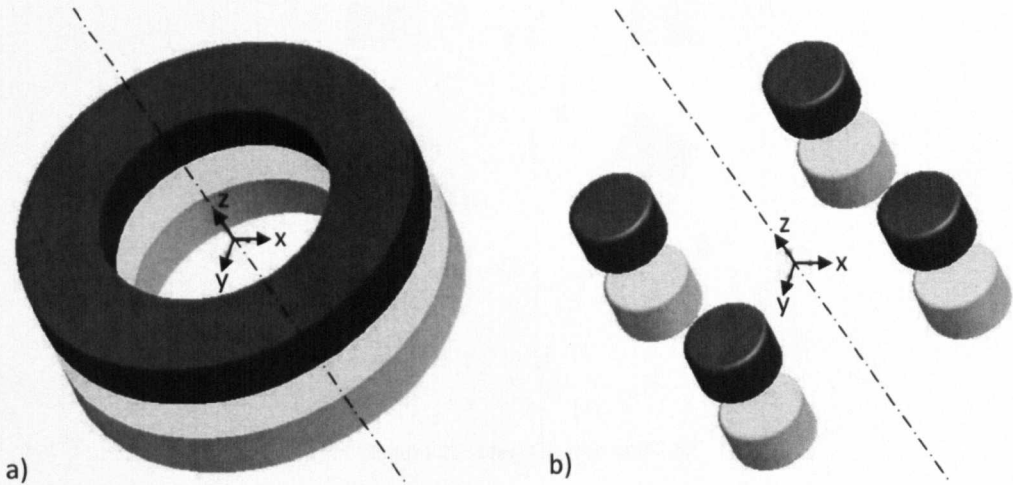
Figure 26: a) Ring magnet bearing. b) Rings substituted for
disc magnets to achieve the same bearing configuration.

The performance of the proposed design must be tested to determine the optimum magnet configuration. Factors that were considered include: the attractive forces between the two components of the drive system at angles of misalignment (around the z-axis), the torque between the two components at various angles of misalignment (around the z-axis), and the restoring torque between the two components at translations of misalignment (along the x- and y-axes) as defined by Figure 22.

3.3.1 Physical Testing - Attractive force between the two parts of the drive system
Method

The attractive force between the two components of the coupling was measured. A variety of magnet holders were designed using Pro/ENGINEER and subsequently 3-D printed using a rapid prototype machine. These magnet holders embody some potential magnetic arrangements which could be used within the CRBP, including a range of angled, conical surfaces (0°,10°, 20° and 30°). Figure 27 identifies the magnet cone angle θ.
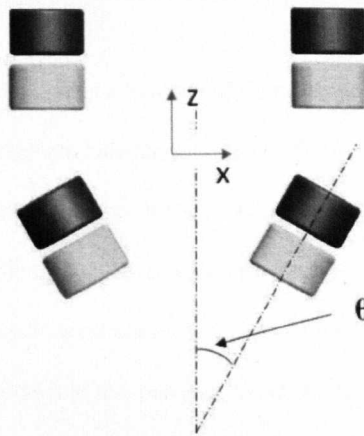
Figure 27: Magnet cone angle θ.

Figure 28 shows the experimental setup. The upper component represents the impeller whilst the lower represents the pump casing. The samples can accept between 0 and 8 individual magnets (magnet dimensions: 8mm diameter by 5 mm – grade N42. e-magnets UK, www.uk-magnets.com). The magnets sit on a pitch-circle diameter of 30 mm. The samples were designed to clamp into a tensile testing machine (Instron 5560 Series fitted with a 50 N 2527 Series Dynacell load cell (Instron, Buckinghamshire, UK).
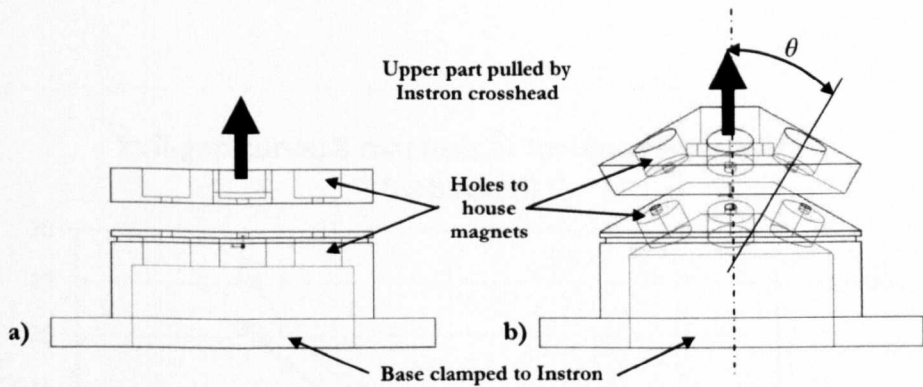
Figure 28: Magnetic pull-off tests shown at 5mm separation. a) 12 magnets at $0°$ cone angle θ. b) 12 magnets at 30° cone angle. Note samples are fully aligned around the z-axis (i.e. in $\emptyset$).

The Instron is capable of measuring force as a function of displacement. The test was started with the two components in contact, with the magnets fully aligned around the z-axis as shown above; the upper piece was drawn vertically away from the lower. The test was repeated for 8 and 12 magnet configurations and under 3 different backing conditions: un-backed, cupped (the magnets are placed into individual steel cups) and plain-backed (i.e. 2 mm thick mild-steel washer), as summarized by Table 13. The measured force is plotted against separation and is shown in the pull-gap curves of Figure 29, Figure 30 and Figure 31. It is important to note that the smallest separation possible is 2 mm due to the material of the magnet holders preventing the magnets from touching.

Table 13: Number of magnets tested at different cone angles under different backing conditions

Backing Type	Cone Angle, θ (Deg)			
	0	10	20	30
Non-Backed	1, 8, 12	8, 12	8,12	8, 12
Cupped Backing	1, 8	8	8	8
Steel Plate Back-Iron	12	N/A	N/A	N/A

Results
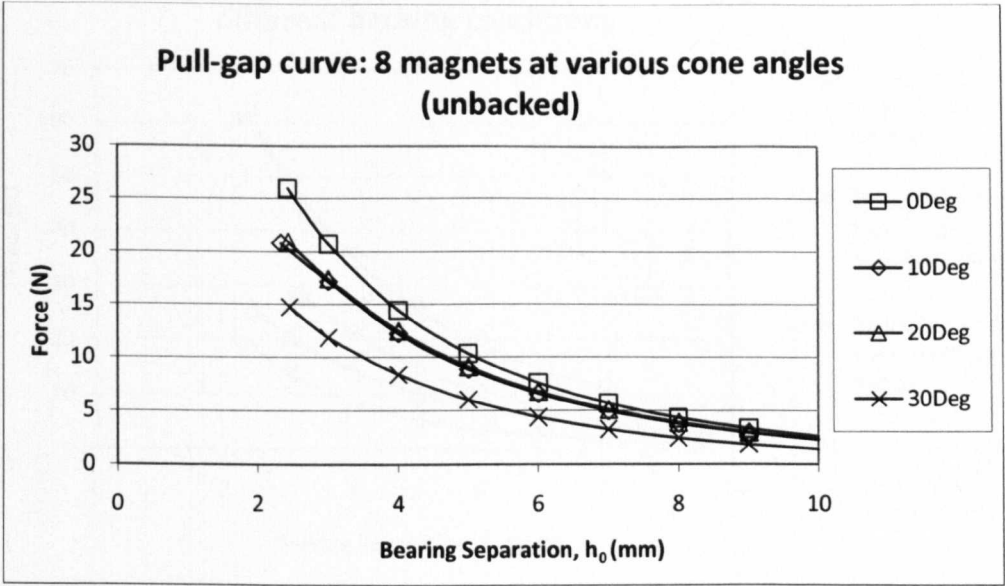
Figure 29: Pull-gap curve for 8 magnet arrangement. No backing condition.
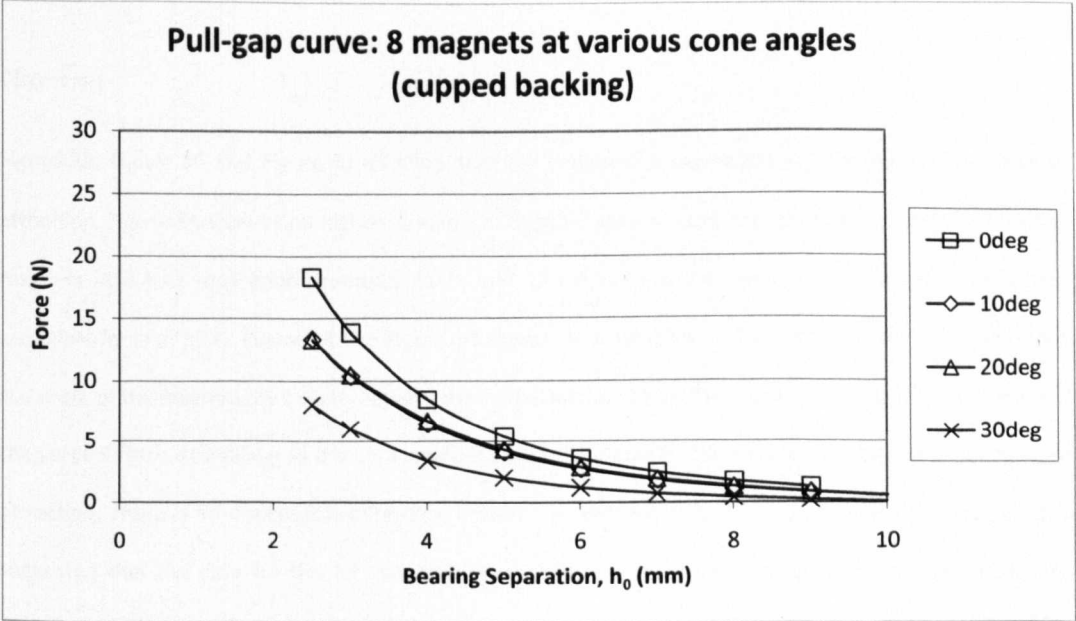
Figure 30: Pull-gap curve for an 8 magnet arrangement.
Cupped backing condition.
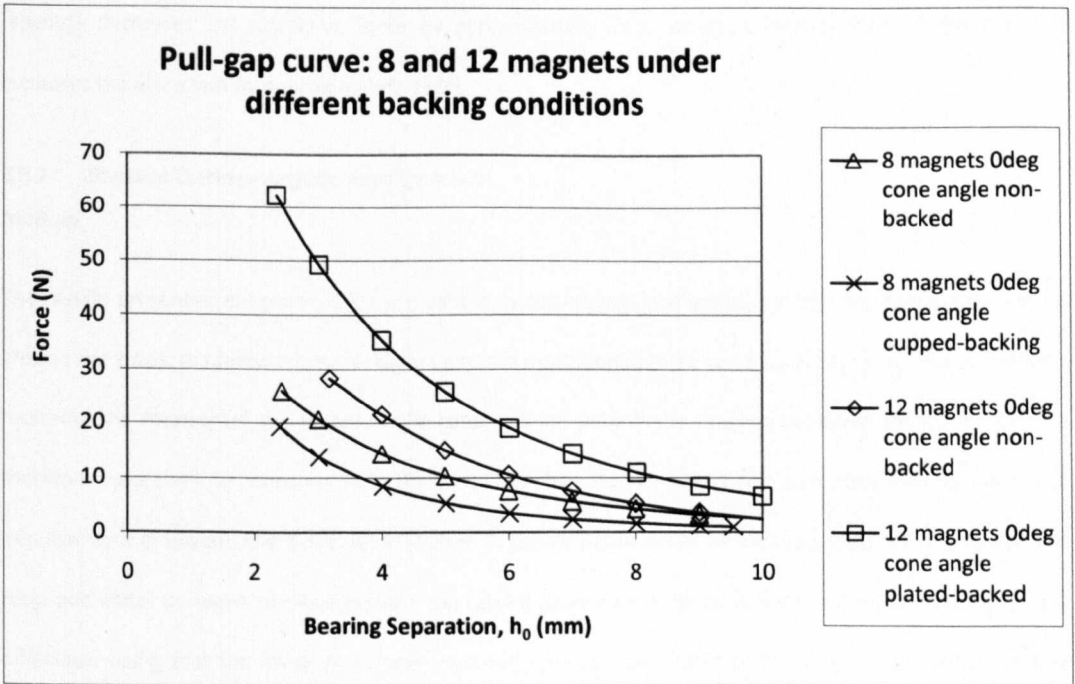
Figure 31: Pull-gap curve for 8 and 12 magnet configurations. No
backing, cupped backing and plain backing conditions.

Discussion

Figure 29, Figure 30 and Figure 31 all show that the smaller the separation gap the greater the force of

attraction. Figure 31 shows that higher numbers of magnets gave a greater force of attraction: 8 non-backed

magnets at 3 mm separation produced 21 N, and 12 magnets at the same separation produces a total

attractive force of 30 N. Figure 29 and Figure 30 show that angling the surface of the components, and thus

the angle of the magnetic flux vector, affects the axial attraction force. This is due to the cosine component of

the vertical force decreasing as the cone angle increases; the greater the cone angle, the lower the force of

attraction. There is no discernable difference between arrangements at 10° and those at 20° however. It is

suggested that the data for the 20° magnetic arrangement is erroneous; the consideration of these data

should be discounted from any discussion. The reason for the erroneous nature of the results was not solidly

identified; possible reasons could lie within the manufacture of the test pieces or within the testing routine,

neither of which were able to be substantiated at time of publication. Figure 31 shows steel cupping of the

magnets decreases the attractive force by approximately 25%, whereas Plain-backing of the magnets increases the attraction by approximately 160%.

3.3.2   Physical Testing - Angular misalignment
Method

The results presented in Section 3.3.1 are valid only for magnet configurations that are completely aligned around the z-axis. In reality, when the drive system is operational, there will be inertial forces due to the fluid retarding the rotation of the impeller; the rotor will lag behind the magnetic rotation of the stator. It is therefore necessary to measure how the force of attraction between the parts will vary at angles of misalignment Ø around the z-axis, as identified in Figure 32. In order to measure axial force between the rotor and stator at angles of misalignment, the testing procedure outlined in Section 3.3.1 was repeated; the difference being that the lower piece was mounted upon a rotary table of the type often used on milling machines. This enabled the two pieces to be held rigid and rotated relative to each other whilst maintaining alignment in all other degrees of freedom. The test was performed only for un-backed 12-magnet configurations over all four cone-angles. The results are shown in Figure 33, Figure 34, Figure 35 and Figure 36.
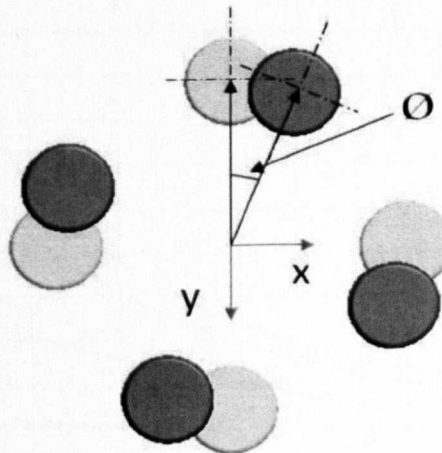
Figure 32: Angular alignment around the z-axis Ø.

Results
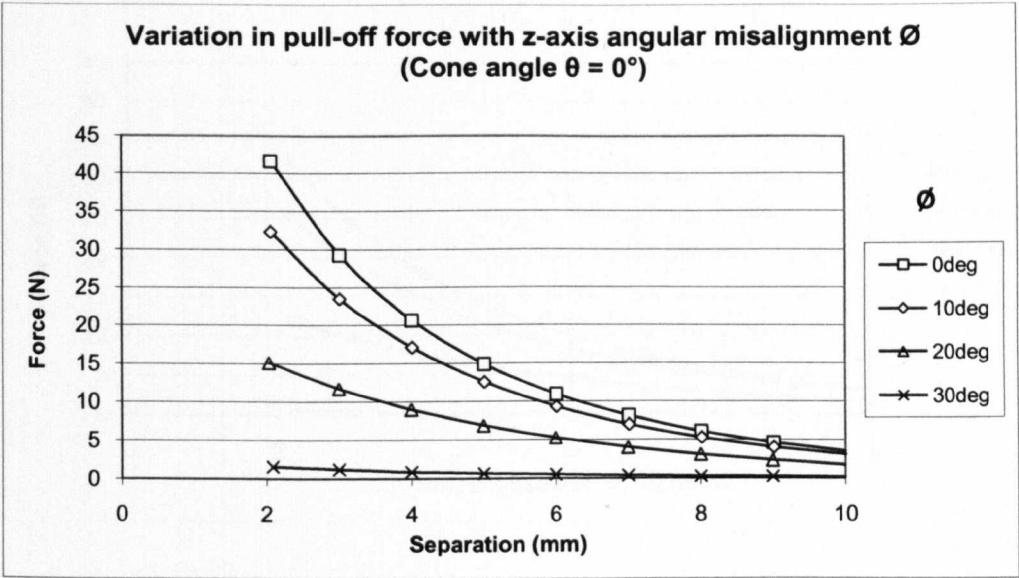
Figure 33: Pull-gap curve for z-axis misalignment Ø. 12
magnet arrangement. Cone angle θ = 0°.
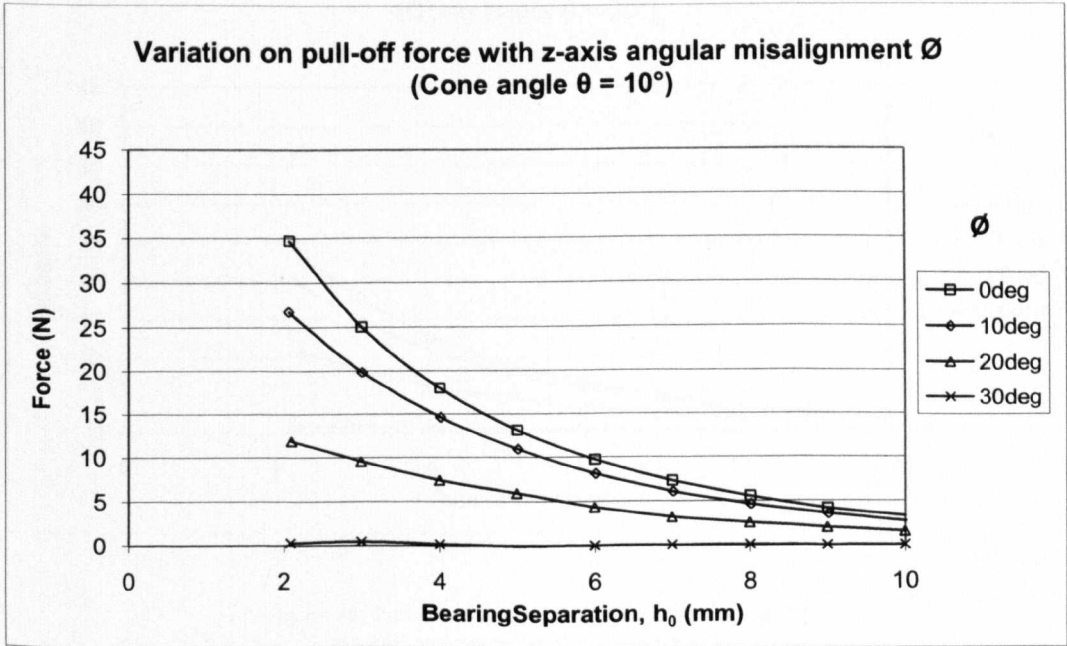
Figure 34: Pull-gap curve for z-axis misalignment Ø. 12
magnet arrangement. Cone angle θ = 10°.
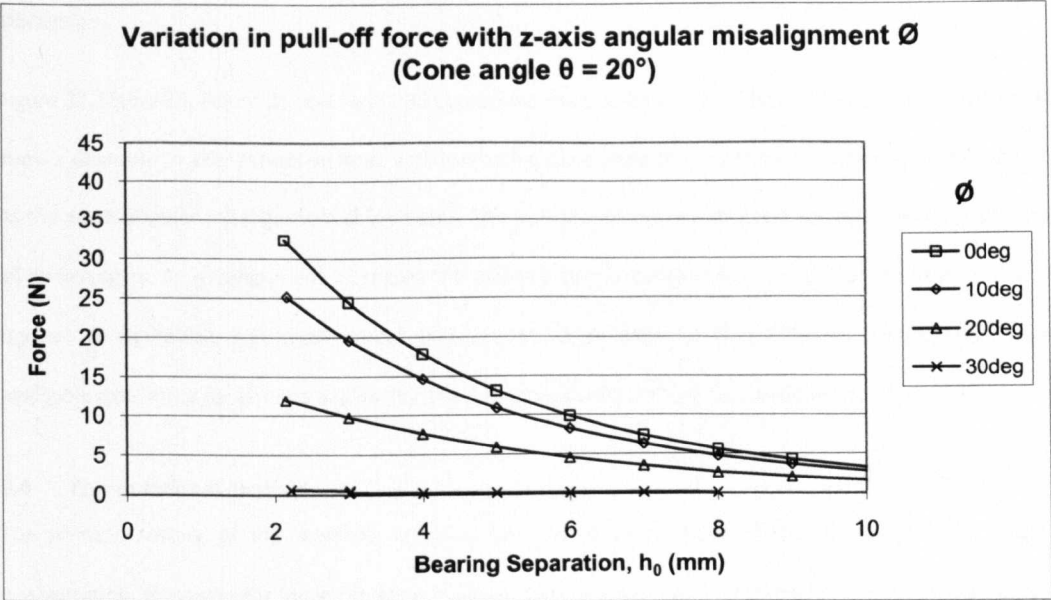
Figure 35: Pull-gap curve for z-axis misalignment Ø. 12
magnet arrangement. Cone angle θ = 20°.
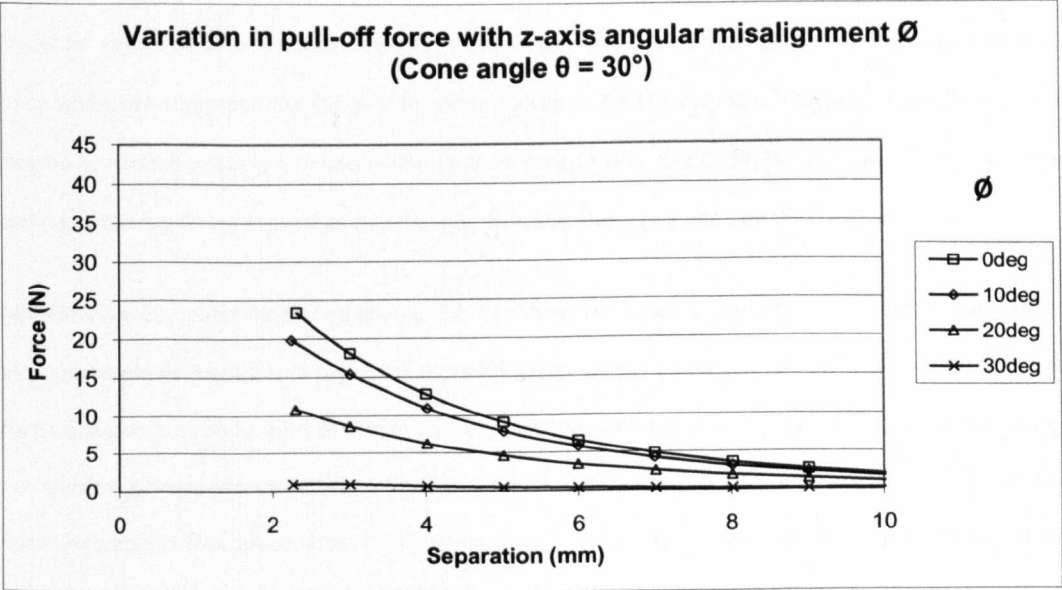
Figure 36: Pull-gap curve for z-axis misalignment Ø. 12
magnet arrangement. Cone angle θ = 30°.

Discussion

Figure 33, Figure 34, Figure 35 and Figure 36 compound the previous pull-off tests in Section 3.3.1; the results show a decrease in axial attractive force with increasing cone angle θ. They show reduction in attractive force as the z-axis angular misalignment $\emptyset$ increases. The pull-gap curves are steepest for zero misalignment over all cone angles. As misalignment increases the pull-gap curves become less steep. For the case of the 12-magnet configuration, full misalignment corresponds to an angle of $\emptyset = 30°$; this configuration shows negligible axial force for all cone angles. For the 8-magnet configurations this angle would be $\emptyset = 45°$.

3.4   Computational Analysis

The physical testing of the magnetic coupling has shown some basic effects of changing the magnet configuration. However, for more complex analyses, some magnet configurations have been modelled using a magnetic analysis software AMPERES v7.0 (Integrated Software Inc., Winnipeg). The main aim of this investigation was to evaluate the radial restoring force when the impeller is displaced along the x- and y-axes, an experimental set-up which is difficult to achieve. The results show the difference between radial restoring forces for setups of different cone angles θ; the inclusion of a cone angle significantly increases this radial force whilst not compromising the axial force for a given radial displacement. Magnets in the drive system may be orientated not only to provide adequate coupling to drive the CRBP, but to provide significant axial *and* radial bearing forces capable of withstanding over 10 g shock excitation on the impeller.

AMPERES is a Computer Aided Engineering (CAE) software package designed to perform full 3D simulations of magnetic physical systems. It provides users with a wide variety of analysis options, including the ability to create contour plots and graphs of field quantities. To perform a simulation in Amperes a geometric model of the physical system was constructed. This was done using the built-in geometric modeller although it is possible to import files directly from CAD packages. Once the geometric model was built, physical properties such as material and magnet flux density vector orientation were assigned. After the physical properties had been assigned, the model was discretized and the solution was calculated by the field solver. (The user can either manually discretize the model or have the self-adaptive solver perform the discretization. This investigation uses the latter.) This software enabled quick and efficient modelling of the magnet

arrangements tested in Sections 3.3.1 and 3.3.2; further analysis that would be difficult to perform experimentally was conducted. Boundary Element Method (BEM) analysis yielded results for the axial force and the torque between the components at angles of misalignment, and shows how the coupling may be used as a radial magnetic component of the hybrid bearing by examining how the radial restoring forces vary as a function of x- and y-axis translations, for increasing cone angles θ.

3.4.1   Boundary Element Methods

BEM is a numerical technique that uses the integral form of Maxwell's equations to solve magnetic field problems. Yildir [88] and Klimpke [89] aid the understanding of these numerical techniques – "A set of boundary integral equations with the unknowns as equivalent sources (i.e. a magnetic field at a point caused by a magnetic dipole) may be obtained by enforcing boundary conditions along material interfaces [88]". Amperes uses the BEM to solve for the equivalent source; the solution is used to calculate the potentials and the fields. To use this method, the model must be discretized into individual sections, or elements. The boundary element solver insists that all physically relevant surfaces and volumes have surface (2D) elements and volume (3D) elements respectively.

In the integral equation formulation, rather than solving for a potential which must be differentiated to find fields, an equivalent source is found that satisfies the prescribed boundary conditions under a function which relates the location and effect of the source to any point on the boundary. This function, called the Green or influence function, effectively eliminates the need of a finite element mesh or a finite difference grid.

Once the source is determined, the potential or derivatives of the potential can be calculated at any point. Provided the problem is piecewise homogeneous, the equivalent source is located only on the boundaries and interfaces of different media.

Klimpke states the main advantages of the BEM (over the domain-type approach) are the accurate modelling of geometry, elimination of differentiation and interpolation to calculate potential or its derivatives, precise results due to the smoothness of the integral operator, and sound means for checking the accuracy of the solution [88, 89]. This is the method employed by AMPERES v7.0 for the purposes of this investigation.

3.4.2 Considerations for BEM Modelling

All surfaces that are on the material interfaces were assigned with 2D-surface elements; that means any surface that separates two different media and thus requires an equivalent source on its surface. In the context of these tests, one of the media was taken as air. In addition to this, in the case of permanent magnetic materials, the common surface between two permanent magnets of the same material with different magnetization directions was also assigned with 2D-surface elements. AMPERES would not produce a solution to the model if 2D-surface elements were not placed.

If the model were to have only linear magnetic materials i.e. material with constant permeability μ, just 2D surface elements could have been used to solve the model. 3D-volume elements must be assigned to the volumes carrying non-linear magnetic materials; as such 3D-volume elements were assigned to any ferromagnetic material. 2D-surface *and* 3D-volume elements are essential for non-linear material volumes. 3D-volume elements were not assigned to permanent magnet materials as they behave linearly when used with their design envelope i.e. not demagnetizing them.

In order to maximise accuracy of the solution, 2D quadrilateral and 3D brick elements were used (as opposed to triangular and tetrahedral respectively). This did however make the model geometry more complicated as all surfaces were 4-sided and all volumes were 6-surfaced. If 2D triangular elements had been implemented in the model, they may have lead to a high concentration of elements in areas of high curvature. 2D quadrilateral elements are advantageous by achieving a more uniform distribution of elements, and have been complemented with the use of 3D brick elements.

Current-carrying volumes need only 3D-volume elements and do not need 2D-surface elements, and should have a relative permeability of 1.

When a tangency condition exists in the model, such as when two cylindrical magnets are next to each other, a huge number of very small 2D-triangular elements will be placed by the program towards the converging tangency condition. To eliminate this problem wherever it existed, the magnets were separated by some negligible distance. However the placement of 2D-quadralateral elements easily solves any problem that

these tangency conditions would cause. (This was not a consideration for this model but does however apply to the testing detailed in Chapter 5.)

Further information is given by Stratton [90] and Lean [91] on the BEM and calculation techniques.

3.4.3   Computational Testing - Validation
Method

In order to ascertain the legitimacy of the BEM analysis the experimental situation seen in Section 3.3.1 was replicated. The geometry was modelled for an 8 magnet arrangement with zero degree cone angle and misalignment ($\theta = 0°$, $\emptyset = 0°$) under non-backed conditions (Figure 37). The simulation was then run where the upper component was translated along the z-axis (i.e. an increasing magnet separation), so as to replicate the experimental setup. A parametric analysis calculated the axial force of attraction as a function of separation gap; results are shown in Figure 38. Further to this, the solution was checked for grid independancy to assertain the validity of the results. Results for grid independency can be seen in Figure 39.
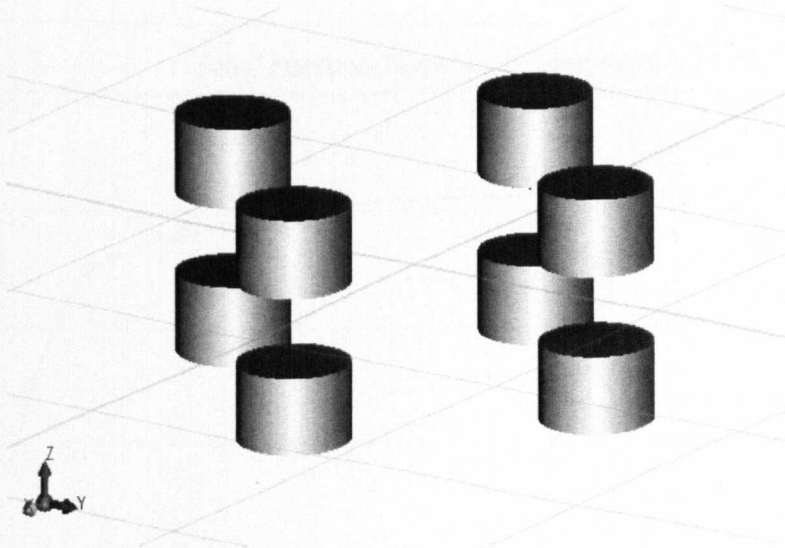
Figure 37: Geometry as modelled in Amperes. 8 magnet
arrangement.. Misalignment $\emptyset = 0°$. Cone angle $\theta = 0°$.

Results

BEM simulation and Experimental Results
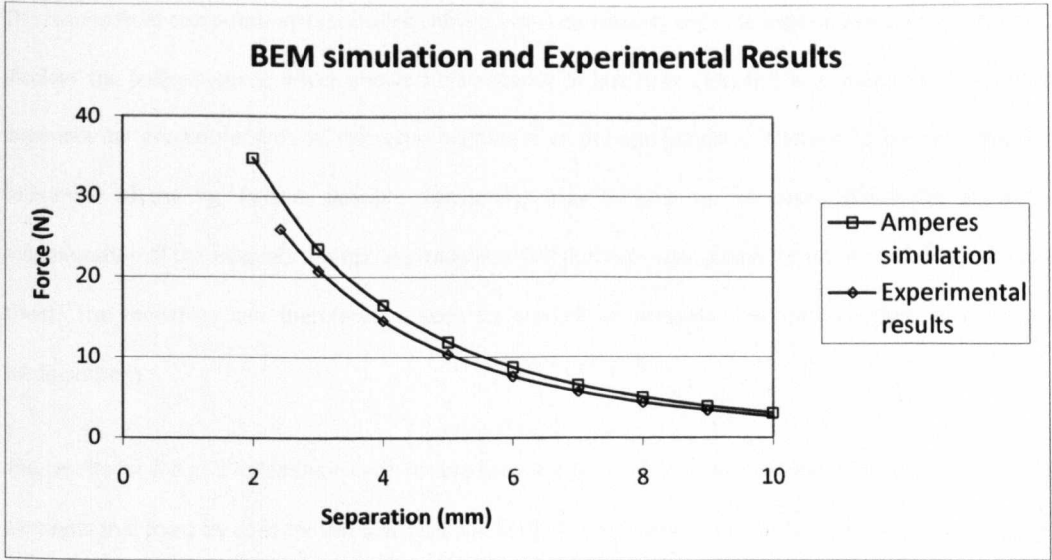
Figure 38: BEM simulation - pull-gap curve for 8 magnet
arrangement. Cone angle, θ = 0°.

Axial Force vs Number of Elements
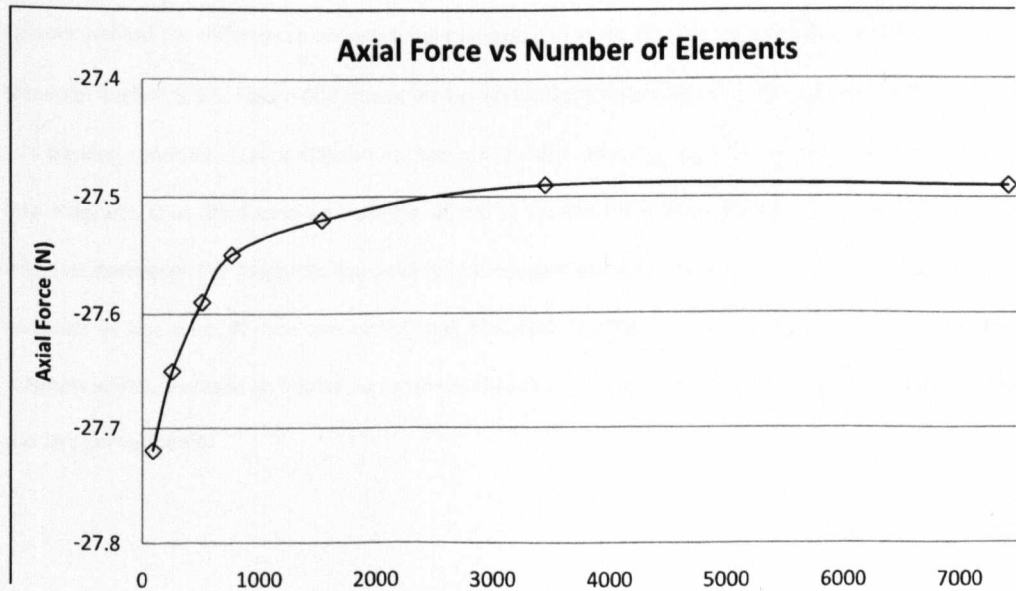
Figure 39: Grid independency showing minimum number of
elements that should be used.

Discussion

The results from computational modelling show a direct correlation with the experimental results. Figure 38 displays the pull-gap curve, which shows a discrepancy of less than 15%; this is attributed to flaws in the experimental procedure such as imprecise alignment of the components, inherent to the manufacturing tolerances of the rig. Further possible discrepancy may be due to the errors introduced during the magnetization of the magnets themselves; magnetic flux densities were taken from the manufacturer's data-sheet. The modelling can therefore be seen to provide an accurate method to model these magnet configurations.

The results for the grid independency check are seen in Figure 39; it shows that the minimum number of 2D elements that must be used for this simulation is 3456. Any increase in elements after this value results in a negligible change in the axial force. The results for this simulation may therefore be taken as reliable.

3.4.4   Computational Testing – Analysis of different backing conditions

Figure 40 shows the magnetic field lines of the magnets under various backing conditions and identifies the reasons behind the differences between the pull-gap curves for the different backing conditions which were shown in Section 3.3.1. Figure 40a shows the un-backed condition without augmentation to the flux lines due to a backing condition. Figure 40b shows that introducing a backing ring channels the magnetic flux path back into magnets, thus producing an increase of the attractive force seen. Figure 40c shows that cupping the magnets decreases the magnetic flux density in the separation gap. There is no flux path linkage between the magnets in this case. It was concluded that the backing ring provides a flux-path linkage between the magnets which results in an increased magnetic flux density, and hence an increased magnetic force between the two components.

Backing Ring - flux lines are
concentrated back into magnet

Cupping the magnets decreases the
flux density in the separation gap

a)   b)   c)

Magnet   Backing Ring   Backing Cup
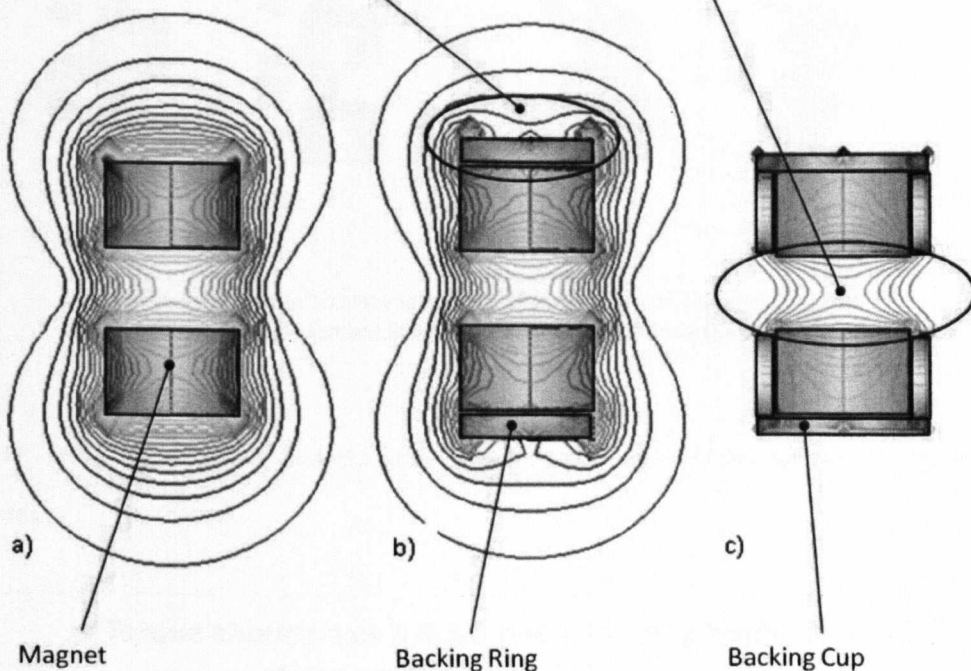
Figure 40: Magnetic field lines for magnets under different backing conditions.
a) No backing. b) Plain backing. c) Cupped backing.

3.4.5   Computational Testing – Influence of cone angle on torque

Method

The purpose of this test is to examine the influence of magnet number and cone angle on torque produced

by the coupling. Models have been produced of 8 and 12 magnet arrangements set at $\theta = 0°$ and $\theta = 30°$. The

upper component was rotated from zero angles of misalignment ($\emptyset = 0°$) though to alignment with the next

repeating unit (60° for 12 magnet arrangement and 90° for 8 magnet one). Figure 41 shows the model as it

appears in the software.
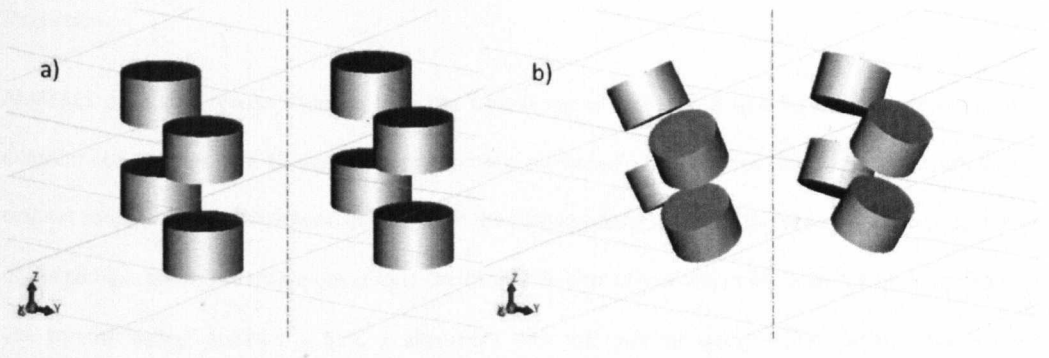
Figure 41: a) 8 magnet arrangement 8. Misalignment Ø = 0°. Cone angle θ = 0°. b) 8 magnet arrangement 8. Misalignment Ø = 0°. Cone angle θ = 30°.

Results

Figure 42   shows the results for how the torque varies through angles of misalignment for the four simulations.
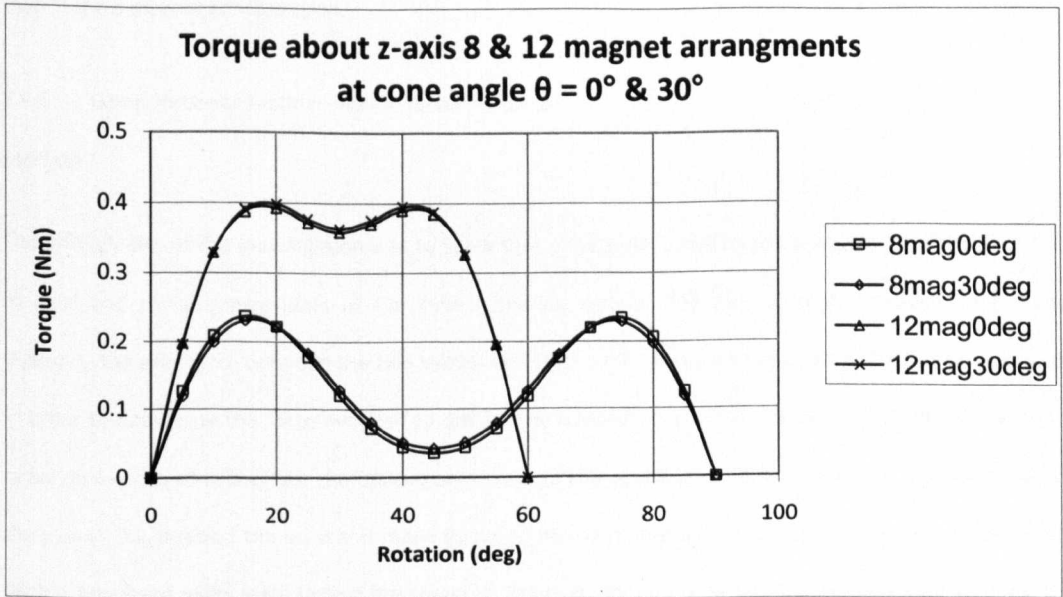
Figure 42: Torque about z-axis 8 & 12 magnet arrangements at cone angle θ = 0° & 30°

Discussion

AMPERES produced results showing how the torque varies between 8 and 12 magnet arrangements at different cone angles. The 12 magnet configurations produced a peak torque approximately 160% that of 8 magnet configurations. There is no difference in the torque produced when the cone angle is varied. For both of the configurations the maximum torque occurs at 25% and 75% of alignment with the next repeating unit. The torque "valley" appears at 50% of alignment with the next repeating unit – this is at the maximum angular separation between the magnets. The tighter, more closely-packed, 12 magnet configuration displays a less distinctive "valley". The first peak occurs at the same angular rotation for both configurations – this is the point at which the magnets are aligned in such way that restoring torque is maximal. The "valley" represents the point at which there is the largest angular separation between the magnets. Since the magnets in the 12 magnet configurations are closer together, the largest possible angular separation is less than in the 8 magnet configuration.

3.4.6   Computational Testing – Radial restoring force

Method

The primary aim of this investigation was to show that a magnetic coupling could be designed that also acts as axial and radial components of the hybrid bearing system. The pull-off tests provided information regarding the axial force between the two components, but no information about the radial forces produced. In order to determine the force required to disturb the coupling in a radial direction, AMPERES simulated a radial push-off test. In this test the upper component of the coupling underwent a planar translation along the y-axis. This enabled the axial and radial forces to be calculated as the upper component is pushed off-centre. Results of radial force testing are shown in Figure 43 for an 8 magnet arrangement with a 0° and 30° cone angle θ (axial gap = 2 mm).

Results
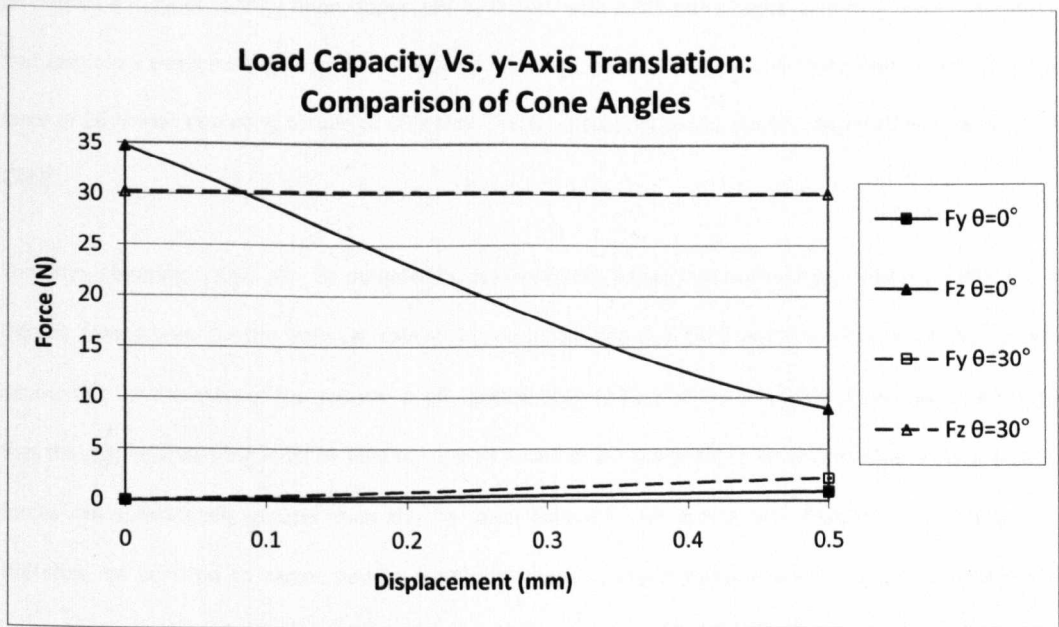
Figure 43: Amperes translation along the y-axis. Introduction of cone angle increases the radial force required to disturb the coupling.

Discussion

For $\theta = 0°$ cone angle there is a sharp drop-off in axial force (35 N to 7.5 N) over a small displacement (0.5 mm) whilst the radial force shows a steady increase over the range. The introduction of a cone angle produces a much more stable configuration. There is no sharp drop-off in the axial force; it remains effectively constant over the first 1 mm displacement. The radial force increases at a greater rate over the range. This shows that the introduction of a cone angle can effectively transform the bearing from a purely axial one to one that is capable of producing bearing forces in all three axes of translation (Δx, Δy, Δz).

3.5   Conclusions

Most importantly, this investigation has shown that it is possible to design a magnetic coupling that acts as the magnetic component of the hybrid bearing system which offers both axial and radial bearing forces. It is proposed that such a coupling may be integrated into the electromagnetic drive system of a CRBP. It is now

possible to predict the full performance characteristics for the magnet configurations tested. For example an un-backed 8 magnet configuration, separated by 5 mm, with a 30° cone angle, operating under conditions that result in a z-axis misalignment of 10° (due to rotor lag), yields a drive system that produces an attractive force of 26 N with operating torque of 0.22 Nm. This is a potential configuration suggested for use in a new CRBP.

The drive / bearing system may be designed by evaluating the forces that are expected within a CRBP, which include forces seen by the impeller caused by perturbations due to external excitation of the system. Accounting for the mass of the impeller itself - approximately 23 g - Newton's Second Law ($\Sigma F = ma$) states that the magnetic bearing must be able to support a load of 2.3 N subject to an acceleration of 10 g; bearing forces are substantially greater than this for axial loading). The appropriate magnet configuration can therefore be selected to accommodate for these forces. Computational modelling enabled testing that otherwise would be difficult to perform through physical testing. It has shown that incorporation of a cone angle into the magnetic arrangement substantially increases the radial bearing force of the coupling without compromising the axial bearing force [83].

The publication *Magnetic Drive System for a New Centrifugal Rotary Blood Pump* [83] summarizes the work carried out in this chapter.

The aim was to identify the influence of different magnetic arrangements on the behavior of the magnetic bearing and how the introduction of a cone angle may be beneficial to any proposed magnetic bearing system. The influence of the electromagnetic forces is not considered in this chapter because the NET electromagnetic force on the rotor is zero. This is due to the nature of a double-three phase motor – the coils are fired in balanced pairs, two phases at once, each with opposing electromagnetic fields. Such a system results in zero net electromagnetic axial and radial force, whilst producing a torque on the impeller – the passive magnetic preload always exists. This principle forms the basis of one of the primary claims in the patent shown in Appendix B.

The second aim of this chapter was to validate the BEM software in order to sanction its use in subsequent chapters. Section 3.4.3 has shown there was a strong correlation between the experimental and computational results. It has been shown that there is a discrepancy of less than 15% in the axial attraction force over a range of magnetic separations. Errors are attributed to misalignment of the experimental rig due to manufacturing tolerances, and the possibility of a non-uniform magnetic flux density within the permanent magnets. The BEM software is used in Chapter 5 to analyze the stiffness and inherent stability of the combined bearing system.

C H A P T E R   4

4   SPIRAL GROOVE BEARINGS

4.1   Introduction

The objective of Chapter 4 is to analyse the performance of the hydrodynamic bearing that forms the complementary component to the magnetic preload, in order to realise the proposed hybrid bearing system. Chapter 4 details the design process involved in choosing optimum bearing geometry by looking at how the different design parameters affect performance. Further to this, Chapter 4 examines the haemolytic performance of the bearing as a function of hydrodynamic film thickness. Also, groove cross-sectional geometry is investigated to evaluate the haemolytic performance, as well as how the bearing affects haematocrit levels of the blood (and associated viscosity) in the bearing gap.

The first readily available account of spiral groove bearings was a paper by Ford, Harris and Pantall in 1957 [92]. It seems however that it may be as long ago as 1949 that the bearing first appeared in a report by Whipple [93], and remained on the classified list until 1957 [94].

A spiral groove thrust bearing (SGB) is a bearing where one of the bearing surfaces is provided with a recurring pattern of grooves that are designated by logarithmic spirals. In principle, the bearing need not be flat; any surface of revolution may be chosen. This chapter is concerned with both flat and conical SGBs.

The bearing operation may be briefly described as followed: When one of the two parts of the bearing is rotated with respect to the other, the viscous fluid in which the bearing is immersed is pumped through the grooves. Depending upon the direction of the rotation and the groove pattern, the fluid may either be pumped towards or away from the axis of rotation; a pressure differential results between the inner and outer radius of the bearing. For any given groove pattern, only one rotational direction gives a positive load capacity - If fluid is pumped from the inner to outer radius there will be a lower pressure at the centre of the bearing than at the outer radius, resulting in a negative pressure acting to effectively suck the two components together. It can be seen therefore that for a SGB to act effectively within a CRBP the direction of

rotation and groove pattern must be arranged as to pump fluid towards the axis of rotation, thus producing a positive load capacity serving to separate the impeller from the casing; this forms the essential non-contact element of the hybrid bearing system. (NB: There does exist the possibility of a partially-grooved SGB, where the bearing grooves terminate midway between the inner and outer radii. Such a set-up would enable an outwardly pumping bearing to provide a positive pressure underneath the bearing surface. However, as it is desirable to encourage maximum washout of the grooves, in the context of a blood-immersed bearing as to minimise thrombus formation, terminating the groove mid-radius can be seen as an undesirable feature.)

In 1966 Muijderman published work on the theory and application of various types of SGBs [94]. Since then, the technology has attracted relatively little attention, with the major focus of application being the use in hard disc drives (HDDs) and other high speed spindle applications [95, 96]. However, in 2004 Kink and Reul first proposed the use of a SGB as a blood bearing for use in miniature blood pumps. They identified SGBs as special type of hydrodynamic bearing that shows excellent load capacity and friction coefficient as compared to other types of hydrodynamic thrust bearings; Table 14 details these advantageous performance characteristics.

Table 14: Comparative data of different types of hydrodynamic thrust bearings. Adapted from [97].

Bearing Type	Plane Slider	Step Bearing	Spiral Groove Bearing
Dimensionless load capacity	0.054	0.047	0.28
Normalised friction coefficient	4.55	6.22	1

There exists two possibilities for the operation of a SGB that pumps fluid towards the centre of the bearing: (i) there can be an outlet for this fluid and hence a transverse flow across the bearing surface that provides washout to the bearing; or (ii) there can be a no outlet for the fluid i.e. a full restriction to the flow across the bearing surface. Muijderman [94] noted that there is no exchange between the fluid within the gap and the outside when there is no transverse flow; this might bring a distinct advantage when using a SGB as a blood bearing as this means that no blood cells will enter the gap once the rotor is started. Kink and Reul [97] have substantiated these assumptions from flow visualization experiments on a 10:1 scale-up model. Moreover, it

has been observed that the few remaining particles within the gap migrate away from the walls to the centre of the gap [98]. This means that in the case of a blood bearing, any red blood cells in the gap will separate from the plasma, and as such the bearing will only be driven by plasma viscosity (~1.2 mPas) [97]. In this chapter the author postulates that there exists the probability of cell exclusion, where the bearing may operate with a viscosity lower than that of whole blood; this cell exclusion has a significant anti-traumatic quality. Testing detailed in this chapter helps to ascertain the degree of cell exclusion from SGBs under various operating conditions.

The aim of this chapter is to evaluate the overall blood compatibility of a SGB. A convenient starting point is to examine the parameters that may affect the load capacity of the bearing, and then compare the theoretical performance against the experimental results (using aqueous glycerol solution). Further to this, and more importantly, the blood compatibility of SGBs has been measured as a function of bearing separation for SGBs and different cross-sectional groove geometry. The results show that experimental performance of the bearings may be as low as 60% of that predicted from the underlying equations; the load capacity of the bearing is dependent upon leakage through the bearing and therefore upon the restriction to flow at the bearing centre - SGBs with no restriction to outflow exhibit a 41-49% percent reduction in load capacity compared to SGBs with a fully restricted outlet.

4.2 Rotating or Non-Rotating Spiral Grooves

There are two ways in which spiral groove bearings may be set up. In a rotating groove system, the grooves are manufactured onto the surface that rotates relative to a stationary surface. In a non-rotating groove system, the surface comprising the grooves does not rotate whilst the counter-face is the one in motion. From a kinematic perspective, there is no difference between the two systems. Considering the fluid dynamics however, the two systems operate quite differently, especially for bearings without transverse flow.

Zou et al. [99] state that when spiral grooves are rotating, the fluid in the grooves is also rotating. The flow of this fluid will cause disturbance through inertial effects (as a consequence of centrifugal force), which acts to destabilize the rotor. Conversely, in a non-rotating groove system, the fluid in the grooves is not rotating; Zou

et al. conclude that, in the case of non-rotating grooves, the fluid distribution is more uniform, and rotor disturbance is reduced due to reduced fluid motion. Testing considered in this chapter therefore employs a non-rotating SGB in order to reduce dynamic effects and aid the stability of the system.

4.3   Manufacture of Spiral Groove Bearing

Muijderman [94] outlines the methods used to calculate the performance of SGBs, together with information on how to form the curvature of the grooves. This section tracks the procedure taken to manufacture the SGBs used in experimental tests and identifies the design parameters that affect the performance. Various manufacturing techniques were trialled and the resulting bearings were measured for accuracy. It was shown that samples manufactured through rapid prototyping methods showed unsatisfactorily low tolerances, and instead the test samples were manufactured using a high accuracy CNC milling machine (NB: It is intended that the bearings be injection moulded for the production solution; such a method was not feasible at this level of testing. The prototyping and associated costs of the bearing are discussed in Section 4.3.3).

4.3.1   Spiral Groove Construction
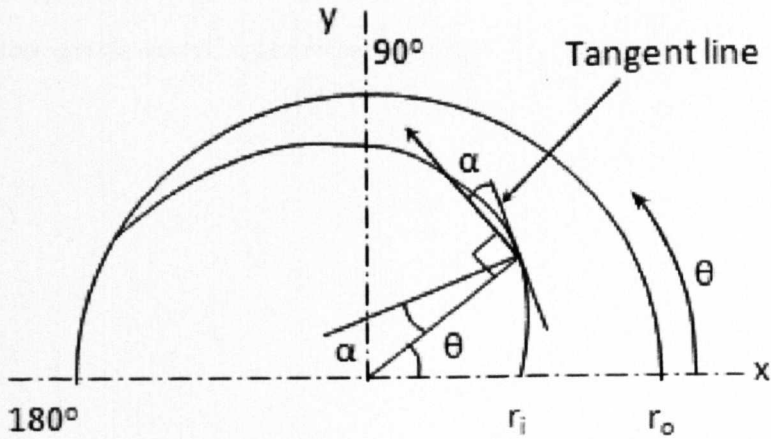
Figure 44: Logarithmic spiral

$$r(\theta) = r_i e^{\theta \tan \alpha}$$

(7)

A logarithmic spiral, as shown in Figure 44, may be drawn using Equation 7; the radius of the spiral is a function of the angular position around the rotational central axis of the bearing. Referring back to Section 2.5.2, the outer radius of the impeller r_o = 22.4 mm. Having set the outer radius r_o, it follows that the larger the bearing surface area the higher the load capacity of the bearing. Setting the inner radius r_i much lower than 12 mm however, shows little increase in the load capacity (see Figure 47). For the purpose of this investigation, the inner radius is taken to be r_i = 12 mm. Details of how changes in the inner and outer radii affect the load capacity of the bearing are seen in Section 4.3.2.

Muijderman [94] outlines the principle behind SGB design and construction. Figure 45 shows the key geometrical features of a SGB; Equations 8 - 13 describe how to produce groove geometry from input parameters as detailed in Table 15 [94]. Although a conical SGB is used in the design of the LVAD as outlined in Chapter 3, further investigation here considers the more simple geometry of planar SGBs due to the complex machining techniques required to make conical spiral grooves; it was more cost and time effective to test planar bearings. It must be noted that whilst machining the conical SGBs would require five-axis machining, the injection moulding of such geometry is no more difficult than the moulding of a planar geometry (the tooling of the mould is however more expensive).

Section A-A
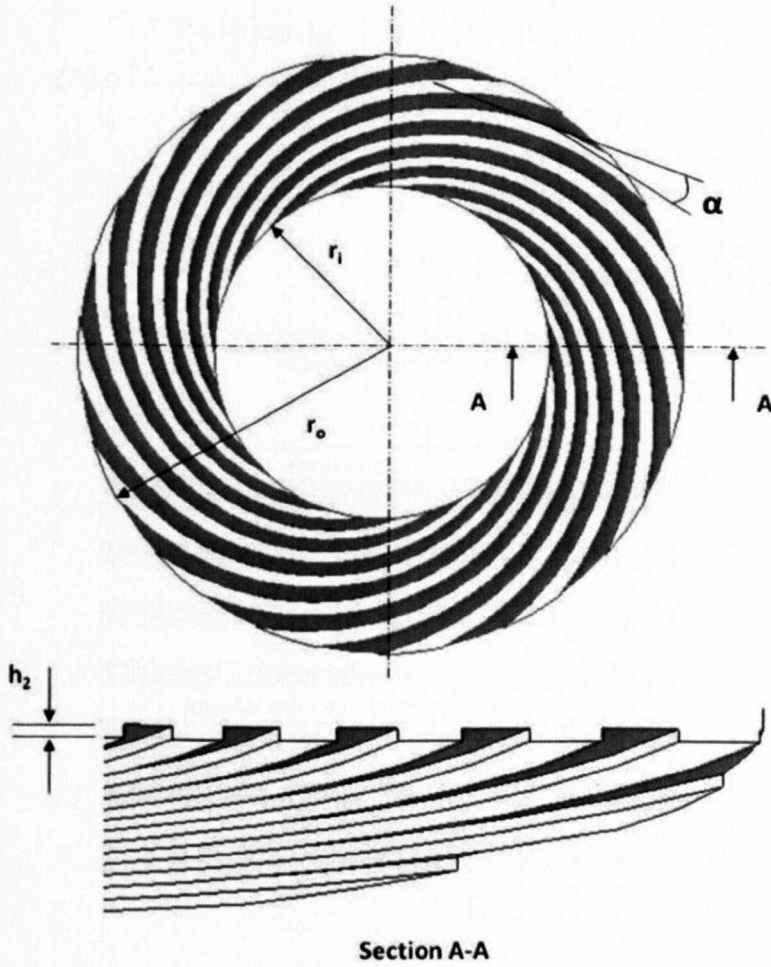
Figure 45: SBG geometry

The dimensional load capacity **F*** (and load capacity **F**) can be calculated from Equation 6.

$$F^* = \frac{Fh_0^2}{r_o^4 \omega \eta} = \frac{3\pi}{2}\left(1 - \lambda^4\right)g_1 C_2$$

(8)

where

$$g_1 = \frac{\gamma H^2 \cot(\alpha)(1-H)(1-H^3)}{(1+\gamma H^3)(\gamma + H^3) + H^3(\cot^2 \alpha)(1+\gamma)^2}$$

$$C_2 = \frac{e^{\frac{-2\pi}{k}\left(1-\frac{2\alpha}{\pi}\right)\tan(\alpha)\frac{2}{1+\gamma}\frac{1+\gamma H^3}{1+H^3}} - \lambda^4 e^{\frac{2\pi}{k}\left(1-\frac{2\alpha}{\pi}\right)\tan(\alpha)\frac{2}{1+\gamma}\frac{1+\gamma H^3}{1+H^3}}}{1-\lambda^4}$$

Table 15: Parameters for spiral groove bearing load
capacity calculation

Parameter	Symbol
Dimensionless load capacity	F^*
Load capacity (N)	F
Outer radius (m)	r_0
Inner radius (m)	r_i
Groove angle (degrees)	α
Film thickness (m)	h_0
Groove height (m)	h_2
Angular velocity (radians / sec)	ω
Relative radial width of groove pattern r_i / r_o	λ
Ridge width to groove width ratio	γ
Viscosity (mPas)	η
Main factor	g_1
Correction factor	C_2

Design Considerations

In reality, the optimum value of the ridge width to groove width ratio γ varies very little from 1 for various

groove geometries, and as such the expressions for the main factor g_1 and the correction factor C_2 may be

simplified to Equations 9 and 10 respectively. The variation in load capacity with changing ridge width to

groove width ratio is shown in Figure 46; it demonstrates the negligible effects of changing this parameter.

However, a choice for sub-optimum bearing performance may be made in order to maximize the washout to

the bearing grooves. Such a system may have a ridge width to groove width ratio < 1. The effects of changing

the ridge to groove ratio may be considered in subsequent work.
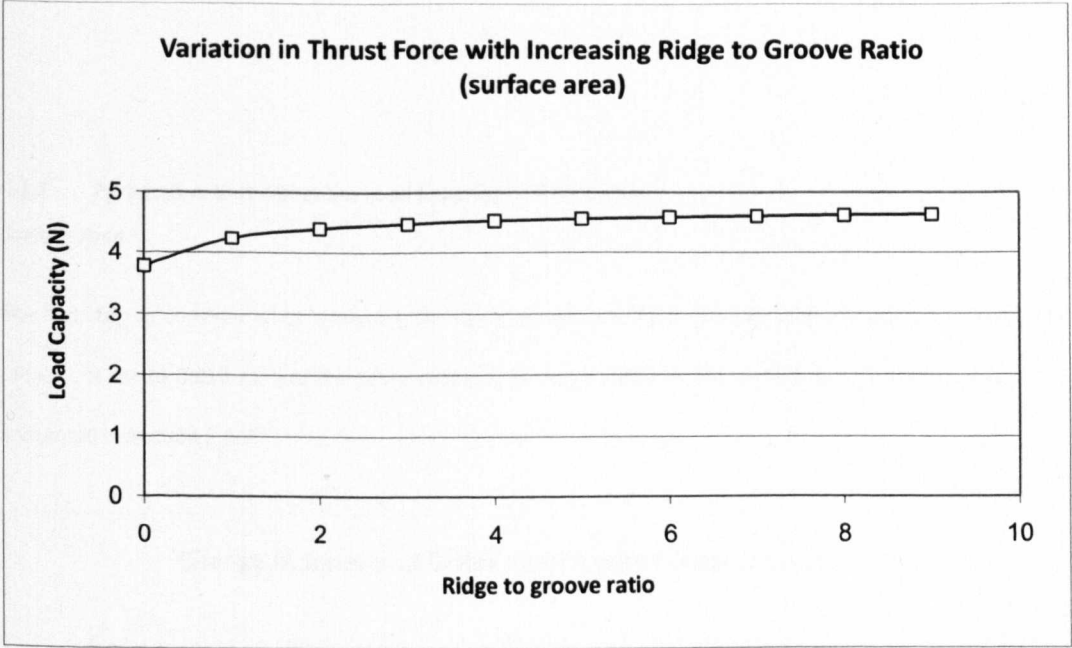
Figure 46: Variation in load capacity with changing ridge
width to groove with ratio

$$g_1 = \frac{H^2 \cot(\alpha)(1-H)(1-H^3)}{(1+H^3)^2 + 4H^3 \cot(\alpha)^2}$$

(9)

$$C_2 = \frac{e^{\frac{-2\pi}{k}\left(1-\frac{2\alpha}{\pi}\right)\tan(\alpha)} - \lambda^4 e^{\frac{2\pi}{k}\left(1-\frac{2\alpha}{\pi}\right)\tan(\alpha)}}{1-\lambda^4}$$

(10)

Where

$$H = \frac{\delta}{1+\delta}$$

(11)

$$\delta = \frac{h_0}{h_2}$$

(12)

$$\lambda = \frac{r_i}{r_o}$$

(13)

4.3.2 Parameters that Affect the Load Capacity of the Bearing

Surface Area

The first step to consider when designing the spiral groove bearing is the geometrical constraints. The inner radius r_i is set to 0.012 m, and the outer radius r_o is set to 0.022 m as specified by the impeller geometry calculated in Section 2.5.2.
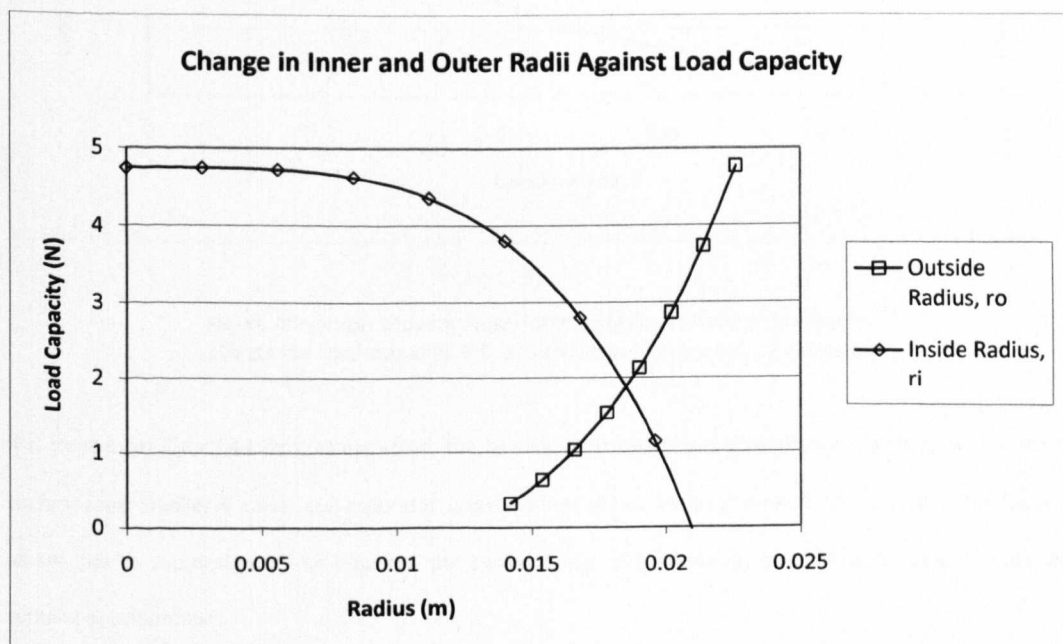
Figure 47: Graph showing how independently changing the inner and outer radii of a SGB affects the load capacity of the bearing.

Figure 47 shows the effect of independently increasing the outer radius r_o from a value equal to the inner radius r_i (0.012 m) to a maximum of 0.022 mm. It is shown that as the outer radius r_o is increased the load

capacity of the bearing increases in a higher order manner. Similarly, as the inner radius r_i is increased from zero towards a value equal to the outer radius r_o the bearing force falls off at an increasing rate towards zero. The effects of the surface area of the bearing are described by the λ-value which is a representation of the surface area of the bearing; these effects are shown by Figure 48.

Graph showing variation in thrust force with increasing lamda value i.e. increasing bearing surface area
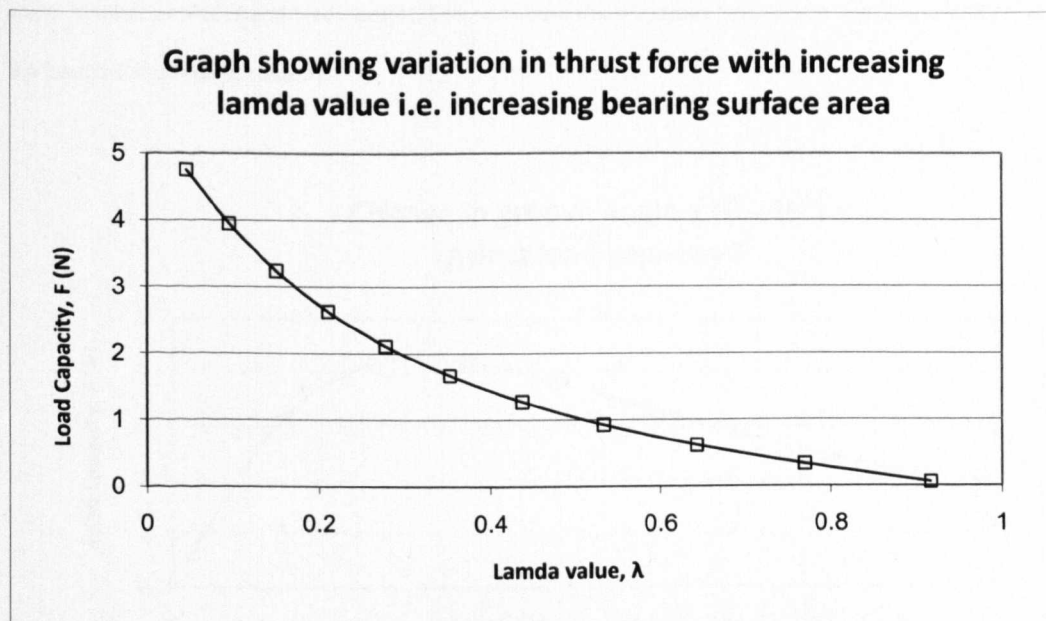
Figure 48: Graph showing how decreasing the surface of the bearing affects the load capacity. NB: as surface area decreases, λ increases.

It is clear from Figure 48 that, as expected, the bearing load capacity is greatest for a bearing with a larger surface area. Smaller λ-values correspond to larger surface areas. As the geometric constraints of the bearing as set due to the design of the impeller, the performance of the bearing must be optimized through the remaining parameters.

Groove Geometry Optimization

There are three physical parameters that may be changed in order to optimise the performance of the

bearing: groove angle α, number of grooves k, and groove height h_2. (It is interesting to note that these three

factors mirror three of the key factors that affect CRBP performance. Impeller design is optimized for blade

angle, number of blades and blade height. This reinforces the principles behind SGB operation; load capacity

is a function of pumping capacity.)
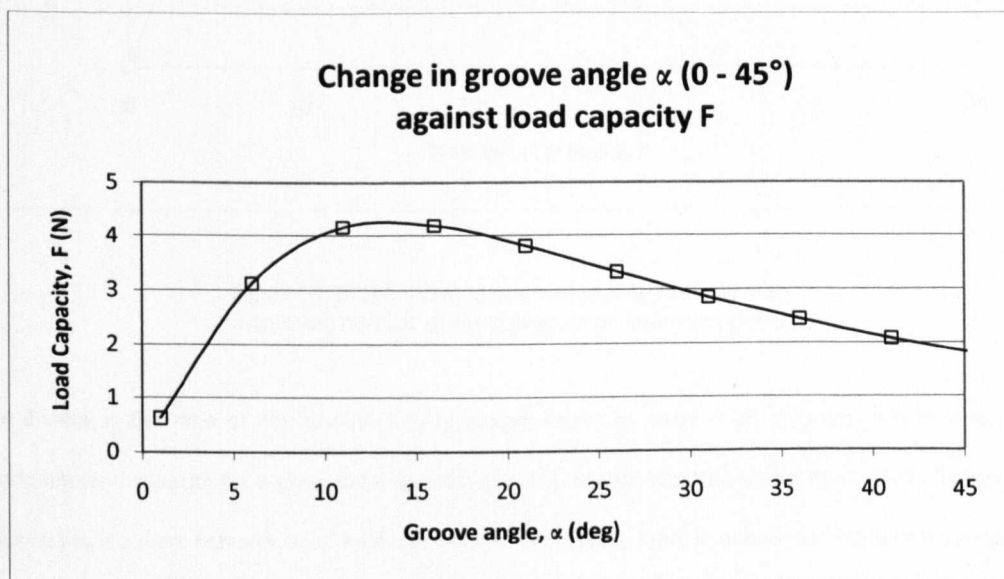
Figure 49: Graph showing variation in load capacity with a
change in groove angle.

Figure 49 shows that the load capacity is maximum at groove angles between 12 - 17°. Therefore, the groove

angle α has been set to $\alpha = 15°$. Figure 50 shows that increasing the number of grooves on the bearing has a

corresponding effect of increasing the load capacity. Increasing the number of grooves from 0 - 5 shows a

dramatic increase in the load capacity (0 N to 3.5 N). Further increasing the number of grooves from 5 to 20

shows an addition effect, increasing the load capacity by an extra 25% to 4.5 N. The number of grooves k has

been set to $k = 15$ in order to optimise the bearing performance whilst maintaining a degree simplicity with

respect to manufacture.

Variation in load capacity F with increasing number of spiral grooves k on bearing surface
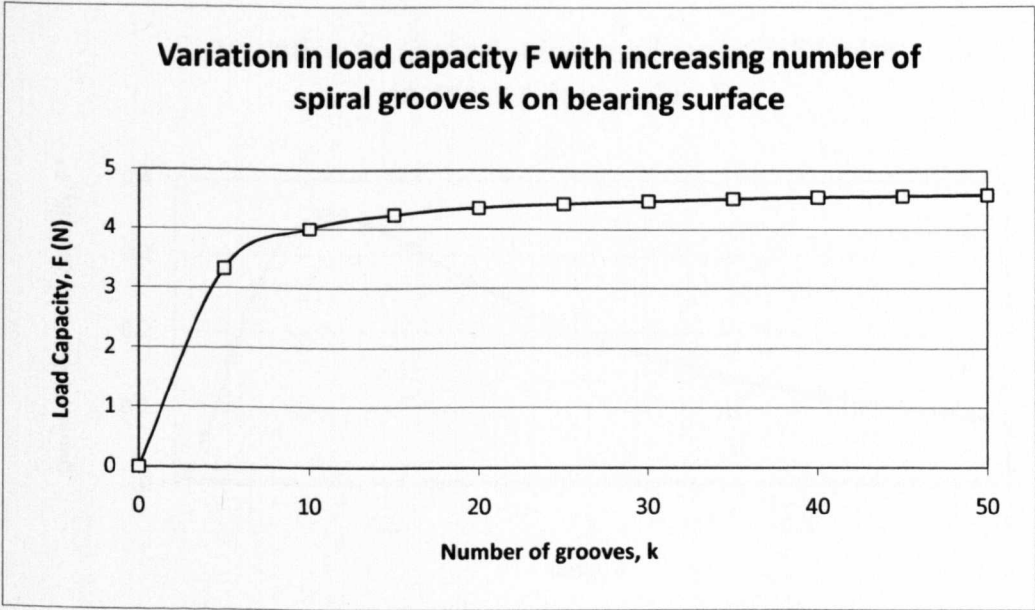
Figure 50: Graph showing variation in load capacity with increasing number of spiral grooves on bearing surface.

The δ-value is the ratio of film thickness h_0 to groove height h_2; there is an optimum film thickness for maximum load capacity for a given bearing geometry. The relationship between groove height h_2 and film thickness h_0 is a more complex one. The δ-value demonstrates that there is an optimum balance between the two parameters; for a specified film thickness there is an optimum groove height, which yields a maximal dimensionless load capacity, as shown by Figure 51. This occurs at a δ-value $\delta = 0.35$.
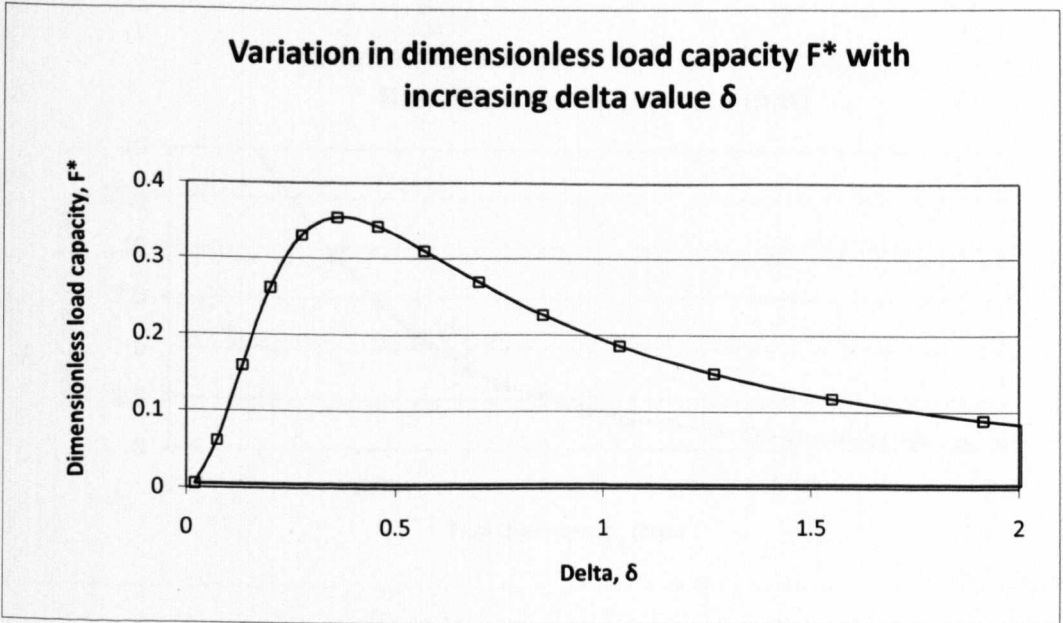
Figure 51: Graph showing variation in dimensionless load
capacity with increasing delta value δ.

In reality however, it is not practical to optimise the groove height for a specified film thickness, as it is not possible to alter the groove height during the operation of the bearing. It becomes prudent, therefore, to recognise how the load capacity varies for changing operational clearances i.e. film thicknesses. Figure 52 shows that the load capacity increases in a higher order fashion as the film thickness decreases for a set groove height h_2; the selection of the groove height and the associated film thickness is instrumental to the performance of the bearing, in reference to its operation in blood. The primary concern is that of cell exclusion within the spiral grooves. For this reason, it is essential to design the grooves such that their height is large compared to that of the maximum dimension of a RBC (~8 µm). The author postulates here that by making this groove height large, it offers the RBCs a "choice" of path through the bearing surface; the choice being that of a region of high shear stress under the bearing ridges as opposed to a region of low shear stress in the grooves. In order to offer the RBCs a reasonable "choice" of path, the ratio of the groove height to film thickness must be sufficiently large as to provide a clear shear differential. The groove height is taken here as $h_2 = 200$ µm as to provide .
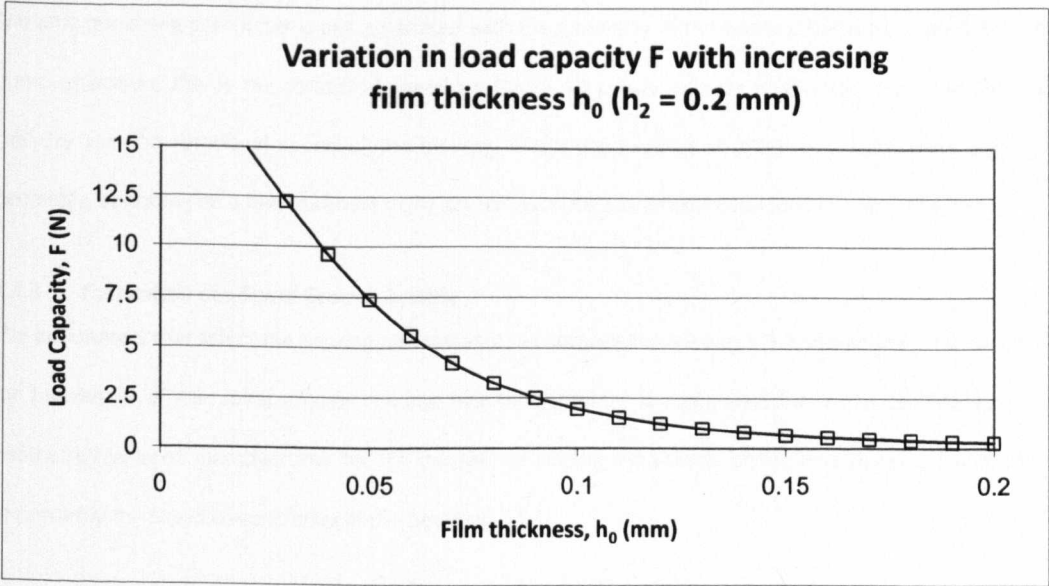
Figure 52: Graph showing how load capacity varies with increasing
film thickness, h_0 (Groove depth set at 200 microns)

Bearing Rotational Speed
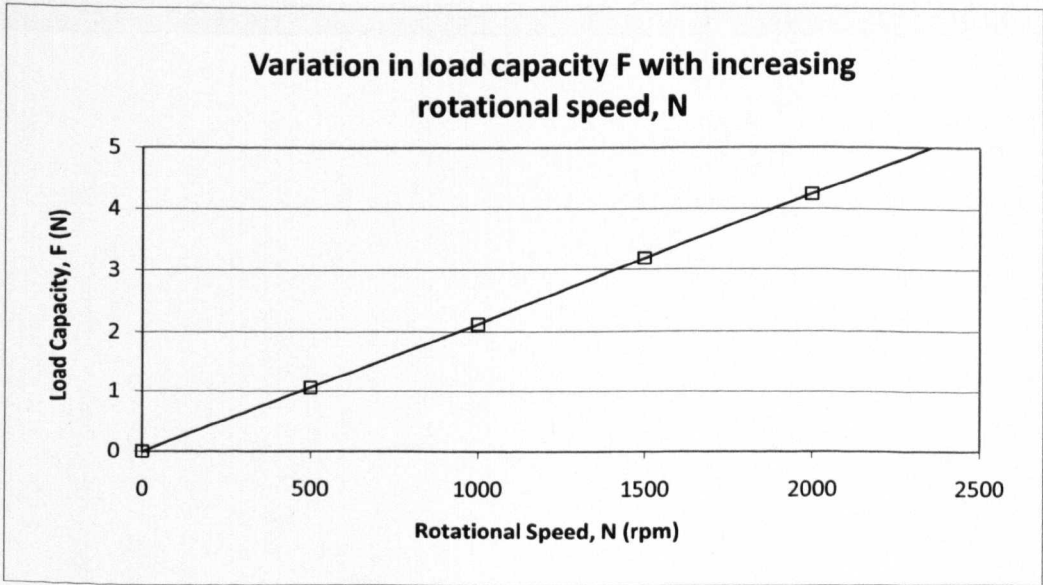
Figure 53: Graph showing variation in load capacity with
increasing rotational speed.

The only remaining parameter is not associated with the geometry of the bearing, but is associated with the pump operation; this is the rotational speed ω. Figure 53 shows a linear relationship between the load capacity and the rotational speed of the bearing. A bearing rotating at 2000 rpm, with above specified geometry, operating on a film thickness of 70 μm for example, has a theoretical load capacity of 4.2 N.

4.3.3   Fabrication of a Spiral Groove Bearing

The parameters that affect the bearing performance, as discussed in Section 4.3.2, identify the choices made for the design of the spiral groove bearing; bearing geometry is summarised in Table 16. The specified geometry has been manufactured for the purpose of testing the validity of the bearing theory and, more importantly the blood compatibility of the bearings.

Table 16: Numerical values for SGB parameters

Parameter	Value
Outer radius r_o	22.4 mm
Inner radius r_i	12 mm
Number of grooves k	15
Groove angle α	15°
Groove height h_2	200 μm

Rapid Prototype Vs CNC Milling

Provisional tests were carried out in order to establish a suitable manufacturing method for the SGB. The bearing was first manufactured using the Viper Si2 SLA machine (3D Systems, Grand Junction, Colorado, USA) machine capable of a resolution of 25 μm. Using this method, samples could be manufactured quickly at very low cost. The surfaces of the samples were measured (7x7 mm) on a Talysurf CLI 1000 precision 3D surface profiler (Taylor Hobson Ltd., Leicester, UK) using an inductive probe with a resolution of 9 nm. Figure 54 displays the results for the rapid prototyped sample; shown is a considerable variation in height across the surface of the bearing with ridge height varying by up to 40 μm. Further to this the, the sides of the grooves show a significant slope with a 4:1 gradient in some cases. Considering that the performance of the bearing is sensitive to small changes in the groove height, the rapid prototype samples are unsuitable for the test procedure.

An alternative was to CNC mill the samples; this was done using a KERN Evo Ultra Precision CNC Milling Centre (KERN Micro- und Feinwerktechnik GmbH & Co. KG, Eschenlohe, Germany). It is clear from the measurements (Figure 55) that there is a marked improvement in the accuracy of the bearing with a much more consistent grove height, flatter tops, and also much steeper sides to the grooves than those produced by the SLA machine.

The author recognises the cost implications that are associated with the necessity to CNC mill components; it was necessary for this investigation to prototype the test sample using a CNC milling machine in order to achieve the required tolerances; options for manufacturing were limited at the time of experiement.
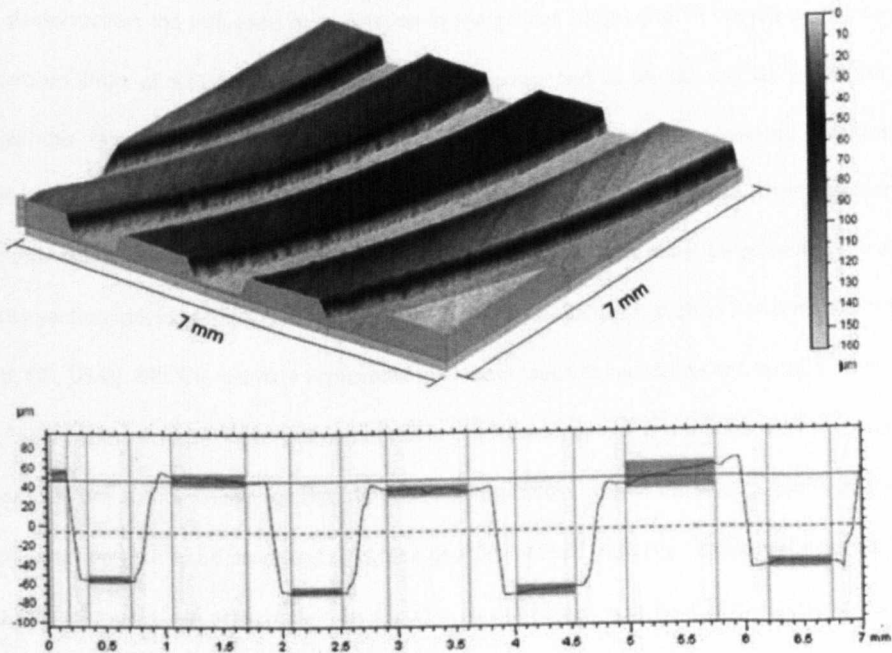
Figure 54: Measurement of SGB – SLA
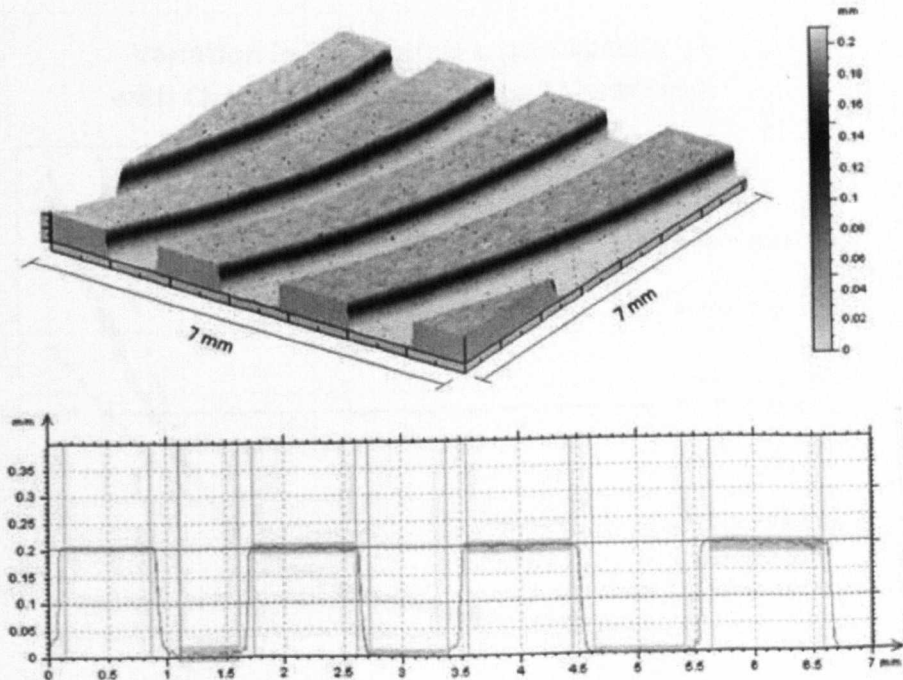
Figure 55: Measurement of SGB – CNC milling

Figure 56 demonstrates the influence of a variation in the groove height due to manufacturing tolerances; top and bottom limits of ±25% (±50 μm on a 200 μm groove) and ±2.5% (±5 μm on a 200 μm groove) characterize the rapid prototyped sample (shown in Figure 55) and the proposed tolerance limits respectively. Figure 56 demonstrates the unsuitability of the rapid prototyped sample. Also demonstrated is a negligible difference in the load capacity across all separation gaps assuming an achievable tolerance of ±2.5% with injection moulded PEEK (tolerances suggested by manufacturers such as Performance Plastics Ltd. (Cincinnati, OH, USA)). NB: The ultimate achievable tolerances (such as roundness and flatness) with injection moulded PEEK components are poorly documented in the literature since few parties wish to mould to such tight tolerances. The author recognises that the required tolerances may, in the end, be too tight and as such the SGB may not be able to be produced using the desired method. However, anecdotal evidence suggests that required tolerances *are* achievable, but are also at the upper-most limit of the process. Even if the required geometry must be produced through CNC machining, the associated cost that is incurred through this process would still be many factors smaller than machining the full impeller and volute geometry.
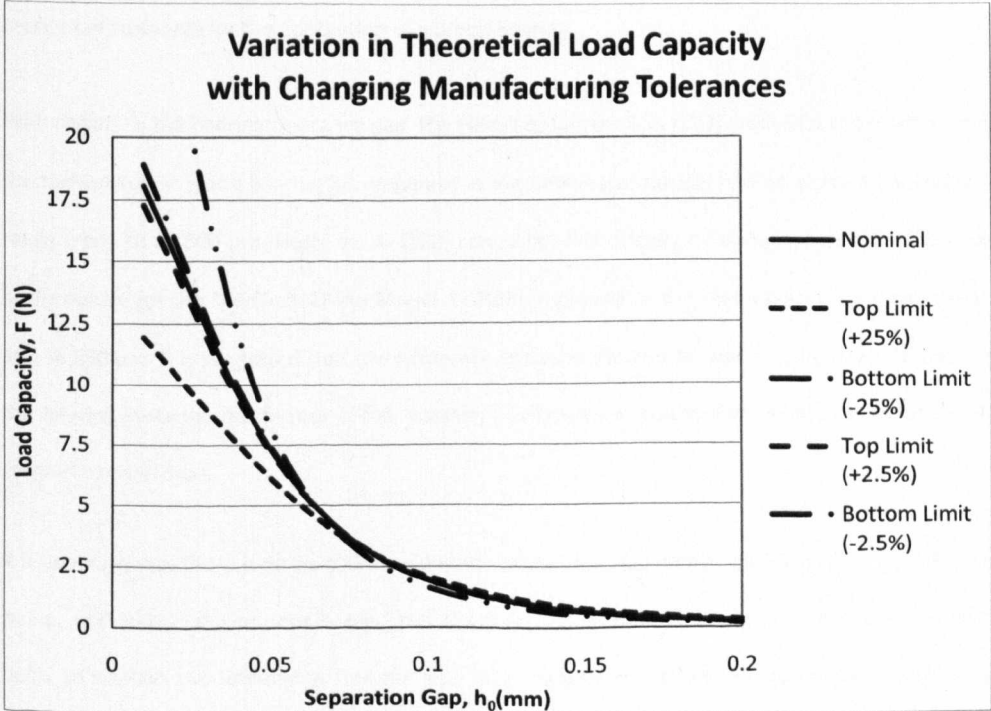
Figure 56: Variation in load capacity over two example tolerance bands

4.3.4 Surface Roughness and Clearance gap

The surface roughness of the bearing has a great influence on the haemolytic performance of the bearing. Monroe et al. [100] demonstrate that a surface roughness less than Ra = 4 μm has a negligible effect on the haemolysis of blood flow between rotating discs, and the haemolysis increases sharply for roughness above 11 μm. It is clear that a slight increase in the surface roughness, especially in the range near that of RBC dimensions (2-8 μm), causes an abrupt increase in the haemolysis. Takami et al. [101] however, state that it is not as essential to have a smooth impeller surface of a centrifugal pump as for use as an LVAD. This may be true for areas of low shear stress and high clearance levels, but for areas of the pump where the blood is exposed to high levels of shear e.g. the blood contacting surface of a SGB, the roughness of surfaces is important. Hoshi et al. [102] expand upon the work of Monroe et al. through analysis of refining the surface finish to 0.1 < Ra < 1.5 μm. They conclude that there is no significant difference between the haemolytic performances over the range of surface roughness tested. The surface roughness is therefore a crucial factor in determining an appropriate manufacturing method, and as such, compounds the unsuitability of the rapid prototype samples with a Ra = 9 μm; the surface roughness of the CNC milled samples is Ra = 0.6 μm, which is more than adequate for the application of a blood bearing.

With regard to the bearing clearance gap, the report of James et al. [103] state that the running clearance of the hydrodynamic blood bearing [as employed in the VentrAssist device] had no effect on haemolysis for the range from 70 to 300 μm. Hoshi et al. [102] contradict this directly by demonstrating that the haemolytic performance [of the MedTech Dispo Model 1 CRBP] improved as the blood path clearance increased from 100 to 250 μm. It is suggested that the difference between the two studies may be down to the disparity of the bearing systems; the former is full, passive, hydrodynamic suspension, whilst the latter is full, active, magnetic suspension.

It is apparent that there is no clear answer to how the bearing gap affects the haemolytic performance of the pump, and indeed the reasons behind this discussion could be many. The work contained in this chapter helps to explain the underlying reasons why SGBs appear to be anti-traumatic despite small operating clearances.

4.4   Physical Testing – Spiral Groove Bearing Axial Force Generation
Method

The aim of this investigation was to measure the load capacity of a spiral groove bearing as a function of separation gap, and compare the results to the theoretical performance predicted by Muijderman [94]. Figure 57 shows the experimental set up. The SGB was machined into the base of the fluid chamber (therefore acting as a non-rotating SGB); the base was mounted on a F256 200 N load cell (Novatech Measurements Ltd., St Leonards-on-sea, East Sussex, UK) which is capable of measurement to a resolution of 0.01 N. The load cell / base unit was mounted on the bed of a Fanuc Robodrill α-T21iE CNC milling machine (FANUC Ltd., Oshino-mura, Japan); the bed was controllable to 1 µm increments in the **x**, **y** and **z** axes. The spindle was mounted in the head of the CNC milling machine such that the face of the SGB and the spindle head were concentric and parallel to ± 2 µm. A chamber lid was attached to the base via a Perspex tube and is clamped down to the base of the chamber. The chamber was sealed around the spindle using a rotating shaft seal that was mounted in the chamber lid. The lid has an inlet, which supplied the fluid to the chamber, and an overflow to ensure that the chamber was fully filled. The base has an outlet that is controlled by a pinch valve such that the flow rate through the chamber can be varied from zero (no flow) to the maximum flow (free flow) rate that the diameter of the outlet allows. Inlets and outlets are 6.5 mm in diameter (area = 33mm^2); this means that the flow restriction from the bearing fluid path i.e. the film height becomes significant at separations below 250 µm. By varying the flow rate through the bearing, the pressure differential across the bearing surface can be varied, allowing for investigation into how leakage from the bearing affects load capacity.

The preliminary experiment was concerned with the correlation of the theoretical to the experimental results. In order to simplify the procedure, the tests were carried out with aqueous glycerol solution of various percentages so as to mimic the possible variation in blood viscosity (1.2 to 3.6 mPas) due to cell exclusion. Before the chamber was filled, the face of the spindle and bearing surface were brought into contact such that the separation gap is set to $h_0 = 0$ µm when the load cell first registers a load. The spindle was then withdrawn to some remote position and was then rotated at 2000 RPM; hence the load capacity was measured by the load cell as a function of separation gap. (The stiffness of the load cell is sufficiently high

(7.8 x 10^6 Nm) such that any force produced by the bearing did not significantly alter the bearing separation.) The temperature of the aqueous glycerol was monitored at inlet and outlet to maintain a constant temperature (room temperature = 22° C) throughout the entire rig and duration of experimentation.

The theoretical load capacity of the bearing was calculated as a function of separation gap h_0 and viscosity using Equation 6 from Section 4.3.1.
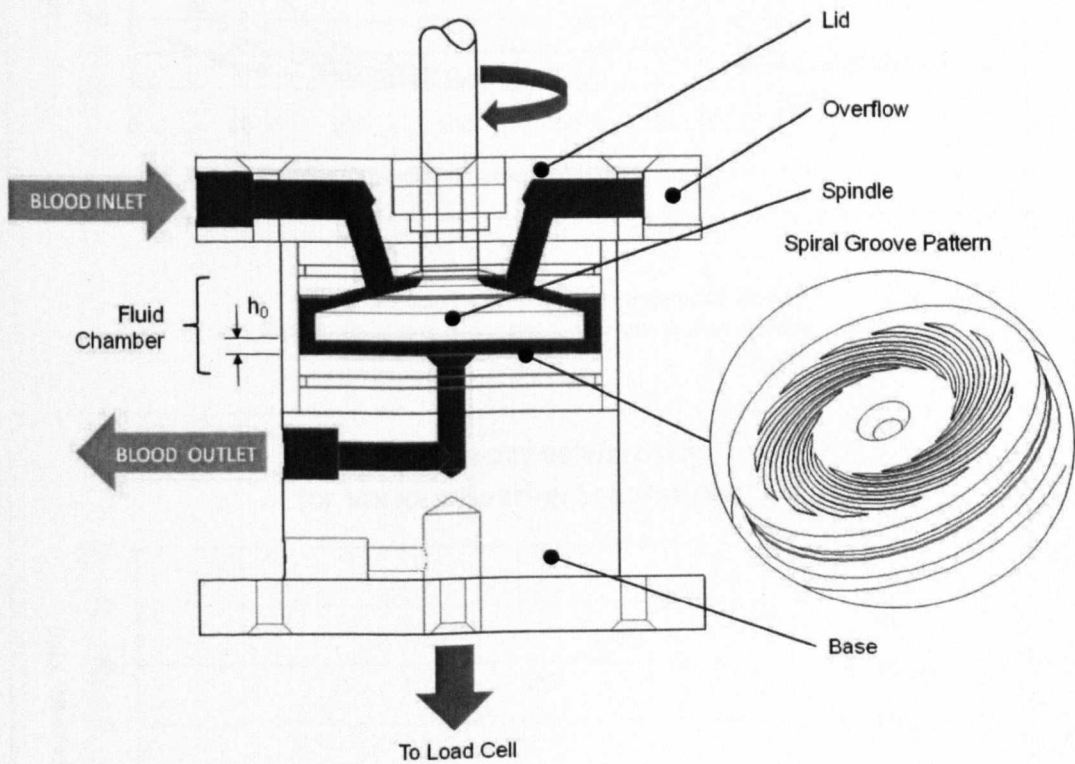
Figure 57: Spiral groove test rig. Cross-section view.

Results
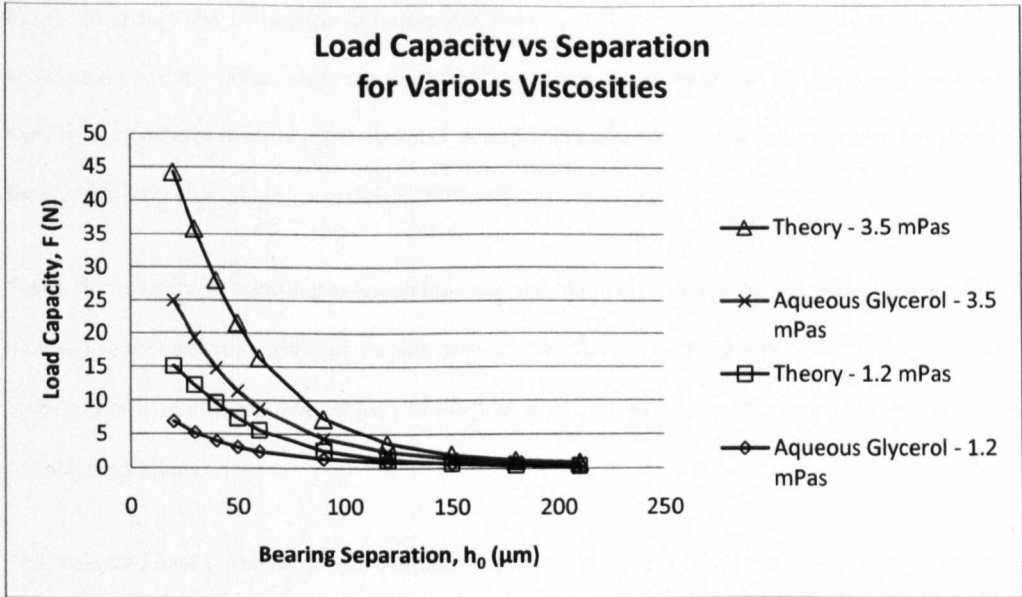
Figure 58: Comparison between theoretical and
experimental load capacities for various fluid viscosities.
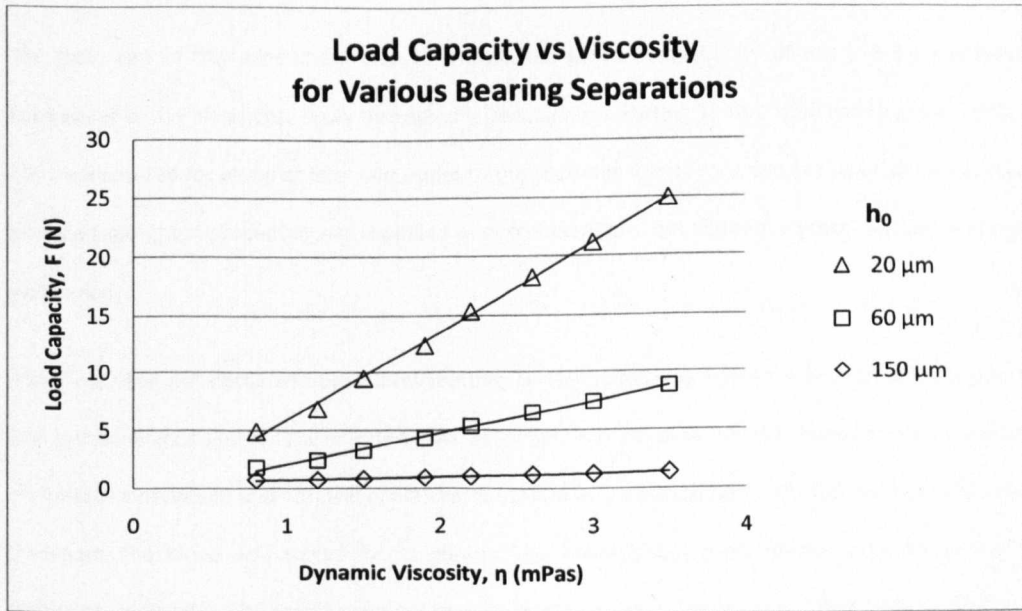
Figure 59: Experimental variation in load capacity with
changing viscosity for different bearing separations.

Discussion

Figure 58 shows the correlation between the theoretical performance of the bearing as predicted by Muijderman and the actual performance of the bearing for given viscosities of aqueous glycerol solutions. Results demonstrate that the SGB operates at approximately 50% of the load capacity predicted by the theory; this drop is consistent over different viscosities.

Figure 59 shows the relationship between the load capacity of the bearing and the viscosity of the fluid in the bearing gap for various separations. Results demonstrate that the load capacity of the bearing is proportional to the viscosity of the fluid; the viscosity of the fluid shows a greater influence over load capacity for smaller bearing separations.

The measured load capacities of the bearing for known viscosities of fluid were used as a reference for the subsequent blood testing.

4.5   Physical Testing - Haemolytic Performance of the SGB
Method

The main aim of this experiment was to analyse the blood compatibility of the SGB by measuring the haemolysis of the blood that flows through the bearing path. Further to this, total haemoglobin (tHb) levels can be measured for blood at inlet and outlet to the chamber. The test rig was set up as shown in Figure 57 and the experiment procedure was repeated as described above, but aqueous glycerol solution was replaced with blood.

The blood used was obtained from a local abattoir; porcine blood was drained directly from the jugular into a pre-anticoagulated vessel. The citrated porcine blood was adjusted to 45% haematocrit by volume via minimal centrifugation and removal of plasma; the blood was around 6 hours old and had been chilled during transport. The blood was tested for its plasma free haemoglobin concentration prior to testing; blood collections with *pfHb* > 20 mg/dL were not used for testing (in accordance with ASTM F1841 [104]).The blood was maintained at 37° C for the duration of the experiment. Samples were placed on ice immediately after being taken.

The test rig was set up as described by the schematic of Figure 57 and is shown in Figure 60 and Figure 61. The load capacity of the bearing was measured as a function of bearing separation; a control rig (no bearing geometry inscribed in the face of the rotating body) was tested and any load capacity caused by a total 7 μm vertical run-out of the rotor (measured at its outer radius) was subtracted from the force generated by the SGB at corresponding bearing separations.
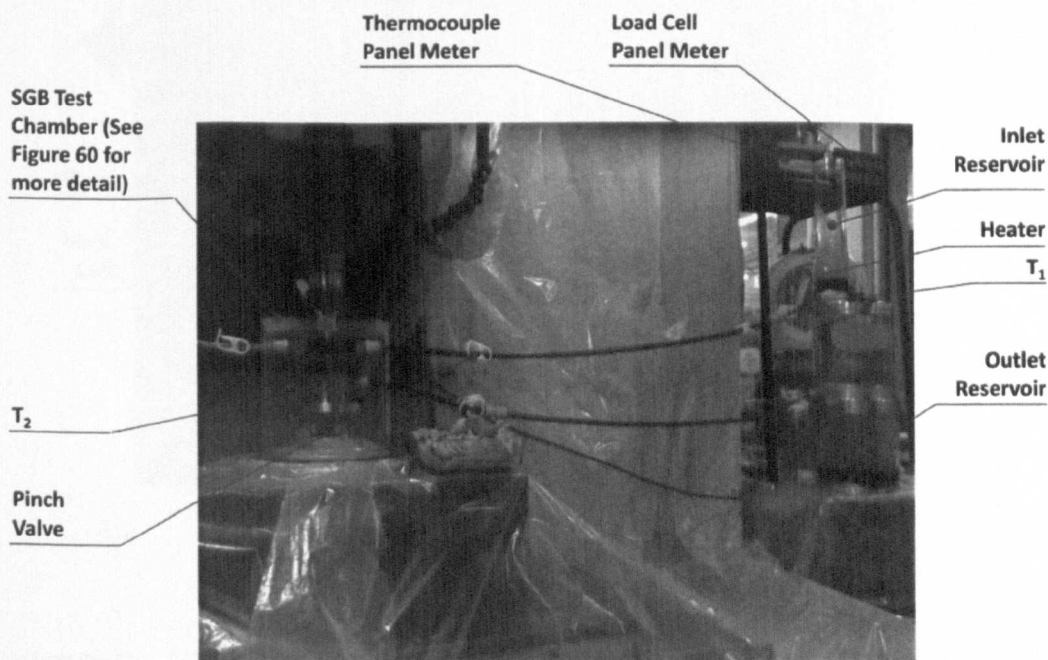
Figure 60: Picture showing experimental setup.

The total haemoglobin levels were measured at inlet and outlet using an IL 682 co-oximeter (Instrumentation Laboratory UK Ltd., Warrington, UK). The haemolysis of the blood was measured using the Harboe assay [105, 106] by comparing levels of plasma free haemoglobin (pfHb) at inlet and outlet to the chamber. Since all surfaces are considered smooth (Ra < 2 μm) and all clearances considered large compared to the bearing gap, it may be said that any difference between the levels of plasma free haemoglobin at inlet and outlet was introduced by damage caused by the high shear levels present in the SGB. The samples were taken using 19 G needles and syringes immediately prior to inlet and after outlet.
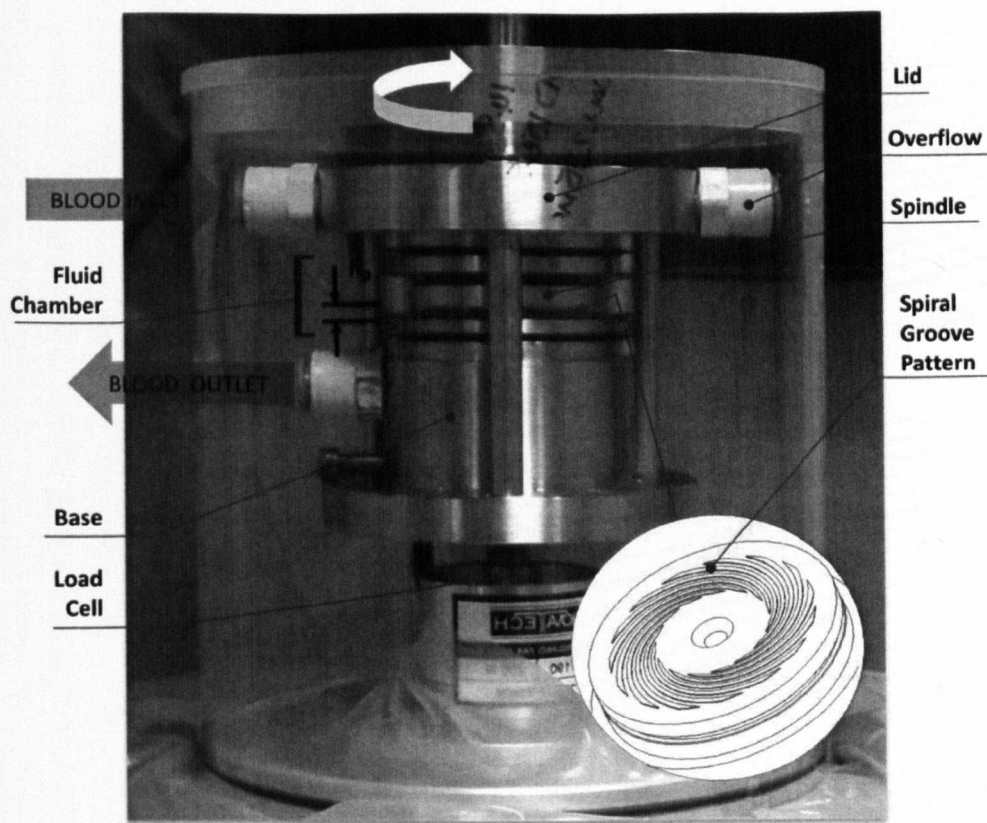
Figure 61: Picture showing close-up of SGB test rig

Further to this, haemolysis and tHb levels have been analysed for three bearings with different cross-sectional groove geometry as shown in Figure 62. Additional tests were conducted in order to estimate the residence time of the blood in SGB by measuring the flow rate though the bearing for each operational bearing separation. Flow rate was determined by recording the volume of blood collected over a discrete time period; the residence time of the blood in the bearing was estimated by dividing the volume of blood under the bearing surface by the volumetric flow rate. Each SGB geometry was tested twice (n=2) and the average of the two tests is presented. Results are tested for outliers through application of Grubb's Test [107].

The Normalised Index of Haemolysis Index (NIH) or the Modified Index of Haemolysis (MIH) cannot be calculated for the experimental set-up described as this is not a recirculating loop and no pumped blood flow rate is available (just bearing flow).
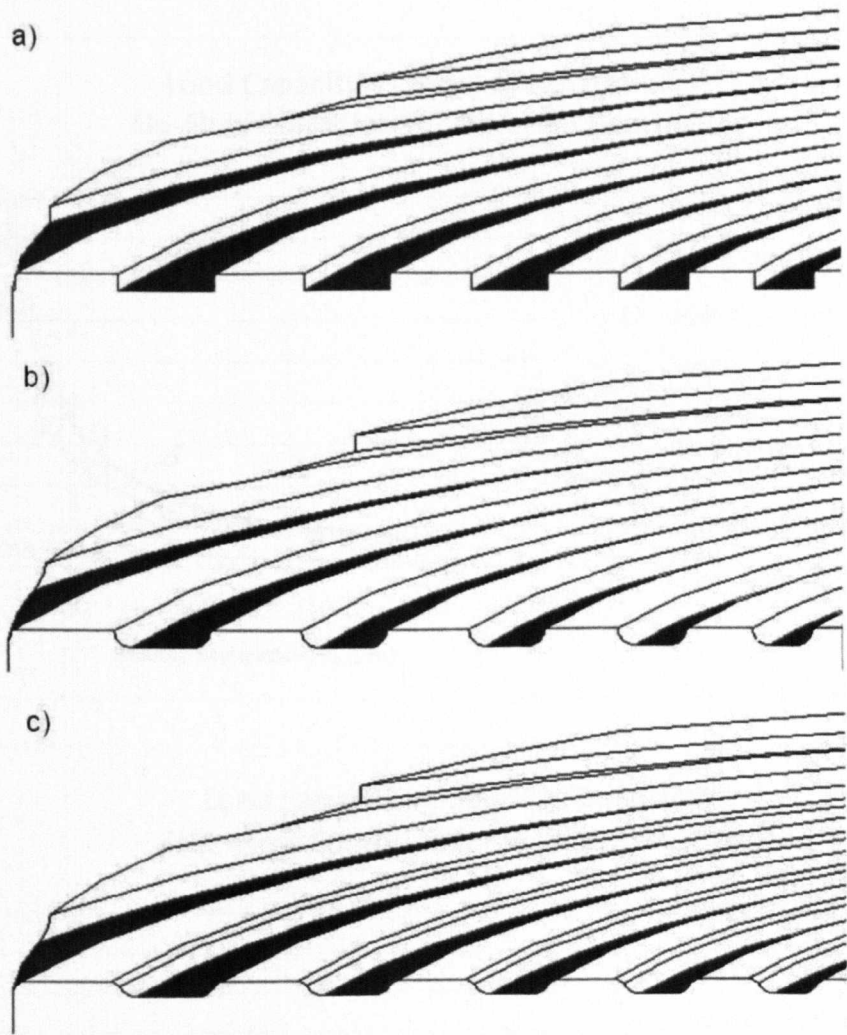
Figure 62: Groove geometry. a) square b) radius at bottom
edge c) radius at bottom edge and chamfer at top edge.

Results

a)

Load Capacity vs Bearing Separation
No-Flow Condition for Different Bearings

◇ Radius & Chamfer - No Flow
○ Radius - No Flow
□ Square - No Flow
△ Control
— ·· Power (Radius & Chamfer - No Flow)
— — Power (Radius - No Flow)
- - - - Power (Square - No Flow)
——— Linear (Control)

b)

Load Capacity vs Bearing Separation
Free-Flow Condition for Different Bearings

◇ Radius & Chamfer - Free Flow
○ Radius - Free Flow
□ Square - Free Flow
△ Control
— ·· Power (Radius & Chamfer - Free Flow)
— — Power (Radius - Free Flow)
- - - - Power (Square - Free Flow)
——— Linear (Control)

Figure 63: Load capacity against bearing separation for different groove cross-section geometry. a) No flow. b) Free flow.
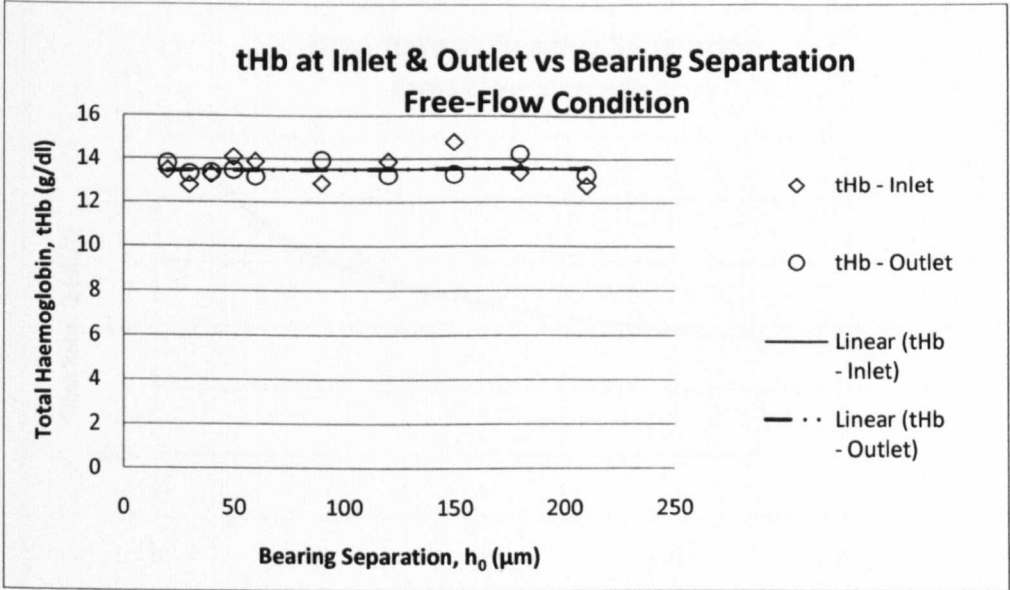
Figure 64: Total haemoglobin levels at inlet and outlet for various bearing separations (example taken from Radius cross-section geometry).
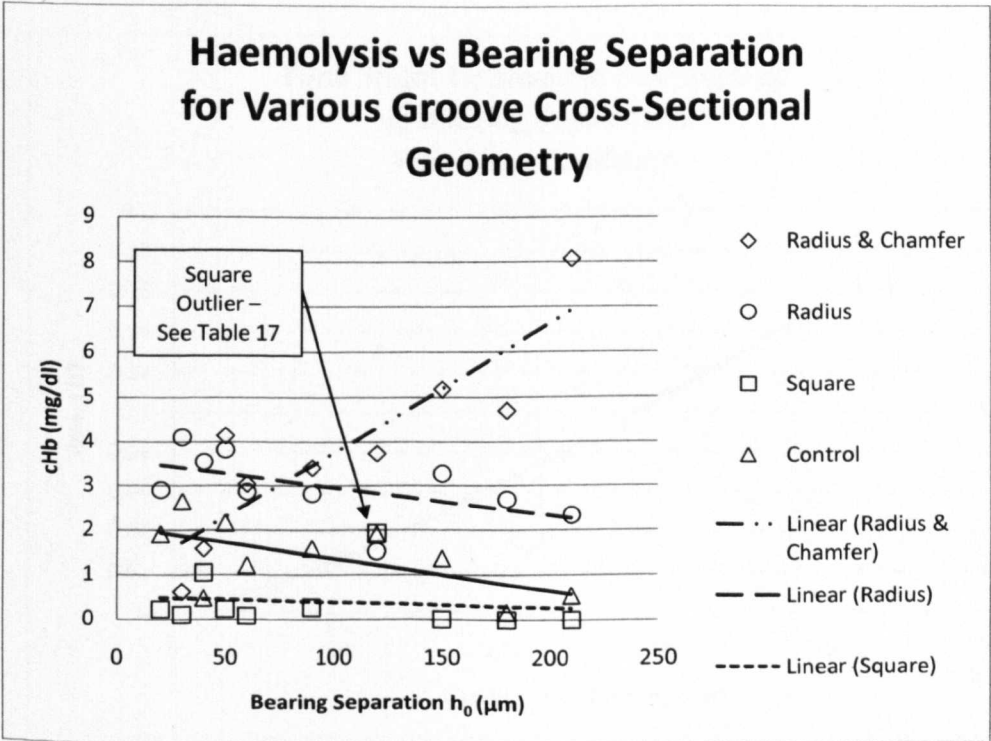
Figure 65: Haemolysis against bearing separation for different bearing geometries.
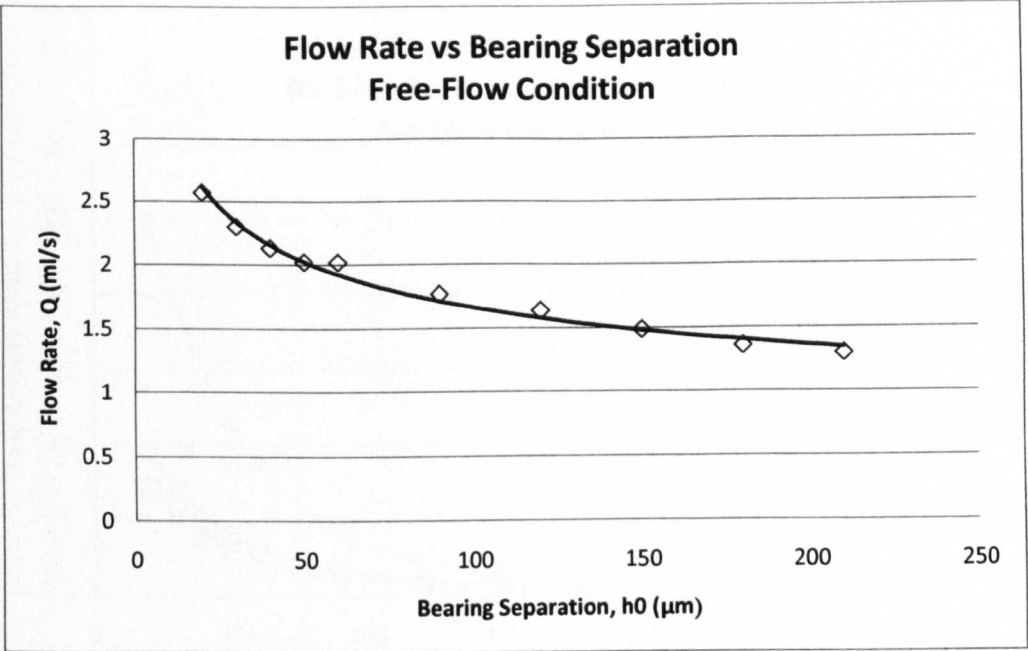
Figure 66: Flow rate of blood through the bearing against bearing separation.
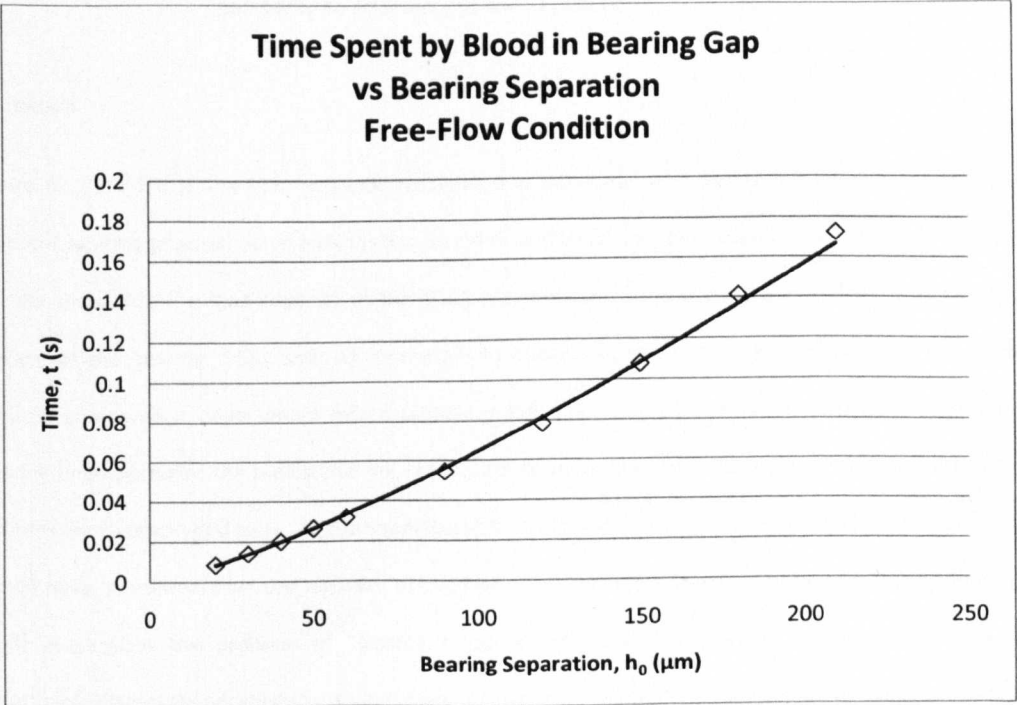
Figure 67: Residence time of blood in bearing gap against bearing separation.
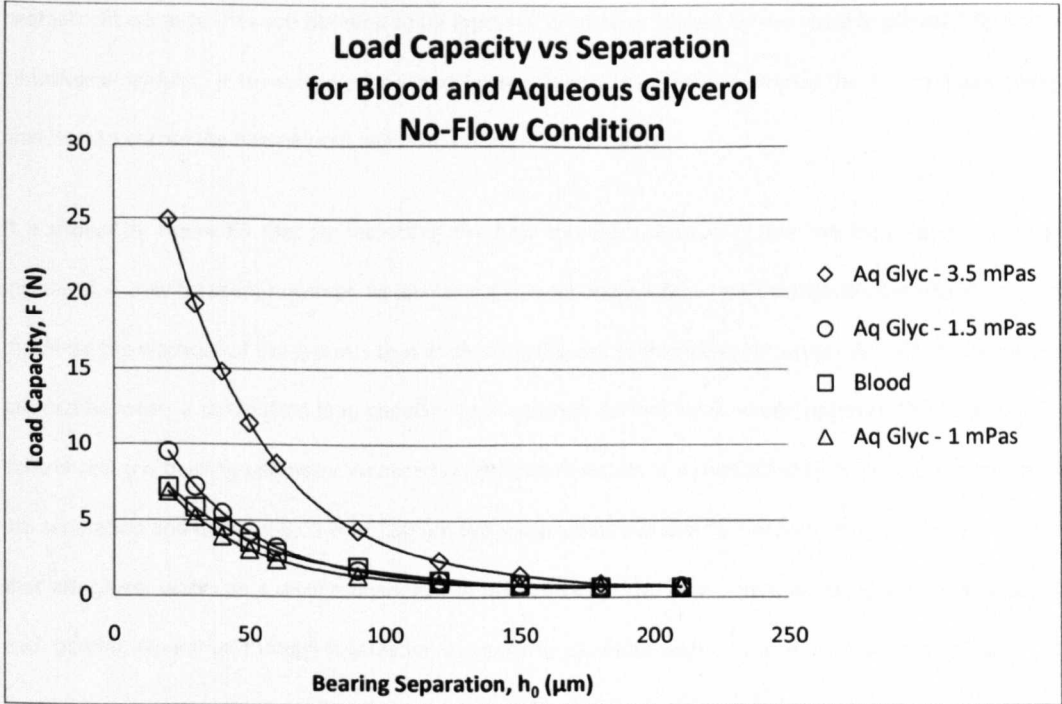
Figure 68: Load capacity of bearing running on blood
compared to aqueous glycerol against bearing separation.

Discussion

Figure 63 details that the load capacity increases asymptotically with decreasing bearing separation for different bearing cross-sectional geometries, for no-flow (Figure 63a) and free-flow (Figure 63b) conditions. Results show that the load capacity of the SGBs is dependent upon the transverse flow rate across the surface of the bearing. SGBs with no restriction to outflow exhibit a 41-49% percent reduction in load capacity compared to SGBs with a fully restricted outlet. The results show that the square cross-sectional bearing underperforms the radius and the radius with chamfer bearing by approximately 25%. Although all samples were centrifuged to adjust the haematocrit levels to 45% RBC by volume, any error in this procedure would have an influence on the viscosity of the blood and therefore the load capacity of the bearing. Bull [108] emphasizes the problem of "plasma trapping", the process whereby normal erythrocytes and deformable discocytes pack tightly on centrifugation such that the trapped fluid could be as high as 4% of the total haematocrit. Bull [108] suggests that a multichannel haematology analyser be used to measure

haematocrit because they are believed to be immune to an error caused by the variable plasma trapping in centrifuged samples. It is recommended that further investigation should employ the use of haematology analysers to ensure the haematocrit levels of the blood are accurate.

It is shown by Figure 63 that by restricting the flow through the bearing that the load capacity may be increased. It may be seen, however, as favourable to encourage a flow rate through the bearing in order to maximise the washout of the grooves thus minimizing the risk of thrombus formation. As such, there exists a balance between a diminished load capacity and washout; further work would optimize this balance. The control test (no bearing geometry inscribed on the rotor) results in a maximal 0.47 N force produced at 20 µm separation and minimal 0.01 N at 210 µm separation. This was due to the vertical run-out of the spindle that affectively works as a wedge bearing. The load capacity has been corrected by appropriate values at each bearing separation through subtraction of any force produced by the control at a given separation.

Figure 64 shows the total haemoglobin level for the blood at inlet and outlet to the bearing over a range of separations; tHb levels are shown be constant between inlet and outlet to the bearing. This means that any red blood cells (RBC) that enter the bearing gap also exit the gap i.e. there is no cell exclusion across the bearing surface as a whole.

Figure 65 shows the change in plasma-free haemoglobin (pfHb) levels between the samples at inlet and outlet for each bearing: The control geometry exhibits negligible levels of haemolysis showing that the rig can add up to 2 mg/dl of pfHb; the square geometry shows maximum amounts of pfHb = 0.5 mg/dl at 20 µm separation and minimum amounts of pfHb = 0.35 mg/dl at 210 µm; the radius geometry shows greater levels of haemolysis ranging from 3.4 mg/dl at 20 µm to 2.3 mg/dl at 210 µm separation. Radius with chamfer geometry show a converse trend displaying maximum haemolysis levels of pfHb = 8.1 mg/dl at 210 µm falling to pfHb = 1.5 mg/dl at 20 µm separation. Grubbs' Test demonstrated that that there was one value detected as an outlying value; details are shown in Table 17; the outlying value is highlighted in the square groove data set in Figure 65.

Table 17: Grubbs' Test results of haemolysis data (Significance level p = 0.05)

SGB Geometry	Mean	Standard Deviation	Critical Standard Deviation	Outlier Detected
Square	0.39	0.63	2.29	Yes (See Figure 65)
Radius	2.98	0.75	2.29	No
Chamfer & Radius	3.83	2.15	2.21	No

Figure 66 describes the flow rate through the SGB as a function of bearing separation; Figure 67 describes the residence time of the RBCs in the bearing gap. As the bearing gap is decreased, the pumping action of the SGB increases (hence the load capacity increases). As such, the residence time falls as the flow rate increases. Figure 67 shows that the maximum residence time is 170 ms at 210 μm separation and the minimum residence time is just 8 ms at 20 μm separation; at 20 μm separation, for a spindle rotating at 2000 RPM, the maximum shear stress seen by the fluid is τ = 806 Pa. According to Paul et al. [102], there are clear thresholds for residence time and shear stress, beyond which haemolysis occurs (residence time above 0.6s and shear stress above τ = 425 Pa). Although the residence time is as low as 1% of that required to cause haemolysis, maximum shear stress seen by the RBCs in the bearing exceeds that of the threshold mentioned by Paul et al; this indicates that SGBs should be haemolytic despite short residence times.

Two important points can be inferred from these results. First of all, the two bearing geometries with sharp leading groove edges (square and radius) exhibit negligible levels of haemolysis. The second point focuses on the radius with chamfer geometry; levels of pfHb fall with decreasing bearing separation. The effect of introducing a chamfer to the leading edge of the groove increases the haemolysis for larger bearing separations; haemolysis at the larger separations is still low however. Given that there is less of a distinct change in shear between the groove and ridge (a less pronounced 'shear front'), as opposed to the sharp edged geometries, some RBCs are drawn into the areas of high shear. Monroe et al. [100] confirm that the introduction of a chamfer leads to increased levels of haemolysis between two rotating discs. This suggests that as the bearing gap is decreased (i.e. as the shear at the spiral groove ridge increases) the RBCs migrate into areas of relatively low shear seen within the spiral groove channels. If this is the case it means that, in the limit, the bearing is operating solely in plasma as the RBCs are excluded from areas of high shear.

The results shown in Figure 68 corroborate the results and discussion above; it shows that the performance of the SGB, when operating in blood, is between the performance curves of the bearing operating in aqueous glycerol of 1 and 1.5 mPas. This confirms that the effective viscosity in the bearing is between 1-1.5 mPas and that all cells have been excluded since the viscosity of plasma is 1.2 mPas.

4.6 Conclusions

The primary aim of this chapter was to investigate the haemolytic performance and of a SGB as a function of bearing gap and groove cross-section geometry. (It is re-emphasised that these SGB tests involved planar bearings for the simplicity of manufacture of the test rig; it is the intention, as mentioned in the preceding and subsequent chapters, to include a conical bearing in the design of the bearing system and resultant CRBP.) Gross results show that SBGs are non-haemolytic; groove cross-section can affect the traumatic performance of the bearing; sharp-edged grooves are less traumatic.

One explanation for the anti-traumatic nature of the bearing might be attributed to the short residence time of RBCs in the SGB, but we suggest here an alternative mechanism is at play – that of exclusion of RBCs from the bearing gap (fluid film). Comparisons to aqueous glycerol tests of known viscosities show that the blood bearing is operating on a viscosity close to that of plasma. The total haemoglobin at entry to the bearing is the same as that on exit from the bearing – there is no cell exclusion across the bearing as a whole. The suggested mechanism for cell exclusion is the migration of RBCs away from areas of high shear stress seen at the ridges to areas of low shear stress seen in the grooves in a fluid regime dominated or delineated by a 'shear front'. The introduction of a chamfer to the leading edge of the groove diminishes the contrast between high- and low-shear regions causing more RBCs to flow in to the high-shear region in the gap and leads to a greater level of haemolysis at larger bearing separations. The chamfered-groove SGB only maintains the delineation between high- and low-shear regions for small bearing separations. As such this chapter suggests a mechanism through which blood bearings do not operate on whole blood but in fact on plasma alone.

There is not a clear 'switch' to cell exclusion. It may be seen a gradual process – the degree of cell exclusion is related to the delineation of the shear front. At larger separation, this delineation is small and as such the

effect of cell exclusion is small. As the bearing gap is decreased, the delineation of the shear front is more apparent. The decreased load capacity due to cell exclusion at larger separations may only be detected using a high accuracy load cell.

The precise geometrical and operational requirements of a SGB which are needed in order to promote an adequate 'shear front differential' that ensures cell exclusion from regions of high shear stress calls for further experimentation; the threshold at which the mechanisms that promote the phenomenon of cell exclusion should be considered in future work in terms of the interaction of the pressures boundaries created by the SGB geometry and the momentum carried by the RBCs in the fluid flow regime.

CHAPTER 5

5   HYBRID MAGNETIC / HYDRODYNAMIC BEARING

5.1   Introduction

This chapter is designed to analyse the suitability of the hybrid magnetic / hydrodynamic bearing that is proposed for use in the new CRBP concept as shown in Figure 24 (Section 2.6.1); its aim is to examine the feasibility of the proposed hybrid bearing system that combines a passive magnetic bearing with a hydrodynamic one. The unity of such technologies allows for the use of magnetic bearing without the need for active control. Chapter 5 then investigates the overall stability of the proposed hybrid bearing / drive system. The performance of the bearings under shock excitation has been estimated through numerical differential methods. The stiffness matrixes for each bearing are produced independently, and then are combined to show that the bearing is inherently unstable due the effects of cell exclusion identified in 4. Modifications are suggested of how the system may be augmented in order to realised the intended design remit. The natural frequencies of the combined bearing are also calculated so show that the bearing will be stable under start-up and full operational conditions.

This study examines the stiffness and inherent stability of the proposed combined bearing system. The conceptual design incorporates a ring of 16 cylindrical (5 mm Ø by 3 mm thick) permanent magnets (grade N42) (e-Magnets UK, Sheffield, UK). The magnets are attached in pairs to a backing ring to form a circle of 8 alternating poles through the thickness of the ring. It was shown in Chapter 3, and by the corresponding paper [83], that incorporation of a cone angle into the magnetic arrangement substantially increases the radial bearing force of the coupling without compromising the axial bearing force. The results in Chapter 3 detailed a number of cone angles ranging from 0° to 30°; an intermediate angle has been chosen based upon a number of design decisions for integration into the hybrid system; accordingly the magnets are arranged on a 15° (included) cone angle. The drive system for the pump consists of six electromagnets (iron cores 4 mm Ø by 10 mm thick) beneath the impeller arranged on a corresponding cone angle; the cores are mounted on a backing ring.

This arrangement of permanent magnets and electromagnets not only forms the drive system for the CRBP but acts as the magnetic bearing. The passive magnetic bearing comprises of the permanent magnets within the impeller and the iron cores of the electromagnets; these same components make up the drive system. A three-phase sinusoidal excitation current is applied to the coils of the electromagnets; the impeller is rotated due to the resultant torque created by the interaction between the oscillating magnetic field of the electromagnets and the alternating poles through the thickness of the permanent magnet ring. The magnetic bearing is complemented by a conical SGB that opposes the forces produced by the magnetic bearing.

The investigation was concerned with the inherent stability of the hybrid bearing system. It analysed the stiffness of each component bearing independently, and combined the results in order to review the natural frequencies of the system. The rotational speed of the impeller was taken to be 2000 RPM for the purposes of this study. The author recognises that this study does not determine the full dynamic characteristics of the device, but highlights that the computational approach undertaken provides a precursor to experimental testing of a prototype through proof of concept of this novel hybrid bearing system.

5.2   Stiffness of Magnetic Bearing

It was possible to predict the stiffness of the magnetic bearing through simulating perturbation of the impeller in relation to the electromagnets. The proposed design for the new CRBP has been modelled using the same BEM software mentioned in Chapter 3. Figure 69 shows the model as seen in the software; it is symmetric about the xz-plane in order to reduce computational requirements.

Modelling considerations have been applied as stated in Section 3.4.2.

Figure 69 shows the 2D-elements assigned to all surfaces of the model. 3D-volume elements are assigned to the impeller backing ring and electromagnet cores, and are not assigned to the permanent magnets, as per Section 3.4.2. The number of 2D quadrilateral elements was 14688. The number of 3D brick elements was 25920.
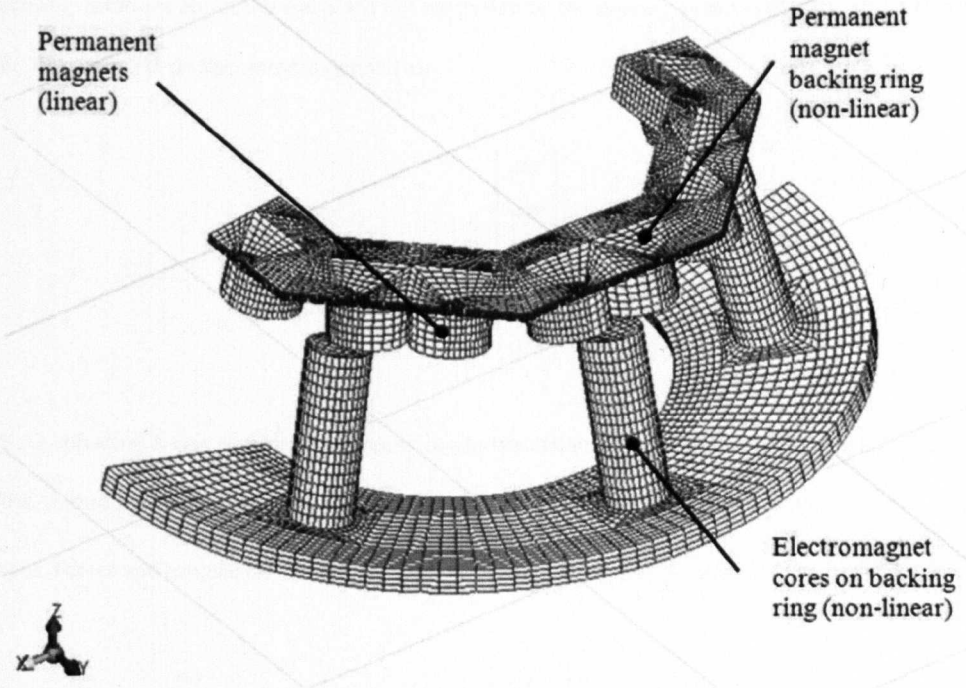
Figure 69: Computational grid. Model is symmetric about the **xz**-plane at y=0. 16 permanent magnets forming an 8 pole magnetic ring on a backing ring. 6 electromagnets on mounting ring (copper coils not shown).

5.2.1 Computational Testing – Magnetic Bearing

Method

The BEM model as shown in Figure 69 has been set such that the magnetic flux gap between the coils and the impeller (modelled as the ring of permanent magnets and backing ring) is 1 mm.

In order to simulate perturbation, the impeller was displaced in the model by ±20 μm along the **x**, **y** and **z** axes. It was also displaced by ±0.00035 radians around the **x** and **y** axes, which resulted in a ±20 μm change in the **z** direction at the outside edge of the impeller. Displacements are denoted by the vector $\underline{q}$ and are defined on rectangular Cartesian coordinates as **Δx**, **Δy**, and **Δz**, which define radial translations along the **x**- and **y**- axes, and axial translation along the **z**-axis; **Δθ$_x$** and **Δθ$_y$** are rotations about the **x**- and **y**- axes

respectively; rotations about the **z**-axis are not controlled by the bearing as this is the axis of rotation of the pump. The change in displacement is defined as:

$$\Delta \underline{q}_\bullet^\bullet = \begin{bmatrix} dz \\ dx \\ dy \\ d\alpha \\ d\beta \end{bmatrix}$$

Using the software, it was possible to compute the forces acting on the impeller in the **x, y** and **z** directions, and the torque around the **x**- and **y**-axes, when the impeller was in the positive and negative displaced positions. Forces and torques on the impeller are denoted by the vector $\underline{f}$, hence:

$$\Delta \underline{f}_\bullet^\bullet = \begin{bmatrix} dF_z \\ dF_x \\ dF_y \\ dM_x \\ dM_y \end{bmatrix}$$

In this way the change in force was recorded over a known displacement. Hence a stiffness matrix was constructed in order to analyse the stiffness of the magnetic bearing. The force and displacement vectors are defined. Matrix $\begin{bmatrix} K \end{bmatrix}$ is defined as the stiffness matrix for the system; through interrogation of Equations 14-19 the following argument shows that the stiffness matrix for the bearing must be symmetric.

$$[K]_\bullet^\bullet = \begin{bmatrix} k_{zz} & 0 & 0 & 0 & 0 \\ 0 & k_{xx} & 0 & 0 & k_{x\beta} \\ 0 & 0 & k_{yy} & k_{y\alpha} & 0 \\ 0 & 0 & k_{\alpha y} & k_{\alpha\alpha} & 0 \\ 0 & k_{\beta x} & 0 & 0 & k_{\beta\beta} \end{bmatrix}$$

Let the vector of forces on the system equal the product of the stiffness matrix and the displacement vector as shown in Equation 14.

$$\Delta \underline{f} = [K] \Delta \underline{q}$$

(14)

An increment of work is

$$\Delta \underline{W} = \frac{1}{2} \underline{f}^{T} \Delta \underline{q} .$$

(15)

where ^{T} denotes the transpose of the vector.

Suppose the displacement is changed from zero to some displacement 1 and then displacement 2

$$\underline{q} = 0 \rightarrow \underline{q} = \underline{q}_1 + \underline{q}_2$$

(16)

Work done moving from $\underline{q} = 0 \rightarrow \underline{q} = \underline{q}_1$ is

$$\Delta W = \frac{1}{2} \left([K] \underline{q}_1 \right)^{T} \underline{q}_1 = \frac{1}{2} \underline{q}_1^{T} [K]^{T} \underline{q}_1$$

(17)

Work done moving from $\underline{q} = \underline{q}_1 \rightarrow \underline{q} = \underline{q}_1 + \underline{q}_2$ is:

Initial force vector = $[K] \underline{q}_1$

Final force vector = $[K] \left(\underline{q}_1 + \underline{q}_2 \right)$

Average force vector = $\frac{1}{2} [K] \left(\underline{q}_1 + \left(\underline{q}_1 + \underline{q}_2 \right) \right) = [K] \underline{q}_1 + \frac{1}{2} [K] \underline{q}_2$

The extra work done is

$$\Delta W = \left([K]\underline{q}_1 + \frac{1}{2}[K]\underline{q}_2 \right)^T \underline{q}_2$$

(18)

The total work done on moving from $0 \rightarrow \underline{q}_1 \rightarrow \underline{q}_1 + \underline{q}_2$ is

$$\Delta W = \frac{1}{2}[K]^T \underline{q}_1^T \underline{q} + \frac{1}{2}[K]^T \underline{q}_2^T \underline{q}_2 + [K]^T \underline{q}_1^T \underline{q}_2$$

(19)

Equation 16 shows that the stiffness matrix for the bearing must be symmetric; there can be no net energy gained from moving from $\underline{q}_0 \rightarrow \underline{q}_1 \rightarrow \underline{q}_2 \rightarrow \underline{q}_1 \rightarrow \underline{q}_0$, exemplified by Figure 70.
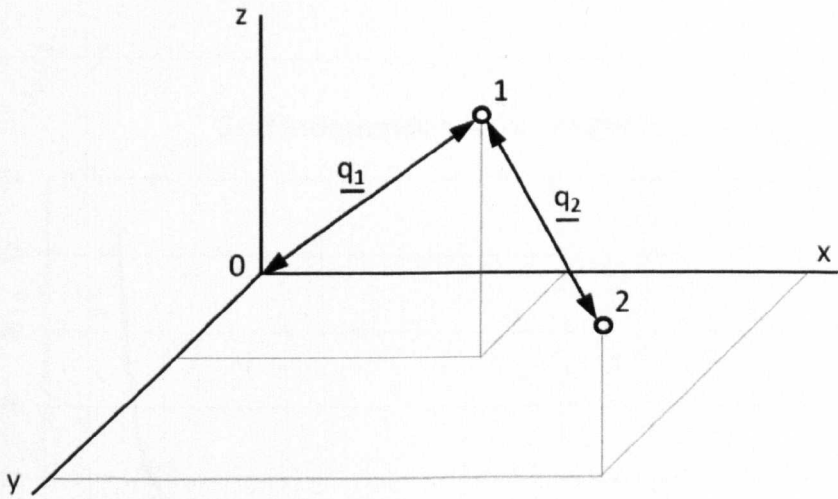
Figure 70: Whatever the route taken from point 0 to point 1 to point 2 and back again, there is no net change in energy or work done.

Results

In order to establish the validity of the results, a grid dependency check was carried out on the computational mesh shown in Figure 69 to establish the minimum total number of elements that must be used in the model so that the answer may be considered accurate; for the purpose of this check, the change in axial force was

calculated for ±20 µm perturbation along the z-axis; results for this check are shown by Table 18 and Figure 71.

Table 18: Number of 2D and 3D elements used for grid independency check.

ΔF (N)	2D elements	3D elements
0.757	29278	53565
0.757	14688	25920
0.762	7310	14417
0.772	3786	6623
0.803	2624	3464
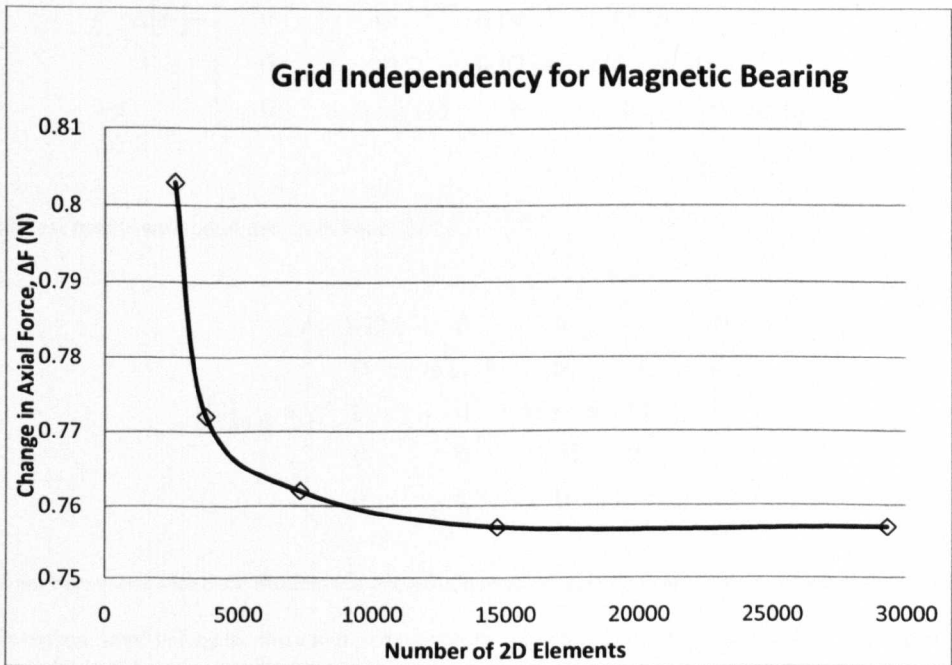
Figure 71: Grid independency showing minimum number of elements that should be used.

Considering the system shown in Figure 69, for the radial and axial displacement components of ±20 µm (=40 µm) and rotational displacements of ±0.0035 radians (=0.007 radians), the force components were computed to be:

$$\Delta[Q] = \begin{bmatrix} 40\times10^{-6} & 0 & 0 & 0 & 0 \\ 0 & 40\times10^{-6} & 0 & 0 & 0 \\ 0 & 0 & 40\times10^{-6} & 0 & 0 \\ 0 & 0 & 0 & 7\times10^{-4} & 0 \\ 0 & 0 & 0 & 0 & 7\times10^{-4} \end{bmatrix}$$

$$\Delta[F] = \begin{bmatrix} -0.757 & 0 & 0 & 0 & 0 \\ 0 & 0.025 & 0 & 0 & -0.00317 \\ 0 & 0 & 0.0413 & 0.0826 & 0 \\ 0 & 0 & 0.0784 & 0.00206 & 0 \\ 0 & -0.00343 & 0 & 0 & 0.00246 \end{bmatrix}$$

The stiffness matrix was calculated from Equation 14.

$$[K]_{MAG} = \begin{bmatrix} -18925 & 0 & 0 & 0 & 0 \\ 0 & 617.5 & 0 & 0 & -4.7 \\ 0 & 0 & 1031.5 & 115 & 0 \\ 0 & 0 & 115 & 2.9 & 0 \\ 0 & -4.7 & 0 & 0 & 3.5 \end{bmatrix}$$

NB: When non-linear magnetic models are analyzed numerically, it is impossible to get absolute zero values. For this reason, small values for the x and y components of force, and moments about the x and y axes (in the order of 1×10^{-5} N) were considered negligible and approximated to zero.

Discussion

The number of elements used for an accurate solution was 25920 3D brick elements and 14688 2D quadrilateral elements; Figure 71 shows further increase in the number of elements yield a negligible increase in accuracy.

The matrix describes the behaviour of the bearing, which shows an axial stiffness approximately equal to -19 kNm^{-1}, indicating that the impeller will be pulled down towards the volute casing which houses the electromagnets. Radial stiffness oscillates between the values of 0.6175 kNm^{-1} and 1.0315 kNm^{-1}, just 0.6 % of the axial stiffness. Rotational stiffness oscillates between a low value of 0.0029 kNm^{-1} and a high value of 0.0035 kNm^{-1}. This oscillation is due to the nature of a 6/8 permanent magnet drive system and may promote cogging of the drive system. It is suggested that further work in the development of the motor consider the net axial force of attraction between the excited coils and the impeller. The influence of pulse-width modulation must be investigated; it is proposed to implement a sinusoidal excitation to the coils in order to maintain a constant net magnetic preload to the impeller.

For the system to be stable all values of the leading diagonal (except k_{zz}) must be positive. Further requirements for stability are for the functions $k_{xx}k_{\beta\beta} - k_{x\beta}k_{\beta x}$ and $k_{yy}k_{\alpha\alpha} - k_{y\alpha}k_{\alpha y}$ to be positive.

$$k_{xx}k_{\beta\beta} - k_{x\beta}k_{\beta x} = 31,108$$

$$k_{yy}k_{\alpha\alpha} - k_{y\alpha}k_{\alpha y} = -3,996,632$$

The results show that the magnetic bearing system is inherently unstable; this is expected from a purely passive magnetic system as stated by Earnshaw's theorem [78]. As a consequence, passive magnetic bearings cannot be used exclusively; it can be shown that "never will a radial bearing be axially stable nor will a thrust bearing be radially stable" [86]. They must therefore be used in conjunction with a mechanical system or active magnetic bearings in order to achieve complete suspension. A passive magnetic bearing will be either a radial bearing if it controls a rotation axis, or an axial one, when it maintains the position of the rotor against

displacement along the axis of rotation [87]. For these reasons the magnetic bearing is coupled with a hydrodynamic bearing to form the complete bearing system.

5.3 Stiffness of Conical Spiral Groove Bearing
Method

The performance of a conical hydrodynamic bearing can be predicted using Equation 17 outlined by Muijderman [94]. Variables are identified in Table 15.

$$F = \frac{K_1 C_2}{2} \frac{\omega}{h_0^2} \frac{\left(\frac{(h_0 \ h_2)}{1+(h_0 \ h_2)}\right)^2 \cot(\alpha)\left(1-\left(\frac{(h_0/h_2)}{1+(h_0/h_2)}\right)\right)\left(1-\left(\frac{(h_0/h_2)}{1+(h_0/h_2)}\right)^3\right)}{\left(1+\left(\frac{(h_0/h_2)}{1+(h_0/h_2)}\right)^3\right)^2 + 4\left(\frac{(h_0 \ h_2)}{1+(h_0/h_2)}\right)^3 \cot(\alpha)^2}$$

(20)

Where

$$K_1 = 3\pi R^4 \eta\left(1-(r_i/r_o)^4\right)$$

$$C_2 = \frac{e^{\frac{-2\pi}{k}\left(1-\frac{2\alpha}{\pi}\right)\tan(\alpha)} - (r_i/r_o)^4 e^{\frac{2\pi}{k}\left(1-\frac{2\alpha}{\pi}\right)\tan(\alpha)}}{1-(r_i/r_o)^4}$$

Section 4.3.2 details the rationale behind the choice of the bearing parameters that make up Equation 20. However, the author recognises the possibility of cell exclusion from the bearing gap based upon the evidence presented in Chapter 4, and as such three cases for the stiffness of the hydrodynamic bearing have been modelled using the groove geometry tested in Chapter 4 (see Table 16).

The first case assumes the viscosity η of whole blood (3.5 mPas).

The second and third cases examine the operation of the bearing considering the effects of cell exclusion. Vidakovic et al. [109] suggest that the use of biological fluids [in the testing of the pump] increases the system

efficiency when compared to the use non-biological fluids of the same viscosity. Since an increase in system efficiency is related to a drop in local viscosity between the bearing surfaces, the possibility of cell exclusion may be shown to exist – a theory further corroborated by the results from Chapter 4. The second and third cases use a viscosity of 2.4 and 1.2 mPas respectively. Table 19 summarizes the three different cases.

Table 19: Parameters for bearing geometry and operation

Parameter	Case 1	Case 2	Case 3
Groove height, h_2 (µm)	200	200	200
Viscosity, η (mPas)	3.5	2.4	1.2

The stiffness matrix for the SBG was constructed using the following procedure: The bearing surface was split into 10 concentric rings, each with 12 segments, to set a 12 by 10 array (Figure 72). The **x, y** and **z** coordinates of the centre of each segment were found, as were the areas of each segment and the **x, y** and **z** direction cosine from the centre of each segment. The hydrodynamic separation gap was set to be the same for each segment.
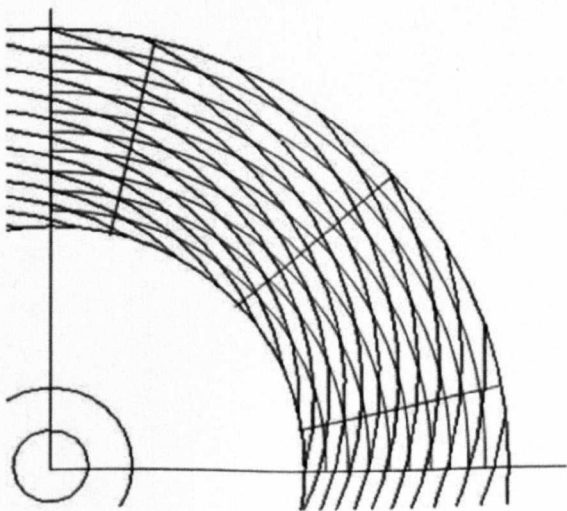
Figure 72: Diagram showing how the conical spiral groove bearing is segmented. 10 concentric rings each with 12 segments. The problem is simplified through symmetry by analysing ¼ of the bearing surface.

Next, the force components on each segment was calculated in the **x**, **y** and **z** directions. This was done by calculating the force on each ring using Equation 20; the force on each segment was approximated to be $1/12^{th}$ of the total force on the ring. The force on each segment was multiplied by the direction cosine for that segment in each of the **x**, **y** and **z** directions; this yields a net force vector on each segment, the sum of which totals the entire force on the impeller bearing surface. In the un-perturbed state, there is no hydrodynamic force unbalance on the impeller.

Perturbation of the impeller was simulated by altering the separation gap; i.e. if the rotor was displaced along the **x**-, **y**- or **z**-axis, or rotated about either the **x**- or **y**-axis, it was possible to calculate the new separation gap for each individual segment. The same displacement criteria used in this hydrodynamic analysis were used in the magnetic analysis as in Section 5.2.1; matrix $[Q]$ is therefore the same. It is now possible to calculate the new force on each segment at the new displacement, and construct the matrix $[F]$. Consequently, the stiffness of the bearing may now be calculated as the change in force is known over known displacements.

NB: Considering the results from Chapter 4, the final values that populate matrix $[F]$ have been taken as 50% of the calculated values as the theory has been shown to over-predict the measured values by a factor of 2.

Results

The stiffness matrix for the SGB was calculated using Equation 14; Table 20 shows the stiffness for the three cases.

Table 20: Spiral groove bearing stiffness

Case	Matrix
Case 1 $h_2 = 200\ \mu m,\ \eta = 3.6\ mPas$	$[K]_{HYDRO-1} = \begin{bmatrix} 165993 & 0 & 0 & 0 & 0 \\ 0 & 2985 & 0 & 0 & -12 \\ 0 & 0 & 2985 & 12 & 0 \\ 0 & 0 & 12 & 54 & 0 \\ 0 & -12 & 0 & 0 & 54 \end{bmatrix}$
Case 2 $h_2 = 200\ \mu m,\ \eta = 2.4\ mPas$	$[K]_{HYDRO-2} = \begin{bmatrix} 110615 & 0 & 0 & 0 & 0 \\ 0 & 1990 & 0 & 0 & -8 \\ 0 & 0 & 1990 & 8 & 0 \\ 0 & 0 & 8 & 36 & 0 \\ 0 & -8 & 0 & 0 & 36 \end{bmatrix}$
Case 3 $h_2 = 200\ \mu m,\ \eta = 1.2\ mPas$	$[K]_{HYDRO-4} = \begin{bmatrix} 55331 & 0 & 0 & 0 & 0 \\ 0 & 995 & 0 & 0 & -4 \\ 0 & 0 & 995 & 4 & 0 \\ 0 & 0 & 4 & 18 & 0 \\ 0 & -4 & 0 & 0 & 18 \end{bmatrix}$

Discussion

The stiffness matrices for the hydrodynamic bearing show a large axial stiffness compared to the radial and rotational stiffness. The axial stiffness is positive and as such the force acts to push the impeller away from the volute casing. A planar SGB exhibits zero radial stiffness. The presence of the cone angle on the spiral groove shows that a radial stiffness has been introduced (components k_{xx} and k_{yy} of $[K]_{HYDRO}$), but this is just 2% of the axial stiffness.

For a bearing operating in whole blood, as in Case 1, the axial, radial and rotational stiffness are 166 kNm^{-1}, 3 kNm^{-1} and 0.05 kNm^{-1} respectively. The rotational stiffness due to radial displacement is 0.012 kNm^{-1}.

Case 2 and Case 3 consider the possibility of cell exclusion; it is shown in Figure 73 that the stiffness of the bearing is proportional to the viscosity of the fluid in the bearing gap. For Case 2, the axial, radial and rotational stiffness are 111 kNm^{-1}, 2 kNm^{-1} and 0.036 kNm^{-1} respectively; the rotational stiffness due to radial displacement is 0.008 kNm^{-1}. Similarly, for Case 3, the axial, radial and rotational stiffness are 55 kNm^{-1}, 1.0 kNm^{-1} and 0.018 kNm^{-1} respectively; the rotational stiffness due to radial displacement is 0.004 kNm^{-1}.
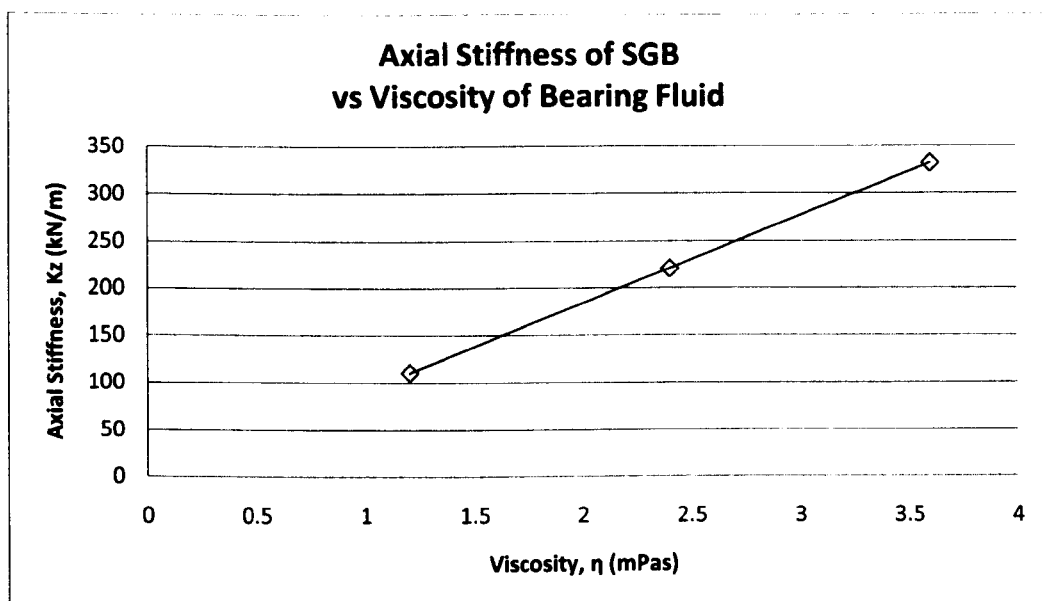
Figure 73: Reduction in SGB stiffness with reduced bearing fluid viscosity

It is noted that this approach neglects squeeze film damping and could in fact under-estimate the stiffness of the hydrodynamic bearing. It is recommended that further investigation would extend this study to include the effects of squeeze film damping in a full dynamic study.

5.4   Combined Hybrid Bearing System

Method

The combined stiffness of the bearing was determined through the addition of the two stiffness matrices. Further to the overall stiffness, the natural frequencies of the system were found through interrogation of

the mass and diametral inertia of the impeller. The full stiffness matrix for the combined bearing system was calculated using Equation 18.

$$[K]_{TOTAL} = [K]_{MAG} + [K]_{HYDRO}$$

(21)

The combined bearing stiffness was calculated using the worst case scenario of a bearing operating solely on plasma i.e. (hydrodynamic case 3).

$[K]_{TOTAL}$ was used to assess the stability of the combined bearing system using the stability criteria $k_{xx}k_{\beta\beta} - k_{x\beta}k_{\beta x}$ and $k_{yy}k_{\alpha\alpha} - k_{y\alpha}k_{\alpha y}$.

The mass matrix for the impeller was constructed by examining the mass and diametral inertia of the impeller. The part has been modelled using Pro/ENGINEER (PTC, Needham, USA) and is shown in Figure 74. The mass matrix about the origin of the BEM model $[M]_{ORIGIN}$ has been formulated.
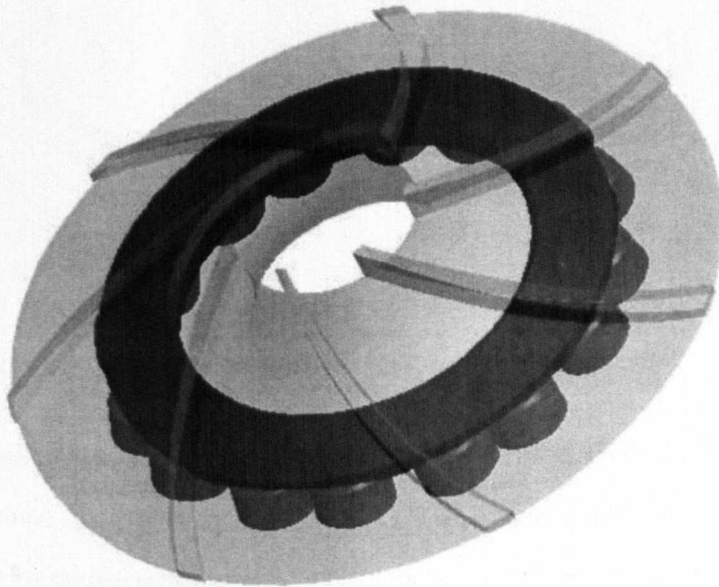
Figure 74: Impeller showing internal ring of permanent
magnets and ferromagnetic backing ring.

NB: All analysis for the bearing stiffness considers translation and rotation about the model origin. Since the centre of gravity (COG) of the impeller model created using Pro/ENGINEER is remote from the BEM model origin at a coordinate (0, 0, 0.773) mm, it was necessary to transform the mass matrix for the coordinates defined as the origin of the model; Figure 75 shows how the impellor COG lies above the model origin. NB: In future analyses it would be prudent to arrange the BEM model origin to be coincident with the impeller COG; this would simplify the study.
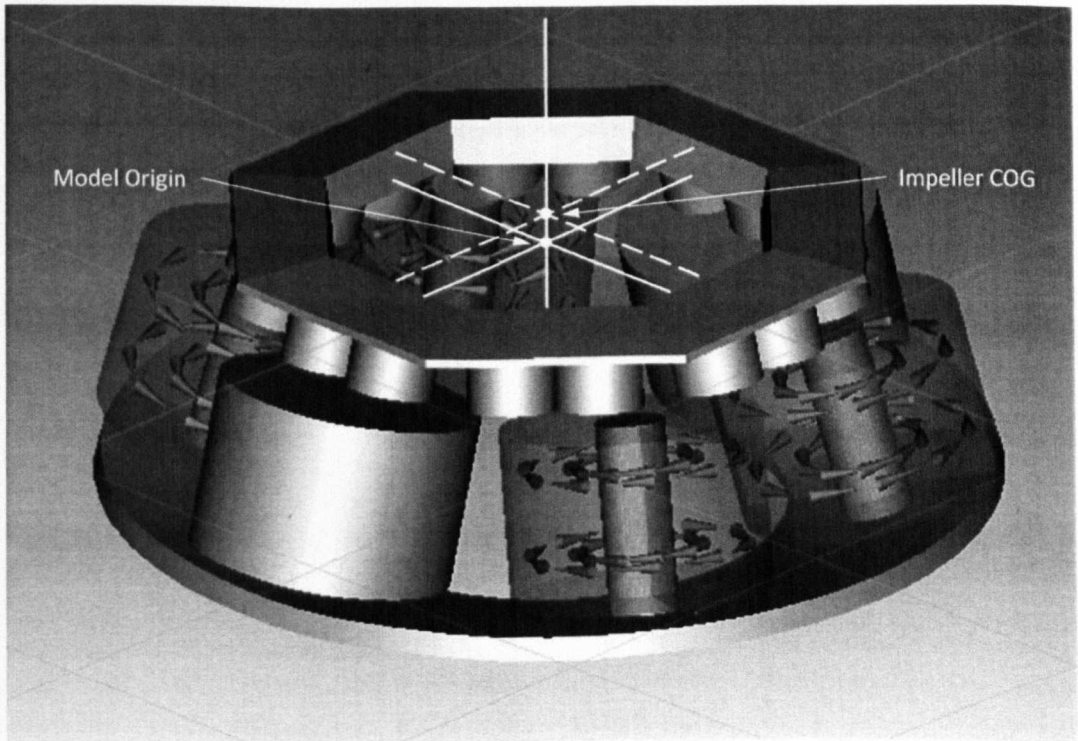
Figure 75: BEM model showing impeller COG and model origin

The natural frequencies for the combined system were calculated as the eigenvalues yielded from the mass and stiffness matrices using MATLAB (The Mathworks, Massachusetts, USA). Five natural frequencies correspond to the five degrees of freedom used in the preceding analysis. For the stable running of the hybrid drive / bearing system the natural frequencies of the system must be sufficiently different from any other excitation frequency, which include:

- External excitation from the patient moving (≈ 5 Hz for an extreme case).

- The rotational frequency of the impeller. 2000 RPM is equivalent to 33.3 Hz.

- The blade passing frequency. For a 7 blade impeller this is 233.1 Hz (=7 x 33.3 Hz).

- Excitation caused by the commutation frequency of the electromagnetic coils. For an 8/6 permanent magnet device there will be 12 commutations per coil per revolution, which for a device running at 2000 RPM is 400 Hz (=12 x 33.3).

Further to the stiffness matrices, the BEM software has been used to simulate the impeller being drawn vertically upwards i.e. away from the electromagnetic cores; the magnetic force of attraction was calculated as a function of bearing separation. The resultant magnetic pull-gap curve is compared to the hydrodynamic load capacity curves obtained in Chapter 4 as a means to investigate the interaction of the two bearing systems.

Results

The combined stiffness matrix is:

$$[K]_{TOTAL} = \begin{bmatrix} 36331 & 0 & 0 & 0 & 0 \\ 0 & 1612.5 & 0 & 0 & -8.7 \\ 0 & 0 & 1026.5 & 119 & 0 \\ 0 & 0 & 119 & 20.9 & 0 \\ 0 & -8.7 & 0 & 0 & 20.9 \end{bmatrix}$$

The combined bearing system shows both stability criteria to be positive.

$$k_{xx}k_{\beta\beta} - k_{x\beta}k_{\beta x} = 33625 \text{ and } k_{yy}k_{\alpha\alpha} - k_{y\alpha}k_{\alpha y} = 7293$$

The mass matrix for the impeller may be constructed by examining its mass and diametral inertia. The part has been modelled using Pro/ENGINEER (PTC, Needham, USA). Figure 74 shows the model of the impeller;

mass $\mathbf{m} \approx 21$ g, diametral inertia $\mathbf{J_D} = 2.14 \times 10^{-6}$ Kgm^2. Then the mass matrix about the centre of gravity

(COG) for the component is:

$$[M]_{COG} = \begin{bmatrix} 2.1 \times 10^{-2} & 0 & 0 & 0 & 0 \\ 0 & 2.1 \times 10^{-2} & 0 & 0 & 0 \\ 0 & 0 & 2.1 \times 10^{-2} & 0 & 0 \\ 0 & 0 & 0 & 2.14 \times 10^{-6} & 0 \\ 0 & 0 & 0 & 0 & 2.14 \times 10^{-6} \end{bmatrix}$$

NB: The centre of gravity is remote from the model origin at a coordinate (0, 0, 0.773) mm. All analysis for the

bearing stiffness considers translation and rotation about the model origin. For this reason it is necessary to

transform the mass matrix for the coordinates defined as the origin of the model. MATLAB yields a result for

the mass matrix about the model origin:

$$[M]_{ORIGIN} = \begin{bmatrix} 2.1 \times 10^{-2} & 0 & 0 & 0 & 0 \\ 0 & 2.1 \times 10^{-2} & 0 & 0 & 1.623 \times 10^{-2} \\ 0 & 0 & 2.1 \times 10^{-2} & -1.623 \times 10^{-2} & 0 \\ 0 & 0 & -1.623 \times 10^{-2} & 0.00214 & 0 \\ 0 & 1.623 \times 10^{-2} & 0 & 0 & 0.00214 \end{bmatrix}$$

The natural frequency for each degree of freedom of the system was calculated as the eigenvalue yielded

from the mass and stiffness matrices; results are shown in Table 21 :
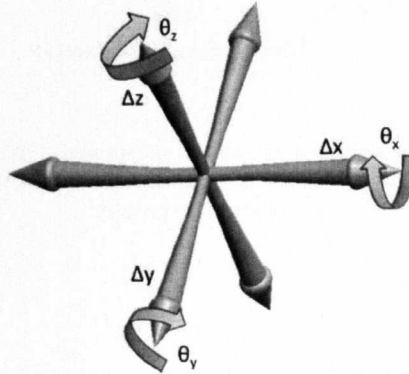
Figure 76: Degrees of Freedom (DOF)

Table 21: Natural frequencies of the system corresponding
to each controlled DOF

Degree of Freedom	Δz	Δx	Δy	$\Delta \theta_x$	$\Delta \theta_y$
Natural Frequency, ω_n (Hz)	501.7	75.4	80.0	903.3	910.8

Figure 77 shows the interaction of the magnetic and hydrodynamic bearings. Displayed is the pull-gap curve

for the magnetic bearing compared to the load capacity curves for a SGB operating on blood and aqueous

glycerol of viscosity 3.5 mPas.
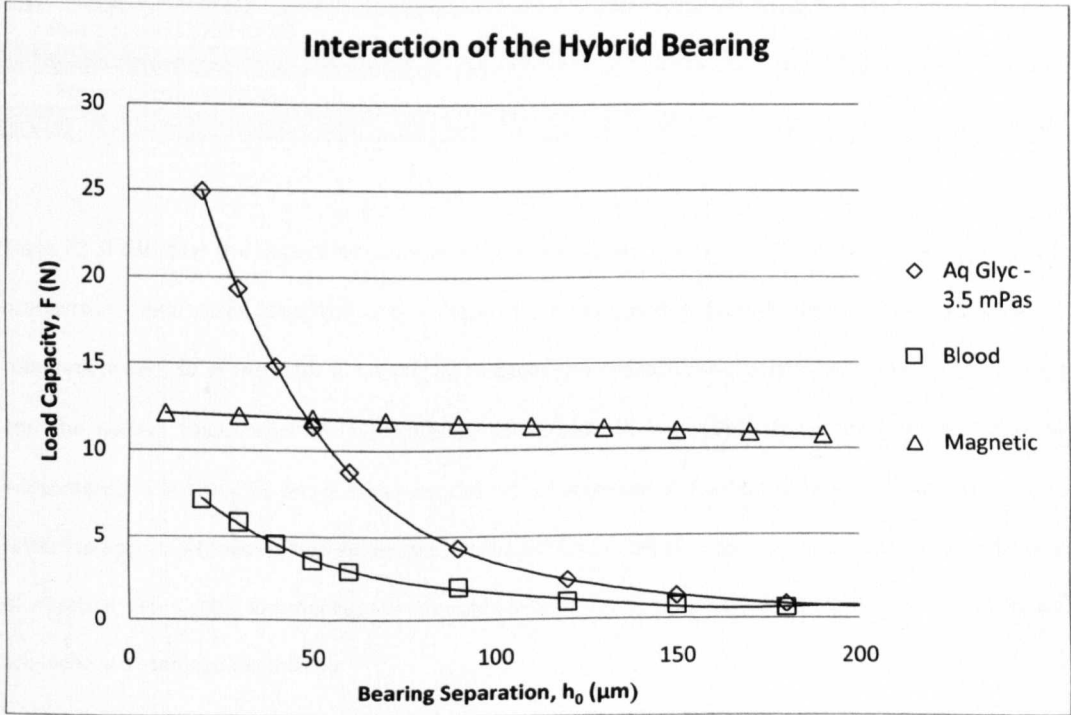
Figure 77: Pull-gap curve for the magnetic bearing compared to the load
capacity curves of a SGB operating on fluid of two different viscosities (SGB data
taken from Chapter 4).

Discussion

The addition of the hydrodynamic bearing to the magnetic bearing transforms the previously unstable

passive magnetic bearing to a stable hybrid bearing. This is shown through satisfaction of the stability criteria.

The natural frequencies of the system have been calculated; these are shown to be sufficiently different from any excitation frequencies identified that may cause the system to behave in an unstable fashion at the operational speed of 2000 RPM. Table 22 shows the identified frequencies that the system must avoid at operational speed, and the calculated natural frequencies of the system.

Table 22: Shows the identified frequencies that the system must avoid at operational speed, and the calculated natural frequencies of the system.

Indentified Frequencies to avoid (Hz)		Natural Frequencies of the bearing, ω_n (Hz)
External excitation	5	75.4
Pump speed (2000 RPM)	33.3	79.6
Blade-passing frequency	233.1	501.7
Electrical commutation	400	903.3
-		910.8

Table 22 shows that the natural frequencies of the bearing are sufficiently different from any potentially problematic frequencies identified above. However, hydrodynamic bearing stiffness is proportional to rotational speed, so as the rotor is running up to speed the hydrodynamic bearing stiffness will be reduced and the natural frequencies are also altered. As a result, it is possible that critical speeds could be encountered in the running range. However, the rate of acceleration must be sufficiently small to cause the system to operate at these critical speeds for a sufficient time in order to build up any appreciable amplitudes of vibration. Lewis [110] summarizes that transient instabilities of extremely short duration *are* possible, but are unlikely to damage the bearing.

Figure 77 describes the interaction of the two bearing systems. It is important to recognise the design intent behind the hybrid bearing. If the impeller were to be displaced along the negative z-axis i.e. towards the bottom of the volute casing, the hydrodynamic bearing would become the dominant bearing, and act to separate the impeller and the casing. If the impeller is displaced along the positive z-axis i.e. towards the top of the volute casing, the magnetic bearing would become the more dominant bearing, and as such act to restore the impeller towards the equilibrium position. Figure 78 exemplifies the intended operation.
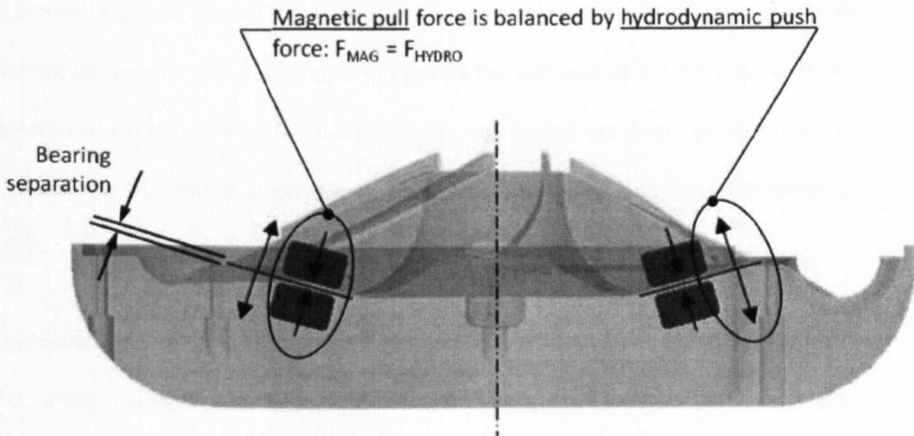
Figure 78: Balance of hydrodynamic and magnetic forces

However, Figure 77 shows that the intended method of operation is not feasible with the selected set-up. It is shown that if the SGB were to operate on whole blood, the load capacity curve of the SGB would balance the magnetic attraction of approximately 12 N at a bearing separation of approximately 50 μm. However, it was shown in Chapter 4 that the SGB was operating on plasma alone due to cell exclusion; the load capacity of a SGB operating on plasma is insufficient to balance the magnetic preload at any hydrodynamic bearing separation.

It has been shown, therefore, that as a consequence of cell exclusion within the bearing grooves that the proposed system must be redesigned in order for the bearing to operate as intended. The load capacity of the SGB may be increased in a number of ways, in order to compensate for the reduced blood viscosity, which include: ramping up the operational speed of the pump; and reducing the height of the grooves. However, if the design remit is considered, as presented in Chapter 2, it is seen as unfavourable to increase the pump speed as this leads to increased shear stresses in the pump and bearing gap, and potentially increased levels of haemolysis and thrombus due to platelet activation. Moreover, an increase in operational speed results in a larger flow rate and pressure head; changing the operational speed would necessitate a redesign of the blade geometry and, indeed, the impeller diameter. Reducing the groove height is also not a tangible solution to the problem as the 'shear front differential' identified in Chapter 4 is promoted by a

larger groove height to film thickness ratio. Reducing the operational bearing separation also increases the 'shear front differential' and consequently increases the potential of the RBCs to avoid areas of high shear stress; levels of haemolysis may be reduced due to augmented cell exclusion. It is may be seen, therefore, advantageous to maintain a larger groove depth to bearing separation ratio in order to encourage cell exclusion.

It is suggested therefore that the magnetic preload should be reduced, either by a reduction in permanent magnet strength and/or size, or by increasing the magnetic flux gap between the impeller and the electromagnets. Both of these options however would result in a reduction in motor efficiency.

5.5   Conclusions

In the first instance, this investigation has predicted the suitability of the hybrid magnetic / hydrodynamic bearing for use in a new CRBP. It has been shown that the superposition of a hydrodynamic bearing onto a passive magnetic bearing may transform a previously unstable system into a stable one, as demonstrated through numerical analysis of the stiffness matrix: $k_{xx}k_{\beta\beta} - k_{x\beta}k_{\beta x}$ and $k_{yy}k_{\alpha\alpha} - k_{y\alpha}k_{\alpha y}$ are both positive.

The natural frequencies for the system were calculated from the eigenvalues yielded from the mass and stiffness matrices; they have been shown to be sufficiently different from any excitation frequencies that may cause the system to become unstable.

The main point to be realized from this analysis, however, is that the proposed set-up of the hybrid bearing is not feasible due to the effect of cell exclusion, which causes the SGB to operate on a reduced viscosity. Recommendations have been made that would allow the hybrid bearing to operate as intended; a simple change to the magnetic flux gap would decrease the magnetic preload and as such allow the two bearing forces to reach an equilibrium.

The author recognises that this study does not determine the full dynamic characteristics of the device. The computational approach undertaken in the study provides a precursor to experimental testing of a prototype through proof of concept of this novel hybrid bearing system. Since the success of devices such as CRBPs are

highly reliant on their bearings, it is necessary to prove that the bearings are theoretically stable before implementation into a prototype.

The work presented here is the subject matter for the publication *A Novel Hybrid Magnetic / Hydrodynamic bearing for a Centrifugal Rotary Blood Pump* – currently accepted and awaiting revision for publication in *Artificial Organs*.

CHAPTER 6

6   CONCLUSIONS

Highlighted in this work is the need for an effective treatment method to the growing worldwide prevalence of congestive heart failure. Annually, there are an estimated 8.75 million deaths caused by congestive heart failure worldwide, representing 15% of all global deaths; of these deaths about 80% occur in low- and middle-income countries [2]. If current trends are allowed to continue, by 2015 an estimated 10 million people annually will die from CHF [3]. Currently, the gold standard for end-stage CHF treatment is an orthotopic heart transplant (OHT). However, only about 3,000 donor organs are available each year which exemplifies the short-comings of OHTs as only current definitive long-term treatment for end-stage CHF. To compound the severity of the situation, organ donations are decreasing [4]. Implantable blood pumps offer an effective treatment to CHF, either as a bridge to transplantation / recovery, or as destination therapy. With the number of sufferers of CHF rising in both the developed and developing world it becomes pertinent to design a cost-effective device. Identified here is the major limiting factor that restricts the prevalence of LVADs as a viable treatment for CHF; that factor is cost.

It is the aim of this project is to dismiss the barriers to market that currently exist by establishing a cost-effective device. By designing a LVAD that may be used as bridge-to-recovery, the market in the developed world is widened to include pre-Stage-4 CHF patients, whilst the potential market in the developed world may be entered. It is proposed to reduce the cost of these devices through implementation of standard, off-the-shelf engineering components to replace those expensive, bespoke parts that must be manufactured for current devices. Further to this, it is proposed to install high through-put processes, such as injection moulding, in order to reduce the cost of manufacture. The process of injection moulding allows for the over-moulding of the stock components identified in Section 2.4 and the integration of ancillary components (such as cannulae) to the main volute casing. The use of the stock components not only reduces the intrinsic cost through the replacement of those bespoke parts, but negates the need for hermetic sealing (laser welding) when combined with over-moulding methods. In this way, complete processes may be removed from

production line. Cost may be further reduced though the use of established biocompatible materials, such as PEEK, in the injection moulding process; the surface treatment of those custom-machined components (such as a diamond-like carbon coating to machined, titanium surfaces) is also unnecessary.

The work presented in this thesis identifies the principle difference between current pump designs; this is their bearing system. It has been proposed here to form a new classification of bearing type that combines a passive magnetic bearing and a hydrodynamic bearing such that the relative potential merits of both systems may be exploited. Through the amalgamation of established design techniques with other more modern design practices a rigorous, adaptive design tool has been produced that CRBP designers may use to quickly obtain full impeller and volute geometry from few input parameters. The geometry output provides a platform from which a new conceptual LVAD has been envisaged.

This investigation has shown, through experimental and computational analysis of the magnetic coupling, that it is possible to integrate the magnetic bearing and the drive system into one component of design; it is possible to design a magnetic coupling that not only acts as the drive system for a CRBP, but as the magnetic component of the hybrid bearing system that offers both axial and radial bearing forces.

A spiral groove bearing has been implemented as the hydrodynamic bearing as part of the hybrid system. Experimental investigation has shown the spiral groove bearing to be anti traumatic, despite a maximal sear stress in the bearing gap of over 800 Pa; Paul et al. [80] state that any regions over 425 Pa are haemolytic. However, a reduction in load capacity alludes that the bearings are operating on a reduced viscosity; this is an indication of cell exclusion within the SGB. Comparisons to aqueous glycerol tests of known viscosities have shown that the blood bearing is operating on a viscosity close to that of plasma. The suggested mechanism for cell exclusion is a "shear front differential" in which RBCs migrate away from an area of high shear stress (such as that under the groove ridges) to an area of comparatively low shear stress (as exists in the groove channels). Investigation into groove geometry shows that sharp-edged grooves help to promote this shear front differential, compared to grooves with a chamfered leading edge. Reducing the operational bearing separation also increases the shear front differential and consequently increases the potential of the RBCs to avoid areas of high shear stress; levels of haemolysis may be reduced due to augmented cell exclusion. It is

may be seen, therefore, advantageous to maintain a larger groove depth to bearing separation ratio in order to encourage cell exclusion.

This investigation has predicted the suitability of the hybrid magnetic / hydrodynamic bearing for use in a new CRBP. It has been shown that the incorporation of the hydrodynamic bearing to the magnetic bearing transforms the previously unstable passive magnetic bearing to a stable hybrid bearing. The stability of the system has been demonstrated through numerical analysis of the stiffness matrix and through satisfaction of the stability criteria. The natural frequencies of the system have been calculated; these are shown to be sufficiently different from any excitation frequencies identified that may cause the system to behave in an unstable fashion at the operational speed of the pump.

The main point to be realized from the analysis of the hybrid bearing system, however, is that the proposed set-up of the hybrid bearing is not feasible due to the effect of cell exclusion, which causes the SGB to operate on a reduced viscosity. The reduction in viscosity reduces the load capacity of the SGB; the magnetic preload on the impeller cannot be balanced by the chosen SGB geometry. Recommendations have been made, as detailed in Table 23, which would allow the hybrid bearing to operate as intended.

Table 23: Summary of recommendations for change to the system

Change	Consequence
Increase pump speed	• Increase load capacity of SGB. • Increased potential for haemolysis and thrombosis due to associated increase in shear rate. • Redesign underlying impeller and volute geometry to compensate for increased operational speed.
Decrease groove height of SGB	• Increase load capacity of SGB. • Potential for increased haemolysis and thrombosis due to decreased shear front differential and reduced groove washout. • Redesign SGB

Decrease magnet volume/strength	• Reduction in magnetic preload.
	• Reduction in motor efficiency.
Increase electromagnetic flux gap	• Reduction in magnetic preload.
	• Reduction in motor efficiency

Table 23 indentifies some of the trade-offs that must be considered in order for the proposed design remit to be realised. There is obviously an ideal design point that exists where the preload of the magnetic bearing is balanced by the hydrodynamic lift force of the SGB. It is of primary concern to the designer that this intended operational point is met. There is however a number of concerns that the designer must address in order to achieve an acceptable intersection point between the two bearing curves (as identified in Figure 77) such that the proposed hybrid bearing may be realised. One simple way to increase the load capacity of the hydrodynamic bearing is to increase the rotational speed of the pump; the associated implications, however, of such a fundamental design change are not insignificant. A change in the pump design speed would require a complete redesign of the impeller and volute geometry in the first instance. Besides, the operational speed of the pump was chosen as to minimise the potential shear stress, and corollary haemolysis, which the blood is subjected to. Another option that is open to the designer would be to alter the geometry of the SGB, specifically the height of the grooves. By decreasing the groove height the load capacity of the SGB would be increased, and demonstrated by Muijderman [94]. There are implications however to this: decreasing the groove height of the SGB could be seen as detrimental to the haemolytic performance of the bearing. By decreasing the groove height, the shear front differential, which is proposed in Chapter 4, would be reduced and the potential haemolysis due to shear would be increased. Further to this, the washout of the SGB would be decreased due to reduced volumetric flow through the grooves, which would increase the risk of platelet adhesion and thrombus formation. It is the opinion of the author that the groove depth of the SGB should be maximised in order to reduce the potential haemolysis and thrombus formation; the precise threshold i.e. the point at which the phenomenon of cell exclusion breaks down with respect to groove height should be the focus of further work.

The salient point here is that the blood pump needs to be designed such that any damage to the blood is minimised, and any blood contacting features should be optimised in order to achieve this, especially if the designs are intended for use as a destination therapy. It is therefore necessary to design around these considerations; with respect to the proposed design, this means that the magnetic preload of the hybrid bearing system must be reduced, through reduction of magnet volume or by increasing the magnetic flux gap, even if this comes at the expense of reduced motor efficiency. In this way the intended mode of operation may be realised for this conceptual, integrated electromagnetic drive system and combined hydrodynamic / magnetic bearing. Recommendations have been made as to the design parameters that may be altered such that the design intent of the proposed system may be realised. Future work must concentrate on the realization of that design intent through the manufacture of a prototype, which can provide a proof-of-concept for the proposed system.

BIBLIOGRAPHY

1.   Mackay, J., Mensah, G., *The Atlas of Heart Disease and Stroke*. 2004: World Health Organisation.
2.   Reddy, K., S., *Cardiovascular Disease in Non-Western Countries*. New England Journal of Medicine, 2004. **350**(24): p. 2438-2440.
3.   WHO, *Preventing Chronic Diseases: A Vital Investment* 2005: WHO.
4.   Edwards, D.O., Boucek, L.B., et al. , *Registry of the International Society for Heart and Lung Transplantation: twenty-fourth official adult lung and heart-lung transplantation report-2007*. Journal Heart Lung Transplant, 2007. **26**(8): p. 782-795.
5.   Moskowitz, A.J., Rose, E. A., Gelijns, A. C., *The cost of long-term LVAD implantation*. 2001, 2001. **71**: p. 195-198.
6.   Douglas, P., Morgan, C., Lee, H., Foster, K. R., *LVAD as Destination Therapy - The Economic Dilemma*, in *IEEE Technology and Society Magazine*. 2004.
7.   Malcolm, J., Arnold, O. *Heart Failure*. 2008 [cited 2009 17/06/09]; Available from: http://www.merck.com/mmhe/sec03/ch025/ch025a.html.
8.   Reddy, K.S., Yusuf, S., *Emerging Epidemic of Cardiovascular Disease in Developing Countries*. Circulation, 1998. **97**: p. 596-601.
9.   Ho, K., et al., *Survival after the onset of congestive heart failure in Framingham Heart Study subjects* Circulation, 1993. **88**: p. 107-115.
10.   Cowie, M.R., *Annotated references in epidemiology*. European Journal of Heart Failure., 1999. **1**: p. 101-107.
11.   Murray, C.J.L., Lopez, A. D., *The glodal burden of disease: a comprhesive assessment of mortality and disability from diseases, injuries and risk factors in 1990 and projected to 2020*. 1996, WHO: Cambridge, MA.
12.   Mirzaei, *Epidemiology of chronic heart failure*, in *Serious and continuing illness policy and practice study*. 2007, The Australian National University and The University of Sydney: Sydney, NSW.
13.   AHA, *Heart disease and stroke statistics - 2004 update*. Circulation, 2004.
14.   Clark, R.A., McLennan, S., Dawson, A., Wilkinson, D., Stewart, S. , *Uncovering a hidden epidemic: a study of the current burden of heart failure in Australia*. Heart, Lung & Circulation, 2004. **13**: p. 266-273.
15.   CCS, *CCS Consensus Document on congestive heart failure 2006*. 2006, CCS.
16.   Tendera, M., *Epidemiology, treatment, and guidelines for the treatment of heart failure in Europe*. European Heart Journal Supplements, 2005. **7**(Supplement J): p. J5-J9.
17.   TIC, *The TIC Times*. 2008, Texas Institute of Cardiology: Texas.
18.   AHA, *Heart disease and stroke statistics - 2009 update*. Circulation, 2009.
19.   AIHW, *Heart, stroke and vascular diseases: Australian facts 2004*. 2004, AIHW: Canberra, ACT.
20.   CCS, *CCS Consensus Document on congestive heart failure 2001*. 2001.
21.   Roundtable, C.P.-e., *Beyond Four Walls: Cost-Effective Management of Chronic Congestive Heart Failure*, in *Washington, D.C.: Advisory Board Company*. 1994.
22.   Davies, M.K., Hobbs, F. D. R.,Davis, R. C., *Prevalence of left ventricle systolic dysfunction and heart failure in the general population: main findings from the ECHOES (Echocardiographic Heart of England Screening) study*. Lancet, 2001. **358**: p. 439-445.
23.   Sutton, G.C., *Epidemicalogical effects of heart failure*. American Heart Journal, 1990. **120**: p. 1538-1540.
24.   Eriksson, H., *Heart failure: a growing public health problem*. Journal of International Medicine, 1995. **237**: p. 135-141.
25.   McMurray, J., McDonagh, T., Morrison, C. E., Dargie, H. J., *Trends for heart failure in Scotland 1980-1990*. European Heart Journal 1993. **14**: p. 1158-1162.
26.   Hobbs, F.D.R., *Clinical burden and health service challenges of chronic heart failure*. European Journal of Heart Failure Supplements (I), 2009. **8**: p. i1-i14.

27. Lopez, A.D., *Assessing the burden of mortality from cardiovascular diseases.* World Health Stat Q, 1993. **46**: p. 91-96.

28. Pearson, T.A., *Cardiovascular disease in developing countries: myths, realities, and opportunities.* Cardiovascular Drugs and Therapy, 1999. **13**: p. 95-104.

29. Mendez, G., F., Cowie, M., R., *The epidemiological features of heart failure in developing countries: a review of the literature.* International Journal of Cardiology, 2001. **80**(2-3): p. 213-219.

30. Chonghua, Y., Zhasou, W., Yingkai, W., *The changing pattern of cardiovascular diseases in China.* World Health Stat Q, 1993. **46**: p. 113-118.

31. Gupta, R., et al., *Correlation of regional cardiovascular disease mortality in India with lifestyle and nutritional factors.* International Journal of Cardiology, 2006. **108**(3): p. 291-300.

32. WHO, *The World Health Report 1999 - Making a Difference.* 1999, WHO: Geneva.

33. Wielgosz, A.T., *The decline in cardiovascular health in developing countries.* World Health Stat Q, 1993. **46**: p. 90.

34. Nicholls, E., S., Peruga, A.,P., Restrepo, H.,E., *Cardiovacular disease mortality in the Americas.* World Health Stat Q, 1993. **46**: p. 134-150.

35. Reddy, K.S., *Cardiovascular diseases in India.* World Heath Stat Q, 1993. **46**: p. 101-107.

36. Ghaffar, A., Reddy, K. S., Singhi, M., *Burden of non-communicable diseases in Sounth Asia.* BMJ, 2004(328): p. 807-810.

37. Muna, W., F.,T., *Cardiovascular disorders in Africa.* World Health Stat Q, 1993. **46**: p. 125-133.

38. Oyoo, G., O., Ogola, E.,N. , *Clinical and socio demographic aspects of congestive heart failure patients at Kenyatta National Hospital, Nairobi.* East African Medical Journal, 1999. **76**: p. 23-27.

39. Antony, K., K., *Pattern of cardiac failure in northern Savannah Nigeria.* Tropical and geophaphical medicine, 1980. **32**: p. 118-125.

40. Williams, J.F.J., Bristow, M. R., Fowler, M. B., et al., *ACC / AHA guidelines for the evaluation and management of heart failure: report of the American College of Cardiology/American Heart Association Task Force on Practice Guidelines (Committee on Evaluation and Management of Heart Failure). .* Journal of the American College of Cardiology, 1995. **26**: p. 1376-1398.

41. Hunt, S.A., et al, *ACC/AHA Guidelines for the Evaluation and Management of Chronic Heart Failure in the Adult: Executive Summary.* Journal of the American College of Cardiology, 2001. **38**(7): p. 2101-2113.

42. Bartlo, P., *Evidence-based application of aerobic and resistance training in patients with congestive heart failure.* Journal of Cardiopulmonary rehabilition and prevention, 2007. **27**(6): p. 368-375.

43. Bryson, C.L., Mukamal, K. J., *The Association of Alcohol Consumption and Incident Heart Failure.* Journal of the American College of Cardiology 2006. **48**: p. 305-311.

44. Walsh, C.R., Larson, M. G., Evans, J. C., *Alcohol Consumption and Risk for Congestive Heart Failure in the Framingham Heart Study.* Annals of Internal Medicine, 2002. **136**(3): p. 181-191.

45. Nelson, K.M., Yeager, B. F. , *What is the role of angiotensin-converting enzyme inhibitors in congestive heart failure and after myocardial infarction? .* The Annals of Pharmacotherapy, 1996. **30**(9): p. 986-993.

46. Waagstein, F., *Beta-Blockers in Congestive Heart Failure: the Evolution of a New Treatment Concept – Mechanisms of Action and Clinical Implications.* Journal of Clinical and Basic Cardiology, 2002. **5**(3): p. 215-223.

47. Ross, A., Hershberger, R. E., Ellison, D. H., *Heart Failure: Pharmacologic Management (Chapter 1),* ed. A.M. Feldman. 2006: Blackwell Publishing.

48. Digiorgi, P.L., Reel, M.S., Thornton, B., Burton, E., Naka, Y., Oz, M.C., *Heart transplant and left ventricular assist device costs.* Journal Heart Lung Transplant, 2005. **24**(11): p. 1997-1998.

49. Copeland, J.G., et al., *Cardiac Replacement with a Total Artificial Heart as a Bridge to Transplantation.* 2004. **351**(9): p. 859-867.

50. MedGadget. *The CardioWest™ TAH-t.* 2006 [cited 24/06/09]; Available from: http://medgadget.com/archives/2006/04/the_cardiowest.html.

51. Sheppard, R. *Life with the mechanical heart.* 2006 [cited 24/06/09]; Available from: www.cbc.ca/.../sheppard/gfx/1829308.jpg.

52. Guinness World Records 2008, *Guinness World Records 2008.* 2008: Guinness World Records Limited.

53. MedGadget. *heartmate_II_lvad.jpg.* 2005 [cited; Available from: http://medgadget.com/archives/img/heartmate_II_lvad.jpg.

54. MedGadget. *HeartMate II Shown Effective In Waiting Transplant Candidates*. 2007 [cited 24/06/09]; Available from: www.medgadget.com/archives/img/heartmateII.jpg.

55. Jarvik Heart. *The Jarvik 2000*. 2008 [cited 24/06/09]; Available from: www.jarvikheart.com/assets/J2K_Xray.jpg.

56. Hetzer, R., Muller, J. H., Weng, Y-G., Meyer, R., Dandel, M., *Bridging-to-recovery*. The Annals of Thoracic Surgery, 2001. **71**(Supplement 1): p. S109-S113.

57. Rose, E.A., et al., *Long-term use of a left ventricular assist device for end-stage heart failure*. New England Journal of Medicine, 2001. **345**(20): p. 1435-1443.

58. Yusuf, S., Pitt, B., *A lifetime of prevention: the case of heart failure*. Circulation, 2002. **106**: p. 2997-2998.

59. AHA, *Long-term survival of HeartMate XVE*. Circulation, 2007. **116**: p. 497-505.

60. Stepanoff, A.J., *Centrifugal and Axial Flow Pumps - Theory, Design, and Application*. 1st ed. 1957, New York: John Wiley &Sons, INC.

61. Lobanoff, V.S., *Centrifugal Pumps - Design & Application*. 2nd ed. 1992: Elsevier Science & Technology.

62. Karassik, I.J., Messina, J. P., Cooper, P., Heald, C. C., *Pump handbook*. 3rd ed. 2001: McGraw-Hill Professional.

63. Morshuis, M., El-Banayosy, A., Arusoglu, L., Koerfer, R., et al., *European experience of DuraHeart™ magnetically levitated centrifugal left ventricular assist system*. European Journal of Cardio-Thoracic Surgery, 2009.

64. Goldstein, D.J., *Worldwide Experience With the MicroMed DeBakey Ventricular Assist Device® as a Bridge to Transplantation*. Circulation, 2003. **108**(Supplement II): p. 272-277.

65. Bearnson, G.B., Jacobs, G. B., Kirk, J., Khanwilkar, P. S., Nelson, K. E., Long, J. W., *HeartQuest Ventricular Assist Device Magnetically Levitated Centrifugal Blood Pump*. Artificial Organs, 2006. **30**: p. 339 – 346.

66. DeBakey, M.E., *A miniature implantable axial flow ventricular assist device*. Annals of Thoracic Surgery, 1999. **68**: p. 637-640.

67. MicroMed Cardiovascular Inc. *Heart Assist 5™*. 2008 [cited 05/05/2009].

68. Wieselthaler, G., Schima, H, Hiesmayr, M., et al., *First clinical experience with the DeBakey VAD® continuous axial flow pump for bridge to transplanation*. Circulation, 2000. **101**: p. 356-359.

69. Savage, E.B., Clarke, R. E., Griffin, W. P., et al., *The AB-180 circulatory support system:summary of development and plans for phase 1 clinical trials*. Annals of Thoracic Surgery, 1999. **68**: p. 768-774.

70. Yamane, T., Maruyama, O., Nishida, M., et al., *The most profiatble use of flow visualization in the elimination of thrombus from the monopivot magnetic suspension blood pump*. Artificial Organs, 2004. **28**: p. 390-397.

71. Terumo Heart Inc. *DuraHeart™*. 2008 [cited 09/07/2009].

72. Esmore, D.S., Kaye, D., Salamonsen, R., Buckland, M., Rowland, M., Negri, J., Rowley, Y., Woodard, J., Begg, J. R., Ayre, P., Rosenfeldt, F.L., *First clinical implant of the VentrAssistTM left ventricular assist system as destination therapy for end-stage heart failure*. Journal Heart Lung Transplant, 2007. **24**: p. 1150-1154.

73. Ventracor. *VentrAssist ® LVAD*. 2007 [cited 09/07/2009].

74. Ayre, P.J., Vidakovic, S.S., Tansley, G.D., Watterson, P.A., Lovell, N.H., *Sensorless flow and head estimation in the VentrAssist™ rotary blood pump*. Artificial Organs, 2000. **24**: p. 585-588.

75. Koster, A., Loebe, M., Hansen, R., Potapov, E., Noon, G., Kuppe, H., Hetzer, R., *Alterations in coagulation after implantation of a pulsatile Novacor LVAD and the axial flow Micromed DeBakey LVAD*. Annals of Thoracic Surgery, 2000. **70**: p. 533-553.

76. Esmore, D., Kaye, D., Spratt, P., Larbalestier, R., Ruygrok, P., Tsui, S., Meyers, D. Fiane, A., Woodard, J., *A Prospective, Multicenter Trial of the VentrAssist Left Ventricular Assist Device for Bridge to Transplant: Safety and Efficacy*. Journal Heart Lung Transplant, 2008. **27**: p. 579-588.

77. Beiter, K.A., Cardinal, J. M., Ishii, K., *Design for Injection Molding: Balancing Mechanical Requirments, Manufacturing Costs, and Material Selection*. Proceedings of the 1995 ASME Design Engineering Technical Canferences (DE-83), Boston, MA., 1995: p. 791-798.

78. Earnshaw, S., *On the nature of the molecular forces which regulate the constitution of the luminiferous ether*. Trans. Camb. Phil. Soc, 1842. **7**: p. pp 97-112.

79. Woodard, J.C., Watterson, P. A., Tansley, G. D., *US Patent 6250880 - Rotary pump with exclusively hydrodynamically suspended impeller*. 2001.

80. Paul, R., Apel, J., Klaus, S., Schugner, F., Schwindke, P., Reul, H., *Shear Stress Related Blood Damage in Laminar Couette Flow.* Artificial Organs, 2003. **27**(6): p. 517-529.

81. Tansley, G., S. Vidakovic, and J. Reizes, *Fluid dynamic characteristics of the VentrAssist rotary blood pump.* Artificial Organs, 2000. **24**(6): p. 483-487.

82. Stepanoff, A.J., *Centrifugal and Axial Flow Pumps - Theory, Design, and Application.* 1st ed. 1948, New York: John Wiley &Sons, INC.

83. Hilton, A., Tansley, G., *Magnetic Drive System for a New Centrifugal Rotary Blood Pump.* Artificial Organs, 2008. **32**: p. 772-777.

84. Furlani, E.P., *Permanent magnet and electromechanical devices.* 1st ed. 2001: Academic Press.

85. Coey, J.M.D., *Permanent magnetism.* Solid State Communications, 1997. **102**(2-3): p. 101-105.

86. Delamare, J., J.P. Yonnet, and E. Rulliere, *A Compact Magnetic Suspension with Only One Axis Control.* Ieee Transactions on Magnetics, 1994. **30**(6): p. 4746-4748.

87. Yonnet, J.P., *Permanent-Magnet Bearings and Couplings.* Ieee Transactions on Magnetics, 1981. **17**(1): p. 1169-1173.

88. Yildir, Y.B., Klimpke, B. W., Prasad, K. M., *Three dimensional analysis of magnetic fields using the boundary element method,* in *Joint EEIC/ICWA.* 1991: Boston, MA, USA.

89. Klimpke, B., *A Hybrid Magnetic Field Solver: Using a Combined Finite Element/Boundary Element Field Approach.* Sensors, 2004. **21**(5): p. 2-6.

90. Stratton, J.A., *Electromagnetic Theory.* 1941, New York: McGraw-Hill book Co.

91. Lean, M.H., *Electromagnetic Field Soulution with the Boundary Element Method.* 1981, University of Manitoba.

92. Ford, G.H., D. Pantall, D., *Principles and Applications of Hydrodynamic - Type Gas Bearings* Proc. Inst. Mech. Eng., 1957. **171**(2): p. 93.

93. Whipple, R., *Herringbone Pattern Thrust Bearing.* Atomic Energy Research Establishment, 1949.

94. Muijderman, E.A., *Spiral Groove Bearings.* 1966: Philips Technical Library.

95. Zou, Q., et al., *Study of flow characteristics of lubricant in spiral-groove bearings by the fluorescent method.* Tribology Transactions, 2005. **48**(2): p. 259-263.

96. Yoshimoto, S., et al., *Stability of water-lubricated, hydrostatic, conical bearings with spiral grooves for high-speed spindles.* Journal of Tribology-Transactions of the Asme, 2002. **124**(2): p. 398-405.

97. Kink, T. and H. Reul, *Concept for a new hydrodynamic blood bearing for miniature blood pumps.* Artificial Organs, 2004. **28**(10): p. 916-920.

98. Barthelmes, G., *Theoretische Untersuchungen zum Einflubder Agglomeration aufdie Rheoogie konzentrierter Suspesionen,* in *Fackultat fur Chemieingenieurwissen und Verfahrenstechnik.* 2000, Universitat Karlsruhe.

99. Zou, Q., Tian, Y., Wen, S., Konno, D., *Dynamic characteristics of spiral groove spindles: comparison between rotating-shaft and fixed shaft designs.* Tribotest, 2006. **12**: p. 83-90.

100. Monroe, J., M., True, D. E., Williams, M. C., *Surface roughness and edge geometries in hemolysis with rotating disc flow.* Journal of Biomedical Materials Research, 1981. **15**: p. 923-939.

101. Takami, Y., Nakazawa, T., Makinouchi, K., Glueck, J., Benkowski, R., Nose, Y., *Effect of surface roughness on hemolysis in a centrifugal blood pump.* ASAIO Journal, 1996. **42**(5): p. M858-862.

102. Hoshi, H., et al., *Hemolytic performance of a MagLev disposable rotary blood pump (MedTech Dispo): Effects of MagLev gap clearance and surface roughness.* Artificial Organs, 2006. **30**(12): p. 949-954.

103. James, N.L., et al., *Evaluation of haemolysis in the VentrAssist implantable rotary blood pump.* Artificial Organs, 2003. **27**: p. 108-113.

104. ASTM, *F1841-97 Standard Practice for Assessment of Haemolysis in Continuous Flow Blood Pumps.* Annual Book of ASTM Standards, 1998.

105. Harboe, M., *A Method for Determination of Hemoglobin in Plasma by Near-Ultraviolet Spectrophotometry.* Scandinavian Journal of Clinical and Laboratory Investigation, 1958. **11**: p. 66-70.

106. Han, V., Serrano, K., Devine, D. V., *A comparative study of common techniques used to measure haemolysis in stored red cell concentrates.* Vox Sanguinis, 2009(DOI: 10.1111/j.1423-0410.2009.01249.x).

107. Grubbs, F., *Procedures for Detecting Outlying Observations in Samples.* Technometrics, 1969. **11**: p. 1-21.

108. Bull, B.S., *Commentary.* Blood Cells, Molecules, and Diseases, 1996. **22**(15): p. 186a-186b.

109.   Vidakovic, S., et al., *Paradoxical effects of viscosity on the VentrAssist rotary blood pump.* Artificial Organs, 2000. **24**(6): p. 478-482.

110.   Lewis, F.M., *Vibration During Acceleration Through a Critical Speed*, in *ASME Appled Mechanicas Division*. 1932: New Haven, Conneticuit.

111.   Tuzson, J., *Centrifugal pump design.* 2000: Wiley-IEEE.

112.   Japikse, D., Marsher, W. D., Furst, R. B., *Centrifugal Pump Design and Performance.* 1997, Vermont: Concepts ETI, Inc.

113.   Lazarkiewicz, S., Troskolanski, A.T., *Impeller Pumps.* 1965: Elsevier.

A P P E N D I X

APPENDIX A: DESIGN CALCULATIONS FOR IMPELLER AND VOLUTE

Example Calculation for Impeller Geometry

From the specified pump head **H** (120 mm Hg = 1.544 m of blood), capacity **Q** (5 L/min = 8.33 x 10^{-5} m^3/s) and chosen rotational speed **N** (2000 RPM), the specific speed n_s of the pump may be calculated. Specific speed is a non-dimensional number used to classify pump impellers by their type and proportions [60].

$$n_s = \frac{NQ^{\frac{1}{2}}}{H^{\frac{3}{4}}} = \frac{2000 \times \left(8.33 \times 10^{-5}\right)^{\frac{1}{2}}}{1.544^{\frac{3}{4}}} = 680 \tag{A1}$$

A.1   Impeller Design Considerations

Vane Discharge Angle

The vane discharge angle is one of the most important element in the centrifugal pump design process, as all design constants depend directly or indirectly on β_2. Selection is based on consideration of the desired steepness of the head-capacity curve as both normal head and capacity increase with angle β_2. If no limitations are applied to the pump characteristic curve, the selection of β_2 should be made for optimum efficiency [60]. Centrifugal pumps have inherently flatter **H-Q** curves than axial pumps; the specific speed of the device is a direct indication of the device type; consequently it becomes prudent to design a device with a low specific speed in order to produce a pump with a shallow **H-Q** curve.

Backward Curved Blades, $\beta_2 < 90°$ - Backward curved blades are recommended for high efficiency, with a blade angle of 22.5° demonstrating best efficiency for common industrial pumps.

Radial Blades, $\beta_2 = 90°$ - A radial blade impeller exhibits a flat performance curve up to 75 percent of BEP, beyond which the curve is very steep [62]. This impeller type is characterised by lower efficiency.

Forward Curved Blades, $\beta_2 > 90°$ - Forward curved blade impellers have received relatively little research attention, and as such an efficient design has not been forthcoming. This may be related to the difficulties in

realising a casing that can catch and convert the high velocity jets leaving the vane tips into pressure, while permitting impulse action [60].

It can be seen therefore that the efficiency of a given pump will decrease with increasing vane discharge angle. However, larger angles may be advantageous in the physiological control of the pump by producing a flatter pump characteristic curve [81]. The vane discharge angle is taken to be 70° with the aim of designing a pump with flat pressure-flow characteristic.

Vane Number

The number of vanes z, is taken as seven, with higher and lower numbers considered. The work of Stepanoff [60] considers the design of six vane impellers which is considered to be the minimum number for machines operating below specific speeds of 5000. This example uses seven vanes to reduce the effects of blade passing frequency (BPF). However, this design procedure enables the designer to account for designs incorporating between three and eight vanes.

Vane Outlet Thickness

The vane outlet thickness s_{u2} is set at 2 mm. This dimension is chosen to provide sufficient rigidity of the design whilst not compromising the blockage of the flow. Again, variation is considered later.

Head Ψ and Capacity Φ Coefficients

Stepanoff presents an empirical relationship between specific speed and the head and capacity coefficients. These values are valid for a six-vane impeller. Coefficient values typically lie in the range $\Psi = 0.4 - 0.7$, and Φ = 0.05 – 0.2 for head and capacity respectively.[111] The capacity coefficient increases whilst head coefficient decreases with vane discharge angle and rotational speed.
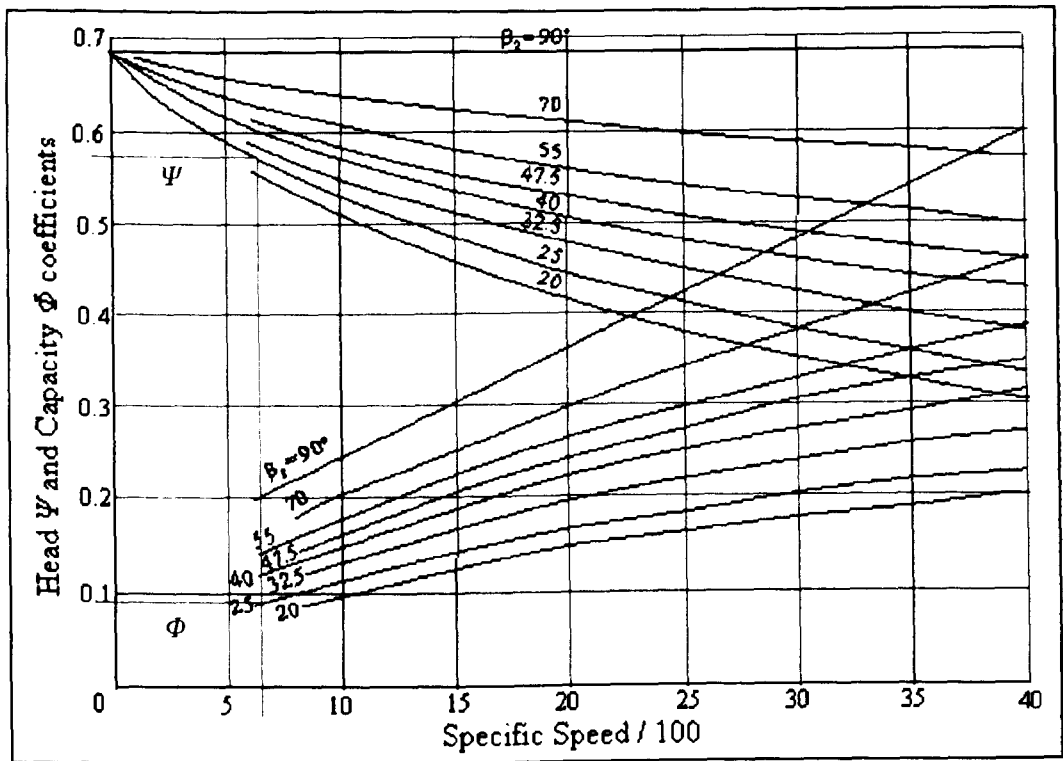
Figure 79: Values of head/flow coefficient for various blade angles [82]

From Figure 79, for an impeller operating with a specific speed of 680, the values for the head and capacity

coefficients are take as:

Head coefficient, Ψ = 0.65; capacity coefficient, Φ = 0.17.

Speed Constant, K_u

The speed constant is the ratio of the actual impeller tip speed u_2 to the free jet velocity U_2 under head **H**.

Stepanoff assumes impellers to have 6 vanes. The speed constant may be inferred from the head coefficient

using the following equation.

$$K_u = \sqrt{\frac{1}{2\psi}} = \sqrt{\frac{1}{2 \times 0.65}} = 0.877 \qquad \text{(A2)}$$

Lobanoff [61] states that the speed constant K_u is affected by the number of vanes. This is because the degree of recirculation is affected and consequently so is the head coefficient. Figure 80 shows how the vane number affects the speed constant.
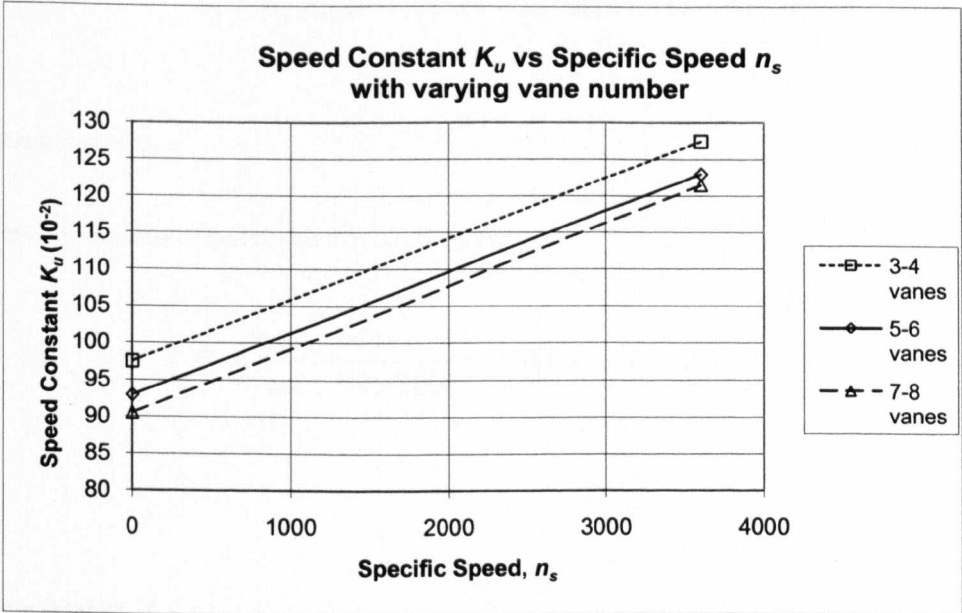
Figure 80: Effect of Vane Number z on Speed Constant K_u [61]

It can be seen that as the vane number increases, the speed constant decreases. From this graph a general rule for conversion of K_u between impellers of different vane numbers can be stated.

K_u for 5 - 6 vane impellers, calculate the value as detailed by Stepanoff.

K_u for 3 - 4 vane impellers, add 0.05 to this value.

K_u for 7 - 8 vane impellers, subtract 0.025 from this value.

This method allows for calculation of K_u at different discharge angles with different vane numbers. This is something that empirical charts do not list.

The value for K_u adjusted for increased vane number is 0.852.

Actual impeller tip speed, u₂

It is now possible to calculate the actual impeller tip speed required to produce the desired pump head.

$$u_2 = K_u \sqrt{2gH} = 0.852 \times \sqrt{2 \times 9.81 \times 1.544} = 4.69 ms^{-1} \qquad \text{(A3)}$$

Impeller Diameter D₂

From this the diameter of the impeller may be calculated.

$$D_2 = \frac{60u_2}{\pi N} = \frac{60 \times 4.69}{\pi \times 2000} = 0.0448m = 44.8mm \qquad \text{(A4)}$$

Capacity Constant, K_{m2}

The capacity constant is the ratio of meridional velocity at impeller discharge c_{m2} to the free jet velocity U_2 under head H. Stepanoff supplies an empirical relationship between specific speed and capacity constant, which is valid only for a 6-vane impeller with vane discharge angle of 22.5°. The capacity constant may be calculated.

$$K_{m2} = K_u \Phi = 0.852 \times 0.17 = 0.145 \qquad \text{(A5)}$$

This method, although accounting for various vane angles, does not yet cater for different blade numbers. Lobanoff details how K_{m2} varies for different vane numbers. From this graph, a conversion factor may be found to convert K_{m2} between different vane numbers.
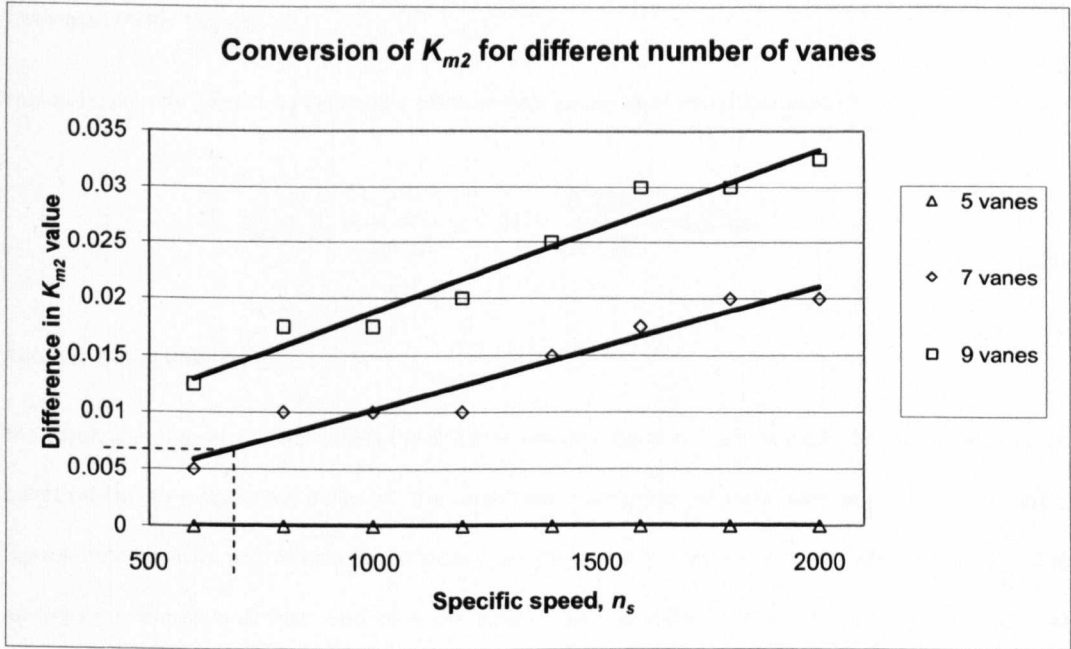
Figure 81: Correction of constant K_{m2} applied to impellers

with different numbers of vanes at different specific speeds

The value of the capacity constant may therefore be adjusted to correct for the number of vanes.

$$K_{m2} = 0.145 + 0.007 = 0.152$$

(A6)

A.2 Vane Outlet Conditions

The Euler absolute discharge velocity vector has magnitude c_2 and direction α_2. First the tangential outlet velocity c_{u2} must be determined by considering the impeller tip speed u_2, the meridional flow velocity c_{m2} and the impeller exit angle β_2.

Meridional Outlet Velocity, c_{m2}

Meridional outlet velocity is the velocity vector that represents the capacity of the pump and may be calculated:

$$c_{m2} = K_{m2}\sqrt{2gH} = 0.152 \times \sqrt{2 \times 9.81 \times 1.544} = 0.836 ms^{-1}$$

(A7)

Tangential Outlet Velocity, cu₂

This outlet velocity is useful by generating pressure head under ideal, one-dimensional flow.

$$c_{u2} = u_2 - \frac{c_{m2}}{\tan \beta_2} = 4.69 - \frac{0.836}{\tan 70''} = 4.37 ms^{-1}$$

(A8)

Absolute Outlet Velocity, c₂

The absolute outlet velocity represents the direction and magnitude of the fluid discharged from the impeller outlet relative to a stationary observer. The magnitude is comprised of radial and tangential components, representing capacity and developed pressure head respectively. Consider first the ideal Euler case that assumes one-dimensional flow, and then the actual case that differs slightly as it accounts for the slip between the vanes.

The magnitude of the outlet velocity vectors are determined by resolving the radial and tangential velocity components.

$$c_2 = \sqrt{c_{m2}^2 + c_{u2}^2} = \sqrt{0.836^2 + 4.37^2} = 4.47 ms^{-1}$$

(A9)

Discharge Angle, α₂

The Euler discharge angle may be calculated from the above velocity parameters. This angle describes the angle of the volute spiral for the ideal condition.

$$\alpha_2 = \frac{c_{m2}}{c_{u2}} \tan^{-1} = \frac{0.836}{4.37} \tan^{-1} = 10.79''$$

(A10)

Actual Outlet Conditions

The actual developed head differs from that predicted by Euler. The relative slip within the impeller vanes increases the outlet velocity angle, which leads to a reduction in tangential velocity and thus developed head.

Slip, σ

The slip factor σ is the ratio of slip to recirculation, and is accounted for in the outlined approach. The slip factor represents the recirculation of fluid between the vanes. It is a function of the vane discharge angle, and may be calculated using the head and capacity coefficients.

$$\sigma = \psi + \Phi \tan(90 - \beta_2) = 0.65 + 0.17 \tan(90 - 70) = 0.712 \tag{A11}$$

Actual Tangential Outlet Velocity

The value of actual tangential velocity used to determine the actual developed head, assuming non ideal flow and incorporating slip, is calculated by relating the head coefficient to the actual impeller tip speed.

$$c_{u2}' = \psi \times u_2 = 0.65 \times 4.69 = 3.05 ms^{-1} \tag{A12}$$

Actual Resolved Outlet Velocity, c₂'

The magnitude of the actual discharge velocity vector is calculated by resolving radial and actual tangential velocities.

$$c_2' = \sqrt{c_{m2}^2 + c_{u2}'^2} = \sqrt{0.836^2 + 3.05^2} = 3.16 ms^{-1} \tag{A13}$$

Actual Outlet Angle, α₂'

The actual discharge angle can be calculated as follows and describes the actual angle of fluid leaving the impeller. It is larger than the predicted Euler angle due to the reduced tangential outlet velocity. This is the angle used to design a coincident angle of volute casing spiral.

$$\alpha_2' = \frac{c_{m2}}{c_{u2}'} \tan^{-1} = \frac{0.836}{3.05} \tan^{-1} = 15.33^{\circ}$$

(A14)

Actual Vane Discharge Angle, β_2'

The actual discharge angle is lower than the designed vane discharge angle due to the reduction in the tangential outlet velocity.

$$\beta_2' = \left(\frac{c_{m2}}{u_2 - c_{u2}'}\right) \tan^{-1} = \left(\frac{0.836}{4.67 - 3.05}\right) \tan^{-1} = 26.98^{\circ}$$

(A15)

A.3 Vane inlet conditions

The design conditions for the inlet prescribe a situation of zero pre-swirl or shock. In order to meet these conditions, there is only one vane inlet angle that exists for each individual application, and is independent of the discharge angle.

Inlet capacity constant K_{m1}

The inlet capacity constant K_{m1} relates the free jet velocity U_2 to the meridional inlet velocity c_{m1}. Figure 82 shows how to calculate the inlet capacity constant K_{m1} from the outlet capacity constant K_{m2}. For various specific speeds the polynomial relationship has been derived from data charts shown by Stepanoff [60].
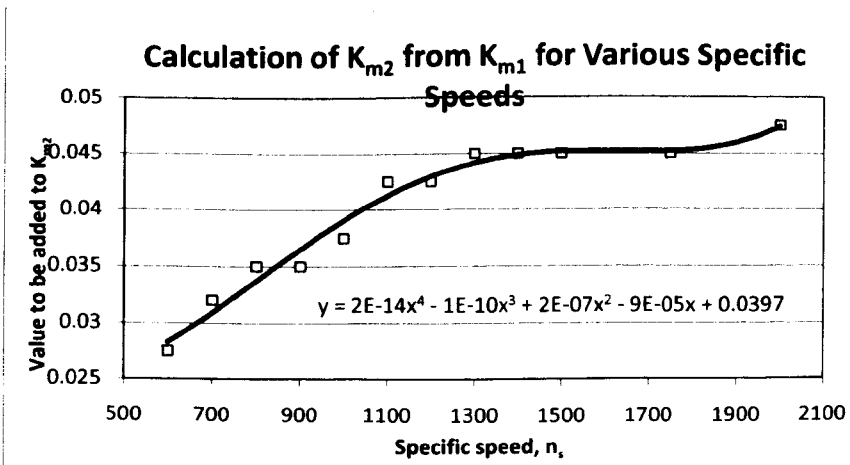
Figure 82: Polynomial correction for K_{m2} at specific speeds

Since values for K_{m2} have already been adjusted to account for different number of vanes, the conversion is a simple addition. At specific speed $n_s = 680$, $K_{m2} = 0.151$:

$$K_{m1} = 0.151 + 0.0395 = 0.191 \qquad \text{(A16)}$$

Meridional inlet velocity c_{m1}

The inlet velocity is calculated for the area ahead of the vane entrance tips. Stepanoff states that the inlet vane thickness s_{u1} is may be neglected as the vanes are tapered to a point at inlet [60].

$$c_{m1} = K_{m1}\sqrt{2gH} = 0.91 \times \sqrt{2 \times 9.81 \times 1.544} = 1.05ms^{-1} \qquad \text{(A17)}$$

Inlet diameter D_1

The value for impeller inlet diameter D_1 is selected to minimise the ratio of the inlet velocity to the outlet velocity (c_1/c_2), thus minimising the possibility of flow separation.

As the inlet diameter D_1 increases, the impeller inlet tip speed u_1 increases and the meridional inlet velocity c_{m1} decreases for any given flow rate. "Evidently an optimum inlet diameter exists that balances these opposing trends and produces a minimum relative velocity" [111]. This is expressed by the equation below.

$$D_1 = 1.533\left(\frac{Q}{\omega}\right)^{1/3} = 1.533\left(\frac{8.33 \times 10^{-5}}{209.4}\right)^{1/3} = 11.3mm \qquad \text{(A18)}$$

Inlet vane height b_1

The inlet vane height b_1 may be calculated as a function of inlet diameter and meridional inlet velocity from the following equation.

$$b_1 = \frac{Q}{\pi D_1 c_{m1}} = \frac{8.33 \times 10^{-5}}{\pi \times 0.00985 \times 0.846} = 0.00319m \qquad \text{(A19)}$$

Impeller inlet tip speed u_1

Impeller inlet tip speed u_1 depends upon the rotational speed **N** and the inlet diameter D_1.

$$u_1 = \frac{\pi D_1 N}{60} = \frac{\pi \times 0.00985 \times 3000}{60} = 1.55 ms^{-1}$$

(A20)

Inlet vane angle β_1

The value of the inlet blade angle β_1 is determined from the impeller inlet diameter D_1, and thus from the inlet tip speed u_1 and the meridional velocity c_{m1}. NB: no pre-rotation is assumed.

$$\beta_1 = \left(\frac{c_{m1}}{u_1}\right) \tan^{-1} = \left(\frac{0.846}{1.55}\right) \tan^{-1} = 28.66^{\circ}$$

(A21)

A.4   Actual inlet vane conditions

Actual inlet vane angle β_1'

Due to the relative recirculation between the vanes, the actual inlet vane angle β_1' is slightly larger than the predicted Euler value. Recirculation is accounted for by selecting a recirculation ratio R_1. The inlet recirculation ratio P_{s1} describes the ratio of shock-less capacity to the rated capacity, and would be lower should the inlet vane thickness s_1 be considered. For single inlet end suction type pumps $R_1 = 1.15 - 1.25$.

$$P_{s1} = R_1 c_{m1} = 1.2 \times 0.846 = 0.015$$

The actual inlet vane angle β_1' is calculated as follows.

$$\beta_1' = \left(\frac{P_{s1}}{u_1}\right) \tan^{-1} = \left(\frac{0.015}{1.55}\right) \tan^{-1} = 33.26^{\circ}$$

(A22)

Unlike the actual vane discharge angle β_2', the actual value for inlet angle β_1' *is* used as the constructed impeller vane angle.

Absolute inlet velocity

Euler states that the inlet vane angle β_1 is designed to eliminate pre-rotation tangential velocity. Therefore the absolute inflow angle is 90° and the absolute inlet velocity c_1 resolves to the value for meridional velocity c_{m1}, hence:

$$c_1 = c_{m1}$$

However, the actual direction and magnitude of the absolute inlet velocity vector c_1' is dependent on vane recirculation. It is possible to determine the magnitude of the actual inlet tangential velocity c_{u1} by considering the meridional velocity c_{m1}, actual impeller inlet vane angle β_1' and the impeller inlet tip speed u_1.

Inlet tangential velocity c_{u1}

$$c_{u1}' = u_1 - \frac{c_{m1}}{\tan \beta_1'} = 1.55 - \frac{0.846}{\tan 33.26^o} = 0.258 ms^{-1}$$

(A23)

Actual absolute inlet velocity c_1'

$$c_1' = \sqrt{c_{m1}^2 + c_{u1}'^2} = \sqrt{0.846^2 + 0.258^2} = 0.884 ms^{-1}$$

(A24)

Actual inlet angle α_1'

$$\alpha_1' = \frac{c_{m1}}{c_{u1}'} \tan^{-1} = \frac{0.846}{0.258} \tan^{-1} = 73.04''$$

(A25)

A.5   Pump Head

The developed Euler head at the design capacity, assuming ideal conditions, is calculated from the Equation A26. Since the vane inlet angle β_1 corresponds to the absolute tangential velocity c_1, the inlet vane angle β_1 is

assumed to be equal to the actual inlet vane angle β_1', and as such the inlet whirl velocity resolves to zero.

Head **H** is expressed as meters of blood.

$$H_E = \frac{1}{g}\left(u_2 c_{u2}\right) = \frac{1}{9.81}\left(5.21 \times 3.86\right) = 2.05m$$

(A26)

The actual developed head accounts for recirculation between the impeller vanes, which acts to reduce the ideal Euler head. The actual values for the pressure head are shown below.

$$H_A = \frac{1}{g}\left(u_2 c_{u2}' - u_1 c_{u1}'\right) = \frac{1}{9.81}\left(5.21 \times 2.76 - 1.55 \times 0.26\right) = 1.43m$$

(A27)

Hydraulic efficiency e_h

Hydraulic efficiency e_h is described as the ratio of the available total dynamic head (i.e. Euler head that neglects losses) to the actual head.

$$e_h = \frac{H_A}{H_E} = \frac{1.43}{2.05} \times 100 = 69.5\%$$

(A28)

A.6   Volute design

Calculations for the sizing of the volute are based upon the principle of constant velocity within the volute channel. If the impeller is designed correctly, and is manufactured just as it was designed, it is possible for the rotating impeller to continually add just the right amount of liquid to this volute area; this prevents the velocity of the liquid from changing. If the velocity of the liquid decreases, the pressure increases. Pressure acting on an area creates a force that displaces the impeller, which will impact on the performance of the pump. Volute designs are derived from the average velocity of the fluid. Since these average velocities change at different pump capacities, the final volute is designed to operate at the best efficiency point (BEP), and the performance conditions may be estimated either side of the BEP [61, 82].

However, centrifugal pumps seldom run at their BEP. When there is not enough head in the system the velocity of the liquid will increase as it approaches the discharge nozzle, causing the pressure to decrease,

thus displacing the impeller. Likewise if there is too much head on the system, some of the fluid will re-circulate back through the cutwater causing the velocity of the liquid to increase, making the pressure fall, and displacing the impeller in the opposite direction. Figure 83 shows a standard volute with the key dimensions; throat area A_{th}, base circle D_3 and the volute radius r_v as a function of angle θ.
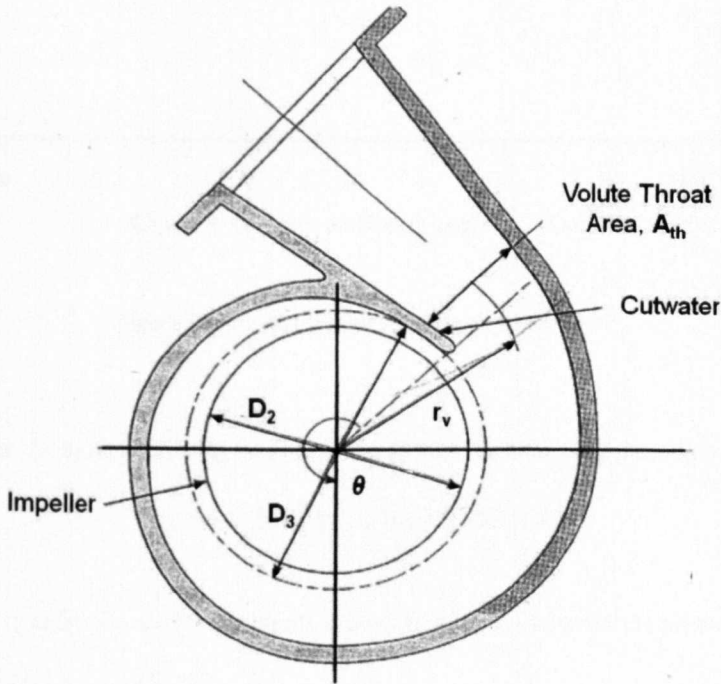
Figure 83: Volute key dimensions (adapted from [112]).

Throat velocity c_3

The volute velocity distribution factor R_{c3} is the ratio of the volute throat velocity c_3 to the impeller actual discharge velocity c_2' and depends on the value of specific speed n_s. The ratio is lower for high specific speed pumps, where the actual discharge angle is larger. The previously calculated value for the impeller absolute velocity discharge angle α_2' is used to select the volute velocity distribution factor from Figure 84.
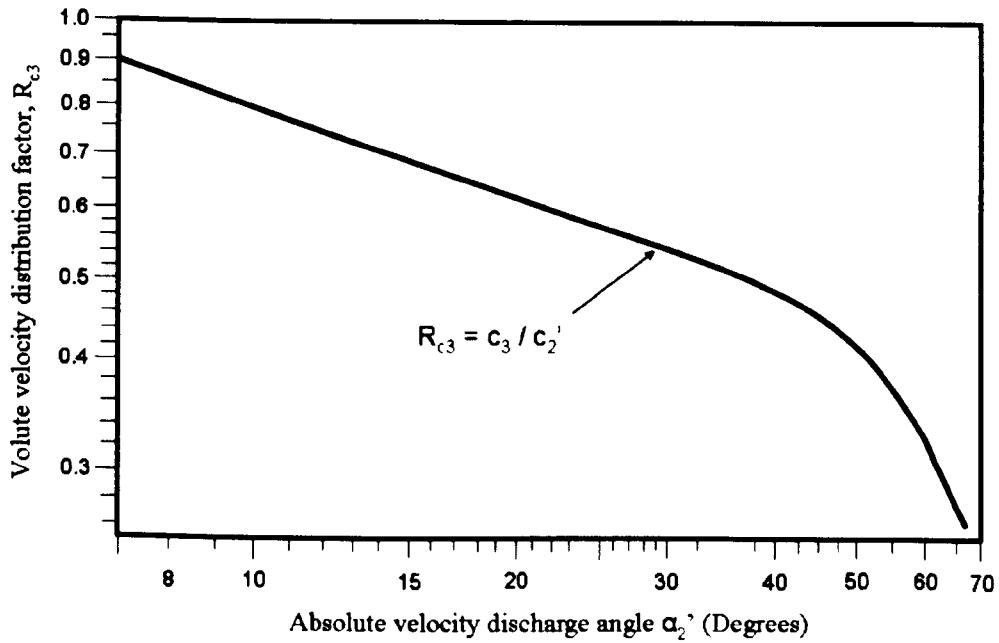
Figure 84: Volute velocity distribution factor [82]

The volute velocity distribution factor R_{c3} may be calculated from the equation derived from Figure 84.

$$R_{c3} = -0.2387 \ln(\alpha_2') + 1.3552 = 0.70$$

It is now possible to determine the throat velocity c_3 by multiplying this factor by the magnitude of the actual discharge velocity c_2'.

$$c_3 = R_{c3}c_2' = 0.681 \times 3.16 = 2.15 m/s \tag{A29}$$

Throat area A_{th}

Once the throat velocity c_3 has been calculated, it is possible to calculate the area of the volute at any angle around the impeller. The throat area is the maximum that the volute area reaches, and is the point at which the entire flow rate Q passes. Lobanoff and Ross describe the throat area A_{th} as the most important parameter in volute design [61]. The throat area is calculated below.

$$A_{th} = \frac{Q}{c_3} = \frac{0.000083}{2.15} = 0.000039 m^2 \qquad (A30)$$

Base-circle D_3

The base-circle diameter determines the distance of the cutwater from the rotational axis, and thus the distance between the impeller and the cutwater. A common approximation for the base-circle diameter is to make it 10% larger than the diameter of the impeller. However, as the base-circle is such a critical design component of the pump, especially when the pump is operating off design conditions (such conditions exist in LVAD design), the exact solution is shown.

If the pumping capacity is lower than the design point, the cutwater will deflect the flow approaching the throat back into the volute resulting in considerable recirculation. If the base-circle is too large then the level of recirculation increases; this reduces the efficiency due to energy being wasted in recirculation of the flow. Conversely, if the base-circle diameter is too small, strong pressure fluctuations are encountered at the blade passing frequency causing an increase in noise.

Setting the base-circle at the correct size ensures that the pressure distributions, and hence the radial forces acting on the impeller remain constant. Further to this, the design of the bearing relies on matching the forces that act on the impeller, highlighting the complexity in the design. If the pressure of the blood entering the pump varies with the diastolic and systolic pressures of the heart, the velocity of the fluid, and therefore the forces acting upon the impeller, will be constantly changing. This also has implications for the design of the magnetic drive system as the pressure in the pump affects the lag angle between the driving and driven components. This in turn affects the force of axial attraction between the two parts which will vary the separation between the impeller and the volute. As the separation changes, the pressure in the hydrodynamic fluid varies, thus altering the force that this bearing generates.

The base circle is expressed as a fraction **P** of the impeller diameter. It represents the minimum diametrical gap between the base circle diameter and the diameter of the impeller. Fraction **P** is selected from Figure 85 in correspondence to the specific speed of the pump; from this the base circle diameter D_3 can be calculated.
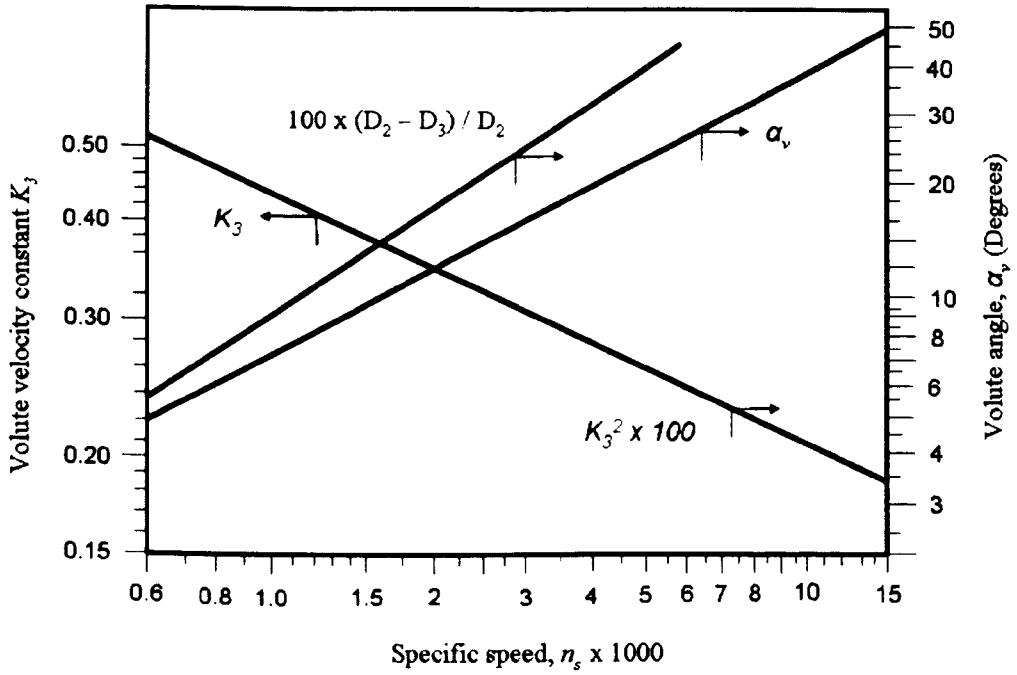
Figure 85: Volute Constants [82]

$$p = \frac{D_3 - D_2}{D_2} = 0.064 \qquad (A31)$$

Alternatively fraction (p) may be calculated from Equation 56 below.

$$p = 0.00008n_s^2 + 0.0096 \qquad (A32)$$

The base circle is then calculated:

$$D_3 = pD_2 + D_2 = 0.064 \times 0.0447 + 0.0447 = 0.0477m$$

(Compare this to the approximated value of 110% of the impeller diameter: $1.1 \times 0.0447 = 0.0492m$. It is shown how this approximation introduces error when designing smaller pumps.)

Volute Width b_3

The volute width b_3 is important in allowing the flow of fluid from the impeller to the volute. There will be the lowest loss in this transition if the impeller discharges liquid into a body of rotating fluid as opposed to a stationary wall. Stepanoff details how the volute width can be determined for applications according to the specific speed of the device [60]. Parameters are shown in Table 24.

Table 24: Volute Width Design Parameters [60]

Specific Speed (n_s)	Volute Width (b_3)
High (≥3000)	1.6 b_2
Medium	1.75 b_2
Low	2.0 b_2
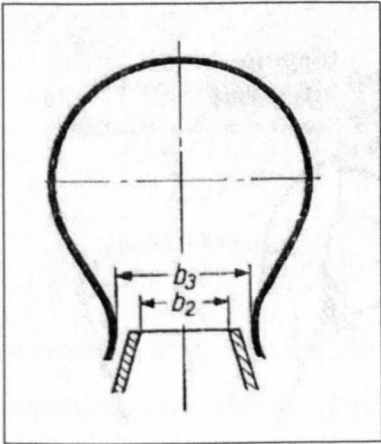
Figure 86: Volute width [113]

The volute width b_3 is calculated below:

$$b_3 = 2b_2 = 2 \times 0.000787 = 0.00157m$$

(A34)

Volute Angle α_v

The volute angle α_v corresponds to the direction of the absolute velocity vector at the impeller discharge α_2'. Shock and separation seen by the fluid is minimised by matching these angles. Efficiency deterioration is

more pronounced with centrifugal pumps employing diffuser vanes surrounding the impellers circumference. Since low to medium specific speed pumps usually employ single volute casing, considerable deviation from this angle is possible with little effect on the efficiency. This is less important in pumps of lower specific speed, to the extent that this design consideration is negligible and may even be dismissed to improve efficiency [60]. An important design consideration however is how the volute angle α_v could affect thrombosis within the pump. If the angle is too small, flow separation and therefore stagnation within the flow may occur just after the cutwater in the discharge nozzle. If the angle is too large a stagnation area may occur to the impeller side of the cutwater. Therefore ignoring the effect that the volute angle introduces may be seen as acceptable in pumps of normal application; when blood is considered as the pumped fluid, thrombolytic considerations must be introduced.

To satisfy the continuity of flow,

$$\alpha_v = \sin^{-1}\frac{A_{th}}{(b_3 D_3 \pi)} = \sin^{-1}\frac{0.000039}{0.00157 \times 0.0477\pi} = 9.15°$$

(A35)

Volute Geometry

Using the above methodology it was possible to calculate the geometry of the volute. Details are shown in the Figure 87. Volute channel cross-sectional areas are calculated as a fraction of the throat area as a function of the position around the impeller.
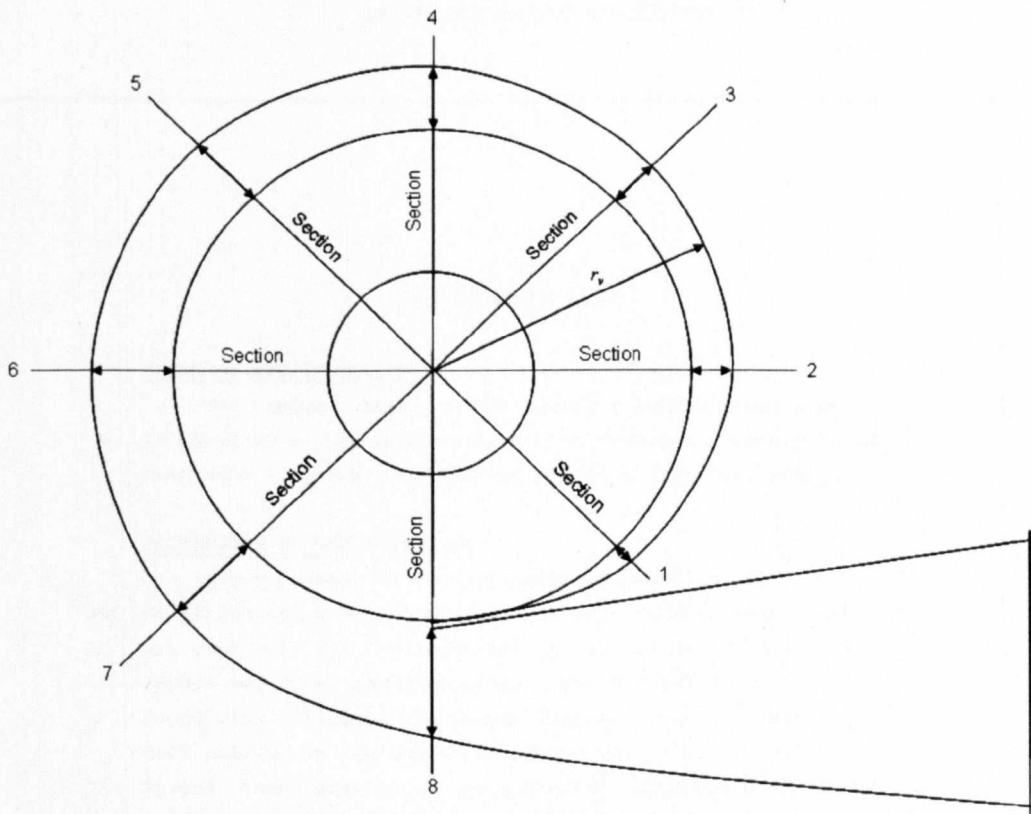
Figure 87: Typical single volute profile [61].

Table 25: Volume of cross-sections around the volute

Section Number	1	2	3	4	5	6	7	8(A_{th})
Volute Area (mm^2)	4.875	9.75	14.625	19.5	24.375	29.25	34.125	39

APPENDIX B: PATENT APPLICATION

- 1 -

ROTARY BLOOD PUMP

FIELD OF THE INVENTION

The present invention relates to a rotary blood pump.
5   In particular, the present invention concerns a rotary blood
pump with a hybrid hydrodynamic/magnetic bearing system.

BACKGROUND OF THE INVENTION

Heart failure is a major cause of death in the
10   developed and developing world; it is estimated that there
are currently 901,500 sufferers in the United Kingdom with
65,000 new cases added annually. The British Heart
Foundation estimates the annual cost of heart failure is
£625 million in the United Kingdom alone. In the United
15   States, these statistics are 5,000,000 sufferers 550,000 new
cases annually and an annual cost to the United States
economy of $296,000 million. The World Health Organisation
estimates that Cardiovascular Disease, around 7% of which is
heart failure, contributed to 1/3 of all deaths worldwide
20   and will be the major cause of death by 2010.

The prognosis for heart failure sufferers is poor with
just less than 40% dying within the first year and with 5%
of all deaths in the United Kingdom, approximately 24,000
per annum, being attributable to heart failure. Around 40%
25   of these patients, suffer from impaired left ventricular
systolic function and could benefit from mechanical support
e.g. with a left ventricular assist device. The best
therapy for many of these patients would be heart
transplantation; however the demand for donor hearts in the
30   United States alone is around 100,000 per annum and far
exceeds the 2,200 donor hearts available per annum. The
other main therapies commonly available are medical, such as

332524

163

2

inotropes, ACE inhibitors, Beta blockers, diuretics and
nitrates, or are mechanical support therapies, such as the
use of total artificial hearts or ventricular assist
devices, of which rotary blood pumps are a subset.

5   There is a continuum of treatment modalities for
patients suffering chronic heart failure. As the disease
progresses patients will receive increasingly aggressive
medical therapies, but most patients become refractory to
medical therapies at some point and their health will

10   decline. Patients eligible for cardiac transplantation
would typically receive medical therapies whilst awaiting
transplantation; if their condition deteriorates then
mechanical "bridge to transplantation" may be adopted in the
form of a mechanical support device such as an intra-aortic

15   balloon pump, extra-aortic balloon pump, or other left
ventricular assist device. Patients who are supported in
bridge to transplantation whilst awaiting transplantation
are in a better state of health at the time of
transplantation, and are more likely to survive transplant

20   surgery and have a better long-term prognosis. Patients
ineligible for transplantation typically follow a medical
therapy-only path, though with the most aggressive health-
care providers may receive mechanical support, e.g. a
ventricular assist device or a total artificial heart in

25   "destination therapy".
        Several mechanical devices are currently available or
are in development which support cardiac function in heart
failure. Rotary blood pumps take blood typically from the
ventricle of the native heart, energise it through the

30   action of a rotating impeller, and deliver the blood to the
ascending aorta. These devices allow the patient to be
ambulatory, to leave hospital, and to have a reasonably

- 3 -

normal lifestyle. Bearing systems used to support the rotor
of rotary blood pumps fall in to three main categories:
mechanical contact bearings, magnetic bearings and
hydrodynamic bearings. Mechanical contact bearings suffer
5   from heat generation which can lead to thrombosis and even
seizure. Mechanical contact bearings also suffer from
mechanical wear which limits their longevity. Magnetic
bearings can be either passive, using permanent magnets
only, or active using permanent and electromagnets and
10   sensors to determine the position of the rotor. Following
Earnshaw's theorem, magnetic bearings require at least one
degree of freedom to be actively controlled for stability,
which can lead to complex sensing and control requirements
and additional power draw. Hydrodynamic bearings typically
15   require large surface areas on their bearing pads and have a
large solidity on the rotor which reduces stage efficiency
and increases power draw (see, for example, the device in US
6,250,880). Additionally rotary blood pumps tend to be
expensive due to the use of exotic materials such as
20   titanium, because of the need for manufacture to very tight
tolerances or positional sensing elements brought about
primarily by the requirements of the system used to bear the
rotor of the blood pump.

     The present invention seeks to provide an alternative
25   rotary blood pump which provides various advantages over
those of the prior art.

332124

- 4 -

SUMMARY OF THE INVENTION

According to a first aspect of the present invention, there is provided a rotary blood pump comprising a rotor and a stator. In this context, the term "rotary blood pump"

5 means a rotary pump suitable for pumping blood. Such a pump could be used, for example, as part of a ventricular assist device. Although the rotary blood pump of the first aspect of the present invention is suitable for pumping blood, it could also be used to pump other fluids if desired.

10 According to the first aspect of the present invention, the rotor of the rotary blood pump defines an axis of rotation, and the rotor has a rotor hydrodynamic bearing surface and rotor bearing magnets. The stator houses the rotor, and the stator has a stator hydrodynamic bearing surface and stator

15 bearing magnets. The rotor hydrodynamic bearing surface and the stator hydrodynamic bearing surface are arranged to form an axial hydrodynamic bearing with a bearing gap between the two hydrodynamic bearing surfaces for the passage of blood. The hydrodynamic bearing is arranged to provide a

20 hydrodynamic force which acts to force the hydrodynamic bearing surfaces axially apart during rotation of the rotor. The stator bearing magnets and the rotor bearing magnets are arranged to form an axial magnetic bearing for preloading the hydrodynamic bearing by providing a magnetic force which

25 acts to force the hydrodynamic bearing surfaces axially together. Note that the stator hydrodynamic bearing surface and the rotor hydrodynamic bearing surface are together referred to as "the hydrodynamic bearing surfaces" for ease of reference.

30 A key feature of the rotary blood pump of the present invention is the axial magnetic preload of the axial hydrodynamic bearings.

332524

- 5 -

The use of a hydrodynamic bearing only on one end of
the rotor, e.g. within a shroud which forms part of the
rotor, allows for the possibility of a semi-open rotor
design with low rotor solidity on the blades of the rotor
5   which do not incorporate any hydrodynamic bearing. This
allows for much improved fluid flow efficiencies on the
rotor blades which leads to extended battery life, or to
less cumbersome batteries for the patient to carry. There
are low energy losses in the bearings such that high pump-
10   stage efficiencies are achieved.

     Another advantage of this design is that, since the
hydrodynamic bearing is preloaded by a magnetic bearing,
rather than by another hydrodynamic bearing, the rotary
blood pump is tolerant of wider manufacturing tolerances and
15   may be manufactured using high-throughput manufacturing
processes including injection moulding. Therefore,
according to a second aspect of the present invention, there
is provided a method of manufacturing the rotary blood pump
of the first aspect, wherein the rotor and the stator are
20   formed by injection moulding.

     The rotary blood pump of the present invention is a
versatile mechanical cardiac prosthesis. It is suitable for
implantation in human patients for the longer-term or
shorter-term treatment of heart failure in bridge to
25   transplant, bridge to recovery or bridge to alternative
therapy, or as a disposable pump used in the very short-
term.

     In one embodiment, the hydrodynamic bearing is the
30   principal bearing component which acts to force the
hydrodynamic bearing surfaces <u>apart</u> in an axial direction.
In other words, there are no significant magnetic bearing

332524

- 6 -

forces acting to push the hydrodynamic bearing surfaces
apart. In a preferred embodiment, the hydrodynamic bearing
is the only bearing component arranged to force the rotor
hydrodynamic bearing surface away from the stator
5   hydrodynamic bearing surface in an axial direction. In
other words, there are no magnetic forces acting to push the
hydrodynamic bearing surfaces apart.

In one embodiment, the hydrodynamic bearing provides
hydrodynamic forces on the rotor in one axial direction
10   only. For example, the hydrodynamic bearing may provide an
upward axial hydrodynamic bearing force which opposes a
downward magnetic axial bearing force, but there is no
downward hydrodynamic bearing force.

In one embodiment, the hydrodynamic bearing surfaces
15   are substantially planar. In an alternative embodiment, the
hydrodynamic bearing surfaces are substantially conical.
This embodiment advantageously allows hydrodynamic forces to
develop in all three translational degrees of freedom and in
two rotational degrees of freedom. Thus, this embodiment of
20   the rotary blood pump has increased stability.

The hydrodynamic bearing may be a spiral groove
bearing, or a pad bearing, for example. However, other
forms of hydrodynamic bearing surfaces are envisaged within
the scope of the invention.
25

In one embodiment, all of the stator bearing magnets
act to preload the hydrodynamic bearing by forcing the
hydrodynamic bearing surfaces axially together. In other
words, a unidirectional axial magnetic preload is applied to
30   the hydrodynamic bearing by the stator bearing magnets. So,
there are no stator bearing magnets which provide an axial
magnetic force component in the opposing direction which

332174

- 7 -

would act to force the hydrodynamic bearing surfaces axially
apart (i.e. which would act to increase the bearing gap).
Thus, a magnetic force is imposed on the rotor only in one
axial direction (e.g. downwards) and all upward force on the
5   rotor is hydrodynamic (in the absence of any shock forces,
etc.).

     Advantageously, the axial magnetic bearing is passive.
In other words, the stator bearing magnets and the rotor
bearing magnets are all passive such that there is no active
10 control of the magnetic bearing forces based on feedback
from one or more sensors. Thus, the rotary blood pump
provides completely passive suspension of the rotor within
the stator.

     In one embodiment, the stator bearing magnets include
15 an array of electromagnets. Advantageously, the stator
bearing electromagnets and the rotor bearing magnets are
arranged to drive rotation of the rotor about the axis of
rotation. Thus, the use of electromagnets as some/all of
the stator bearing magnets allows for the possibility of
20 driving rotation of the rotor about the axis of rotation
using the stator bearing magnets and the rotor bearing
magnets. In other words, the magnets used to form the axial
magnetic bearing are also used for the purpose of driving
the rotation of the rotor about the axis of rotation. This
25 is essentially achieved by applying time varying currents to
the various stator electromagnets at their circumferential
locations around the rotor, whilst at the same time ensuring
that the same overall axial magnetic force is applied to the
bearing. Alternatively, the stator may further comprise an
30 array of driving electromagnets that are distinct from the
stator bearing magnets, such that the array of driving
electromagnets is used to drive rotation of the rotor about

332124

169

- 8 -

the axis of rotation, whereas the stator bearing magnets are
used to form part of the axial magnetic bearing. Thus, in
this embodiment, the driving and bearing magnetic functions
are performed by different sets of magnets. In one
5   embodiment, the stator bearing magnets array include an
array of permanent magnets. Thus, the stator bearing
magnets may in fact include permanent and/or electromagnets.

     In one embodiment, the stator comprises a substantially
10   conical surface at an end of the stator remote from the
hydrodynamic bearing surface, and the rotor comprises a
substantially conical profile at an end of the rotor remote
from the hydrodynamic bearing surface. Other known non-
conical embodiments are also envisaged within the scope of
15   the claims. For example, a spline-fitted or linear curve
configuration may be used for the end of the rotor remote
from the hydrodynamic bearing surface (i.e. the end of the
rotor including the blades). See, for example, Figure 5 and
the associated description later in the application.
20

     In one embodiment, the magnetic axes of the stator
bearing magnets and the magnetic axes of the rotor bearing
magnets are parallel to the axis of rotation. The magnetic
axes of the stator bearing magnets may be radially offset
25   from the magnetic axes of the rotor bearing magnets. In
addition to the axial magnetic forces, this embodiment
provides radial magnetic forces which gives stability
against radial translations of the rotor position within the
stator housing.
30   In an alternative embodiment, the magnetic axes of the
stator bearing magnets and the magnetic axes of the rotor
bearing magnets are angled with respect to the axis of

332674

- 9 -

rotation. The angle may be between 0° and 180°, with the
limiting cases of 0° and 180° giving parallel axes as
described above. This is another way of providing radial
magnetic bearing forces for giving magnetic control in
5 additional magnetic degrees of freedom (as well as the axial
direction).

In one embodiment, the magnetic axes of the stator
bearing magnets are coaxial with the magnetic axes of the
rotor bearing magnets.

10 In one embodiment, the axial magnetic bearing is
attractive. In this case, the hydrodynamic bearing surfaces
are disposed between the stator bearing magnets and the
rotor bearing magnets, and there is an attractive magnetic
force between the stator bearing magnets and the rotor
15 bearing magnets so as to force the hydrodynamic bearing
surfaces axially together. This is the preferred
embodiment. Alternatively, the axial magnetic bearing is
repulsive. In this case, the rotor bearing magnets are
disposed between the stator bearing magnets and the
20 hydrodynamic bearing surfaces, and there is a repulsive
magnetic force between the stator bearing magnets and the
rotor bearing magnets so as to force the hydrodynamic
bearing surfaces axially together. This alternative
"repulsive" configuration is less stable than the preferred
25 "attractive" configuration, and would therefore ideally be
used in conjunction with stator bearing magnets including an
array of actively-controlled electromagnets.

Advantageously, the magnitude of the axial force
30 generated by the magnetic bearing is approximately half the
magnitude of the maximum opposing axial force able to be
generated by the hydrodynamic bearing. The maximum axial

337624

The University of
Nottingham

- 10 -

force able to be generated by the hydrodynamic bearing is
generated as the hydrodynamic bearing surfaces are moved
very close together and the bearing gap approaches zero. In
this embodiment, there is equal resistance to bearing
5   touchdown provided in both axial directions (i.e. both the
positive and negative axial directions) under shock loading
conditions. Thus, gravity and shock loading on the rotor in
the downward direction may be accommodated by hydrodynamic
forces, whereas upward disturbing forces (shock or patient
10   standing on their head) may be accommodated by magnetic
forces only. The magnitude of the axial force generated by
the magnetic bearing need not be exactly 50% of the
magnitude of the maximum opposing axial force able to be
generated by the hydrodynamic bearing; axial magnetic forces
15   having a magnitude of, say, between 10 and 90% of the
maximum opposing axial force able to be generated by the
hydrodynamic bearing are also envisaged within the scope of
the invention.

20   **BRIEF DESCRIPTION OF THE DRAWINGS**
       Embodiments of the present invention will now be
described by way of example with reference to the
accompanying drawings in which:
       Figure 1 is a schematic cross-sectional view of a
25   rotary blood pump in accordance with one embodiment the
present invention;
       Figures 2A and 2B are schematic representations of two
alternative embodiments of the rotor hydrodynamic bearing
surface of the rotary blood pump of Figure 1;
30   Figure 3 is a schematic partial cross-section of an
alternative hydrodynamic bearing of the rotary blood pump of
Figure 1;

332524

172

- 11 -

Figure 4 shows two alternative embodiments of the
rotary blood pump of Figure 1 with differing magnet
configurations; and
Figure 5 is a perspective view of an alternative shape
5   of rotor which could be used in the rotary blood pump of the
present invention.

DETAILED DESCRIPTION OF A PREFERRED EMBODIMENT
Figure 1 is a schematic illustration of a cross-section
10 through a rotary blood pump 10 according to one embodiment
of the present invention. The rotary blood pump 10 of
Figure 1 has many features in common with a standard
configuration of a radial (i.e. centrifugal) pump. The
rotary blood pump 10 has a stator 12 which houses a rotor
15 14. The rotor 14 rotates within the stator 12 about an axis
of rotation AA'. In Figure 1, the axis of rotation AA' is
shown aligned with the Z-axis for simplicity. Very roughly,
the rotary blood pump 10 approximates a conical shape with
the axis of rotation AA' extending along the axis of the
20 cone.
The stator has a first end 12a at the narrow end of the
cone shape and a second end 12b at the wide planar end of
the cone. The size of the stator 12 increases from the
first end 12a towards the second end 12b. The stator has
25 two openings which respectively form an inlet 16 and an
outlet 18 of the rotary blood pump 10 for the passage of
blood.
The inlet 16 is located at the first end 12a of the
stator 12 and extends axially (i.e. along the axis of
30 rotation AA' of the rotary blood pump 10). The second end
12b of the stator 12 is substantially formed as a disc which
extends perpendicular to the axis of rotation AA'. In

332574

173

- 12 -

Figure 1, the direction of rotation of the rotor 14 within
the stator 12 is shown by arrow R and is clockwise when
viewed from above through the inlet 16.

The outlet 18 is located near the disc-shaped second
5   end 12b of the stator 12 at an edge of the disc (i.e. at a
distance from the axis of rotation AA'). A volute 29
collects blood as it flows off the rotor 14. In the
embodiment of Figure 1, the cross-sectional area of the
volute 29 increases as a function of circumferential
10   position around the Z-axis in the direction of rotation
indicated by the arrow R. For example, as shown in Figure 1
the volute 29 has a relatively small cross-sectional area on
the left hand side 29a increasing to a relatively large
cross-sectional area on the right hand side 29b. Then the
15   volute 29 has its largest cross-sectional area on the right
hand side 29b in Figure 1, at which point the volute 29
extends outwards in the Y-direction to form the outlet 18 of
the rotary blood pump 10. Thus the second end 12b of the
stator 12 is asymmetric due to the increasing size of the
20   volute 29. The outlet 18 extends substantially
perpendicular to a plane including the axis of rotation AA';
in Figure 1, this plane is the X-Z plane such that the
outlet 18 extends in a direction parallel to the Y-axis
(i.e. into or out of the page). It is also envisaged within
25   the scope of this invention that other volute arrangements
may be used for the collection of blood as it flows off the
rotor; these arrangements would include a circular
essentially concentric volute along with split volutes
widely known in radial pump design.
30   The rotor 14 also has a substantially conical outer
profile as it increases in size from a first end 14a at the
narrow end of the cone to a substantially disc-shaped second

332424

- 13 -

end 14b at the planar end of the cone. The rotor 14 has
blades 20 which each extend from the first end 14a and
increase in size as they extend to the second end 14b. The
rotor has a bore 21 which extends axially from the first end

5   14a to the second end 14b. In alternative embodiments, the
bore 21 may be omitted.

        As an alternative to the substantially conical outer
profile of the rotor 14 shown in Figure 1, other non-conical
shapes of outer profile are also envisaged within the scope

10   of the invention. See, for example, the alternative shape
of rotor 14 shown in Figure 5. In Figure 5, the rotor 14 is
essentially discoid but with a slight rise towards its axis
of rotation AA'. Thus, each blade 20 comprises an upper
surface 19 in the form of a low swept curve.

15   The stator 12 includes stator magnets 22, and the rotor
14 includes rotor magnets 24. In the cross sectional view
of Figure 1, two stator magnets 22a and 22b and two rotor
magnets 24a and 24b are shown, but there may be more. The
rotor magnets 24 are permanent magnets. The stator magnets

20   22 include stator electromagnets for driving rotation of the
rotor 12 about the axis of rotation AA'. The stator magnets
24 additionally include magnets to provide a magnetic axial
bearing as described further below. The bearing magnets may
be electromagnets and/or permanent magnets (i.e. the use of

25   electromagnets is not essential for the bearing magnets, cf.
the drive magnets). Advantageously, a single set of
electromagnets may be used both to drive rotation of rotor
12 and to act as an axial magnetic bearing, although
different sets of magnets could alternatively be used for

30   these different purposes.

        In use, a time-varying current is applied to the stator
electromagnets so as to drive rotation of the rotor 12 by

3325324

- 14 -

magnetic coupling between the stator electromagnets and the
rotor magnets 24. The rotation of the rotor 12 and the
associated rotor blades 20 causes blood to flow through the
rotary blood pump 10 from the inlet 16 to the outlet 18. In
5   other words, blood is caused to flow through the rotary
blood pump 10 through the action of the blades 20
incorporated into the rotor 12 as it rotates under the
influence of the magnet coupling produced by the stator
electromagnets and the rotor magnets 24.
10

      The rotary blood pump 10 uses a non-contact hybrid
hydrodynamic/magnetic bearing system to allow the rotor 12
to rotate within the stator. The non-contact hybrid
hydrodynamic/magnetic bearing system suspends the rotor 14
15   within the stator 12. Depending on the type of stator
magnets 22 used, the rotor 14 may be suspended completely
passively within the stator 12, as described below.

      The hydrodynamic bearing is formed from two
20   substantially planar hydrodynamic bearing surfaces 26 and 28
with a bearing gap 30 therebetween for the passage of blood.
The stator hydrodynamic bearing surface 28 is an interior
substantially circular surface of the stator 12 at the
second end 12b. The rotor hydrodynamic bearing surface 26
25   is an exterior surface of the rotor 14 at the second end 14b
of the rotor 14; the rotor hydrodynamic bearing surface 26
is substantially circular with a central aperture 27 formed
by the axial bore 21. The bearing surfaces 26 and 28 face
each other in use.
30   For hydrodynamic forces to be developed within the
bearing gap 30 under relative rotation of the rotor 14 and
the stator 12 about axis AA', the width W of the bearing gap

332524

- 15 -

30 varies circumferentially in the direction of rotation
indicated by the arrow R.

Figure 2 shows two alternative embodiments of the rotor
5   hydrodynamic bearing surface 26 which provide a suitable
variation in the width W of the bearing gap 30 when the
stator hydrodynamic bearing surface 28 is flat. It is of
course feasible in an alternative embodiment that the rotor
hydrodynamic bearing surface 26 is flat and variations in
10   the width W of the bearing gap are achieved instead by
height variations incorporated into the stator hydrodynamic
bearing surface 28.

Figure 2A shows a "spiral groove bearing" configuration
of the rotor hydrodynamic bearing surface 26. In
15   particular, the rotor hydrodynamic bearing surface 26 is
substantially planar but comprises a series of shallow
spiral grooves 32 between raised lands 34. Each groove 32
is arcuate and extends from an edge of the rotor
hydrodynamic bearing surface 26 adjacent the central
20   aperture 27 to the circumferential peripheral edge of the
rotor hydrodynamic bearing surface 26. All of the grooves
32 are curved in the same sense around the annular rotor
hydrodynamic bearing surface 26. In Figure 2A, the grooves
curve in a forwards direction relative to the direction of
25   rotation R; however, it is envisaged that backward-curving
grooves 32 could be used instead. The difference in height
between the grooves 32 and the lands 34 may be in the region
of 5μm to 100μm and it is this height difference that
facilitates the development of hydrodynamic bearing forces
30   between the rotor hydrodynamic bearing surface 26 and the
stator hydrodynamic bearing surface 28. The difference in
height between the grooves 32 and the lands 34 may take the

332524

- 16 -

form of a step change or a chamfer or may be curved, for
example. As shown in Figure 2A, the direction of rotation R
of the rotor 14 is anticlockwise when viewed from below.
Figure 2B shows a "pad bearing" configuration of the
5   rotor hydrodynamic bearing surface 26. In particular, the
rotor hydrodynamic bearing surface 26 is substantially
planar but comprises a series of much wider raised lands 38
which each vary in height from a minimum at the leading edge
38a of the land 38 to a maximum at the trailing edge 38b of
10 the land 38. The difference in height between the leading
38a and trailing 38b edges of the lands 38 may be in the
region of 5μm to 100μm and it is this height difference that
facilitates the development of hydrodynamic bearing forces
between the rotor hydrodynamic bearing surface 26 and the
15 stator hydrodynamic bearing surface 28. As shown in Figure
2B, deeper radially disposed grooves 36 may be incorporated
into the rotor hydrodynamic bearing surface 26 in addition
to the variable height lands 38. The grooves 36 improve the
flow of lubrication fluid between the outer periphery and
20 the central aperture 27, thereby preventing starvation of
the hydrodynamic bearing.

In the embodiment of Figure 1 which incorporates
substantially planar hydrodynamic bearing surfaces 26 and
25 28, hydrodynamic forces are developed which provide control
over one translational degree of freedom, namely the axial
Z-direction as shown in Figure 1, and two rotational degrees
of freedom, namely rotation about the X and Y axes as shown
in Figure 1. It should be noted that the hydrodynamic
30 bearing only provides hydrodynamic forces which act on the
rotor 14 in one axial direction (i.e. upwards in the +Z
direction in Figure 1). These hydrodynamic forces must be

332624

178

- 17 -

sufficient to withstand the opposing magnetic preload force
(discussed below) and any disturbing forces (shock and
gravitational loading).

The axial bore 21 allows for the passage of blood
5   therethrough in use. This ensures that there is always
blood present in the hydrodynamic bearing to thereby prevent
bearing starvation.

Rather than the hydrodynamic bearing surfaces 26 and 28
10 being substantially planar as described above, they may
instead be substantially conical as shown in Figure 3, which
is a partial cross-section of an alternative hydrodynamic
bearing of the rotary blood pump 10. This "conical
hydrodynamic bearing" embodiment employs radial as well as
15 axial hydrodynamic forces so as to provide control over the
two other translational degrees of freedom, namely
translation along the axes X and Y which are perpendicular
to the axis of rotation AA' in Figure 1.

In this conical hydrodynamic journal bearing
20 embodiment, the bearing gap 30 between the stator 12 and the
rotor 14 is defined by the essentially conical hydrodynamic
bearing surfaces 26 and 28.

The rotor hydrodynamic bearing surface 26 is formed as
a frustroconical surface due at least to the presence of the
25 central aperture 27 at the end of the axial bore 21. In
addition, as shown in Figure 3, there may be an optional
annular land 31 on the end of the rotor 14 around the exit
of the axial bore 21. In this case, the axial bore 21 has a
smaller diameter than the annular land 31. The
30 frustroconical rotor hydrodynamic bearing surface 26
projects outwards from the rotor 14 in Figure 3 such that

1325624

- 18 -

the rotor hydrodynamic bearing surface 26 is essentially
convex.

In Figure 3, the stator hydrodynamic bearing surface 28
is a conical surface which forms a conical aperture in the
5   stator 12 for receiving the outwardly-projecting (convex)
frustroconical rotor hydrodynamic bearing surface 26. Thus,
in the embodiment of Figure 3, the stator hydrodynamic
bearing surface 28 is essentially concave such that the
rotor 14 is received within the stator 12 at the
10   hydrodynamic bearing.

In an alternative embodiment, the stator hydrodynamic
bearing surface 28 could incorporate a central land such
that the stator hydrodynamic bearing surface 28 would be
formed as a frustroconical surface. In a further
15   alternative embodiment, the rotor hydrodynamic bearing
surface 26 could be essentially concave and the stator
hydrodynamic bearing surface 28 could be essentially convex
such that the stator 12 would be received within the rotor
14 at the hydrodynamic bearing.

20   It will be appreciated that, rather than being formed
as substantially planar or substantially conical surfaces as
described above, the hydrodynamic bearing surfaces 26 and 28
could instead be formed substantially as portions of a
sphere or other surfaces formed by rotating an arbitrary
25   curve through 360°.

As for the above embodiment which incorporates
substantially planar hydrodynamic bearing surfaces 26 and
28, the width W of the bearing gap 30 in the embodiment of
Figure 3 varies circumferentially in the direction of
30   rotation indicated by the arrow R. A "spiral groove
bearing" or a "pad bearing" configuration may be used on the

332624

180

- 19 -

rotor hydrodynamic bearing surface 26 or the stator
hydrodynamic bearing surface 28 in this regard.

If the rotor 14 is pushed downwards (in direction -Z)
towards the stator 16, it meets resistance due to the need
5   for blood to be expelled from the bearing gap 30. The width
W of the bearing gap 30 between the hydrodynamic bearing
surfaces 26 and 28 may also vary radially (i.e. in the
direction indicated by the arrow F in Figure 3). If the
bearing gap 30 at larger radius is smaller than the bearing
10 gap 30 closer to the axis, then this resistance will be
greater as it will be harder for the blood to exit the
bearing gap 30. This effect is known as "squeeze-film
damping". In Figure 3, the bearing gap 30 is shown to
increase radially (i.e. the bearing gap 30 increases with
15 increasing distance from the axis AA'). This results in
less resistance, from squeeze-film damping, to any downward
force on the rotor 14 which acts to reduce the axial bearing
gap 30. In particular, the resistance is less than would be
the case if the bearing gap 30 reduced with increased radial
20 distance from axis AA'.

As for the planar embodiment of Figure 1, the
hydrodynamic bearing in Figure 3 is arranged to force the
rotor hydrodynamic bearing surface 26 away from the stator
hydrodynamic bearing surface 28 in an axial direction on
25 average. There will also be some radial components to the
hydrodynamic bearing forces in the embodiment of Figure 3.
However, when the rotor 14 is completely aligned with the
stator 12 such that both hydrodynamic bearing surfaces 26
and 28 are symmetrically disposed about the axis of rotation
30 AA', the radial hydrodynamic forces will cancel out over the
whole rotor 14 so that the net force is purely axial. In
this configuration, the axis of rotation AA' is aligned with

132474

181

- 20 -

central axes of both the stator 12 and the rotor 14. Of
course, if the rotor 14 is displaced radially (e.g. in
direction X or Y) with respect to the stator 12 such that
the central axes of the rotor 14 and the stator 12 are no
5   longer aligned, then the radial hydrodynamic forces will
become unbalanced. For example, if the rotor 14 is
displaced in direction +Y with respect to the stator 12,
then a hydrodynamic force will be developed in direction -Y
with the effect of restoring the rotor 14 back to the centre
10   of the stator 12 such that the central axes of the stator 12
and the rotor 14 are aligned once again.

Turning to the magnetic part of the non-contact hybrid
hydrodynamic/magnetic bearing system, Figure 4 shows
15   alternative embodiments of the rotary blood pump 10 with
differing magnet configurations. In both cases, only the
rotor 14 and the stator magnets 22 of the stator 12 are
shown. The stator 12 itself is omitted for simplicity. In
the main embodiment described below, the same stator magnets
20   22 are used both to drive rotation of the rotor 14 and to
form part of an axial magnetic bearing. Both magnetic
embodiments shown in Figure 4 use substantially planar
hydrodynamic bearing surfaces 26 and 28, as described above
with reference to Figure 1. However, other forms of
25   hydrodynamic bearing surfaces 26 and 28 could alternatively
be used, as described above with reference to Figure 3.

In the "axial motor" magnet configuration of Figure 4A,
the stator magnets 22 have magnetic axes 23 which are
30   aligned parallel to the axis of rotation AA' of the rotor
14. In addition, the rotor magnets 24 have magnetic axes 25
which are aligned parallel to the axis of rotation AA' of

332574

- 21 -

the rotor 14. Both the rotor magnets 24 and the stator
magnets 22 are spaced from the axis of rotation AA' in
Figure 4A, however this is not essential if separate
electromagnets are used to drive rotation of the rotor 14
5   within the stator 12. The hydrodynamic bearing is located
in between the stator magnets 22 and the rotor magnets 24.
The interaction between the magnetic fields of the stator
magnets 22 and the rotor magnets 24 leads to high axial
magnetic forces acting on the rotor 14. In particular,
10   there is a strong attractive axial magnetic force between
the stator magnets 22 and the rotor magnets 24 which acts to
pull the rotor downwards (i.e. in direction -Z) such that
the rotor hydrodynamic bearing surface 26 is forced axially
towards the stator hydrodynamic bearing surface 28, thereby
15   acting to reduce the bearing gap 30 of the hydrodynamic
bearing.

Thus the interaction between the stator magnets 22 and
the rotor magnets 24 acts as a magnetic bearing which
provides an unbalanced downward axial magnetic force (in
20   direction -Z in Figure 1) which acts to preload the
hydrodynamic bearing formed between the hydrodynamic bearing
surfaces 26 and 28. The hydrodynamic bearing is an integral
part of the bearing system and relies on the unbalanced
downward axial magnetic load to oppose the upward
25   hydrodynamic bearing force.

As it rotates about the axis of rotation AA' in use,
the rotor 14 is suspended within the stator 12 by a
combination of hydrodynamic and magnetic forces. The
magnetic configuration forces the rotor 14 downward (i.e. in
30   direction -Z in Figure 1) onto the hydrodynamic bearing so
as to preload the hydrodynamic bearing to make the rotor 14
stable. If a shock is imparted to the rotary blood pump 10

332524

- 22 -

(e.g. through the patient falling over), the hydrodynamic
bearing is sufficiently stiff so as to prevent the rotor 14
coming in to contact with the stator housing 12. Clearly,
such "touchdown events" are undesirable for efficient
5   working of the rotary blood pump 10. The magnetic bearing
formed by the stator magnets 22 and the rotor magnets 24
incorporates magnetic forces that are sufficiently strong as
to prevent the first end 14a of the rotor 14 and the rotor
blades 20 from touching the adjacent internal surfaces of
10 the stator 12 if the rotary blood pump 10 is inverted or
shocked in a direction which causes upward displacement of
the rotor 12 (i.e. displacement of the rotor 12 in direction
+Z in Figure 1). The maximum practical hydrodynamic bearing
force might be roughly twice the magnetic preload such that
15 equal resistance to bearing touchdown is provided in both
the upward (+Z) and downward (-Z) directions under shock
loading conditions. In other words, the downward magnetic
force is about 50% of the maximum envisaged hydrodynamic
force, which is largest when the hydrodynamic bearing
20 surfaces 26 and 28 come close together such that bearing gap
30 approaches zero. Thus, gravity and shock loading on the
rotor 14 in the downward direction are accommodated by
hydrodynamic forces, whereas upward disturbing forces (shock
or patient standing on their head) are accommodated by
25 magnetic forces only. However it is envisaged that other
ratios of magnetic preload vs maximal hydrodynamic force
might be used to optimise bearing stability.
        As shown in Figure 4A, radial magnetic force components
may be introduced by offsetting the axes 23 of the stator
30 magnets 22 by a distance D relative to the axes 25 of the
rotor magnets 24. The rotary blood pump 10 of this
embodiment might have increased stability as this magnet

132524

184

- 23 -

configuration allows tuning of the translational degrees of
freedom of the rotor in the X and Y directions whilst also
imparting control over two rotational degrees of freedom
(namely rotation about the X and Y axes) whilst allowing
5   rotation of the rotor 14 around the axis of rotation AA'
(i.e. the Z-axis). In an alternative embodiment, the axes
23 of the stator magnets 22 are aligned with the axes 25 of
the rotor magnets 24. In this case, D=0 such that the axes
23 and the axes 25 are located at the same distance from the
10   axis of rotation AA'. This configuration maximizes the
attractive magnetic force between the stator magnets 22 and
the rotor magnets 24 at the expense of radial force
components.

15   In the magnet configuration of Figure 4B the magnetic
axes 23 of the stator magnets 22 and the magnetic axes 25 of
the rotor magnets 24 are angled at an angle α with respect
to the axis of rotation AA'. The angle α between the
magnetic axes 23 and 25 and the axis of rotation AA' may be
20   anywhere between 0° and 360°. This "angled" embodiment
naturally provides radial magnetic bearing components.
However, when the rotor 14 is centred with the stator 12,
the radial magnetic forces cancel out over the whole rotor
14 so that the net force is purely axial. In some
25   embodiments, there may be a small radial bias on the rotor
to yield greater bearing stability. In Figure 4B, the
magnetic axes 23 of the stator magnets 22 and the magnetic
axes 25 of the rotor magnets 24 are all at the same angle
with respect to the axis of rotation AA'. In Figure 4B, the
30   magnetic axes of each pair or stator and rotor magnets 22
and 24 are coaxial; for example, the magnetic axes 23 and 25
of the first pair 22a and 24a of rotor and stator magnets

337174

185

- 24 -

are coaxial, and the magnetic axes 23 and 25 of the second
pair 22b and 24b of rotor and stator magnets are coaxial.
Thus, the stator magnets 22 are located further from the
axis of rotation AA' than the rotor magnets 24 in an axial
5   direction, and the magnetic axes 23 and 25 are angled
inwards toward the axis of rotation AA', thus providing a
radial magnetic bearing force component along with the main
axial magnetic bearing force component. In alternative
embodiments, different angles of inclination to the axis of
10   rotation AA' could be used for the magnetic axes 23 and 25
of the stator 12 and the rotor 14 respectively, including
outward angling of the axes 23 and 25. In situations where
there is a linear translation in direction X and/or Y of the
magnetic axes 25 of the rotor magnets relative to the
15   magnetic axes 23 of the stator magnets 22, the "angled"
embodiment of Figure 4B also provides advantages over the
"axially aligned" embodiment of Figure 4A. With the
"axially aligned" embodiment of Figure 4A, the axial
magnetic bearing force falls off steeply as the translation
20   increases. However, in the "angled" embodiment of Figure
4B, the fall off is very small indeed. Linear translations
of this type would occur if there were a linear translation
of the rotor 14 with respect to the stator 12.

25   The magnetic bearing is completely passive in a
preferred embodiment. By "passive", we mean that there is
no active control of the magnetic bearing forces based on
feedback from one or more sensors as to the position of the
rotor 14 within the stator 12. In this case, the stator
30   bearing magnets and the rotor bearing magnets are all
completely passive (i.e. they are either permanent magnets
or passive, non-controlled electromagnets). Thus, the

133534

186

- 25 -

rotary blood pump 10 can provide completely passive
suspension of the rotor 14 within the stator 12.

Nonetheless, the present invention does not preclude
the use of active magnetic components in addition to or
5   instead of passive magnetic components. Thus, there may be
sensors provided to give some active suspension of the rotor
14 by the stator magnets 22 and the rotor magnets 24 in
axial and/or radial directions.

10   Known rotary blood pumps which use a first hydrodynamic
bearing to force the rotor upwards axially, and a second
hydrodynamic bearing to force the rotor downwards axially
require high levels of precision in the manufacturing
process to ensure that the bearing gaps on the opposing
15   hydrodynamic bearings are a suitable size. In contrast, the
rotary blood pump 10 described herein has a single
hydrodynamic bearing preloaded by a magnetic bearing. This
design means that there is no need for a precise width of
gap between the housing stator 12 and the end 14a of the
20   rotor 14 axially remote from the hydrodynamic bearing.
Thus, the rotary blood pump 10 is tolerant of wider
manufacturing tolerances and may be manufactured using high-
throughput manufacturing processes including injection
moulding. Thus, advantageously, the rotor 14 and the stator
25   12 may be manufactured by injection moulding from bio-
compatible rigid materials such as Polyetheretherketone
(PEEK). A moisture barrier would then be required to
prevent the magnets 22 and 24 from rusting in use. Suitable
moisture barrier materials include gold or nitride coatings.
30   The use of injection moulding techniques means that the
rotary blood pump 10 may be manufactured more cheaply than
existing rotary blood pumps, so may be more widely used in

332624

- 26 -

the developing world as well as for shorter term
applications.

During start-up of the rotary blood pump 10, there is
5   initially no upward hydrodynamic force due to the lack of
rotation of the rotor 14 within the stator 12. Furthermore,
there are no secondary bearings (e.g. magnetic bearings) to
provide an alternative form of upward force during the
start-up period before the hydrodynamic forces are developed
10   by high enough rotation speeds. Therefore, at start-up,
there will briefly be wear on the hydrodynamic bearing
surfaces 26 and 28 during the first half revolution or so of
the rotor 14. In cardiac applications, the rotor 14 should,
of course, only be started once in the patient and possibly
15   a couple of times during manufacture. Thus, there is
negligible damage to the hydrodynamic bearing surfaces 26
and 28. Nonetheless, a coating may be add to the
hydrodynamic bearing surfaces 26 and 28 to act as a
secondary bearing during these very brief start-up periods
20   if desired.

Although preferred embodiments of the invention have
been described, it is to be understood that these are by way
of example only and that various modifications may be
25   contemplated.

332174

- 27 -

CLAIMS:

1.   A rotary blood pump comprising:
       a rotor defining an axis of rotation, the rotor having
5   a rotor hydrodynamic bearing surface and rotor bearing
magnets; and
       a stator which houses the rotor, the stator having a
stator hydrodynamic bearing surface and stator bearing
magnets;
10   wherein the rotor hydrodynamic bearing surface and the
stator hydrodynamic bearing surface are arranged to form an
axial hydrodynamic bearing with a bearing gap therebetween
for the passage of blood, the hydrodynamic bearing being
arranged to provide a hydrodynamic force which acts to force
15   the hydrodynamic bearing surfaces axially apart during
rotation of the rotor; and
       wherein the stator bearing magnets and the rotor
bearing magnets are arranged to form an axial magnetic
bearing for preloading the hydrodynamic bearing by providing
20   a magnetic force which acts to force the hydrodynamic
bearing surfaces axially together.

2.   The rotary blood pump of claim 1 wherein the
hydrodynamic bearing is the principal bearing component
25   which acts to force the rotor hydrodynamic bearing surfaces
axially apart in use.

3.   The rotary blood pump of any preceding claim wherein
the hydrodynamic bearing provides hydrodynamic forces on the
30   rotor in one axial direction only.

333524

189

- 28 -

4.   The rotary blood pump of any of claims 1 to 3 wherein the stator and rotor hydrodynamic bearing surfaces are substantially planar.

5   5.   The rotary blood pump of any of claims 1 to 3 wherein the stator and rotor hydrodynamic bearing surfaces are substantially conical.

6.   The rotary blood pump of any preceding claim wherein
10   there are no stator bearing magnets which act to force the hydrodynamic bearing surfaces axially apart.

7.   The rotary blood pump of any preceding claim wherein the stator bearing magnets and the rotor bearing magnets are
15   passive.

8.   The rotary blood pump of any preceding claim wherein the stator bearing magnets include an array of electromagnets.
20

9.   The rotary blood pump of claim 8 wherein the stator bearing magnets and the rotor bearing magnets are further arranged to drive rotation of the rotor about the axis of rotation.
25

10.   The rotary blood pump of any of claims 1 to 8 wherein the stator further comprises an array of driving electromagnets that are distinct from the stator bearing magnets, the array of driving electromagnets being arranged
30   to drive rotation of the rotor about the axis of rotation.

352124

- 29 -

11. The rotary blood pump of any preceding claim wherein the stator bearing magnets include an array of permanent magnets.

5   12. The rotary blood pump of any of claims 1 to 11 wherein the magnetic axes of the stator bearing magnets and the magnetic axes of the rotor bearing magnets are parallel to the axis of rotation.

10 13. The rotary blood pump of claim 12 wherein the magnetic axes of the stator bearing magnets are radially offset from the magnetic axes of the rotor bearing magnets.

14. The rotary blood pump of any of claims 1 to 11 wherein
15 the magnetic axes of the stator bearing magnets and the magnetic axes of the rotor bearing magnets are angled with respect to the axis of rotation.

15. The rotary blood pump of any of claims 1 to 12 or claim
20 14 wherein the magnetic axes of the stator bearing magnets are coaxial with the magnetic axes of the rotor bearing magnets.

16. The rotary blood pump of any of claims 1 to 15 wherein
25 the hydrodynamic bearing surfaces are disposed between the stator bearing magnets and the rotor bearing magnets, an attractive magnetic force being provided between the stator bearing magnets and the rotor bearing magnets so as to force the hydrodynamic bearing surfaces axially together.
30

17. The rotary blood pump of any of claims 1 to 15 wherein the rotor bearing magnets are disposed between the stator

332574

191

- 30 -

bearing magnets and the hydrodynamic bearing surfaces, a
repulsive magnetic force being provided between the stator
bearing magnets and the rotor bearing magnets so as to force
the hydrodynamic bearing surfaces axially together.

5

18. The rotary blood pump of any preceding claim wherein
the magnitude of the axial force generated by the magnetic
bearing is approximately half the magnitude of the maximum
opposing axial force able to be generated by the

10 hydrodynamic bearing.

19. The rotary blood pump of any preceding claim wherein
the rotor comprises a semi-open rotor design with low rotor
solidity.

15

20. A method of manufacturing the rotary blood pump of any
preceding claim wherein the rotor and the stator are formed
by injection moulding.

20 21. A rotary blood pump substantially as herein described
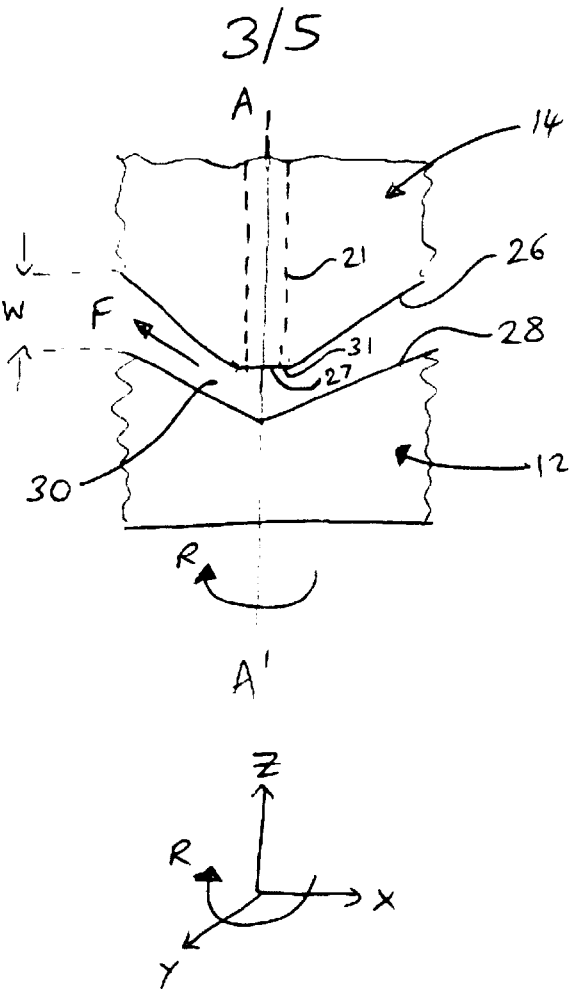with reference to the accompanying drawings.
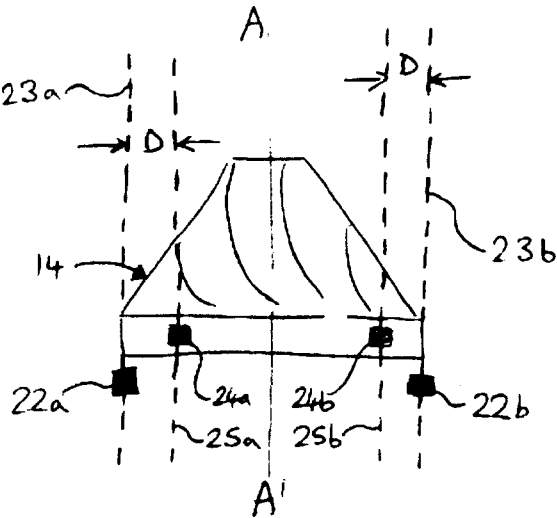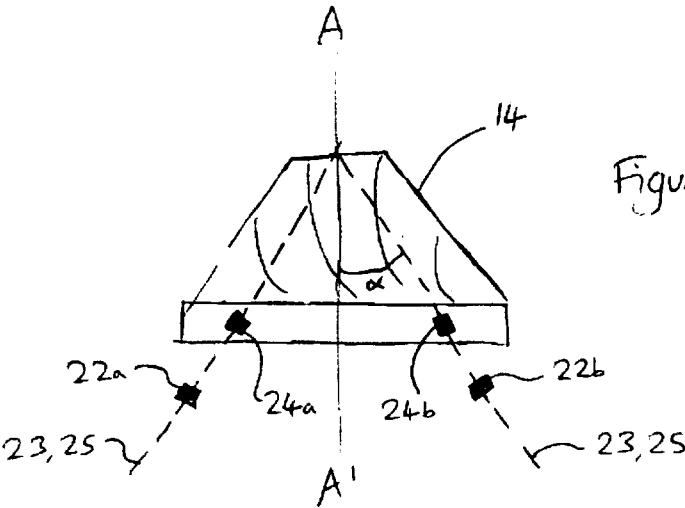
332524

Figure 1
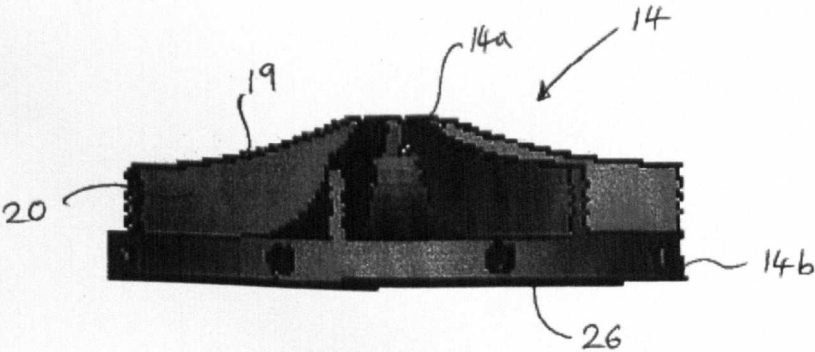
2/5

Figure 2A

Figure 2B

3/5
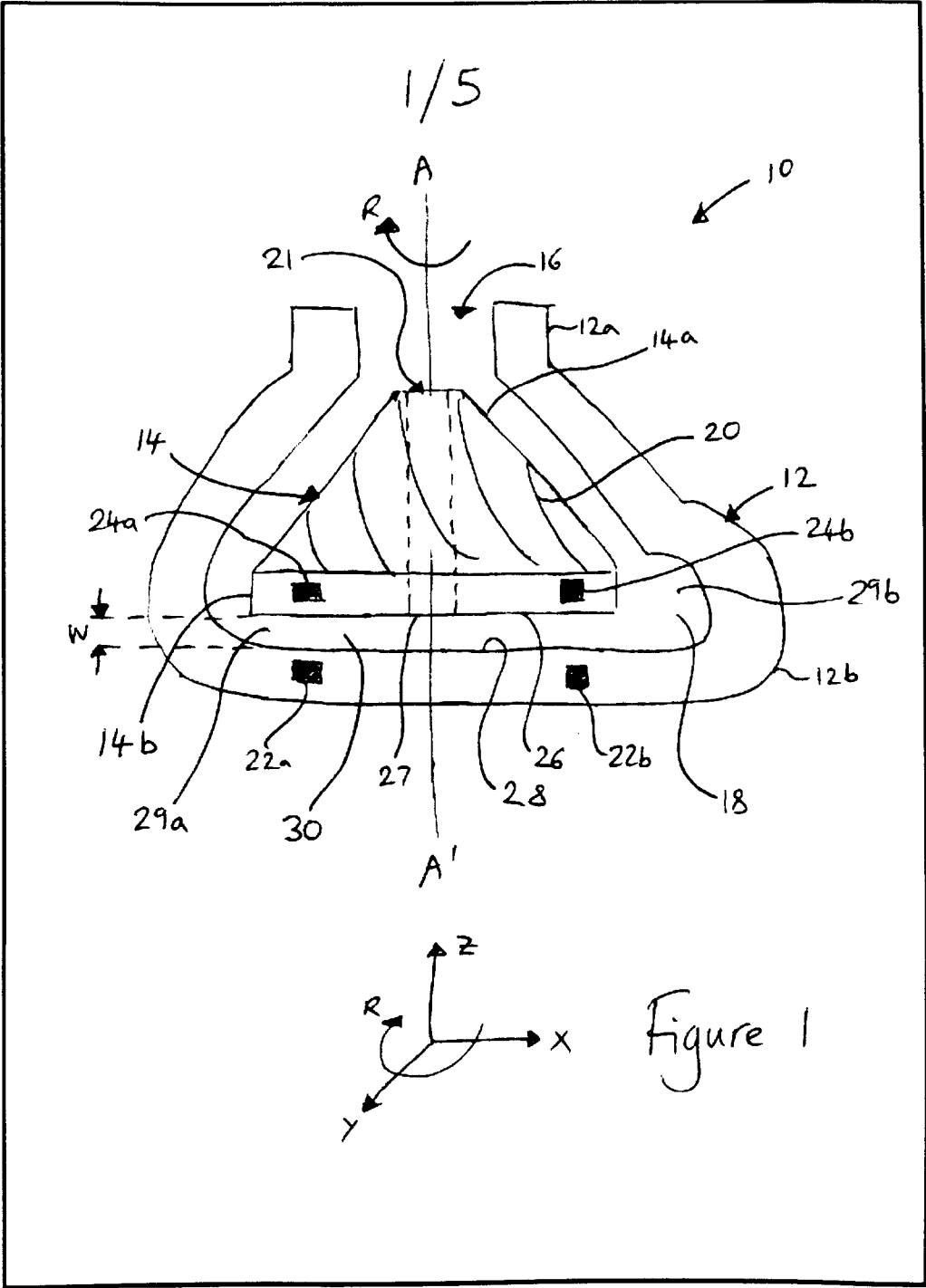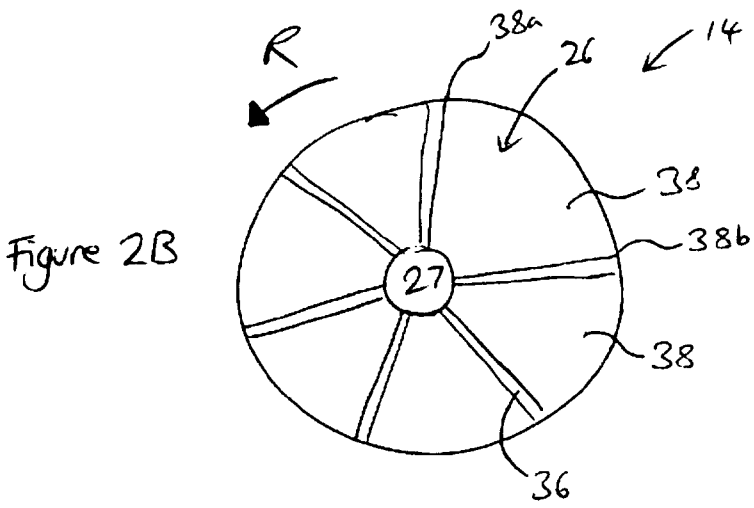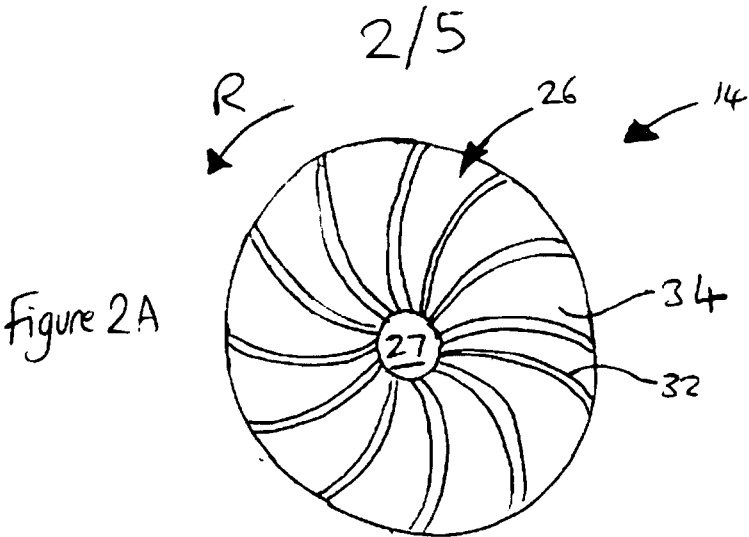
Figure 3

4/5

Figure 4A

Figure 4B

5/5

Figure 5